Circuit Quantum Electrodynamics in a Magnetic Field

Lüthi, Florian

DOI
10.4233/uuid:5986ee2b-e9e6-42ed-a932-bddd5e78648e

Publication date
2019

Document Version
Final published version

Citation (APA)
Lüthi, F. (2019). *Circuit Quantum Electrodynamics in a Magnetic Field*. [Dissertation (TU Delft), Delft University of Technology]. https://doi.org/10.4233/uuid:5986ee2b-e9e6-42ed-a932-bddd5e78648e

CIRCUIT QUANTUM ELECTRODYNAMICS IN A MAGNETIC FIELD

CIRCUIT QUANTUM ELECTRODYNAMICS IN A MAGNETIC FIELD

Dissertation

for the purpose of obtaining the degree of doctor
at Delft University of Technology
by the authority of the Rector Magnificus Prof. Dr. Ir. T.H.J.J. van der Hagen,
Chair of the Board for Doctorates,
to be defended publicly on Monday 25 March 2019 at 10:00 o'clock

by

Florian LÜTHI

Master of Science in Physics,
Eidgenössische Technische Hochschule Zürich, Switzerland,
born in Schwyz, Switzerland.

This dissertation has been approved by the promotors.

Composition of the doctoral committee:

Rector Magnificus,	Chairperson
Prof. dr. L. DiCarlo,	Delft University of Technology, promotor
Prof. dr. ir. L. P. Kouwenhoven,	Delft University of Technology, promotor
Independent members:	
Prof. dr. Y. M. Blanter	Technische Universiteit Delft
Prof. dr. C. W. J. Beenakker	Leiden University
Prof. dr. C. M. Marcus	University of Copenhagen, Denmark
Prof. dr. J. P. Pekola	Aalto University, Finland
Dr. A. Geresdi	Delft University of Technology

Printed by: Gildeprint, Enschede – www.gildeprint.nl

Cover: Artistic impression of the devices discussed in this work.
Design by Cheyenne Hensgens.

Casimir PhD Series, Delft-Leiden 2019-07

ISBN 978-90-8593-388-5

An electronic version of this dissertation is available at `http://repository.tudelft.nl/`.

To all those holding the ladders I climbed to scale the shoulders of giants,
and to all those shaking the ladders just enough to force me to take a firm grip.

CONTENTS

Summary / Samenvatting / Zämefassig **xi**

1 Introduction **1**
1.1 Qubits as flux noise sensors . . . 2
1.1.1 Flux noise from a two-level system . . . 5
1.1.2 Flux noise in the presence of hyperfine coupling . . . 8
1.2 Quantized conductance enabling semi-digital gates . . . 13
1.3 Charge parity detection for topological quantum computing . . . 14
1.4 Coupling transmons to different quantum systems . . . 14
1.5 Thesis overview . . . 15

2 Semiconducting-Superconducting hybrid transmon devices **17**
2.1 Engineering atoms . . . 18
2.2 Andreev bound states and Josephson junctions . . . 18
2.2.1 Andreev reflection . . . 19
2.2.2 Andreev bound states . . . 20
2.2.3 Situation in nanowires . . . 21
2.2.4 SIS junctions and split junctions . . . 23
2.3 Transmons . . . 25
2.3.1 The Hamiltonian in the charge basis . . . 25
2.3.2 From the Cooper-pair box to the transmon . . . 26
2.3.3 Flux tunability of SIS and SNS transmons . . . 28
2.3.4 Voltage tunability of SNS transmons . . . 31
2.4 Circuit Quantum Electrodynamics . . . 32
2.4.1 Resonators . . . 33
2.4.2 Dispersive Readout . . . 36

3 Fabrication of CQED chips with nanowire transmons **39**
3.1 Substrate and base layer . . . 40
3.2 Nanowires . . . 41
3.2.1 Deterministic placement . . . 42
3.2.2 Image recognition software . . . 42
3.3 Defining the SNS junction . . . 46
3.4 Contacting the nanowires . . . 47
3.5 Optimizations for field compatibility . . . 47
3.5.1 Holes to avoid vortex formation . . . 48

3.5.2 NbTiN airbridges . . . 49

4 Coherence and noise characterization of SNS transmons at zero field 51
4.1 Introduction . . . 52
4.2 Voltage tunable devices . . . 52
4.2.1 CW spectroscopy . . . 52
4.2.2 Extracting noise figures from time-domain characteristics . . . 54
4.2.3 Coherence limitation given a noise PSD . . . 58
4.3 Flux-tunable split-junction device . . . 60
4.3.1 Spectroscopy . . . 60
4.3.2 Time-domain characteristics . . . 60
4.4 Strongly coupled TLSs. . . . 62
4.4.1 Ramsey-based detection . . . 62
4.4.2 Spectroscopic signatures . . . 64
4.5 Conclusions . . . 65

5 Opening Pandora's box: Applying an in-plane magnetic field 67
5.1 Introduction . . . 68
5.2 Response of the resonators . . . 68
5.3 Spectroscopic features of the qubits . . . 71
5.4 Time-domain characterization . . . 73
5.4.1 Energy relaxation . . . 73
5.4.2 Dephasing . . . 76
5.5 Flux-tunable split-junction devices in $B_{||}$ . . . 78
5.6 Conclusions . . . 80

6 Adding the in-plane field as a parameter to the toolbox of CQED 83
6.1 Introduction . . . 84
6.2 Bulk CQED elements . . . 84
6.3 Qubits . . . 87
6.3.1 Vector field control . . . 87
6.3.2 Partially covered wires . . . 89
6.4 Flux control in the in-plane magnetic field . . . 91
6.4.1 Technical improvements . . . 91
6.4.2 Measurements of the spectrum . . . 94
6.4.3 Time-domain characterizations . . . 96
6.5 Conclusion . . . 99

7 Conclusion and Outlook 101
7.1 Conclusion . . . 102
7.2 Looking into the future . . . 103
7.2.1 Flux-noise in a magnetic field . . . 103
7.2.2 The future of SNS transmons . . . 105
7.2.3 SNS qubits as charge-parity detectors in a magnetic field . . . 106

7.2.4 Alternative junctions for field-compatible transmons 107
7.2.5 Signatures of Majorana zero modes 107
7.2.6 Coupling to spin qubits 109

A Appendix A: Experimental setup **111**
A.1 CQED measurement setup 112
A.1.1 Microwave setup 112
A.1.2 Read-out line 112
A.1.3 dc-Biasing 113
A.1.4 Controlled noise injection 114
A.1.5 Control software 114
A.2 The low-temperature environment 114
A.3 The solenoid setup 116
A.3.1 Single-axis solenoid 116
A.3.2 Vector-field solenoid 117
A.4 50 mK radiation shield 118

Acknowledgements **119**

Curriculum Vitæ **125**

List of Publications **127**

References **129**

SUMMARY

Quantum computers promise to solve certain problems such as quantum chemistry simulations much more efficiently than their classical counterparts. Although it is still unclear what material system will ultimately host large-scale quantum computers, solid-state systems are promising candidates due to their inherent scalability and advanced fabrication techniques that can be adapted from comparable technologies. Crucially, a future quantum computer will depend on the quality of its most fundamental building block, the quantum bit, or qubit. Qubits, although ideally insensitive to potential noise, are very susceptible to slight changes in their environment. Therefore, they do not only make the building block for quantum computers, but are also precise sensors.

One of the most studied solid-state implementations of a qubit is the transmon, a weakly anharmonic oscillator based on superconducting capacitive and nonlinear inductive elements. Typically, $Al - AlO_x - Al$ superconductor-insulator-superconductor Josephson junctions are used for the latter. The interaction of the transmon with the control circuitry, typically superconducting resonators, is described by circuit quantum electrodynamics. In this PhD thesis, a more recently demonstrated type of qubit is further developed and studied in detail using circuit quantum electrodynamics. In these qubits, the Josephson element of the transmon is replaced with indium arsenide nanowires, forming a superconductor-normal metal-superconductor junction. In addition to the standard flux tunability, these qubits can also be voltage tuned. Due to the compatibility of all the materials used with an applied magnetic field, this type of qubit is a good candidate to be used as a precise and accurate sensor in a magnetic field. The goal of this work is to introduce the in-plane magnetic field as a new tuning knob to the toolbox of circuit quantum electrodynamics.

Advances in material science, especially the epitaxial growth of an aluminum shell directly on the indium arsenide nanowire, have enabled the fabrication of nanowire transmons with state-of-the-art coherence. An understanding of their workings in a zero-field environment is important before applying a magnetic field. Thus, we characterize the noise these qubits are subject to (Chapter 4) and find a strong coupling of charge two-level systems to their Josephson energy next to the expected weakly coupled flux and voltage noise.

Applying a magnetic field reveals that coherence in these qubits can be observed up to 70 mT, substantially above the superconducting gap of bulk aluminum (Chapter 5). Effects limiting the performance include the thick and fully covering aluminum shell, and the alignment and stability of the magnetic field. The use of different nanowires, the installation of a persistent-current vector solenoid and additional magnetic shielding then enables the operation of voltage- and flux-tunable devices in a magnetic field (Chapter 6). This constitutes a good starting point for circuit quantum electrodynamics experiments in a magnetic field, such as the investigation of the microscopic origin of flux-noise.

SAMENVATTING

Kwantumcomputers beloven bepaalde problemen, zoals kwantumchemiesimulaties, veel efficiënter op te lossen dan hun klassieke tegenhangers. Hoewel het nog steeds onduidelijk is welk materiaal systeem uiteindelijk grootschalige kwantumcomputers zal huisvesten, zijn vaste stof systemen veelbelovende kandidaten vanwege hun inherente schaalbaarheid en geavanceerde fabricagetechnieken die kunnen worden aangepast vanuit vergelijkbare technologieën. Een toekomstige kwantumcomputer is cruciaal afhankelijk van de kwaliteit van zijn meest fundamentele bouwsteen, de kwantumbit, of qubit. Alhoewel ze idealiter ongevoelig zijn voor potentiële ruis, zijn qubits zeer vatbaar voor kleine veranderingen in hun omgeving. Daarom vormen ze niet alleen de bouwsteen voor kwantumcomputers, maar zijn ze ook precieze sensoren.

Een van de meest bestudeerde vaste stof implementaties van een qubit is de transmon, een zwak anharmonische oscillator gebaseerd op supergeleidende capacitieve en supergeleidende niet-lineaire inductieve elementen. Meestal worden $\mathrm{Al}-\mathrm{AlO_x}-\mathrm{Al}$ supergeleider-isolator-supergeleider Josephson-juncties gebruikt voor dat laatste. De interactie van de transmon met de regelschakelingen, typisch supergeleidende resonatoren, wordt beschreven door circuit kwantumelektrodynamica. In dit proefschrift wordt beschreven hoe een meer recent gedemonstreerd type qubit verder wordt ontwikkeld en in detail wordt bestudeerd met behulp van circuit kwantumelektrodynamica. In deze qubits wordt het Josephson-element van de transmon vervangen door indiumarsenide nanodraden, waardoor een supergeleider-normaal metaal-supergeleider junctie wordt gevormd. Naast de standaard flux-afstemmo- gelijkheden, kunnen deze qubits ook met spanning worden afgestemd. Vanwege de compatibiliteit van alle gebruikte materialen met een toegepast magnetisch veld, is dit type qubit een goede kandidaat om gebruikt te worden als een precieze en nauwkeurige sensor in een magneetveld. Het doel van dit proefschrift is om het magnetische veld in het vlak als een nieuwe afstemknop toe te voegen aan de toolbox van de circuit kwantumelektrodynamica.

Ontwikkelingen in de materiaalkunde, in het bijzonder de epitaxiale groei van een aluminium schil direct op een indiumarsenide nanodraad, hebben de fabricage van nanodraad transmons mogelijk gemaakt met state-of-the-art coherentie. Een goed begrip van hun werking in een nulveldomgeving is belangrijk voordat een magnetisch veld wordt aangelegd. We karakteriseren dus de ruis waaraan deze qubits onderhevig zijn (Hoofdstuk 4) en vinden een sterke koppeling van ladings tweeniveausystemen met hun Josephsonenergie naast de verwachte zwak gekoppelde flux en ladingsruis.

Het aanleggen van een magnetisch veld laat zien dat de coherentie in deze qubits kan worden waargenomen tot 70 mT, aanzienlijk boven het kritische magneetveld van bulk aluminium (Hoofdstuk 5). Effecten die de prestaties beperken zijn de dikke en volledig dekkende aluminium schil en de uitlijning en stabiliteit van het magnetische veld. Het gebruik van

verschillende nanodraden, de installatie van een persistent-current vectorsolenoïde en extra magnetische afscherming maken vervolgens de werking mogelijk van voltage- en flux-afstembare systemen in een magnetisch veld (Hoofdstuk 6). Dit vormt een goed startpunt voor kwantumelektrodynamicaexperimenten in een magnetisch veld, zoals het onderzoek naar de microscopische oorsprong van fluxruis.

ZÄMEFASSIG

Quantecomputer verspräched gwüssi Problem wie Quantechemiesimulatione dütlich effizienter z löse als ihri klassische Pendants. Es isch nach wie vor unklar, weles Materialsystem schlussendlich brucht werde wird zum grossskaligi Quantecomputers z baue. Allerdings sind Implementatione wo uf Festkörpersystem beruhed ufgrund vo ihrer inhärente skalierbarkeit und fortgschrittne Fabrikationsmethode wo aapasst werde chönd vo ähnliche Technologie vielversprächendi Kandidate. En zuekünftige Quantekomputer wird stark vo de Qualität vo sine fundamentelle Baustei, de Quantebits, oder Qubits, abhange. Obwohl Qubits idealerwiis nüt vo allfälligem Ruusche merke würed, sind si eifach beiiflusst vo chlinste Veränderige i ihrer Umgäbig. Entsprechend sind si also nöd nur di fundamentelle Baustei vo Quantecomputer, aber au sehr präziisi Sensore.

Eini vo de meiststudierte Variante vonerem Festkörperqubit isch s Transmon, en schwach anharmonische Oszillator wo userem supraleitende Kondensator und enere supraleitende, nödlineare Induktivität bestaht. Typischerwiis werded $Al - AlO_x - Al$ Supraleiter-Isolator-Supraleiter Josephsonübergäng für di letzteri brucht. D Wächselwürkig vonerem Transmon mit sinere Kontrollelektronik, meistens supraleitendi Resonatore, isch dur d Schaltchreisquanteelektrodynamik beschribe. I dere Doktorarbet wird en neulich demonstrierte Typ vo Qubits mithilf vo de Schaltchreisquanteelektrodynamik wiiter entwicklet und gnauer studiert. I dene Qubits wird s Josephsonelemänt vonerem Transmon miterem Indiumarsennanodraht wo en Supraleiter-Normalleiter-Supraleiter Übergang macht ersetzt. Zuesätzlich zu de standardmässige Regulierbarkeit mit magnetischem Fluss chönd die Qubits au mit elektrischer Spannig reguliert werde. Wil alli Materialie wo für d herstellig vo dene Qubits brucht werded kompatibel mit Magnetfälder sind, sind die Qubits gueti Kandidate um als präziisi und gnaui Sensore inerem Magnetfeld iigsetzt z werde. S Ziil vo dere Arbet isch s Magnetfäld i de Ebeni vom Chip als neue Parameter id Werchzüügchiste vo de Schaltchreisquanteelektrodynamik iizfüehre.

Fortschritt i de Materiaalwüsseschafte, speziell s epitaxielle Wachse vo Aluminiumschale direkt uf de Indiumarsennanodröht, händ ermöglicht, Nanodrahttransmons mit de beste Kohäränzziite härzstelle. Es isch wichtig es guets Verständnis vo ihrne Eigeschafte inere Nullfäldumgäbig z ha bevor es Magnetfäld aagleit wird. Drum charakterisiered mer di verschidene Ruuschprozäss wo die Qubits gspüüred (Kapitäl 4), und finded näbst em erwartete schwach kopplete Ruusche im magnetische Fluss und de elektrische Spannig e starchi Kopplig vo Ladigszweiniveausystem zu de Josephsonenergie vo de Qubits.

Wänn mer es Magnetfeld aaleit gseht mer, dass die Qubits Kohäränz bis zu 70 mT zeiged, was dütlich über em kritische Fäld vo dickem Aluminium isch (Kapitäl 5). Sache wo d Leistig vo dene Qubits beschränked sind under anderem di dicki und vollumgäbendi Aluminiumschale, sowie d Uusrichtig und d Stabilität vom Magnetfäld. D verwändig vo andere

Nanodröht, d Installation vonerem Vektromagnet mit Duurstrom und zuesätzlichi Schild gäge Magnetfälder ermöglichts, Qubits wo mit magnetischem Fluss und mit elektrischer Spannig regulierbar sind inerem Magnetfäld z kontrolliere (Kapitäl 6). Das isch also en guetä Startpunkt für Schaltchreisquanteelektrodynamikexperiment inerem Magnetfäld, wie zum Biispil d Undersuechig vom mikroskopische Uursprung vom Ruusche im magnetische Fluss.

1 INTRODUCTION

1

When the word qubit is mentioned, a natural thought is quantum computation. This computing paradigm that promises to solve some complex problems more efficiently is an exciting application of quantum mechanics. A lot of research and development work has gone into making quantum bits in various material systems. One of the currently more promising systems towards realizing a medium-scale quantum computer are transmons. These weakly anharmonic, superconducting resonators can be made using established micro-fabrication techniques. They can be coupled to each other and to the outside world. The theory describing this is called circuit quantum electrodynamics (CQED).

A key measure of performance of these circuits is their quantum coherence. Any noisy process that couples to the qubits will reduce it. On the one hand side this is a bad thing, because it means that their ability to perform interesting computations is limited. On the other hand side, it also means that these qubits are highly sensitive detectors, especially when operated in a CQED environment. Various interesting physical processes take place in the presence of magnetic fields. So far, CQED has been limited to fields that are lower than the critical field of bulk aluminum, which is a standard material for key components of transmons. Hence, the development of a CQED system that can withstand magnetic fields will allow for interesting experiments.

This chapter does not try to give an introduction to the large field of CQED, or even quantum computing. There is literature doing this already [1]. The goal of this chapter is rather to motivate why it is desirable to have a CQED platform that can operate in magnetic fields. For this, we will look in detail at one of the limiting factors of superconducting circuits nowadays, flux noise. It is expected that more information about its nature can be gained if it is also investigated in a magnetic field. After that, further possible experiments with the system developed in this thesis are discussed.

1.1 Qubits as flux noise sensors

Nowadays, many schemes for quantum computing with superconducting qubits rely on changing the frequency of these qubits. This is most commonly done by threading a flux through the SQUID loop that defines the Josephson energy of the qubit, and is referred to as flux-tuning (Chapter 2). But every knob that can be used to control properties of the qubit is also a potential source of noise and decoherence. If there is noise in the flux threaded through the SQUID loop, the qubit frequency will change unpredictably. This frequency noise manifests itself effectively as a noise in the phase of quantum state stored in the qubit. This leads to decoherence. The reduction in coherence due to flux noise is a limiting factor for many experiments and applications.

In order to reduce the effect a certain noise has on the system, two measures can be taken. On the one hand side it is possible to reduce the sensitivity of the system to this noise. In the case of SQUID-loop-based qubits suffering from flux noise, this can be done by the use of asymmetric Josephson junctions [2, 3]. With this method, the qubit frequency will respond less strongly to an applied flux. Therefore, also flux noise will have less of an effect on the qubit frequency, leading to reduced dephasing. On the other hand, the absolute noise can

be reduced. To do so, knowledge of its source is required. It has been shown that not the noise of the biasing electronics at room temperature, but rather on-chip noise sources are the dominant contributions. The problem of flux noise has already been observed a long time ago [4, 5], but the direct identification of its microscopic origin remains an open challenge.

There is a wealth of possible candidates that lead to flux noise, ranging from nuclei with nonzero magnetic moment in the bulk of the substrate to electron spins of adsorbed molecules on the surface of the chip. Over time, theoretical and experimental works were able to rule out some of these possible candidates. Nonetheless, an effective suppression of on-chip flux noise (for example by means of improved fabrication techniques) requires precise knowledge about its nature. I will outline here what the possible candidates causing flux noise are, what possible interactions between them are and whether it is possible to rule them out as the dominant source of flux noise. Then I will discuss the two most likely systems models that theoretically describe what happens if a magnetic field is applied.

In general, flux noise is observed to have a spectral density $\mathcal{S}(f)$ that is roughly A/f^{α} ($\alpha \leq 1$), with an amplitude of $\sqrt{A} \sim 1 - 10\ \mu\Phi_0$ at 1 Hz. This property is observed to be roughly independent of the SQUID loop size and the materials used, and the noise power tends to increase with decreasing temperature [4, 6, 7]. The spectrum has been measured to be $1/f^{\alpha}$ like over many orders of magnitude in frequency. The slope α has been found to depend on temperature and the SQUID loop geometry. A possible and quite general explanation for $1/f$ noise is a distribution of two-level systems (TLS) with a magnetic moment that switch their states with a wide distribution of switching rates [8, 9]. The distribution of switching rates determines the magnitude of the flux noise.

In an intuitive model, flux noise is due to the presence of electron spins in surface traps. The electron can, thermally activated, hop between different states, that each have a fixed spin direction. This hopping would therefore lead to a changing magnetic flux through the SQUID loop [7]. However, the density of defect sites required to produce typically measured levels of flux noise is orders of magnitude higher than what is expected for glassy materials [10, 11]. Further on, it has been possible to largely rule out the presence of two-level systems (TLS) in the bulk of the substrate to have a strong effect on the qubits [12–14]. Nuclear magnetic moments themselves give a too weak contribution and their frequency spectrum does not match the experimental results [7, 15]. With a scanning SQUID microscope, it was possible to determine the surface spin density to be $\sim 4 \cdot 10^{17}/\mathrm{m}^2$ [16]. This is in good agreement with the surface spin density of $\sim 5 \cdot 10^{17}/\mathrm{m}^2$ extracted from the temperature dependence of flux threading a SQUID loop [17]. These surface spins could also be determined to be paramagnetic (to follow a $1/T$ temperature law) [16–18]. However, an interaction between the spins is required to explain the magnitude of the flux noise given this surface density [11]. This is supported by the fact that a model solely relying on thermally activated switchers would predict a decrease in noise with lower temperature, contradicting observations [19]. In fact, there are indications that the spin-ensemble is close to a spin-glass transition [11, 20]. Obtaining a good understanding of flux noise therefore means obtaining a good understanding of defect sites potentially being responsible for hosting the observed

surface spins and interactions between the surface spins. This understanding is crucial in order to reduce flux noise.

Let us now discuss what sites and defects could host paramagnetic electron spins responsible for flux noise. If dangling bonds at the interface between silicon and its oxide host only one electron, it would lead to a paramagnetic electron spin [21]. Also metal-induced gap states can produce local moments if there is some disorder at the metal-insulator interface [22]. A further possibility are adsorbed molecules on the surface of the device [23, 24]. For example, molecular oxygen could bind to the surface via Lewis-base defect sites [25, 26] Their density matches the observed surface spin density on AlO_x [27]. A recent experiment shows that passivation of the surface with molecules that have no magnetic moment (in that example NH_3) can substantially reduce the observed flux noise [28]. An electron spin resonance experiment confirms this, and shows that the adsorbents are from a single species in a doublet with a spin of $S = 1/2$ and a g factor of 2.0 [27]. Although it does not exclude other effects, this furthers indicates that molecular oxygen is a likely source. The same experiment could also evidence the presence of physisorbed atomic hydrogen on the surface. This atom also has a magnetic moment, and can therefore lead to flux noise too.

Solely the presence of magnetic moments is not enough to explain the observed level and temperature dependence of flux noise. There needs to be an interaction between the magnetic moments. A theoretical suggestion is that spin-diffusion is mediated by a Ruderman-Kittel-Kasuya-Yosida (RKKY) interaction that couples the electron spins via cooper-pairs in the superconductor [15, 29–31]. This interaction produces a spin glass, and can be shown to produce $1/f$-like flux noise [32]. It is important to note that RKKY interactions conserve the total spin and magnetization. There is, however, experimental evidence that spin and total magnetization are not conserved [16]. Although this does not exclude the presence of an RKKY interaction, it does require that another interaction be present which does not conserve the total spin and magnetization [33]. Possible such interactions are spin-orbit, hyperfine and magnetic dipole-dipole. Neutral gold atoms have an orbital angular momentum of zero, therefore the spin-orbit interaction can be neglected [16, 33]. In the case of physisorbed atomic hydrogen, the hyperfine interaction is 1.42 GHz. Its hyperfine transition can be experimentally observed [18, 27]. The coherent interaction alone would not lead to flux noise at other frequencies, but if further nuclei interact with the hydrogen electron spins a wide distribution of relaxation rates can be obtained. This will again lead to $1/f$ noise [33]. In comparison, magnetic dipole-dipole interactions are much weaker. With a typical distance $r \approx 7$ nm between dipoles, given by the measured surface spin density, their energy is

$$\frac{H}{h} = \frac{\mu_0 \mu_B^2}{4\pi r^3} \approx 5 \text{ MHz}, \tag{1.1}$$

and can therefore be neglected as well. Here, μ_0 is the magnetic permeability and μ_B is the Bohr magneton.

In summary, it is likely that the observed flux noise stems from two sources. The first are surface adsorbents with a magnetic moment. It has been observed to be a $S = 1/2$ doublet state of a single spin species, with a g-factor of 2.0 [27]. A likely candidate is O_2^- captured at Lewis base defect sites [25, 26]. This is confirmed by passivation of the surface with a

non-magnetic molecule which lead to a significant reduction in flux noise [28]. The second contribution is likely from electron spins of physisorbed atomic hydrogen which is present on the surface of the device. The spins of the hydrogen electron undergo a hyperfine interaction with their nuclei. This could be directly measured in an ESR experiment [27] and in the noise spectrum of a superconducting qubit [18]. If further on these electron spins also interact via some other channel that switches their state, this will also lead to $1/f$ flux noise.

In both of these pictures, the application of a magnetic field would change the noise spectrum. I will now discuss two models that describe the behavior of the identified likely candidates in a magnetic field. The first model (Section 1.1.1) is fairly generic, it assumes a two-level system with an energy splitting between the two states. Increasing this energy splitting will reduce the switching rates, therefore leading to a suppression of flux noise. An example for a system described by this model is molecular oxygen on the surface of the device. The second model (Section 1.1.2) treats the hyperfine-split physisorbed hydrogen atoms. Due to the coherent hyperfine interaction, the previously discussed model does not apply anymore. A pseudo-trotterization approach is used to capture both the coherent interaction and the probabilistic relaxation of the electron states.

1.1.1 Flux noise from a two-level system

Let us assume a fairly generic two-level system with an energy splitting ΔE between its states $|\uparrow\rangle$ and $|\downarrow\rangle$. The following calculations are general, but let us consider these states to correspond to the spin of an electron in the vicinity of the SQUID loop. Switching between the states will change the flux threaded through the SQUID loop. If there is a large distributions of switching rates, we will see that this leads to $1/f$ noise.

The states of the TLS will switch due to a finite temperature T. We denote the transition rate from $|\uparrow\rangle$ to $|\downarrow\rangle$ ($|\downarrow\rangle$ to $|\uparrow\rangle$) as $\Gamma_{\uparrow\downarrow}$ ($\Gamma_{\downarrow\uparrow}$). The ratio between the transition rates can be derived from the Maxwell-Boltzmann distribution to be

$$\frac{\Gamma_{\uparrow\downarrow}}{\Gamma_{\downarrow\uparrow}} = e^{\frac{\Delta E}{k_B T}}, \tag{1.2}$$

where k_B is the Boltzmann constant. In the steady state, the probability of finding the system in $|\uparrow\rangle$ ($|\downarrow\rangle$) is given by $p_{\uparrow,\mathrm{ss}}$ ($p_{\downarrow,\mathrm{ss}}$), where

$$\begin{aligned} p_{\uparrow,\mathrm{ss}} &= \frac{1}{1+e^{\frac{\Delta E}{k_B T}}}, \\ p_{\downarrow,\mathrm{ss}} &= \frac{1}{1+e^{-\frac{\Delta E}{k_B T}}}. \end{aligned} \tag{1.3}$$

More generally, the equation of motion of the system probability can be solved. This allows us to express the probability $\vec{p}(t)$ to be in either state at time t,

$$\vec{p}(t) = e^{A\cdot t}\vec{p}(0), \text{ where } A = \begin{pmatrix} -\Gamma_{\uparrow\downarrow} & \Gamma_{\downarrow\uparrow} \\ \Gamma_{\uparrow\downarrow} & -\Gamma_{\downarrow\uparrow} \end{pmatrix}, \tag{1.4}$$

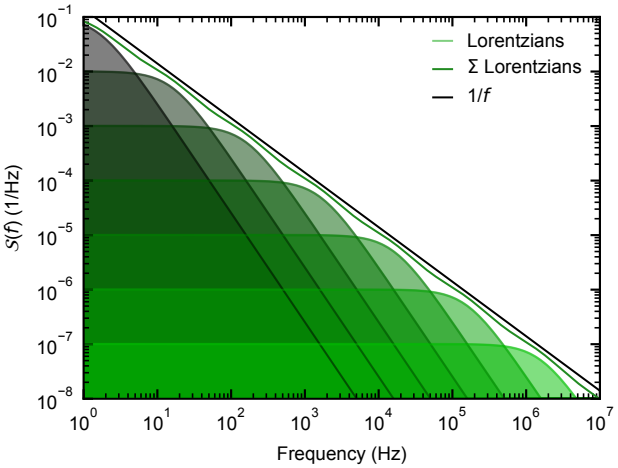

Figure 1.1: A single two-level system that switches between two states produces a Lorentzian spectrum (green to black curves). The sum over a certain distribution of such switchers (Σ Lorentzians) approximates a $1/f$ spectrum.

where the basis $(|\uparrow\rangle, |\downarrow\rangle)$ is used. This system is time invariant, therefore we can write its autocorrelation function as

$$\begin{aligned} E(\tau) &= \langle x(t)x(t+\tau)\rangle \\ &= p_{\uparrow,\mathrm{ss}}\left(p_{\uparrow\uparrow}(\tau) - p_{\uparrow\downarrow}(\tau)\right) - p_{\downarrow,\mathrm{ss}}\left(p_{\downarrow\uparrow} - p_{\downarrow\downarrow}(\tau)\right) \\ &= 1 + \mathrm{sech}^2\left(\frac{\Delta E}{k_\mathrm{B}T}\right)\mathrm{e}^{-\Gamma\tau}, \end{aligned} \tag{1.5}$$

where we denote the absolute rate $\Gamma = \Gamma_{\uparrow\downarrow} + \Gamma_{\downarrow\uparrow}$. We used the fact that we average over all times t to insert the steady-state populations. Characteristically for switching processes, the autocorrelation function decays exponentially over time.

The knowledge of the autocorrelation function allows us to calculate the spectrum of the system. The Wiener-Khinchin theorem states that the spectrum is just the Fourier-transform of the autocorrelation function,

$$\int(f) = \int_{-\infty}^{\infty} E(\tau)\mathrm{e}^{-2\pi i\tau f}\mathrm{d}\tau = \delta(f) + 2\cdot\mathrm{sech}^2\left(\frac{\Delta E}{k_\mathrm{B}T}\right)\underbrace{\frac{\Gamma}{\Gamma^2 + 4\pi^2 f^2}}_{\text{Lorentzian}}. \tag{1.6}$$

The spectrum is Lorentzian, scaled with a prefactor that we will discuss later. This is characteristic for a single random switcher [8]. If now the spectra of many such switchers with a distribution of switching rates are summed up (Figure 1.1), the total spectrum gets a $1/f$ shape [9]. Note that a rate distribution according to a uniform barrier density is required for this.

Let us now assume such a uniform barrier distribution of the switchers, which is equal to a dirstribution of $T_1 = 1/\Gamma$ that satisfies

$$P(T_1) = D/T_1 \text{ with } \int P(T_1)\mathrm{d}T_1 = 1, \tag{1.7}$$

where D is a normalization factor. For this to be applicable, the states of the switchers under consideration must have an interaction leading to such a rate distribution [15, 33]. To

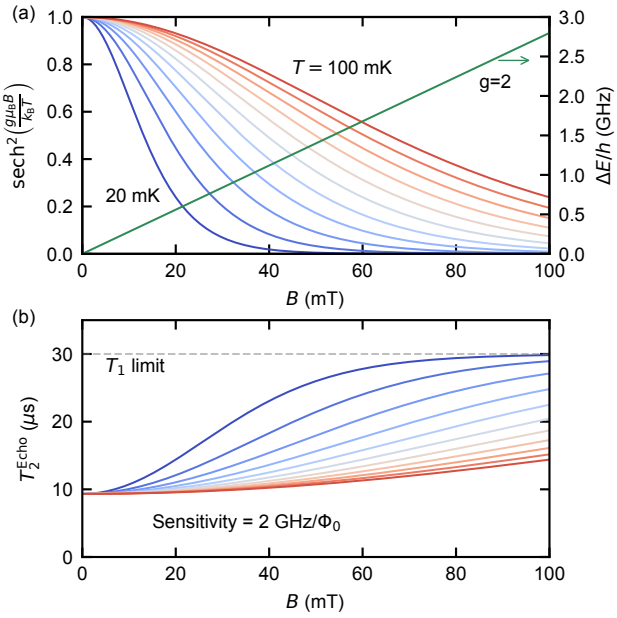

Figure 1.2: Effect of temperature and magnetic field on flux noise. (a) Dependence of the flux noise prefactor on magnetic field for different temperatures (curves). The Zeeman energy splitting increases linearly with applied field (green, right axis). (b) For realistic device parameters, an increase in T_2^{Echo} is expected when a magnetic field is applied.

obtain the spectrum of the ensemble of the switchers, we integrate a single spectrum over the distribution of rates,

$$\begin{aligned}\mathcal{S}(f) &= \int P(T_1)\cdot 2\cdot \mathrm{sech}^2\left(\frac{\Delta E}{k_\mathrm{B}T}\right)\frac{1/T_1}{1/T_1^2+4\pi^2 f^2}\mathrm{d}T_1 \\ &= \frac{D}{2}\mathrm{sech}^2\left(\frac{\Delta E}{k_\mathrm{B}T}\right)\cdot\frac{1}{f}.\end{aligned} \tag{1.8}$$

This indeed produces the observed $1/f$ spectrum (Figure 1.1). In order to obtain the magnitude of the flux noise, the coupling of a single spin to the SQUID loop needs to be known. This will yield a proportionality factor linking the flux noise with $\mathcal{S}(f)$. The proportionality factor depends strongly on the interaction under consideration and the geometry and determining it therefore exceed the range of the discussion here.

Nonetheless, it is instructive to look at the dependence of the noise spectrum on the energy splitting of the two-level system. Let us come back to the before mentioned case of a $g = 2.0$ spin system that undergoes a Zeeman splitting in a magnetic field B. The energy difference between the two states is then given as

$$\Delta E = g\mu_\mathrm{B}\cdot B = 28\,\frac{\mathrm{GHz}}{\mathrm{T}}\cdot B\cdot h. \tag{1.9}$$

Accordingly, as the field increases (ΔE increases, the prefactor of Equation (1.8) decreases [Figure 1.2(a)]. The effective temperature of the spin ensemble is unclear, but application of a magnetic field on the order of 100 mT leads to a significant change in the prefactor.

Typically, in the present system of transmon qubits, the level of flux noise is determined by measuring coherence as a function of applied flux [3, 34, 35]. Let us express the effect of a magnetic field in terms of measurable properties of a flux-tunable transmon qubit with

realistic parameters. We will discuss later (Chapter 4) that an energy relaxation time $T_1 = 15\ \mu$s, a flux noise level of $10\ \mu\Phi_0$ at 1 Hz are realistic. Typically, off the flux sweetspot, the coherence of transmon qubits is limited by flux noise. If we examine the coherence of a qubit at a point with flux sensitivity of $2\ \mathrm{GHz}/\Phi_0$, the Echo coherence time will be limited to $T_2^{\mathrm{Echo}} \sim 10\ \mu$s. Application of a magnetic field will then start to quench out the dynamics of the spins, reducing the flux noise. Based on this [Equation (1.8)], an increase in T_2^{Echo} is predicted. As the effective temperature of the spin bath is not known, the effect of an applied magnetic field on T_2^{Echo} is shown for various temperatures. Even for pessimistic estimates of the spin bath temperature, an increase of T_2^{Echo} is expected. Measuring the field and temperature dependence of the device will therefore allow us to extract information about the spin bath. This will help to further our understanding of the microscopic origin of flux noise.

1.1.2 Flux noise in the presence of hyperfine coupling

Let us now consider the more specific case of electrons of physisorbed atomic hydrogen. Their presence on AlO_x surfaces has been experimentally confirmed [18, 27]. These electrons undergo a hyperfine interaction with their nucleus. This coherent interaction itself will not lead to a $1/f$ flux noise spectrum. But if the electron spins also undergo other interactions with surrounding defects, analogeusly to what was discussed in Section 1.1.1, a $1/f$ flux noise background can appear. Here, we give a basic model for how this happens and what the effect of temperature and magnetic field on the system is. In order to also model the coherent interaction, we need a different approach from before.

One way of obtaining the spectrum of a bath of electrons that undergo a hyperfine interaction with their nucleus and switches due to further interactions is to simulate time traces of the electrons. As their evolution is not unitary – they undergo probabilistic switches – it is not possible to simply evolve their quantum state. Instead, the state is evolved for a time step Δt, after which it is probabilistically switched. This is repeated many times to generate a trace for the expectation value of the electron state. The power spectral density of such a trace is obtained by its Fourier transform. Many spectral densities of traces with varying switching rates are averaged to produce an approximation to the spectrum of the bath. Another way of obtaining the spectrum would be to solve the Lindblad master equation.

Let us first study the spectrum of the hyperfine split atomic hydrogen in a magnetic field. The Hamiltonian of the hyperfine interaction,

$$\hat{H}_{\mathrm{Hyperfine}} = h\frac{A_{\mathrm{Hyp}}}{4}\vec{\hat{S}}\cdot\vec{\hat{I}}, \text{ where } \vec{\hat{S}}, \vec{\hat{I}} = \begin{pmatrix}\hat{\sigma}_x\\ \hat{\sigma}_y\\ \hat{\sigma}_z\end{pmatrix}, \tag{1.10}$$

couples electron and nucleus. More precisely, it couples the states $|\uparrow\Downarrow\rangle$ and $|\downarrow\Uparrow\rangle$, where $|\uparrow\rangle$, $|\downarrow\rangle$ indicates the electron and $|\Uparrow\rangle$, $|\Downarrow\rangle$ indicates the nuclear state. We call the set of basis states $\{|\uparrow\Uparrow\rangle, |\uparrow\Downarrow\rangle, |\downarrow\Uparrow\rangle, |\downarrow\Downarrow\rangle\}$ the computational basis. The interaction strength is given by $A_{\mathrm{Hyp}} = 1.42$ GHz, and h is the Planck constant.

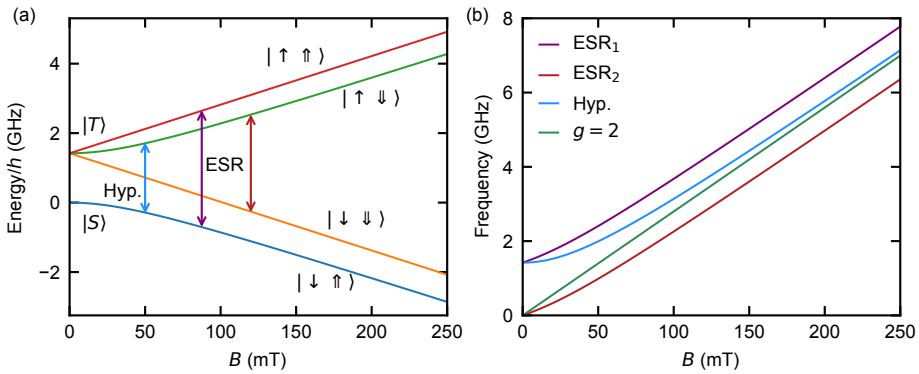

Figure 1.3: Hyperfine spectrum of atomic hydrogen. (a) The energy levels of Equation (1.12) as a function of applied field. (b) The electron-spin resonance transitions between the hyperfine split levels, the energy of the hyperfine splitting and the $g = 2$ Zeeman split transition as a function of magnetic field.

If a magnetic field is applied, both the electron and nucleus undergo a Zeeman splitting. However, because the nuclear magnetic moment is three orders of magnitude smaller than the magnetic moment of the electron, we take the Hamiltonian to only act on the electron,

$$\hat{H}_{\text{Zeeman}}(B) = -\frac{g\mu_{\text{B}}}{2} B \cdot \hat{\sigma}_{\text{z}} \otimes \hat{\text{id}}. \tag{1.11}$$

The combined Hamiltonian

$$\hat{H}(B) = \hat{H}_{\text{Hyperfine}} + \hat{H}_{\text{Zeeman}}(B) \tag{1.12}$$

describes the coherent evolution of the system under consideration. It can be diagonalized for each value of magnetic field, and its spectrum is shown in Figure 1.3(a).

At zero magnetic field, the eigenstates of the Hamiltoninan in Equation (1.12) are singlets and triplets in the computational basis. The ground state is the singlet, and the higher-energy triplets are degenerate. More general, the eigenstates of $\hat{H}(B)$ are $|\uparrow\Uparrow\rangle$, $|\downarrow\Downarrow\rangle$, $|\alpha\rangle$ and $|\beta\rangle$. The latter two are superpositions of $|\uparrow\Downarrow\rangle$ and $|\downarrow\Uparrow\rangle$. If a large magnetic field is applied, they are better and better described in the computational basis. Next to the hyperfine transition, there are also electron resonance transitions [Figure 1.3(b)]. These transitions leave the state of the nucleus unchanged but switch the electron spin.

Now we discuss how the time evolution of the electron state expectation value $\langle\sigma_{\text{z}}\rangle$ can be simulated. In the following, we will consider states $|\psi\rangle$ whose time evolution is given by the Hamiltonian in Equation (1.12). Additional to this unitary evolution, also stochastic switching events of the electron state occur. Therefore, the time evolution is modeled stepwise. At every step, the state $|\psi(t)\rangle$ is first evolved coherently for a time step Δt under $\hat{H}(B)$,

$$|\psi(t + \Delta t)\rangle = \text{e}^{-\frac{i\Delta t}{\hbar}\hat{H}(B)} |\psi(t)\rangle . \tag{1.13}$$

Then, similar to Equation (1.4), the state stochastically undergoes a relaxation event. Due to its much slower time dynamics, we assume the nuclear state to be fixed and only the electron

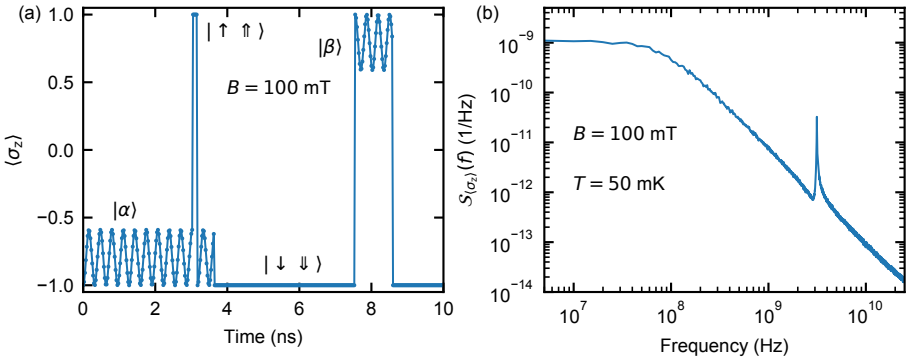

Figure 1.4: (a) Example for a generated trace of the electron state expectation value. If the state is in a superposition of $|\uparrow\Downarrow\rangle$ and $|\downarrow\Uparrow\rangle$ it will undergo a coherent evolution as these are not eigenstates of Equation (1.12). Next to the coherent evolution, also stochastic jumps of the electron state occur. (b) Averaged power spectral density traces in (a). The spectrum, averaged over many switcher traces for a fixed rate. As characteristic for TLSs, the spectrum has a Lorentzian shape. On top of the Lorentzian, a peak at the frequency of the coherent oscillation is observed.

state to switch. Later on, we will generate such traces with relaxation rates taken from a distribution. The excitation and relaxation rates have a ratio given by the Maxwell-Boltzmann distribution [Equation (1.2)]. The switching probability $p_{\mathrm{sw,a}}$ from $|\psi(t)\rangle$ to a computational state $|\psi_a\rangle$ is given as

$$p_{\mathrm{sw,a}} = \Delta t \sum_{\mathrm{c}} \Gamma_{\mathrm{ca}} |\langle\psi(t)|\psi_{\mathrm{c}}\rangle|^2, \tag{1.14}$$

where $\{|\psi_{\mathrm{c}}\rangle\}_{\mathrm{c}}$ are the computational states and Γ_{ca} the switching rates from state $|\psi_{\mathrm{c}}\rangle$ to $|\psi_{\mathrm{a}}\rangle$. In case a switching event occurs, the state $|\psi(t+\Delta t)\rangle$ is set to be the computational state $|\psi_{\mathrm{a}}\rangle$ to which it switched. If no relaxation event occurs, the state is evolved for the next time step according to Equation (1.13). Therefore, if the state is in either $|\alpha\rangle$ or $|\beta\rangle$, $\langle\sigma_{\mathrm{z}}\rangle$ oscillates with the (B-dependent) hyperfine frequency. With this procedure traces of $\langle\sigma_{\mathrm{z}}\rangle$ are generated [Figure 1.4(a)].

Next, the power spectral density (PSD) of this trace is calculated. It is given by

$$\mathcal{S}_{\langle\sigma_{\mathrm{z}}\rangle}(f) = \frac{\Delta t}{N}\left|\sum_{\mathrm{n}=1}^{N}\langle\sigma_{\mathrm{z}}\rangle_{\mathrm{n}} \mathrm{e}^{-i2\pi n f \Delta t}\right|^2 = \frac{\Delta t}{N}\left|\mathcal{FFT}\left(\langle\sigma_{\mathrm{z}}\rangle\right)\right|^2, \tag{1.15}$$

where N is the number of time steps the state was evolved for. To obtain a meaningful signal, the PSD of many (> 100) traces needs to be averaged. If only a single switching rate is used, the spectrum is effectively a Lorentzian [Figure 1.4(b)]. In addition to that, there is a peak at the hyperfine frequency. This is due to the coherent evolution of the states $|\alpha\rangle$ and $|\beta\rangle$.

Let us now consider a more realistic scenario, where many different switching rates are contributing. Many traces are generated, and every time a rate Γ is randomly chosen from

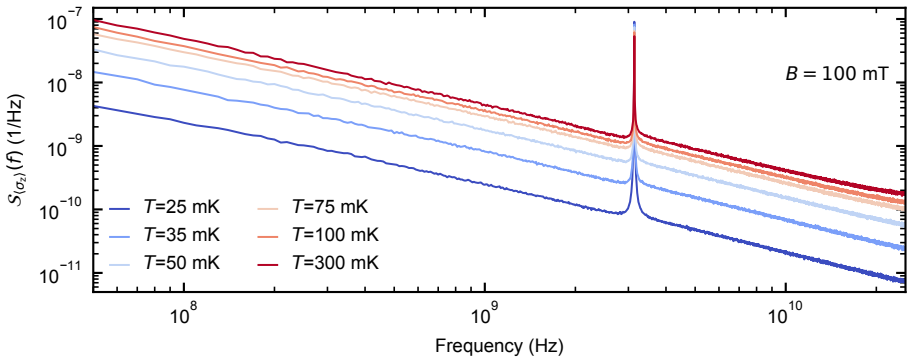

Figure 1.5: Spectrum of the switcher traces, averaged over different switching rates. The field is fixed at 100 mT while the temperature is changed. The $1/f$ background increases with temperature. Correspondingly, the peak due to the hyperfine interaction reduces in magnitude.

a distribution $P(\Gamma)$ [Equation (1.7)]. This produces a $1/f$ spectrum with a clear peak at the frequency of the hyperfine interaction (Figure 1.5). To verify the procedure, we repeat it for varying temperatures while keeping the field fix. Clearly, the background is reduced with decreasing tempeature. This is in agreement with what we expect from Equation (1.8). Note that the peak of the hyperfine splitting becomes less pronounced and wider as the temperature increases. This is because the switching rates and the relative populations of the states $|\uparrow\Uparrow\rangle$ and $|\downarrow\Downarrow\rangle$ increase.

Let us now focus on the situation where the temperature is kept fixed and the field is increased. Again, we observe a reduction of the background, in agreement with Equation (1.8). The slight increase of $\mathcal{S}_{\langle\sigma_z\rangle}(f)$ at low fields is because the isotropy of Equation (1.12) is being broken as the applied magnetic field increases. The peak in the spectrum changes its frequency and is also reduced in magnitude [Figure 1.6(a)]. The frequency at which the peak occurs increases with magnetic field according to the hyperfine splitting frequency [Figure 1.6(b)] This is expected, as the hyperfine interaction that effectively acts as a drive between $|\uparrow\Downarrow\rangle$ and $|\downarrow\Uparrow\rangle$ is further and further detuned with increasing magnetic field.

Analogous to Figure 1.2, we now study the expected Echo coherence times given the noise spectrum (Figure 1.7). The expected Echo coherence times of a flux-sensitive qubit can be calculated from the obtained noise spectrum (Section 4.2.3). The same, realistic device parameters of $T_1 = 15$ μs and a sensitivity of 2 GHz/Φ_0 are assumed. Establishing the precise relation between $\mathcal{S}_{\langle\sigma_z\rangle}(f)$ and the flux noise is left for further studies. Here, we assume proportionality and normalize the flux noise for each temperature such that at $B = 0$ mT it is 10 $\mu\Phi_0$ at 1 Hz. A larger frequency range of the noise spectrum is required to calculate the expected T_2^{Echo} than is reasonably obtainable with direct simulations of switcher traces. Therefore, Lindblad master equation simulations are used to generate Figure 1.7 [36]. In order to be consistent with the model (no decay in the nuclear states), only

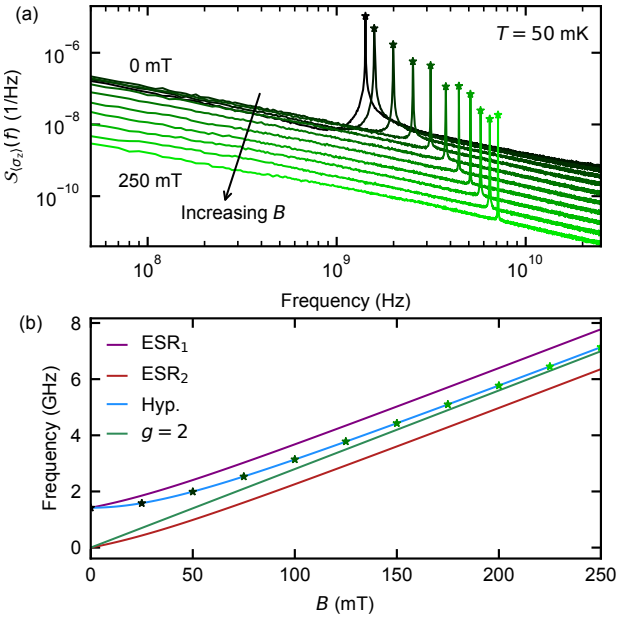

Figure 1.6: (a) Spectrum of switcher traces averaged over different switching rates. The temperature is kept constant at 50 mK while the field is changed. The $1/f$ background reduces with increasing field. The frequency of the hyperfine interaction peak increases with field, but its magnitude decreases. (b) Comparison to the hyperfine spectrum. The extracted peak frequency from (a) matches the field-dependent hyperfine frequency.

the four collapse operators that change the electron state are taken into account. In the toy model under consideration, the rates Γ corresponding to the collapse operators $|{\downarrow}\Uparrow\rangle\langle{\uparrow}\Uparrow|$ and $|{\downarrow}\Downarrow\rangle\langle{\uparrow}\Downarrow|$ are assumed to be the same, irrespective of the applied field. The rates of the inverse processes are then calculated to satisfy the ratio given by the Boltzmann factor according to the energies given in Figure 1.3(a). This does not respect the detailed balance of the system. Note that the initial decrease in T_2^{Echo} is due to the breaking of the isotropy of Equation (1.12) as the applied magnetic field increases. If only a $\sigma_z \otimes \sigma_z$ is present, this effect is not observed.

Note that these simulations do not capture the full reality of the situation. For example, they do not take into account how much the field of a single electron spin couples to the

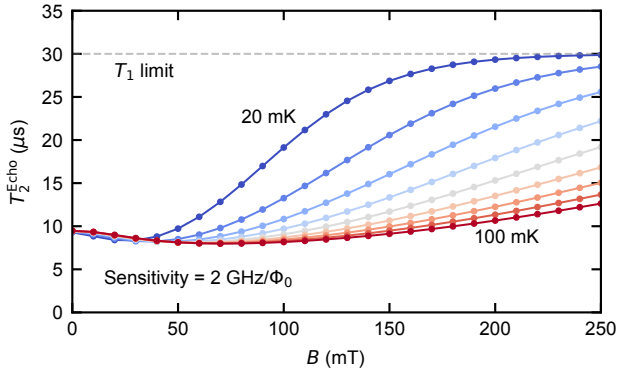

Figure 1.7: For realistic device parameters, the Echo coherence time of a flux-sensitive transmon is expected to increase. The assumed flux noise results from hyperfine-split hydrogen atoms with a distribution of switching rates.

SQUID loop. Therefore, the simulations do not yield directly a prediction of the flux noise in the device. Further on, the interactions leading to the distribution of relaxation rates of the electron spins are not explicitly taken into account here. They are just assumed to yield a distribution of relaxation rates of the electron spin. More precise models will be required to distinguish between different potential origins of flux noise. Nonetheless, the models still qualitatively indicate what will happen to the flux noise if it is subjected to magnetic field. Importantly, they show that, within the experimentally addressable parameter regime, a clearly measurable suppression of the flux noise can be achieved.

1.2 Quantized conductance enabling semi-digital gates

The transmon qubits studied in this thesis rely on a Josephson junction that is formed based on semiconducting nanowires to provide the nonlinear inductance (Chapter 2). The Josephson energy of the nanowires can be tuned in-situ using voltage side gates, changing the qubit frequency f_{01} [37, 38]. These qubits are called gatemons. Note that the conductance of the nanowire (and therefore its Josephson energy) is an erratic function of the applied side-gate voltage. This tunability can be used to perform voltage-controlled z gates on a single qubit [38] and gates between two qubits [39]. Further on, it also allows to operate voltage-controlled quantum busses [40]. All these operations are sensitive to noise in the applied gate voltage V_G. Noise in V_G leads to a noise in f_{01} because of the non-trivial (and unpredictable) dependence of $f_{01}(V_G)$.

Nanowires where the conductance is quantized have been demonstrated [41–43]. In such a situation, the Josephson energy increases stepwise with V_G. In the ideal case, the conductance of the nanowire is insensitive to small changes in V_G in the middle of a conductance plateau. This means that f_{01} of a gatemon with a wire that is in a regime of quantized conductance is insensitive to noise on V_G. This could greatly enhance the performance of the gatemon, as noise in V_G is a strong source of decoherence (Chapter 4).

A further exciting application of gatemons with nanowires in the quantized conductance regime are semi-digital gates. The typical way to perform single-qubit z gates is to change f_{01} as a function of time t. Here, this would be done by changing V_G. The single-qubit phase ϕ that is acquired is given by the frequency difference Δf_{01} integrated over the gate time,

$$\phi = \int_{t_0}^{t_f} \Delta f_{01}(V_G(t))\mathrm{d}t. \tag{1.16}$$

The acquired phase is therefore sensitive to noise in V_G during the gate time. In the case of perfectly quantized conductance, this dependence would be largely suppressed as small deviations in V_G would not lead to a change in f_{01}. However, the acquired phase is still sensitive to errors in the timing. In a similar manner it might be possible to implement two-qubit gates that are more resilient to noise. Such semi-digital gates might prove to be useful in qubit control which is due to the analog character of its gates inherently error prone [44].

1

1.3 Charge parity detection for topological quantum computing

Quantum computations are inherently prone to errors because their fundamental building blocks, qubits, are imperfect. To mitigate the effects of errors on single qubits that are part of a large code, involved and elaborate schemes are required [45–47]. An appealing alternative is therefore a quantum computer that is inherently protected from errors, a topological quantum computer [48–50]. The necessary ingredients for a possible scheme are a one-dimensional semiconducting nanowire with strong spin-orbit interaction and a high g-factor, a magnetic field along the wire axis and superconductivity [51–53]. The quantum states in such an implementation are stored non-locally, and are therefore insensitive to decoherence [54]. The readout in such schemes relies on the mapping of the quantum state onto a charge parity [55]. Also more recent schemes use this principle [56, 57]. Therefore, efficient charge parity detection is required to perform readout on such quantum computers.

Nanowire based transmon qubits are well-suited to act as charge-parity detectors in topological quantum computation schemes. The materials used, field compatible superconductors and nanowires, make the fabrication requirements of these transmons comparable to the above mentioned necessary ingredients for topological quantum computers. The use of a nanowire junction instead of the typically used Josephson junction based on Al and AlO_x eliminates the problem of the low critical magnetic field of bulk Al [58]. The use of NbTiN and nanowire junctions opens the door to operating such qubits at fields of ~ 0.5 T, the typical requirement for the above mentioned application. Further on, transmons are good charge-parity detectors [59, 60]. Ramsey-based techniques allow detection of small frequency shifts. Therefore, the qubit system discussed in this thesis makes a good candidate to perform these tasks.

1.4 Coupling transmons to different quantum systems

Superconducting qubits in a circuit quantum electrodynamics architecture can exhibit high coupling rates to their control knobs, which allows experimentalists to perform fast operations on them [61, 62]. However, their coherence is comparatively low, which makes the execution of long and complex quantum algorithms challenging so far [63]. On the other hand, electron spin ensembles from crystal defect sites can store quantum states for a long time [64]. This makes them attractive candidates for quantum memories (a quantum hard drive). However, the direct coupling to such system typically is rather low. Therefore, combining these two systems could allow for fast operations and long storage times [65].

The strong coupling between electron spins ensembles and superconducting coplanar waveguide resonators has been demonstrated [66, 67]. In subsequent work, even the coupling to a superconducting qubit could be shown [68]. Application of a magnetic field would polarize the spin ensemble and shift its frequencies to higher fields, improving performance [69]. This scheme could be extended to also address nuclear spins via hyperfine coupling [70] or allow conversion from microwave to optical photons [71]. Further on, the coupling to other quantum computing platforms that require magnetic fields can be realized [72, 73].

1.5 Thesis overview

I started my PhD around the time when the first two demonstrations of hybrid super-conducting-semiconducting transmon devices were published [37, 38]. Where the implementation in Copenhagen was mostly focusing on demonstrating coherence in voltage-tunable circuits, the work done in Delft was aiming at understanding the physics of both, voltage- and flux-tunable devices. This defined an interesting starting point for the project. Would it be possible to make coherent flux- and voltage-tunable devices that push the coherence times towards those of standard transmons? Would they make for useful qubits? And would these devices be able to withstand magnetic fields, just as we hoped for?

In Chapter 2, I discuss the theoretical basics needed for a single-qubit cQED experiment. Starting from the idea of engineering artificial atoms, I will discuss their building blocks. I focus on how the Josephson junction in standard transmons differs from the one in nanowire transmons, and what that means for the spectrum of these devices.

Chapter 3 describes the fabrication process that combines standard cQED fabrication techniques with the nanowire etching and contacting. I will also highlight the fabrication improvements made to increase the field compatibility of the devices. This includes holes in resonators and qubits to avoid vortex formation and NbTiN air-bridges.

Then, in Chapter 4, I show the basic characterizations of flux- and voltage-tunable nanowire transmon qubits. I address the question whether these qubits have a shot at being useful for large-scale quantum computation. A detailed investigation of their noise background reveals a previously unknown noise process.

In Chapter 5, I study the effects of an applied in-plane magnetic field to the qubits that were discussed in Chapter 4. This is the first demonstration of coherence of superconducting qubits in magnetic fields exceeding the superconducting gap of aluminum. Based on the response of the devices to the magnetic field, I identify several factors that limit their performance.

In Chapter 6, I address the limitations for field compatibility. A first demonstration of a flux-tunable split-junction device operating in in-plane magnetic fields exceeding the gap of aluminum is given.

I summarize the results and findings of this thesis in Chapter 7, and give an outlook for future possibilities.

2 SEMICONDUCTING-SUPERCONDUCTING HYBRID TRANSMON DEVICES

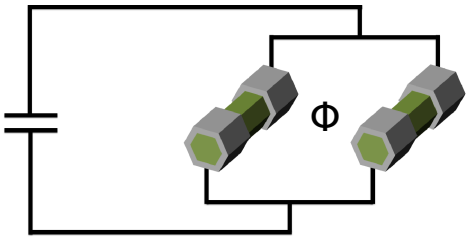

Figure 2.1: Schematic of a flux-tunable split-junction nanowire transmon.

In this chapter, the theoretical basics of the devices studied in this thesis are discussed.

2.1 Engineering atoms

Nature provides us with almost ideal two-level systems that can be used as qubits. For example, trapped ions [74] or electron and nuclear spins of single dopant in purified silicon [75] can encode quantum states. However, it is also possible to engineer two-level systems. This can be done in various ways, for example by defining quantum dots in a two-dimensional electron gas [76] with superconductors [77–79]. The approach of engineered qubits, typically solid-state systems, has the advantage that it can rely on existing lithographic fabrication techniques and it gives freedom in the choice of parameters. The price to pay is, however, that in current implementations of fully engineerable systems the coherence times are comparatively short [63, 75, 80]. It is therefore important to reduce the noise these circuits are subject to by means of cleaner fabrication or better filtering and to make them more insensitive to these noise processes by smart design of the circuits and parameter choices.

In this chapter, we describe how the transmon [62], one of the most promising qubits for medium-scale quantum computing, emerged from its predecessor, the Cooper-pair box (CPB) [77, 81], and how its properties change when its key component, the Josephson junction, is formed by a proximitized semiconducting nanowire [82–85]. Transmons are essentially anharmonic LC oscillators that can be brought into their quantum ground state. This imposes two requirements, a nonlinear element and a circuit with low dissipation. Without a low dissipation rate the quantum information is quickly lost. Therefore, the use of superconducting materials is a natural choice. Further on, superconducting materials offer, in the form of Josephson junctions [86], a way to implement dissipationless, nonlinear inductances. These provide the required anharmonicity of the oscillator, enabling us to use them as qubits.

We will begin with a brief discussion of what happens at a normal conductor — superconductor (NS) interface and how this leads to Andreev bound states (ABS) in a SNS junction. From there on, we will see how this phase-dependent ground-state energy leads to the Josephson effect (Section 2.2). We will then turn to the energy levels of CPBs and transmons, and discuss the effect of different types of Josephson junctions (Section 2.3). Special attention will be given to how the nanowire transmons differ from the standard transmons based on superconductor — insulator — superconductor (SIS) junctions. Finally, we will see how to interface with these artificial atoms in the framework of circuit quantum electrodynamics (Section 2.4). Because this is an experimental thesis, the theoretical discussions aim to provide intuition for the underlying physics, and will refer to other works for rigorous derivations. We will rather focus on solving the Hamiltonian describing the qubit and exploring various features of it.

2.2 Andreev bound states and Josephson junctions

In this section, we will discuss how the nonlinear inductance required to make the above described anharmonic oscillators comes about. We will discuss briefly how Andreev reflections occur at the interface between a superconductor and a semiconductor, and how Andreev bound states manifest themselves in SNS junctions. We will see how these bound states

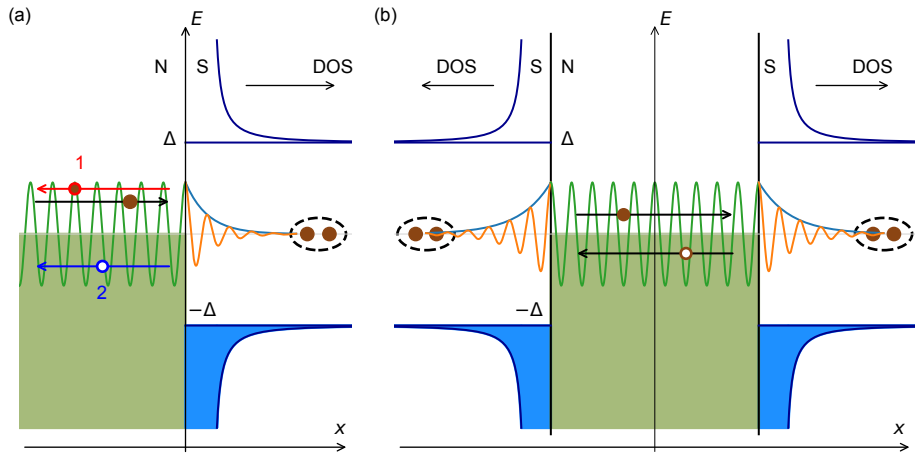

Figure 2.2: Schematic of the relevant processes at NS and SNS interfaces. (a) An electron with $E < \Delta$ is coming from the normal conductor where it is described as a plane wave. When it reaches the superconductor, it can either undergo a specular reflection (1) and no charge transfer happens, or can back-reflect a hole (2) and a charge of $2e$ is transferred into the superconductor. A Cooper-pair is created and the quasi particles are described by an evanescent wave in the superconductor. Note that the waves have the same energy but are shifted for readability. (b) The Andreev bound state extends with evanescent waves into the superconductors and is a superposition of a hole and an electron in the normal part.

lead to a supercurrent between the two superconductors, and from that derive the Josephson effect.

2.2.1 Andreev reflection

Let us now consider the interface between a normal conductor and a superconductor. When an electron or a hole hits the NS interface, three things can happen. If the electrons or holes in the normal conductor have an energy $E > \Delta$, where Δ is the superconducting gap (for aluminum Δ is around 45 GHz$\cdot h$ or 0.3 meV), they can directly enter the superconductor and are quasiparticles there. If their energy is less than the gap energy, no quasiparticle states are available and they will be back-reflected and no charge transfer will occur (specular reflection) [Figure 2.2(a)]. The third process, the Andreev reflection [87], enables charge transport even in the case of $E < \Delta$. There, an electron from the normal conductor can be reflected as a hole at the NS interface, adding a Cooper-pair of charge $2e$ to the superconductor. Note that this process conserves the momentum, as $\hbar k_\mathrm{h} = \hbar k_\mathrm{e} - 2E/v_\mathrm{F}$. As $|E| \ll E_\mathrm{F}$ ($E_\mathrm{F} \sim 1 - 10$ eV is the Fermi energy), $k_\mathrm{h} \approx k_\mathrm{e} \approx k_\mathrm{F}$, but the hole velocity is opposite to that of electrons.

Now we will try to give an intuitive understanding of the steps necessary to derive the precise relations. For a more elaborate and thorough description, the reader is directed to

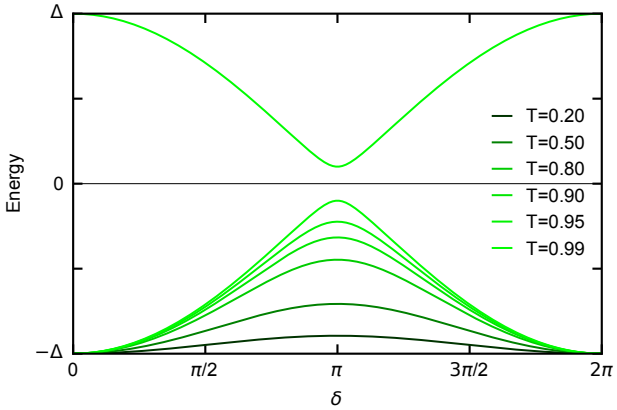

Figure 2.3: Energy of an Andreev bound state for different transmission probabilities versus phase difference of the superconductors. The excited state energy is only indicated for $T = 0.99$.

references [88–94] where the calculations are performed in detail. Excitations in a metal with superconductivity are described by the Bogoliubov – de Gennes (BdG) equation which describes the energy of electron- and hole-like wave functions, and mixes them in the presence of superconductivity. In the absence of superconductivity, the solutions of the BdG equation for both the electron- and hole-like parts are just plane waves. In the presence of superconductivity, and for energies below the gap, there are no quasiparticle states available that extend through the whole superconductor. Let us consider an ideal NS interface (no scattering), and only a single conduction channel (as there is not mixing between channels). We match the quasiparticle wave functions and their derivatives for the superconducting and the normal part at the interface. The solution in the normal conductor takes the form of an incoming electron and a back-reflected hole (with the acquired reflection amplitude depending on superconducting phase, Δ and E) as plane waves. In the superconducting part, there is only an evanescent solution. It has a complex momentum, which means that the wave function is exponentially decaying in the superconductor. The length scale over which this happens is the superconducting coherence length ξ (for Al, $\xi \sim 1.6\ \mu$m [95]).

2.2.2 Andreev bound states

Now that we have some intuition for what happens at the NS interface we turn to the SNS junction. We focus again on the intuitive understanding and refer the reader interested in a rigorous derivation to references [84, 88–93, 96]. The geometry we considered is one-dimensional, with two semi-infinite superconductors with phase difference δ separated by a coherent conductor of length l [Figure 2.2(b)]. According to the Landauer formalism [97], the conduction is fully described by the set of transmission channels $\{T_i\}$ of the conductor. We can consider only a single channel because Andreev reflections do not mix conduction channels. For now we assume that l is smaller than the superconducting coherence length ξ (short-junction limit), and will later argue that this is indeed the case in the devices presented in this thesis. The coherent conductor is therefore modeled as a scattering impurity that is a repulsive delta function.

We can consider in a pictorial view an electron (hole) in the coherent conductor of the above described geometry with energy small compared to the gap. As the electron (hole) reaches the NS interface, it will be reflected as a hole (electron), which in turn will undergo the same process at the other interface. This leads to a finite motion of the electron/hole, and therefore bound states with discrete energy levels. This information is used to write an ansatz for a solution of the ABS wave functions. It is the sum of electron- and hole-like solutions of the Bogoliubov-de Gennes equation in the superconducting parts of the geometry, multiplied with a spatially decaying exponential around the scatterer as the state has to be bound. The ansatz needs to fulfill two conditions, yielding one equation each: Its left and right limits around the scatterer need to be the same, and the Schrödinger equation, integrated over a small interval around the scatterer, needs to hold. In the Andreev approximation ($\Delta \ll \mu$), these two equations can each be written as scattering matrices and be plugged into one another. The combined equation then has the form of an eigenequation. Its solutions yield the ABS energies that depend on the transmission probability T and the phase difference of the superconductors δ,

$$E_{\mathrm{ABS}}(T, \delta) = \pm\Delta\sqrt{1 - T\sin^2(\delta/2)}. \tag{2.1}$$

The ABS energies are shown in Figure 2.3 for various transmission probabilities. For temperatures of $\sim$ 100 mK, temperature dependent corrections [96, 98] are only relevant around $\delta = \pi$ and for transmissions $T \gtrsim 0.95$. It is worth noting that transmission probabilities of $T = 0.98$ have been achieved in devices with comparable wires [99]. Further effects that could require corrections are [91] the finite-sized barrier, the fact that a semiconductor is used (which might invalidate assumptions on the k-vectors), and the spatial dependence of Δ due to the proximity effect and scattering. Taken all this into account, it is fascinating that Equation (2.1) describes the behavior in many experiments quite well [37, 98–100].

We will need the ABS energy to derive the properties of SNS and SIS junctions and explain several peculiarities of the spectrum of nanowire based transmons. It will turn out to be handy to use the Fourier decomposition of the ABS energy in order to use it in computations. Because Equation (2.1) is even, the Fourier decomposition is given as

$$E_{\mathrm{ABS}}(T, \delta) = \pm\sum_n E_{\mathrm{J}_n}(T)\cos(n\delta), \tag{2.2}$$

with the components

$$E_{\mathrm{J}_n}(T) = \frac{2\Delta}{\pi}\int_0^\pi \sqrt{1 - T\sin^2(\phi/2)}\cos(n\phi)\mathrm{d}\phi, \tag{2.3}$$

as shown in Figure 2.4. Where for small T the first term is clearly dominant, this no longer holds true for $T \sim 1$ and also higher order contributions need to be taken into account. Further on, the E_{J_n} are not linear in T and their sign alternates with n. As the higher-order terms fall off strongly, only the E_{J_n} for $n \leq 7$ are taken into account for computation.

2.2.3 Situation in nanowires

Let us now investigate the transport in the nanowires. The semiconducting band gap of InAs is large in comparison to the superconducting gap of Al. Therefore, the states that contribute

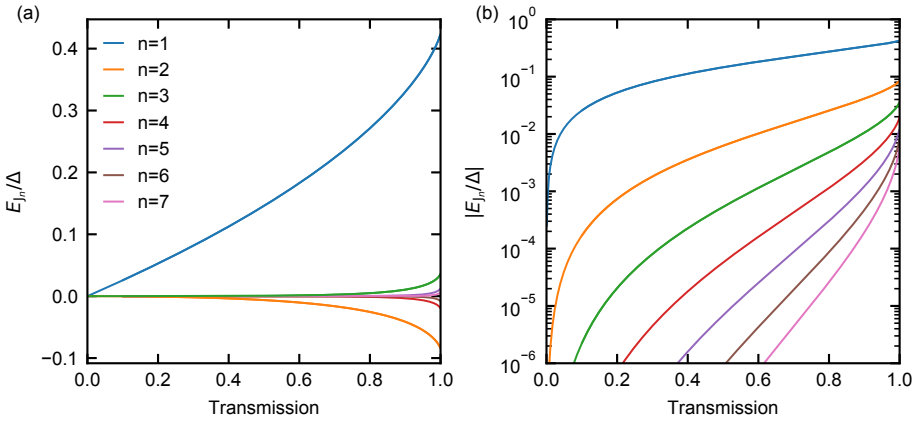

Figure 2.4: Fourier components of the Andreev bound state energy versus transmission probability. Note that the coefficients are not linear in T and alternate in sign. As they fall of strongly with n, only 7 components are used in subsequent computations.

to electron and hole transport are confined in the InAs nanowire and are only weakly influenced by the superconducting shell. The dispersion relation is given as

$$E_\mathrm{p} = \frac{\hbar^2}{2m_\mathrm{e}} k_\mathrm{p}^2, \text{ with } k_\mathrm{p} = \frac{2\pi}{\lambda_\mathrm{p}} = \frac{p\pi}{d}, \tag{2.4}$$

where d is the length in the respective direction. The energy difference between subsequent levels is $\Delta E_{\mathrm{p,p-1}} \propto 1/d^2$. This means that the energy levels in radial direction (the nanowire radius is $\sim$ 50 nm) are much further spaced than in longitudinal direction (the nanowire length is $2-10$ μm) where they essentially form subbands (Figure 2.5). This leads to effectively one-dimensional charge transport. Each subband whose minimum is below the Fermi energy E_F can therefore host an ABS. The total phase-dependent energy of the junction is therefore given as the sum of the ABS energies E_i in each subband,

$$E_\mathrm{J}(\delta) = \sum_\mathrm{i} E_{\mathrm{ABS,i}}(\delta) = \Delta \sum_\mathrm{i} \sqrt{1 - T_\mathrm{i} \sin^2(\delta/2)}. \tag{2.5}$$

From measurements and calculations in this work it is not possible to strictly prove that the nanowire junctions used really operate in the short junction limit. Here we try to highlight the reasoning why the short junction limit still yields a good description [101]. From independent measurements it is known that the the typical mean free path in InAs nanowires is around $l_\mathrm{MFP} \sim 100$ nm [102] and the Fermi velocity $v_\mathrm{F} \sim 10^8$ cm/s [103]. Measurements of nanowires of the same batch as used in Chapter 4 have shown to have an induced superconducting gap of $\sim 45\,\mathrm{GHz}\cdot h$ [83], roughly the same as that of bulk aluminum [58]. We can therefore expect a superconducting coherence length $\xi_0 = \hbar v_\mathrm{F}/\pi\Delta \sim 1100$ nm [101, 104] in the proximitized InAs leads. The junction coherence length [84] is $\xi_\mathrm{J} = \sqrt{\xi_0 l_\mathrm{MFP}} \sim$ 300 nm. The typical junction length in this work is $L \sim 200$ nm $\lesssim \xi_\mathrm{J}$, indicating that we

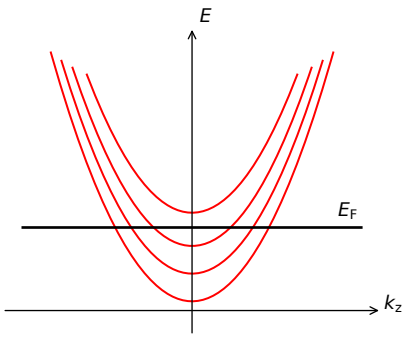

Figure 2.5: Schematic of the subbands contributing to the transport. In the non-confined direction of the nanowire the electrons are free to travel, yielding the parabolic shape of the subbands. Subbands below the Fermi energy host an Andreev bound state contributing to the transport through the wire. Sidegate tuning changes the relative energy of the subbands with respect to the Fermi energy.

are rather in an intermediate regime which might give corrections. However, we observe that the short-junction model describes the spectrum of the devices under test well. Further on, several recent experiments using similar nanowires have shown to yield good agreement to a short junction theory [37, 98, 100, 105].

The phase dependent energy in Equation (2.5) leads to a supercurrent in the ground state. The time derivative of the energy,

$$\frac{\mathrm{d}E}{\mathrm{d}t} = \frac{\partial E(\delta)}{\partial \delta}\frac{\mathrm{d}\delta}{\mathrm{d}t}, \tag{2.6}$$

is essentially the power. We know that in superconductors the phase change over time is related to the potential of the corresponding superconductor, $\dot{\delta} = 2eV/\hbar$ [92]. The power is the product of current and voltage, hence we can write

$$I(\delta) = \frac{2e}{\hbar}\sum_{\mathrm{i}}\frac{\partial E_{\mathrm{i}}}{\partial \delta} = \frac{e\Delta}{2\hbar}\sum_{\mathrm{i}}\frac{T_{\mathrm{i}}\sin(\delta)}{\sqrt{1-T_{\mathrm{i}}\sin^2(\delta/2)}}. \tag{2.7}$$

In the case of high transmission probabilities, this leads to a skewed sinusoid (Figure 2.6) [37, 98]. Taking the time derivative of this equation allows us to calculate the inductance as

$$L = V\left(\frac{\mathrm{d}I}{\mathrm{d}t}\right)^{-1}, \tag{2.8}$$

yielding

$$L_{\mathrm{SNS}}(\delta) = \frac{\hbar^2}{e^2\Delta}\cdot\sum_{\mathrm{i}}\left[\frac{\left(1-T_{\mathrm{i}}\sin^2(\delta/2)\right)^{3/2}}{\cos(\delta)\left(1-T_{\mathrm{i}}\sin^2(\delta/2)\right)-\frac{T_{\mathrm{i}}^2}{4}\sin^2(\delta)}\right] \tag{2.9}$$

which is nonlinear.

2.2.4 SIS junctions and split junctions

Another limit of interest is the superconducting-insulating-superconducting (SIS) tunnel junction. It is characterized by many transmission channels ($\sim 10^4/\mu\mathrm{m}^2$ [106–108]) with low transmission probabilities $T_{\mathrm{i}} \ll 1$. Using this area density of channels, typical junction sizes

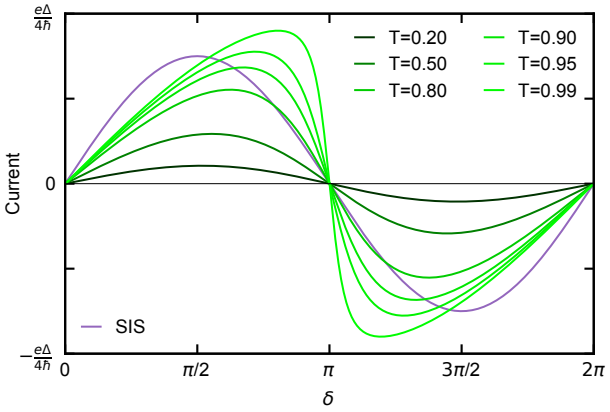

Figure 2.6: Current phase relation of an Andreev bound state with transmission probability T. As T increases, the CPR gets more and more skewed. An SIS junction (shown with $\sum_i T_i = 0.75$) has a purely sinusoidal CPR.

in our group [2] of $\sim 0.04\ \mu\mathrm{m}^2$, and typical room-temperature resistance values, we expect several hundred transmission channels of $\sim 1\%$ transmission each. We can approximate Equation (2.7) as

$$I(\delta) = \left(\frac{e\Delta}{2\hbar}\sum_i T_i\right)\sin(\delta) = \frac{\pi\Delta}{2e}G_\mathrm{N}\sin(\delta) = I_\mathrm{crit}\sin(\delta), \tag{2.10}$$

which leads to a sinusoidal current-phase relation (Figure 2.6). For this we used the Landauer formula [92] and expressed the critical current I_crit in terms of the normal state conductance G_N of the junction (Ambegaokar-Baratoff formula) [109]. Note that Equation (2.10) is also known as the DC Josephson effect. The corresponding Josephson energy of an SIS junction is therefore given as

$$E_\mathrm{J,SIS}(\delta) = -E_\mathrm{J}\cos(\delta),\ \text{with}\ E_\mathrm{J} = \hbar I_\mathrm{crit}/2e. \tag{2.11}$$

The corresponding inductance is

$$L_\mathrm{SIS}(\delta) = \frac{\hbar}{2eI_\mathrm{crit}\cos(\delta)}, \tag{2.12}$$

which is also nonlinear.

It is instructive to discuss the concept of a superconducting quantum interference device (SQUID), which enables tuning the supercurrent through the Josephson junction with an external flux. The SQUID is a superconducting loop enclosing an area A with a Josephson junction in each of its two arms. The total current though the SQUID is then the sum of the current in each junction,

$$I_\mathrm{tot} = I_\mathrm{crit,A}\sin(\delta_\mathrm{A}) + I_\mathrm{crit,B}\sin(\delta_\mathrm{B}), \tag{2.13}$$

with phase drops δ_A and δ_B across the junctions. Taking the integral of a magnetic field B over the SQUID area lets us write

$$\delta_\mathrm{A} - \delta_\mathrm{B} = \frac{2\pi}{\Phi_0}\int B\cdot \mathrm{d}A = 2\pi\frac{\Phi}{\Phi_0} = \varphi, \tag{2.14}$$

with φ the reduced flux, where we implicitly used Stokes theorem to convert the area integral of a field to a contour integral (through the superconductor and the junctions) of its vector potential and know that there is a zero phase shift along the closed contour. Thus, the total current through the SQUID is

$$I_{\text{tot}} = I_{\text{crit,A}} \sin(\varphi + \delta_{\text{B}}) + I_{\text{crit,B}} \sin(\delta_{\text{B}}). \tag{2.15}$$

2.3 Transmons

In the introduction of this chapter we discussed that an anharmonic oscillator in its quantum ground state can be seen as a qubit. We identified LC resonators with a nonlinear inductance as good candidates for this approach. In the previous section the nonlinear inductance provided by the dissipationless Josephson effect was investigated. In this section we bring the Josephson junction together with a capacitor and discuss how to make a transmon qubit, and how it behaves.

2.3.1 The Hamiltonian in the charge basis

The Hamiltonian of an anharmonic LC oscillator has a capacitive part, described by the charging energy E_{C}, and an inductive part, described by the Josephson energy E_{J}. The charging energy is defined by the total capacitance of the transmon, and the Josephson energy is determined by the Josephson junction. Using the conjugate variables of Cooper-pair number imbalance $\hat{n}$ and superconducting phase difference $\hat{\delta}$ between the two islands, the Hamiltonian of the system can be written as [110]

$$\hat{H} = 4E_{\text{C}}\hat{n}^2 - E_{\text{J}}(\hat{\delta}). \tag{2.16}$$

In the following discussion we will see that the properties of this system can vary substantially depending on the ratio of $E_{\text{J}}/E_{\text{C}}$ and the form of E_{J}.

The Hamiltonian of Equation (2.16) only describes an isolated single-junction device. In the case of a split-junction qubit that is flux tunable, the Josephson energy needs to be expressed with the flux dependence described in Equation (2.15). Further on, there is a charge background of the environment that can influence the charge states on the islands. Taking these two contributions into account, we can rewrite Equation (2.16) to

$$\hat{H} = 4E_{\text{C}}(\hat{n} - n_{\text{g}})^2 - \sum_n E_{\text{J,A}_n} \cos(n\hat{\delta}) - \sum_n E_{\text{J,B}_n} \cos\left(n(\varphi - \hat{\delta})\right), \tag{2.17}$$

where n_{g} is the background charge and φ the flux through the SQUID loop.

Performing calculations with the Hamiltonian in the form of Equation (2.17) is not very convenient because it contains two conjugate variables. It becomes much easier if we rewrite Equation (2.17) in the charge basis, using

$$\mathrm{e}^{\pm i n\hat{\delta}} |N\rangle = |N \pm n\rangle, \tag{2.18}$$

where $|N\rangle$ denotes the charge state of N excess Cooper-pairs on one of the islands with respect to the other. Note that the charge states with $\hat{n}|N\rangle = N|N\rangle$ the eigenvalues and

eigenfunctions form a complete, orthonormal basis of the Hilbert space. We keep the Josephson energy as the Fourier decomposition of a general form [see Equation (2.3)] and express its n-th component in the charge basis as

$$E_{\mathrm{J}_n}\cos(n\hat{\delta})\,|N\rangle = \frac{E_{\mathrm{J}_n}}{2}\left(e^{in\hat{\delta}} + e^{-in\hat{\delta}}\right)|N\rangle = \frac{E_{\mathrm{J}_n}}{2}\left(|N+n\rangle + |N-n\rangle\right). \tag{2.19}$$

Hence, the term E_{J_n} describes the transfer of n Cooper-pairs across the Josephson junction.

We use this to write Equation (2.17) in the charge basis,

$$\begin{aligned}\hat{H} = 4E_{\mathrm{C}}\sum_n \left(N-n_g\right)^2 |N\rangle\langle N| - \sum_n \frac{E_{\mathrm{J,A}_n}}{2}\left(|N\rangle\langle N+n| + |N+n\rangle\langle N|\right)\\ - \sum_n \frac{E_{\mathrm{J,B}_n}}{2}\left(e^{in\varphi}|N\rangle\langle N+n| + e^{-in\varphi}|N+n\rangle\langle N|\right),\end{aligned} \tag{2.20}$$

With a potential relative charge offset n_{g} on the capacitor islands. We express the contribution of the n-th Fourier component to the Josephson energy,

$$\frac{E_{\mathrm{J}_n}}{2} = \frac{E_{\mathrm{J,A}_n}}{2} + \frac{E_{\mathrm{J,B}_n}}{2}e^{-in\varphi},$$

to write the full matrix of the Hamiltonian as

$$\hat{H}(n_{\mathrm{g}},\varphi) = \begin{bmatrix} \ddots & & & & \iddots \\ & 4E_{\mathrm{C}}(1-n_{\mathrm{g}})^2 & -\frac{E_{\mathrm{J}_1}}{2} & -\frac{E_{\mathrm{J}_2}}{2} & \\ & -\frac{E^*_{\mathrm{J}_1}}{2} & 4E_{\mathrm{C}}{n_{\mathrm{g}}}^2 & -\frac{E_{\mathrm{J}_1}}{2} & \\ & -\frac{E^*_{\mathrm{J}_2}}{2} & -\frac{E^*_{\mathrm{J}_1}}{2} & 4E_{\mathrm{C}}(1-n_{\mathrm{g}})^2 & \\ \iddots & & & & \ddots \end{bmatrix}. \tag{2.21}$$

The terms on the diagonal correspond to the contribution of the charging energy. The entries on the n-th off-diagonal describe the tunneling of n Cooper-pairs across the junction. The eigenvalues of Equation (2.21) are the energy levels of the system and can be computed numerically. Unless otherwise stated, we will truncate the number of charge states to 61 for all the following calculations. This is because the contributions of higher charge states fall off stronger than exponentially (Figure 2.8) and a 61×61 matrix is still fast to diagonalize on a normal computer.

2.3.2 From the Cooper-pair box to the transmon

With the possibility to compute the energy levels of the system, we will now discuss the influence of the various parameters. First, we will revisit the difference between the Cooper-pair box and the transmon [62]. For this we will assume the Josephson energy to be purely sinusoidal, reflective of an SIS junction. We will investigate how the energy levels depend on n_{g}, and what that implies for the wave function. Then, we will look at the tuning mechanisms of both SNS and SIS transmons and highlight the implications for anharmonicity.

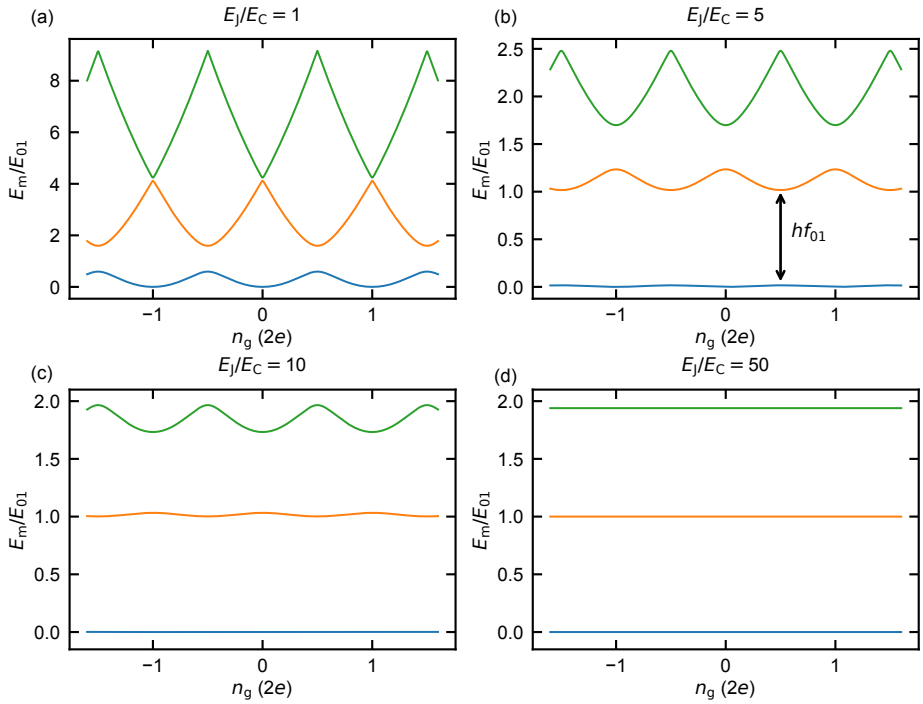

Figure 2.7: Lowest lying energy levels plotted as a function of n_g for different ratios of Josephson to charging energy. While for low ratios the transition energy between the eigenstates is strongly dependent on n_g (a-c), this dependence is strongly suppressed for ratios > 30 (d) and the transition is exponentially insensitive to n_g.

Early implementations of the anharmonic LC oscillators as qubits were suffering from short coherence times due to their strong sensitivity to n_g [77, 111]. These so-called Cooper-pair boxes only had fairly small total capacitances, making their E_J/E_C ratios ~ 1, leading to a strong dependence of the transition frequency f_{01} on n_g [Figure 2.7(a)]. On-chip charge noise (the noise in n_g) is hard to reduce, therefore a better approach is to reduce the sensitivity to it. This can be achieved by increasing the ratios of E_J/E_C, see Figure 2.7(b-d). By increasing the total capacitance between the transmon islands C_Σ, basically making the geometrical capacitance of the islands to each other much bigger than the capacitance due to the Josephson junction, $E_C = (2e)^2/2C_\Sigma$ is reduced. By increasing E_J, the coupling between adjacent charge parabolas [compare Figure 2.7(a)] is increased, effectively flattening them and making them insensitive to changes in n_g. The price to pay is a reduction in the anharmonicity $\alpha = f_{12} - f_{01}$, setting a limit to how fast qubit control pulses can be without leaking into the second excited state [112].

This is a good example of how the sensitivity to noise can be strongly reduced by smart design of artificial atoms. Indeed, the demonstration of the first transmons has lead to a major

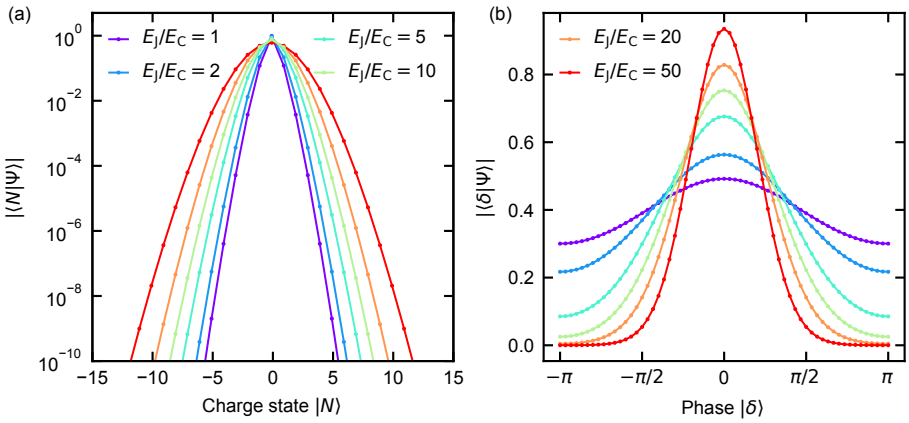

Figure 2.8: Wave function of the lowest energy levels at different values of E_J/E_C. (a) Absolute value of the wave function in the charge basis. Low E_J/E_C ratios lead to a wave function with only few charge states (purple). More charge states contribute as the E_J/E_C ratio is increased (red). (b) Absolute value of the wave function in the phase basis. As the E_J/E_C ratio increases the wave function becomes better defined in phase.

improvement in dephasing times in comparison to CPBs [113, 114]. It also paved the way for further advances. Recently echo dephasing times of $> 200\ \mu$s have been demonstrated [63].

The nature of the qubit states drastically changes when increasing E_J/E_C. The wave function $|\Psi\rangle$ of the ground state is the eigenvector corresponding to the lowest eigenvalue of Equation (2.21) and can be written as $|\Psi\rangle = \sum_N \Psi_N |N\rangle$. Whereas the qubit states for the CPB are mostly encoded in one charge state, this is no longer true for transmons with a large ratio, see Figure 2.8(a). The comparatively large Josephson coupling mixes adjacent charge states and the wave function spreads out over many charge states. Effectively, the qubit states are no longer charge states but plasma modes. It is also possible to look at the wave function in the phase basis. As phase and charge are conjugate variables, this is most easily done by a discrete Fourier transform of the wave function calculated in the charge basis,

$$\Psi(\delta) = \frac{1}{\sqrt{2\pi}} \sum_N \Psi_N e^{i\delta N}. \tag{2.22}$$

As the E_J/E_C ratio increases, the wave function becomes better and better defined in phase [Figure 2.8(b)]. The qubits presented in the experimental chapters of this thesis generally have an E_J/E_C ratio of at least 30 and are therefore not limited by noise in n_g that couples via E_C.

2.3.3 Flux tunability of SIS and SNS transmons

Although changing f_{01} with voltage is not desirable, as we have just discussed, it is still useful when qubits have a knob that tunes their frequency. In fact, it is a prerequisite for many experiments [2, 115, 116] and some implementations of quantum error correcting codes [47]. A pop-

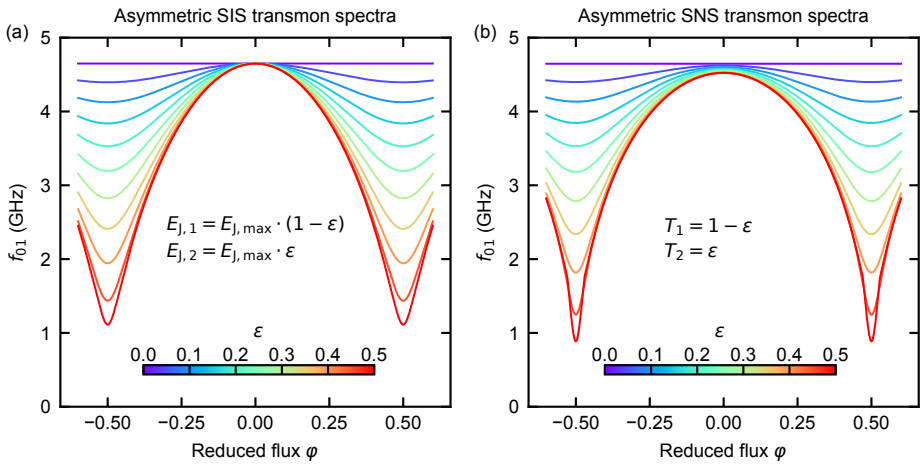

Figure 2.9: Flux tunability of SIS and SNS transmons. (a) Frequency spectrum of an SIS transmon with various asymmetry values. (b) Frequency spectrum of an SNS transmon where each junction has only one channel, for various asymmetries.

ular way of achieving frequency tunability of transmon qubits is to make split-junction devices that are flux tunable. Essentially, the single Josephson junction is replaced by a SQUID loop, and the current through the SQUID loop is controlled with the applied flux [Equation (2.15)].

In the case of SIS junctions, the maximum tunability is achieved when symmetric junctions are chosen [Figure 2.9(a)]. This can be seen as choosing $E_{J,A_1} = E_{J,B_1} \neq 0$ as the only non-zero coefficients in Equation (2.17). The maximum frequency of the qubit is then approximately $f_{01}h \approx \sqrt{8E_J E_C} - E_C$ [62] (for the simulations we choose the experimentally obtained value of $E_C/h = 278$ MHz). The minimum f_{01} is found at the full frustration point ($\Phi = \Phi_0/2$) where E_J vanishes and the qubit is essentially a quantum dot with $f_{01}h \approx 4E_C$. It is worth noting, however, that close to the full frustration point the qubit is highly flux sensitive, making the qubit susceptible to flux noise [28, 34, 35, 117]. This problem can be reduced by choosing asymmetric junctions ($E_{J,A_1} \neq E_{J,B_1}$), therefore reducing the tuning range and the flux sensitivity, and reducing the effect of flux noise [2, 3]. The frequency spectrum of qubits with asymmetric junctions are depicted in Figure 2.9(a).

By replacing the SIS Josephson junctions of the SQUID loop with nanowire junctions, flux tunable nanowire transmons can be obtained. In these devices, the standard case is to have asymmetric junctions as microscopic differences will determine their transmission coefficients. In Figure 2.9(b), we study the flux dependence of the flux tunable SNS transmon. For the ease of illustration we assume that there is only one transmission channel in each junction, and the sum of the transmission coefficients is 1. Note that the sweetspot frequency decrease is due to the varying contribution of E_{J_2} that has an opposite sign to E_{J_1} and is not linear in T (compare Figure 2.4). In the case of asymmetric junctions, or away from the full frustration point, the spectrum is comparable to the spectrum of SIS transmons because the E_{J,A_1} and E_{J,B_1} contributions to E_J are dominant. However, in the case of roughly symmetric junctions,

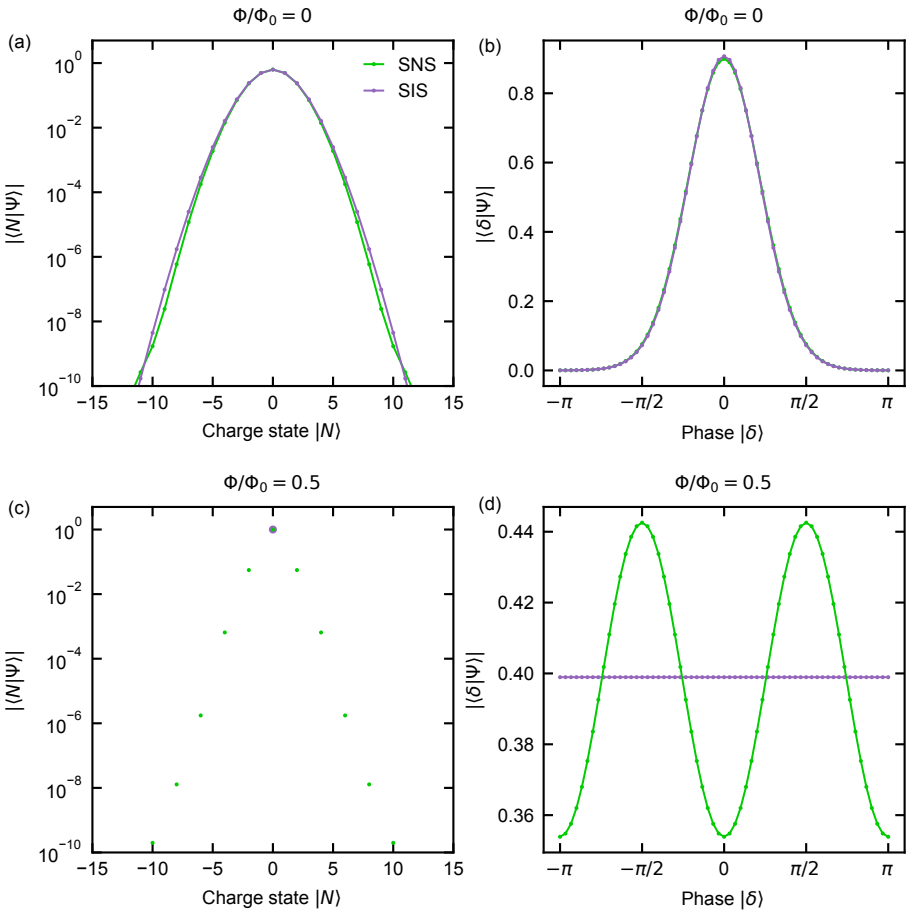

Figure 2.10: Comparison of the wave functions of symmetric flux-tunable SIS and SNS transmons. At the flux sweetspot (a, b) the wave functions are practically identical and defined by plasma modes. At the full frustration point (c, d), the SIS wave function occupies only one charge state due to the vanishing E_J. However, the SNS wave function distributes over even charge states due to the E_{J_2} coupling.

a qualitatively different behavior can be observed around the full frustration point. Because the E_{J_1} terms cancel out, the E_{J_2} contributions become dominant, leading to a double-well potential [37]. This means that around the full frustration point, the qubit states no longer are plasma modes but rather persistent currents like in a flux qubit [118].

The qualitative change in qubit states is highlighted in Figure 2.10 using the example of a symmetric SIS and a symmetric SNS transmon. In both cases, the E_J/E_C ratio is ~ 40. At the sweetspot, the wave functions are almost identical. Both are in the transmon regime where the wave function is a plasma mode that is distributed over several charge states and is well-defined in phase, Figure 2.10(a, b). At the full frustration point, the SIS transmons wave

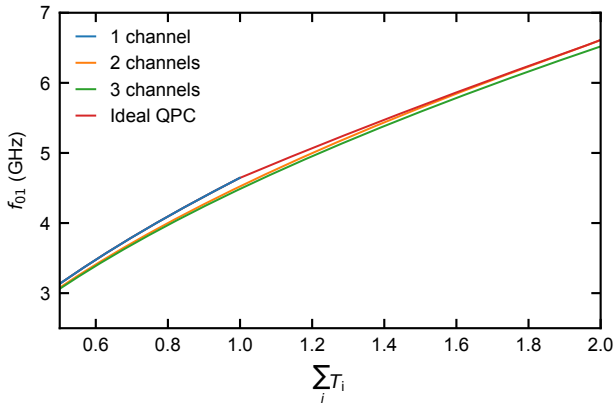

Figure 2.11: The frequency of a SNS transmon increases with the increasing sum of transmission probabilities $\sum_i T_i$. Because E_{J_2} is nonlinear in T, small differences in f_{01} arise between different toy models of the underlying channel configuration.

function is defined by only a single charge state because there is no Josephson coupling hybridizing adjacent charge parabolas [Figure 2.10(c)]. This means that the phase of the wave function is completely undefined [Figure 2.10(d)]. This is completely different for the symmetric SNS transmon: while the E_{J_1} contribution also vanishes (see Equation (2.20)), the E_{J_2} contribution couples the even charge parabolas to each other. The ground state wave function is therefore spread out over only the even charge states, and has a π-periodicity in phase. Practically, this means that the Cooper-pair parity is conserved and the two lowest-lying energy states have an overlap $|\langle 0|\,\hat{N}\,|1\rangle|$ that is exponentially small in E_{J_2}. Fermi's golden rule tells us that this small overlap leads to a strongly suppressed energy relaxation rate, and effectively a *protected qubit*.

2.3.4 Voltage tunability of SNS transmons

In contrast to SIS junctions, nanowire junctions can be tuned *in-situ* using a voltage side gate [37–39, 82, 101, 119]. Due to the altered electrostatic potential, the wave function of the ABS junction will change, therefore changing the transmission probability. A changed transmission probability will in turn change E_J (see Equation (2.1)) and therefore f_{01}. This is in contrast to the flux tuning, where flux-independent part of E_J stays unchanged. If more and more positive voltages are applied, further transmission channels will lie within the Fermi energy and contribute to the transport through the wire (Figure 2.5).

The voltage side gate does not provide deterministic control over the number and transmittivity of the channels. It is therefore not possible to map the effect of the applied side gate voltage on the qubit frequency. We can, however, express f_{01} in terms of its transmission channels, see Figure 2.11. The junction can be described with toy models that lead to slightly different f_{01} and considerably different α (Figure 2.12). Given a certain value of f_{01} and E_C, we can therefore estimate the sum of all transmission coefficients $\sum_i T_i$.

Rather than gaining a quantitative understanding, the intention of the discussion of these models is to get a feel for how f_{01} and α change depending on the model used [101]. In the simplest model, only one transmission channel contributes to the transport. This of course sets a limit to the maximal f_{01} given a fixed E_C. Also, the absolute anharmonicity $|\alpha|$ is

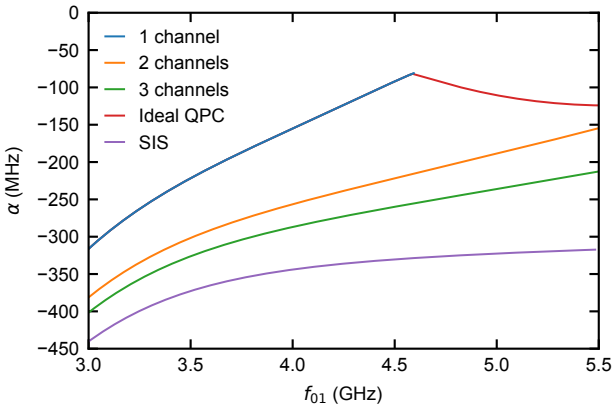

Figure 2.12: Anharmonicity vs f_{01} for different models of the Josephson energy. The anharmonicity decreases if more channels are active in the junction. The case of an SIS junction constitutes a lower limit to the anharmonicity.

minimal in this case, and considerably smaller than $|\alpha|$ of an SIS transmon, which is bounded by E_C for large E_J/E_C ratios. This model can be extended in different ways, for example by assuming several transmission channels of all equal transmission probabilities. There is a small correction in f_{01} due to the nonlinear increase of E_{J_2} with increasing T, but a strong increase in $|\alpha|$. This is not surprising, however, as it is taking the limit of only one channel to the limit of an SIS junction. A further model is the ideal quantum point contact (QPC), where transmission channels are filled subsequently such that at most one is partly filled. This model sets a lower limit to $|\alpha|$.

It is experimentally not possible to directly probe the number and transmittivity of the channels of the junction. While f_{01} gives an indication on the sum of all transmission channels, $\sum_i T_i$, $|\alpha|$ only gives an indication how many channels are dominant. In the case of a flux tunable qubit it is possible to fit the spectrum of the qubit and gain information about the transmission values, compare Chapter 4 and reference [37]. However, this directly assumes a certain number of channels in each junction. This also highlights that it is not possible to convincingly prove that the junctions operate in the short-junction limit.

2.4 Circuit Quantum Electrodynamics

In order to investigate the transmons for which we have laid out the theoretical framework in the previous sections of this chapter, we need to be able to interface them. If the coupling of the transmons to the outside world is not strictly controlled, they will lose their quantum information quickly. Further on, the direct coupling to transmons is weak, making it hard to get information from them. Both of these problems can be solved at once by coupling the transmon to a cavity, here an on-chip resonator [61]. The resonator provides a controlled environment by limiting the number of modes the transmon sees (and can decay into) and increases the coupling to the transmon. The interaction between the qubit and a resonator is described by circuit quantum electrodynamics [110] (cQED). The relevant rates are indicated in Figure 2.13.

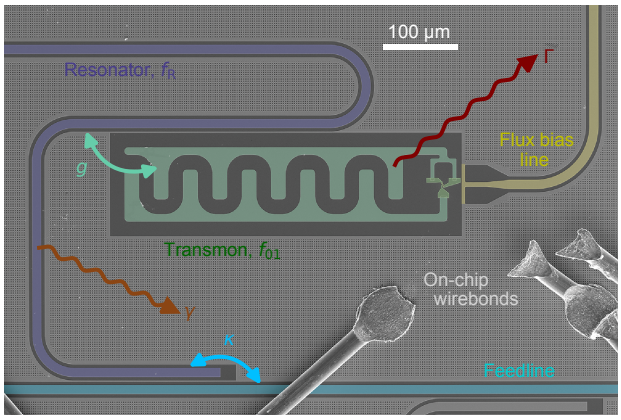

Figure 2.13: A transmon with frequency f_{01} and decay rate Γ coupled with coupling strength g to a readout resonator with frequency f_R and internal loss rate γ. The resonator couples to the outside world (feedline) with rate κ. The flux bias line can be used to control f_{01}.

2.4.1 Resonators

The resonators used here are fabricated in a coplanar waveguide geometry [120]. In order to maximize the number of resonators and qubits on chip we choose to use $\lambda/4$ resonators capacitively coupled to the central feedline (Figure 2.13). Like this, a frequency-multiplexed readout of each individual resonator is possible [121]. Let us now consider a $\lambda/4$ resonator with resonance frequency f_R coupled to the feedline. The frequency dependent transmission S_{21} through the feedline around f_R is given as [122, 123]

$$S_{21}(f) = A\left(1 - \frac{\frac{Q_l}{|Q_e|}e^{i\theta}}{1 + 2iQ_l\frac{f-f_R}{f_R}}\right), \tag{2.23}$$

where A is the transmission amplitude off resonance. The resonator is characterized by the loaded quality factor Q_l, which is defined as

$$Q_l = \frac{f_R}{\Delta f}, \tag{2.24}$$

where Δf is the line width of the resonator, and related to the internal quality factor Q_i and the coupling quality factor Q_c by

$$1/Q_l = 1/Q_c + 1/Q_i. \tag{2.25}$$

Further on, $Q_e = |Q_e|\exp(-i\theta)$ is complex-valued. Its real part $\mathrm{Re}(1/Q_e) = 1/Q_c$ and its imaginary part yields an asymmetry in the resonator line shape. Figure 2.14 shows $|S_{21}|$ of the discussed situation as a function of frequency ($\theta = 0$) with indicated f_R and Δf. From the transmission dip depth the ratio Q_l/Q_i can already be estimated without performing a fit to the data.

A more detailed model for S_{21} that will be used to describe the properties of the resonators presented in this work is given by [122]

$$S_{21}(f) = A\left(1 + \alpha\frac{f-f_R}{f_R}\right)\left(1 - \frac{\frac{Q_l}{|Q_e|}e^{i\theta}}{1 + 2iQ_l\frac{f-f_R}{f_R}}\right)e^{i(\phi_v f + \phi_0)}. \tag{2.26}$$

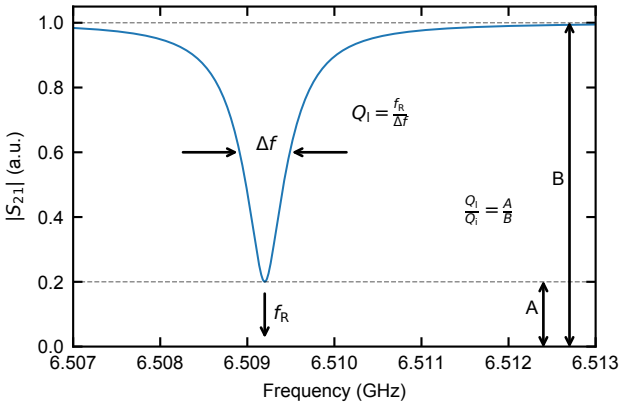

Figure 2.14: Feedline transmission around f_R of a $\lambda/4$ resonator. On resonance, photons acquire a phase of π in the resonator and interfere destructively with incoming photons, leading to a reduced transmission. Low transmission values at f_R indicate a large Q_i in comparison to Q_l.

This model takes a frequency-dependent linear slope α of the transmission line and the propagation delays ϕ_0 and $\phi_v f$ to and from the sample into account.

Let us discuss the role of the quality factors further. Besides the way Q_l is defined in Equation (2.24) it can intuitively be thought of as the number of oscillations the resonator undergoes before the energy in the resonator is decayed to $e^{-2\pi} \approx 0.2\,\%$ of the initially stored energy. The physically important quantities are Q_i and Q_c as described in Equation (2.25). The coupling between feedline and resonator can be chosen geometrically [124] and determines the rate $\kappa = f_R/Q_c$ at which photons leak out of the cavity into the feedline (Figure 2.13). A large value of κ will increase the readout speed [125] but also reduces the qubit T_1 via the Purcell effect [126, 127]. It is therefore important to find a compromise between the two effects. In this work, we generally use $Q_c \approx 10^4$. On the other hand, $\gamma = f_R/Q_i$, the photon loss rate, should be as small as possible because photon losses directly lead to loss of information during the readout and are indicative for losses that will also affect the qubit. Effects reducing Q_i include dielectric losses at various interfaces, spurious modes, radiation, and vortices [35, 122, 128–131]. Appropriate design [12, 132, 133], shielding of the experiment [134] and fabrication [122, 135] can minimize these losses. Turning this around, resonator tests that study Q_i versus various parameters can be a valuable tool to determine limiting factors of qubit T_1.

The value of f_R is controllable by design and fabrication. We consider a standard geometry of a coplanar wave guide with film thickness d (usually, $d \sim 200$ nm) and a center conductor with width w (usually, $w = 12\ \mu$m) that is symmetrically separated by a gap of width s (usually, $s = 6\ \mu$m) from the ground. The value of f_R can be estimated based on the phase velocity and length of the resonator, with additional contributions due to the loading of the resonator. The phase velocity is given by

$$v_{Ph} = 1/\sqrt{\mathcal{C}_l^g(\mathcal{L}_l^g + \mathcal{L}_l^k)} = \frac{c}{\sqrt{\varepsilon_{eff}}}, \tag{2.27}$$

where $\mathcal{L}_l^k$ is the kinetic inductance per unit length, and $\mathcal{C}_l^g$ and $\mathcal{L}_l^g$ are the geometric capacitance and inductance per unit length. It can also be expressed as the speed of light, c,

divided by the effective refractive index of the medium which is given by $\sqrt{\varepsilon_{\text{eff}}}$ where ε_{eff} is the effective relative dielectric permittivity (we assume non-magnetic materials, therefore $\mu_r = 1$). The characteristic impedance of the resonator is then given as

$$Z_{0,\text{R}} = \sqrt{\frac{\mathcal{L}_\text{l}^\text{g} + \mathcal{L}_\text{l}^\text{k}}{\mathcal{C}_\text{l}^\text{g}}}. \tag{2.28}$$

The geometrical contributions per unit length are given by [136, 137]

$$\mathcal{L}_\text{l}^\text{g} = \frac{\mu_0}{4}\frac{K(k_0')}{K(k_0)} \quad \text{and} \quad \mathcal{C}_\text{l}^\text{g} = 4\varepsilon_0\varepsilon_{\text{eff}}\frac{K(k_0)}{K(k_0')}, \tag{2.29}$$

where μ_0 is the vacuum permeability and ε_0 is the vacuum permittivity. K denotes the complete elliptic integral of the first kind,

$$k_0 = \frac{w}{w+2s} \quad \text{and} \quad k_0' = \sqrt{1-k_0^2}. \tag{2.30}$$

In the limit of $d \to 0$ and an infinitely extending geometry, ε_{eff} is the average of the relative dielectric permittivities of the substrate, ε_{Si}, and vacuum. Hence, $\varepsilon_{\text{eff}} = (\varepsilon_{\text{Vacuum}} + \varepsilon_{\text{Si}})/2 = (1+\varepsilon_{\text{Si}})/2 \sim 6.2$ as at ~ 10 K, $\varepsilon_{\text{Si}} = 11.45$ [138]. It is possible to calculate ε_{eff} more accurately [136, 139], but as the kinetic inductance effectively also changes ε_{eff} [Equation (2.27)] measurements are needed to determine this value precisely. Sticking with $\varepsilon_{\text{Si}} \sim 6.2$, we get $\mathcal{C}_\text{l}^\text{g} \sim 160$ pF/m and $\mathcal{L}_\text{l}^\text{g} \sim 400$ nH/m as typical values. Further on, finite-element simulations help to determine $\mathcal{C}_\text{l}^\text{g}$ better [137, 140].

The kinetic inductance contributions arise due to the inertia of the Cooper-pairs in the superconductor. It can be quantified as [141]

$$\mathcal{L}_\text{l}^\text{k} = \mu_0 \frac{\lambda^2}{dw} g(s, w, d) \tag{2.31}$$

with

$$g(s,w,t) = \frac{1}{2k_0^2 \cdot K(k_0)^2}\left[-\ln\left(\frac{d}{4w}\right) - k_0 \ln\left(\frac{dk_0}{4}\right) + \frac{2(w+s)}{w+2s}\ln\left(\frac{s}{w+s}\right)\right],$$

where λ is the magnetic (London) penetration depth of the superconducting film [104]. In the limit of low temperatures and dirty superconductors (electron mean free path $l_{\text{mfp}} \ll \xi$), λ is given as [142]

$$\lambda \approx \sqrt{\frac{\hbar\rho}{\pi\mu_0\Delta}} \approx 105(\text{nm}) \cdot \sqrt{\frac{\rho(\mu\Omega\text{cm})}{T_\text{c}(\text{K})}}, \tag{2.32}$$

where ρ is the effective resistivity and T_c is the superconducting transition temperature of the film. For NbTiN, typical values are $\rho \sim 100$ $\mu\Omega$cm, $T_\text{c} \sim 15.2$ K, $\lambda \sim 270$ nm and $\xi \sim 3.8$ nm [142–145]. Therefore, typical values of $\mathcal{L}_\text{l}^\text{k}$ are 280 nH/m, making it a substantial fraction of the total inductance [146]. This makes $v_{\text{Ph}} \sim 92$ m/μs, but strongly dependent on geometry and film properties — for precise resonator targeting the precise knowledge of this number is crucial. Note that changes in the thickness of the film or the geometry of the

resonator (e.g. by puncturing it with holes) will change the value of $\mathcal{L}_l^k$. Bringing together these expressions, the length l of a $\lambda/4$ resonator can be determined via

$$f_{0,R} = v_{Ph}/4l. \tag{2.33}$$

This is the frequency of the uncoupled resonator, however a coupling to the outside world (e.g. via a feedline) will change its resonance frequency. For f_R of ~ 7 GHz, a common value in the work presented here, $l \sim 3.3$ mm.

Let us now highlight what happens to the resonator frequency when the resonator is coupled to a feedline with a coupling described by Q_c. A thorough discussion and derivation of this effect can be found in Ref. [120], here we give the tools needed to account for it. We assume that $Q(f) \gg 1$ which is in the cases considered satisfied. Further on, let the feedline have a characteristic impedance Z_0, usually $Z_0 = 50\ \Omega$. The resonator impedance Z_R depends on what type of resonator is used. It is given by

$$Z_R \approx \frac{4}{\pi} Z_{0,R} \text{ for } \frac{\lambda}{4}, \text{ and } Z_R = \frac{2}{\pi} Z_{0,R} \text{ for } \frac{\lambda}{2} \tag{2.34}$$

resonators, where $Z_{0,R}$ is given by Equation (2.28). This links to l via

$$Z_R = \frac{1}{\pi f_{0,R} C_l^g l}. \tag{2.35}$$

The loaded resonator frequency f_R is then given as

$$f_R = f_{0,R} \cdot \left(1 - \sqrt{\frac{Z_R}{2Q_c Z_0}}\right). \tag{2.36}$$

Equations (2.34) to (2.36) therefore provide the tools necessary to account for the frequency shift due to the loading of the resonator. For a typical situation with Q_c of 10^4 and $f_{0,R} = 7$ GHz, the shift is $f_{0,R} - f_R \sim 50$ MHz.

2.4.2 Dispersive Readout

The interaction between transmons and resonators in the single-excitation manifold can be described with the Jaynes-Cummings Hamiltonian [147]. The general model describes the interaction between a two-level system with a quantized mode of a bosonic field. Originally developed to study the absorption and emission properties of atoms in a cavity it is also applicable in this situation. In the second quantization formalism, the Hamiltonian reads as

$$\hat{H}_{JC} = \hat{H}_{atom} + \hat{H}_{field} + \hat{H}_{interaction} = -hf_{01}\frac{\hat{\sigma}_z}{2} + hf_R \hat{a}^\dagger \hat{a} + \frac{hg}{2}\left(\hat{a}\hat{\sigma}_+ + \hat{a}^\dagger \hat{\sigma}_-\right), \tag{2.37}$$

where f_{01} is the transmon frequency, $\hat{\sigma}_z = |g\rangle\langle g| - |e\rangle\langle e|$, f_R the resonator frequency, $\hat{a}^\dagger$ ($\hat{a}$) the photon creation (annihilation) operators, g the coupling strength and $\hat{\sigma}_+ = |e\rangle\langle g|$ and $\hat{\sigma}_- = |g\rangle\langle e|$) the qubit raising and lowering operators respectively. The first part of the Hamiltonian describes the energy of the two-level system and the second part the energy of the photons in the cavity. The last part describes the interaction between the two: excitations can be swapped from the qubit to the resonator and vice versa.

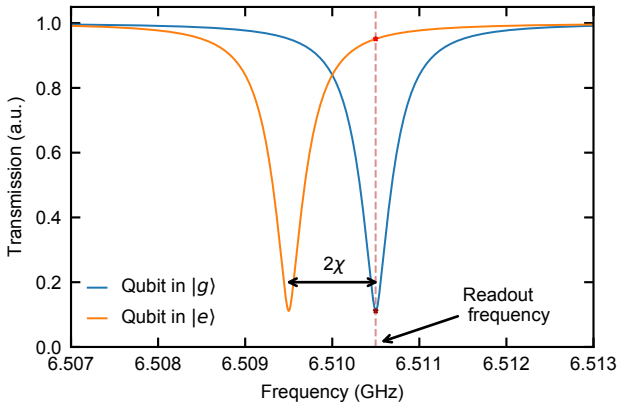

Figure 2.15: Schematic of the dispersive readout. Depending on the qubit state, the resonance frequency is shifted by $\pm\chi$ from the bare resonator frequency. A transmission measurement at a fixed frequency (readout values indicated with red stars) is therefore a good way to discern the qubit states.

In the limit of large detunings, $|\Delta_f| = |f_{01} - f_R| \gg g$, the interaction between qubit and cavity no longer manifests itself as an exchange of excitations between the two, but as a shift in qubit and resonator frequency [110]. The qubit experiences a photon-number dependent frequency shift, and the resonator experiences a qubit-state dependent frequency shift. Making the dispersive approximation, and introducing the dispersive shift $\chi = g^2/\Delta_f$, the Hamiltonian becomes

$$\hat{H}_{\text{dispersive}} = -hf_{01}\frac{\hat{\sigma}_z}{2} + hf_R\hat{a}^\dagger\hat{a} + \chi\hat{a}^\dagger\hat{a}\hat{\sigma}_z. \tag{2.38}$$

The qubit-state dependent shift in the resonator frequency can be used for qubit readout, see Figure 2.15. Measuring the feedline transmission at a frequency close to f_R yields a qubit state dependent signal (red and dark red stars). This readout technique is used throughout this thesis. Further details on readout and control of the qubit can be found in Appendix A.

3 FABRICATION OF CQED CHIPS WITH NANOWIRE TRANSMONS

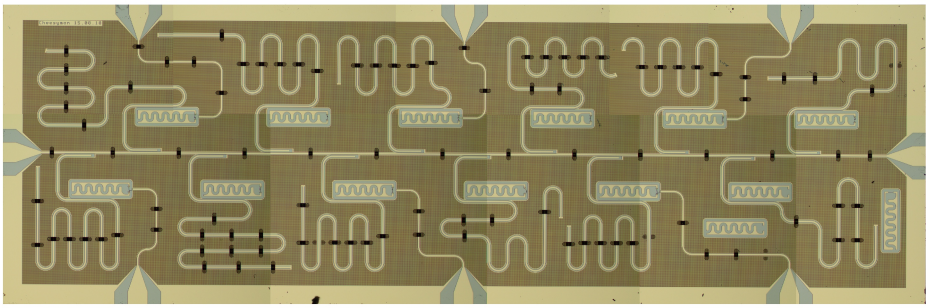

Figure 3.1: A fabricated nanowire transmon test chip with NbTiN airbridges. The horizontal feedline serves as in- and output for control and readout pulses. The 12 qubits are coupled to the feedline via their dedicated resonator. Ports on top and the bottom serve as voltage and flux-bias lines. Chip dimensions are 2×7 mm, chip ID is Cheesymon_NK_I4.

Having described how nanowire tranmons work theoretically in Chapter 2, I outline their fabrication here. Special attention will be given to the fabrication steps that are not standard in CQED, and the measures taken to increase the magnetic field compatibility of the studied devices.

Parts of this chapter have been published in *PRL* **120**, 100502 (2018).

Setting up a new experiment becomes considerably easier if it is possible to rely on existing, established components. This also holds true for the fabrication aspect of the experiments presented in this thesis. As far as possible, the fabrication steps are held as close as possible to established recipes for superconducting transmons with SIS junctions in a planar geometry [2, 122, 148–151]. Transmons fabricated following these recipes have shown T_1 of 40 μs and T_2^* of 35 μs [2, 44, 149]. We can therefore exclude that fabrication steps used there would limit T_1 and T_2^* to below the above-mentioned values. Additionally, using this well-established NbTiN-based fabrication procedure will provide the sample with an inherent resilience towards externally applied in-plane magnetic field.

The initial goal of the work presented here was to gain an understanding of possible limitations and noise processes affecting nanowire transmons. In order to get as much statistics as possible and because the fabrication yield of nanowire transmons is (in our experience) limited, a qubit test chip with many qubits is fabricated, see Figure 3.1. The fabrication essentially consists of three mayor steps:

- defining the base layer with coplanar waveguides (CPWs), the holey ground and qubit capacitor paddles;
- deposition, etching and contacting of the nanowires;
- and the forming of microwave crossovers to improve the on-chip microwave hygiene.

While the base layer fabrication can follow the CQED recipes standardly used in the group, the techniques for making coherent nanowire junctions still had to be developed. In order to reduce fabrication complexity, most of the chips that are discussed in this thesis used on-chip wirebonds as microwave crossovers connecting ground planes on both sides of CPW structures. In the subsequent sections the respective fabrication processes are outlined. The discussion will follow the order of the fabrication steps.

3.1 Substrate and base layer

Standardly, our group uses silicon (Si) substrates with a niobium titanium nitride (NbTiN) film as a starting point for fabrication of planar CQED devices [122, 142, 152]. The high-resistivity Si wafer is first cleaned with a hydrofluoric acid (HF) dip to remove the surface oxides. The surface is then passivated with hexamethyldisilazane (HMDS) to prevent re-oxidation. The prepared wafer is transferred as fast as possible into the vacuum of the load-lock of the NbTiN sputtering tool where the NbTiN film is deposited.

The large-scale CQED features (Figure 3.2) are defined using electron-beam (e-beam) lithography and a reactive-ion etch. A layer of resist is spun on the NbTiN film and the desired base-layer features are patterned using e-beam lithography. After developing the patterned resist, the parts of the NbTiN film that should be removed are exposed. With a sulfur hexafluoride (SF_6) reactive-ion etch, the exposed NbTiN is etched away, leaving the resist-covered parts of the chip unharmed. After stripping the remaining resist, the base layer is defined.

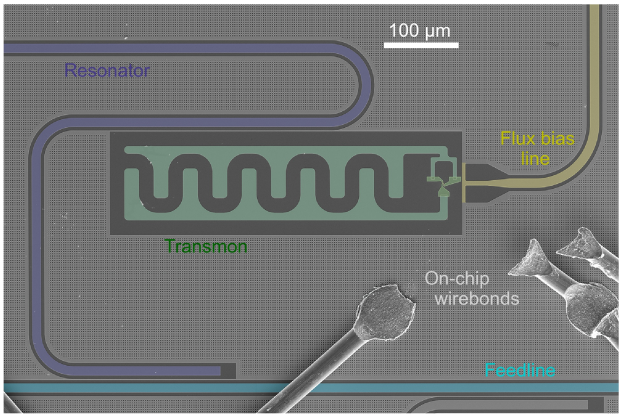

Figure 3.2: False-colored SEM micrograph showing the CQED elements. Microwave control pulses are sent via the common feedline (cyan) through the resonator (blue) to the flux-tunable transmon (green) which can be tuned by a current through the flux-bias line (yellow). On-chip wirebonds (grey) connect ground planes to suppress microwave slot modes.

3.2 Nanowires

The choice of the nanowires used to make the Josephson junction has a big impact on T_1 and T_2^* of the nanowire transmons. First demonstrations of nanowire transmons in Delft did not focus on demonstrating long coherence times, but rather on the physics that can be observed in them [37]. In the paralleling work done in Copenhagen [38], coherence times of $\sim 1\ \mu$s could be observed. A striking difference between the two experiments are the nanowires used: Whereas in Delft bare InAs nanowires were contacted with NbTiN, in Copenhagen InAs nanowires were contacted with an epitaxially grown Al shell.

It is only due to a breakthrough in material science that it is possible to grow an Al shell *epitaxially* on an InAs core [153]. The atomically precise matching of the Al shell with the InAs core can be seen in the high-resolution TEM picture in Figure 3.3(a). The Al can be deposited either on a few facets or fully around the hexagonal InAs core to form a full-shell wire [see Figure 3.3(b)]. Theoretical results indicate that disorder in the semiconductor-superconductor interface can lead to a soft induced superconducting gap [154, 155]. Epitaxy is the ultimate limit of order for this interface, and indeed induces a hard gap in the nanowire [see Figure 3.3(c, d)] [83].

Nanowire transmons that show high coherence times crucially rely on nanowires with an epitaxially grown shell. The hard induced superconducting gap means that the energy relaxation via quasiparticle tunneling [59, 156, 157] is suppressed, leading to longer T_1 [158]. Further on, the epitaxially grown Al shell guarantees a good interface between the Al and the InAs core, avoiding potential dissipation due to lossy oxides on the surface of the nanowire core. The devices discussed in this thesis rely on nanowires that have an epitaxially grown shell, either full or covering only two facets.

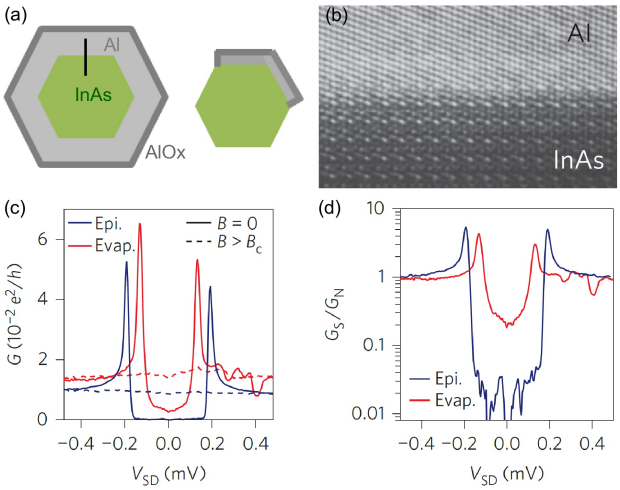

Figure 3.3: (a) Schematic cross-section of full-shell and partial shell nanowires. (b) Transmission electron micrograph of the epitaxial interface along the cut in (a). (c) Differential conductance as function of the source-drain voltage for an epitaxial wire (blue) and a control wire with evaporated Al shell (red). Normalized differential conductance showing a subgap conductance suppression by a factor $\sim$ 100. Figure adapted from [83], with permission.

3.2.1 Deterministic placement

The nanowires are transeferred from their growth substrate [Figure 3.4(a)] to the junction regions on-chip using a nanomanipulator [159]. The nanomanipulator consists of an optical microscope with an xyz micrometer screw stage that can be used to control a fine (400 nm tip) tungsten needle [Figure 3.4(b)]. In order to place a wire in the junction region, it first needs to be detached from the growth substrate, which can be done using the tip of the needle. Once the wire is lying on the growth substrate, it can be picked up with the needle [Figure 3.4(c)] aided by van der Waals forces. The needle is then brought to the junction region where the wire can be placed deterministically on the substrate [Figure 3.4(d)]. This process must be done for each wire individually. Importantly, the wires must not be bent during this process as this would damage their crystalline structure.

An alternative method of nanowire placement is the tissue deposition method: A clean-room tissue is brought in contact with the growth substrate to pick up nanowires [160]. Shaking the tissue over the chip will then deposit nanowires everywhere on the chip. We do not use this method because it consumes large amounts of growth substrate and deposits nanowires in undesired places.

3.2.2 Image recognition software

The advantage of the top-down fabrication common in CQED is compromised for NW transmons: a bottom-up fabrication approach is required for individual NWs. Each NW has a dif-

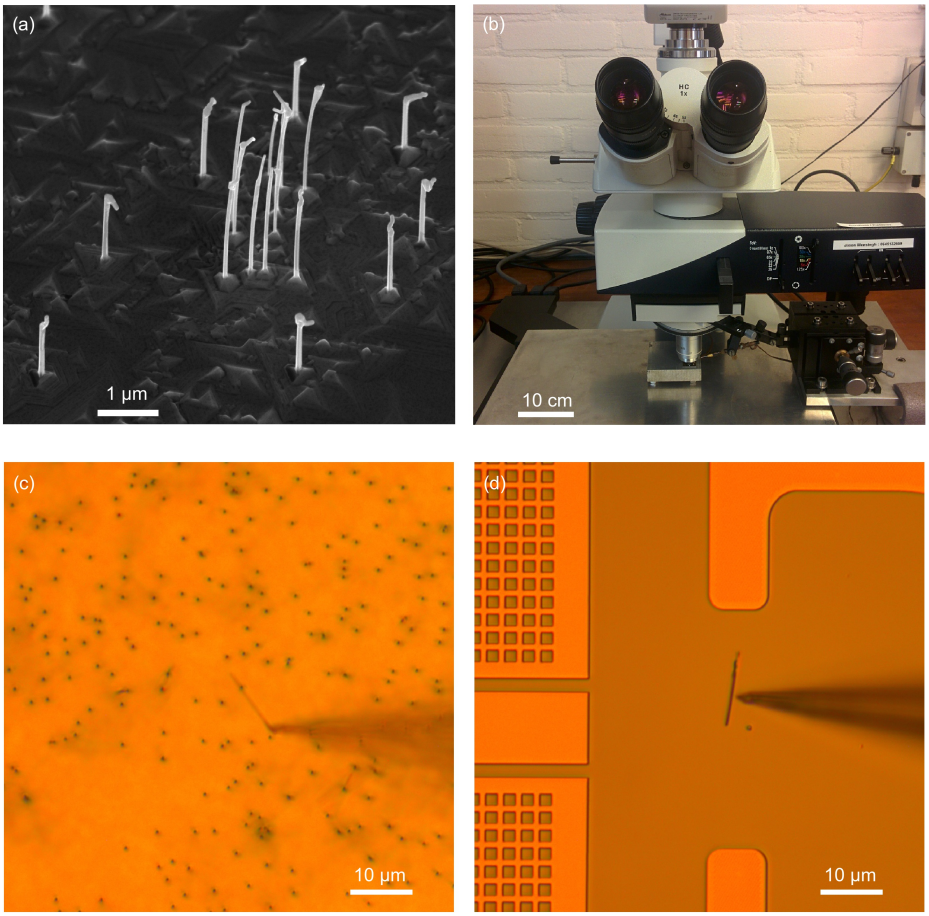

Figure 3.4: Deterministically transferring nanowires to the junction area. (a) SEM micrograph of nanowires on their growth substrate (nanowire batch QDEV #492). (b) Photograph of the nanomanipulator setup. The needle can be finely controlled with the micrometer xyz stage while looking at it through an optical microscope. (c) View through the optical microscope of the nanomanipulator. The needle is picking up a nanowire on the growth substrate. (d) The wire is then transferred to the junction area where it is deposited.

ferent position with respect to the corresponding qubit leads, hence etch mask and contacts (including sidegate) must be individually designed for each qubit. To reduce the turnaround time, Thijs Stavenga wrote software to automatically generate these masks using optical dark field images as part of his Master end project [compare Figure 3.5(a)] [161, 162].

After the deterministic deposition of the nanowires, a layer of PMMA e-beam lithography resist is spun on the chip which will later serve as an etch mask to define the junction. In order to ensure a good etchant flow, we choose the resist layer to be ~ 200 nm, only twice as thick as the nanowire. Spinning resist for the first time after the nanowire deposition can slightly move them. Hence, the images that serve as the input for our image recognition software are only taken after this process.

Our image recognition software employs a suite of filtering procedures and feature detection algorithms to reliably design etch and contact masks. First, the image is low-pass filtered with a Gaussian point spread function. This reduces the sensitivity to possible dirt in the junction area. The image is then binarised using Otsu's thresholding method [163]. To further reduce the chance of picking up uninteresting features (such as the holes in the ground plane) and increase the stability of the procedure, a morphological filter combines adjacent areas [164]. The Canny edge detection algorithm finds all contours present in the image. These are compared to the known shape of the leads to select the best match [cyan and yellow in Figure 3.5(b)] [165]. The scaling, rotation and offset of the image are determined using a Hough transformation and fitting the analytical shape of the leads to the extracted contours (red) [166]. This allows the definition of a coordinate system. The NW is then determined as the contour between the leads enclosing the largest area. The orientation and position of the NW are determined by the smallest rectangle encompassing the NW contour. This allows correct detection of the NW in ~ 93 % of the cases. The position and orientation information is used to create the pattern file for the etch windows [blue in Figure 3.5(b)]. Similarly, the extracted information can also be used to place and connect contacting regions predefined with respect to leads and wire using a distance minimizing routine as well as bringing the voltage sidegate close to the wire [blue in Figure 3.5(c,d)]. These contours are used to generate the pattern file for the contact mask.

The performance of the image recognition software is sufficient for our purpose. The NW width is only 130 nm, well below the diffraction limit (500 nm) and the effective width of the wire in the image (~ 1 μm). The achieved rms error in sidegate placement is 140 nm. Further improvements in fabrication accuracy could be achieved by using SEM instead of optical micrographs. This, however, comes at the cost of a substantially increased fabrication iteration time.

With some adjustments, the image recognition software is able to handle different baselayer structures. This is especially handy if there is an etching or contacting recipe optimization to be done. Instead of fully functioning CQED chips, dedicated test structures can be used. This not only reduces the production time of the baselayers, but also increases the number of test sites, hence yielding more statistics.

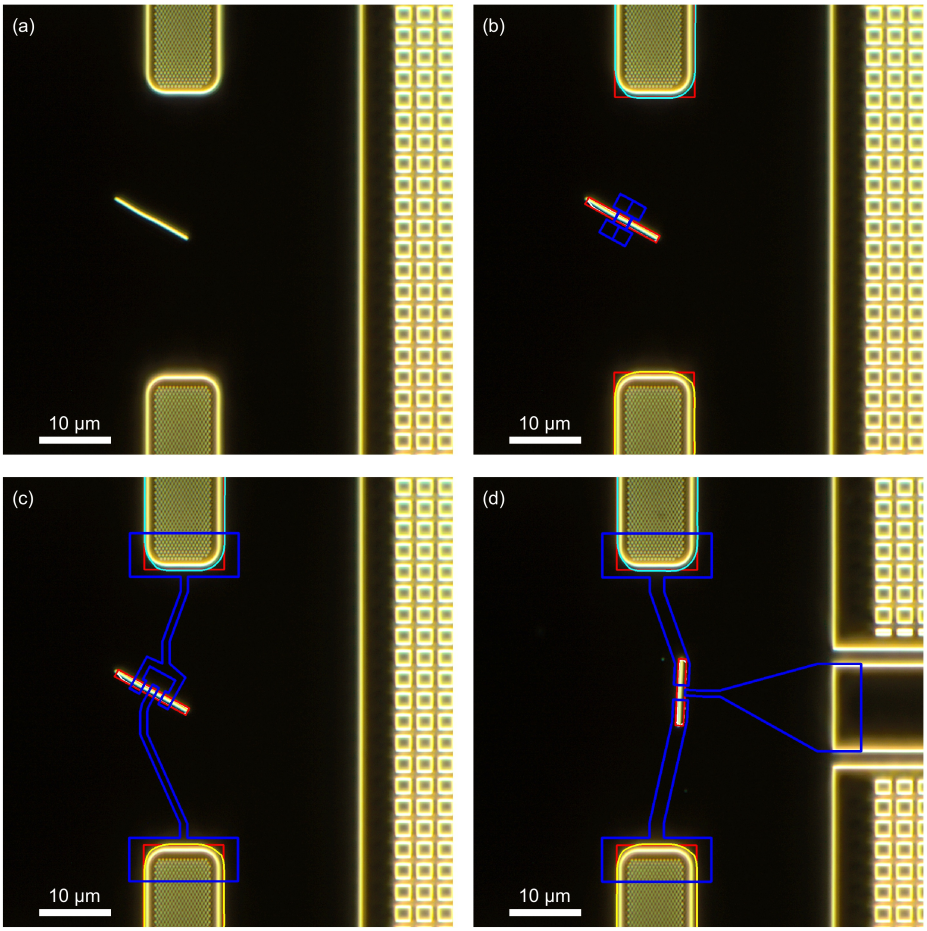

Figure 3.5: The working principle of the image recognition software. (a) The optical dark field picture to be analyzed. It shows the nanowire (center), qubit leads (top and bottom) and the adjacent holey ground (right). (b) The contours of the leads are detected (yellow and cyan). They are fitted with rectangles (red) to define the (rotated) coordinate system in the picture. Subsequently, the nanowire is fitted with a rectangle (red). The extracted position information of the nanowire is used to automatically define the etch mask (blue) for the nanowire. (c, d) The software automatically generates the contact mask for both, flux-tunable split-junction devices and gatemons.

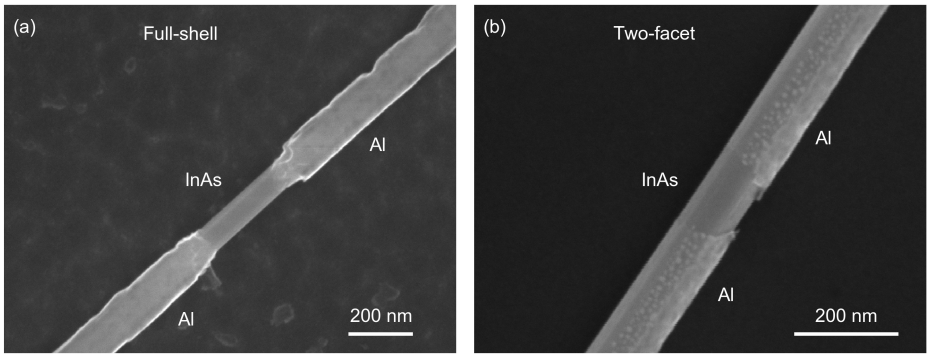

Figure 3.6: SEM micrographs showing the result of the Transene D wet-etch process. Where the resist mask leaves the wire exposed, the epitaxially grown Al-shell is removed. The etched region defines the SNS junction, Crucially, the InAs core is not attacked. (a) Etch of a full-shell wire. (b) Etch of a wire with a partial Al shell.

3.3 Defining the SNS junction

The SNS junction is defined by a wet-etching procedure that removes parts of the Al shell. The etchmask generated by the image recognition software is patterned onto the PMMA resist layer. After patterning and development, the $\sim 150-200$ nm wide nanowire segments that need to be etched are exposed while the rest of the nanowires and the chip are covered in resist. The wet etchant used (Transene D [167], 12 s, 52.6 °C for full-shell nanowires, 48.2 °C for partially covered nanowires) is selective enough that no damage of the InAs core of the nanowire can be detected in SEM micrographs (Figure 3.6). In order to keep the etching process as controlled as possible, two dips in separate beakers of cold H_2O of 5 and 30 s follow immediately after the etching. The chip is then blow-dried and transferred to 55 °C acetone to strip the resist. After this procedure, the N segment of the SNS junction is defined. Note that in some cases SEM micrographs revealed that there were still Al residues in the junction area. However, it was not possible to establish a correlation between relaxation or dephasing times of the qubit and the presence of such residues.

The etching process is a critical step in the fabrication procedure, and controlling the width and quality of the etch window are fabrication challenges. Etching the AlO_x layer is slow in comparison to etching Al, which can lead to etching under the resist mask. This problem is further enhanced as etching Al is exothermic, which leads to local heating. Because the etch rate is highly temperature dependent [167], this makes it hard to precisely control the etch. Our approach to minimize the local heating effect was to maximize the liquid flow around the etching area. To this end a thin resist layer and longer etch windows with pads on the ends [compare Figure 3.5(b)] are used. Further on, the sample must be stirred well during the etching procedure. This effect is much more dramatic for thick Al shells, hence it is considerably harder to make narrow etch windows for that case.

Due to the strong non-linearity of the etch rate, also other (failed) approaches to defining the SNS junctions were explored. Instead of using a resist etch mask, we tried contacting the nanowire first, using the NbTiN contacts as an etch mask. This procedure reduced the fabrication complexity as no separate etch mask needed to be defined. Although SEM micrographs did not show suspicious features, working qubits could not be demonstrated with this approach. The use of other etchants [168, 169] also did not yield the desired results. Therefore, the Transene-based etching recipe is used for all the devices presented in this thesis.

3.4 Contacting the nanowires

Once the SNS junction in the nanowire is defined it must be galvanically connected to the capacitor plates such that it can operate as a transmon. The mask with the contacts generated by the image recognition software is patterned on a PMMA resist layer. After developing, the regions where NbTiN needs to be deposited are exposed, whereas the rest of the chip is still covered in resist. The Al shell of the nanowires has a layer of insulating AlO_x on it which must be removed in order to electrically contact the nanowire. Then, without breaking the vacuum, the NbTiN contacts are deposited [Figure 3.7(a)].

The native AlO_x of the Al shell is removed by an Ar plasma etch. The challenge of this fabrication step is that the Ar plasma etch removes the AlO_x much more slowly than the Al beneath it. This means that etching power and time need to be well calibrated in order to remove the oxide layer while still not etching through the complete Al shell and damaging the crystalline structure of the InAs core. We found that a pressure of 3 mTorr and a microwave power of 50 W for 3 min in the SuperAJA, the sputtering tool used, yields good results.

Once the bare Al is exposed, it can be connected to the qubit leads by sputtering NbTiN contacts. It is imperative that the vacuum not be broken in the meantime. The thickness of the contacts is chosen such that they are roughly 50% thicker than the nanowires. Because the NbTiN deposition is a sputtering process, it is challenging to avoid the formation of standing edges [compare Figure 3.7(c), white features at the edges of the contacts and the sidegate] — even the use of bilayer resist structures with an undercut did not substantially reduce them. In this process also the voltage sidegates for gatemons are defined.

3.5 Optimizations for field compatibility

Although the high in-plane critical field of NbTiN gives the bulk CQED elements on the chip an inherent field compatibility, it is important to take precautions that also small perpendicular fields can be tolerated. This can be achieved by patterning small holes in the center conductor and near adjacent ground plane of the CPW resonators as well as in the qubit leads. These small holes allow the magnetic field to pass through the superconducting film without forming dissipative vortices [131, 146, 170–172]. Also, the thickness reduction of the NbTiN film from the standardly used 200 nm to 70 nm helps to avoid vortex formation [146, 173]. Further on, we developed NbTiN airbridges to replace Al on-chip wirebonds. Like this it is possible

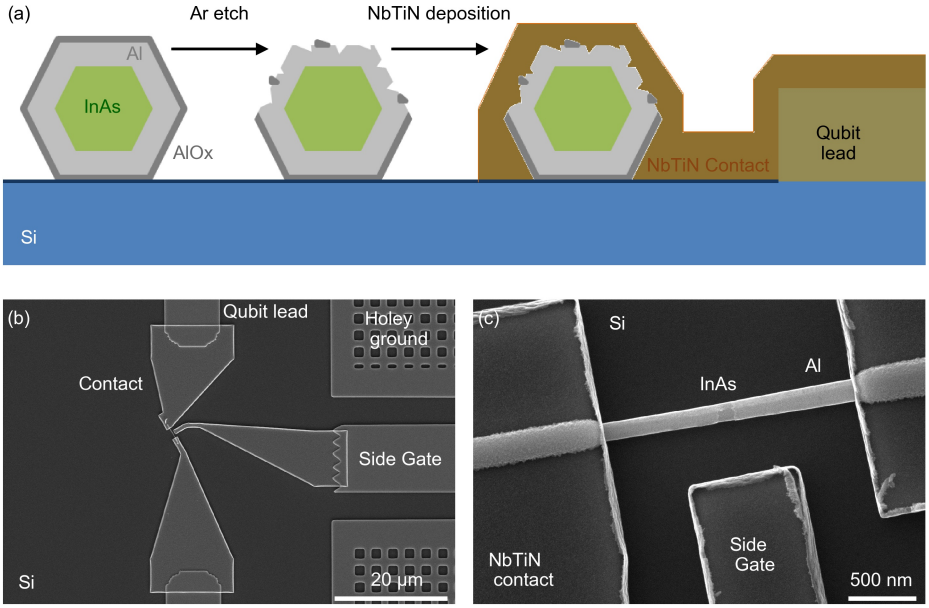

Figure 3.7: Contacting the nanowire with NbTiN. (a) Schematic of the process. In order to make a galvanic contact to the Al shell, the native AlO_x is removed with an argon (Ar) plasma etch. Then, without breaking the vacuum, NbTiN is sputtered onto the sample to define the contacts between the qubit leads and the nanowire as well as the voltage sidegate (for gatemons). (b) SEM micrograph of the junction region. The NbTiN contacts connect the qubit leads to the nanowire and define the voltage sidegate (for gatemons). (c) Zoom-in SEM micrograph of the junction area showing nanowire, contacts and voltage sidegate.

to ensure good microwave hygiene while avoiding additional sources of dissipation in fields exceeding 6 mT. The results of these measures are discussed in Chapter 6.

3.5.1 Holes to avoid vortex formation

The holes to avoid vortex formation can be patterned in the same lithography step as the large-scale CQED features. The design of the hole patterns was automated by Joep Assendelft as part of his Master end project [174]. Patterning the resist layer with the holes (patterned in a triangular lattice with a 500 nm lattice constant and hole radius $r = 50$ nm) requires a smaller e-beam than for the larger features in order to still get well-rounded holes. The additional holes increase the e-beam writing time substantially, therefore only CPW resonator center conductors and the adjacent ground as well as the qubit capacitor paddles are patterned with small holes (Figure 3.8). Roughly a third of the writing time of $\sim$ 15 min per chip as shown in Figure 3.1 is used for these small holes, although they only constitute a small fraction of the exposed area. The ground planes are patterned with much larger, 2×2 μm, holes that can be written faster and serve the same purpose. In order to avoid

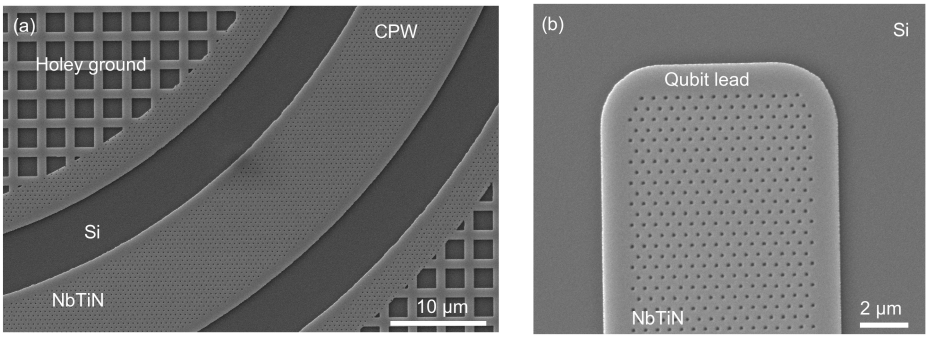

Figure 3.8: SEM micrographs showing the holes to avoid vortex formation. (a) A CPW section with 100 nm diameter holes in the center and adjacent outer conductor. In order to reduce e-beam lithography writing time, the ground plane has larger holes. (b) Qubit lead with 100 nm holes to avoid vortex formation.

overdosing, a 1 μm wide region at the edge of the conductors is not patterned with holes — future generations of devices can still be optimized for this. After developing the written resist mask, the exposed NbTiN can be removed with a SF_6 reactive ion etch. Changing the film thickness and introducing holes into the resonator changes the kinetic inductance. Therefore, the new phase velocity needs to be determined in order to reliably target resonator frequencies. Where the standard 200 nm thick NbTiN films have a typical phase velocity of $1.11 \cdot 10^8$ m/s, this is reduced due to the increase in kinetic inductance to $0.99 \cdot 10^8$ m/s when a 70 nm thick film is used. If additionally holes are present in the center conductor of the resonator, the kinetic inductance of the resonators changes by $\sim 10\%$ [174] and the phase velocity is $\sim 0.97 \cdot 10^8$ m/s.

3.5.2 NbTiN airbridges

Due to the high density of elements on the chip, proper microwave hygiene is important. In order to suppress cavity slot modes, ground planes need to be electrically connected. To reduce fabrication complexity, initial versions of the nanowire chips presented in this thesis used on-chip wirebonds instead of airbridges. In Section 5.4.1, we will discuss that Al on-chip wirebonds lead to a reduction in the background quality factor the qubits experience once a magnetic field exceeding 6 mT is applied. The standard Al airbridges commonly used in our group [2, 148–151] are therefore not an alternative. However, airbridges made of a superconducting material such as NbTiN that can withstand more substantial fields are a good option.

As NbTiN films are brittle and therefore susceptible to cracks in the resist layers, several fabrication improvements were needed to make the NbTiN airbridges reliable. These improvements were developed together with Thijs Stavenga. The airbridges extend into the third dimension because they are deposited over a reflown PMGI resist pedestal. The exact

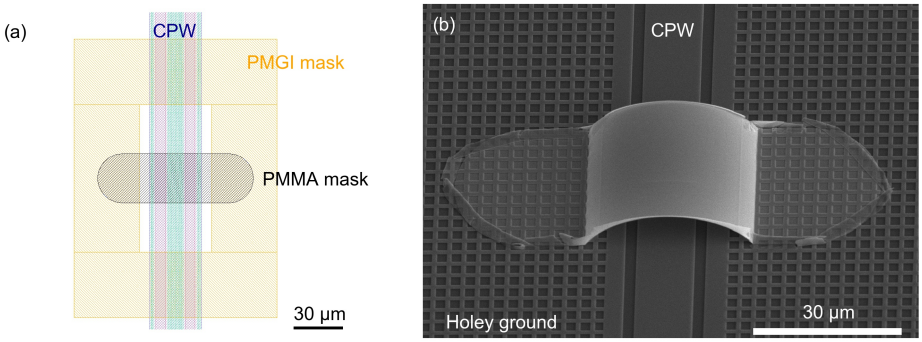

Figure 3.9: Fabrication of NbTiN airbridges. (a) Design file of the resist structures used to define an airbridge crossing a CPW. Crucially, the PMGI pedestal that will be reflown to define the rounding of the airbridge is disconnected from the rest of the PMGI layer to reduce stress and avoid cracks. The band-aid shape in the PMMA bilayer that defines the airbridge is preferable over a rectangular one as there are no corners from which cracks can originate. (b) SEM micrograph of a NbTiN airbridge over a CPW.

shape of the airbridges is defined by a pattern written in a PMMA bilayer resist. Once the PMMA bilayer is deposited, there is a large amount of stress in the resist layers that can lead to cracks and therefore defects in the airbridges. This stress can also lead to the nanowires breaking or detaching from the contacts. These effects can be avoided by taking the following measures: there needs to be a cut-out around the qubits in the PMGI layer to avoid nanowires detaching; the PMGI pedestals over which the airbridges are defined need to be separated from the rest of the PMGI layer [compare Figure 3.9(a)]; the PMGI layer should be in (cleanroom-)air for at least 12 hours to rehydrate before spinning the PMMA bilayer; the PMMA bilayer needs to be baked with a gentle temperature profile; and the airbridges should be defined with a band-aid shape to avoid corners that serve as nucleation points for cracks [compare Figure 3.9(a)]. In combination, these methods yield a comparatively low-stress resist structure and allow us to deposit crack-free NbTiN airbridges [Figure 3.9(b)].

4

COHERENCE AND NOISE CHARACTERIZATION OF SNS TRANSMONS AT ZERO FIELD

F. Luthi, T. Stavenga, O. W. Enzing, A. Bruno, C. Dickel, N. K. Langford, M. A. Rol, T. S. Jespersen, J. Nygård, P. Krogstrup, L. DiCarlo

Before bringing the nanowire qubits into a new, more challenging regime where a parallel magnetic field is applied, a basic understanding for these qubits under optimal conditions is required. In this chapter, measurements of the spectroscopic features, the coherence and relevant noise processes of nanowire transmons at zero field are presented and discussed.

Parts of this chapter have been published in *PRL* **120**, 100502 (2018).

4.1 Introduction

Research on nanowire transmons was started in parallel in Delft and Copenhagen [37, 38]. Whereas the work in Copenhagen focused on demonstrating coherence and voltage z-gates in gatemons, the work in Delft investigated next to gatemons also the physics of flux-tunable split-junction devices. Further work in Copenhagen [39] has shown improved coherence times over the first demonstrations and two-qubit gates between neighboring gatemons. CQED devices based on SNS junctions offer further exciting possibilities, such as voltage-controlled coupling buses [40] or integration on two-dimensional electron gases [175].

In this chapter, we combine cQED techniques that have proven to yield high coherence times [2] with InAs nanowires that have a hard induced superconducting gap. We demonstrate state-of-the-art flux- and gate-tunable CQED devices based on SNS junctions. Ultimately, the focus of our work is on studying these devices in a parallel magnetic field. But before applying a magnetic field, however, it is important to know the performance and the limitations of these qubits in optimal, field free conditions. In this chapter, we discuss the spectrum of voltage tunable gatemons and flux-tunable split-junction devices as well as a general framework to quantify the noise they are subject to. Next to weakly coupled voltage- and flux noise, a direct coupling of charge two-level systems to the Josephson energy of these circuits is observed.

4.2 Voltage tunable devices

4.2.1 CW spectroscopy

Let us first study the spectrum of a gatemon as a function of the applied side-gate voltage V_G (Figure 4.1). Tuning V_G changes E_J by altering the transmissions T_i and the number of channels hosting an ABS, hence altering the qubit frequency f_{01} (Section 2.3.4). At each value of V_G, first the resonator is measured [Figure 4.1(b)] and its resonance frequency f_R is determined. Then, using standard two-tone spectroscopy [176], f_{01} is determined [Figure 4.1(c)]. Using the same principle but driving the qubit excitation tone ~ 10 dB harder also the transition between the ground state and the second excited level, f_{02}, can be determined [101]. The V_G tuning is repeatable upon small excursions (1-2 V), except for isolated deviations which we attribute to charge traps changing state (indicated by grey vertical lines in Figure 4.1). These changes — some are reproducible, others are stochastic — lead to jumps in f_{01}. Therefore, an easy tracking of f_{01} during the scan that is based on f_{01} of the previous V_G value will quickly lose the qubit. To circumvent this problem a guess of f_{01} is made based on the measured f_R using the dressed-state picture [110]. We can approximate f_{01} by

$$f_{01} \approx f_{\text{bare}} - \frac{(g/2\pi)^2}{f_R - f_{\text{bare}}}, \tag{4.1}$$

where g is the qubit-resonator coupling and f_{bare} the bare resonator frequency. Using this guess, f_{01} is easily found after a jump by measuring f_R and scanning around the guess value. Turning this method around allows us to extract $g/2\pi = 60.8$ MHz.

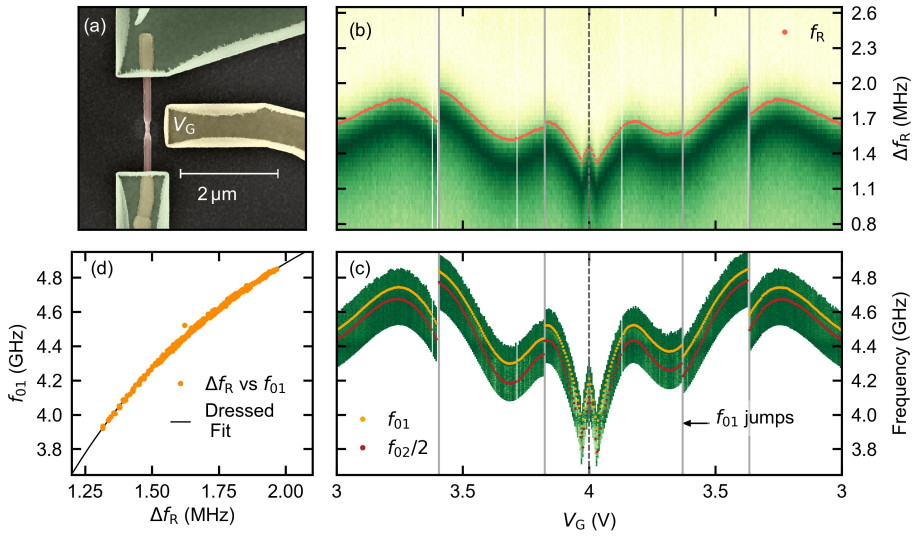

Figure 4.1: Spectroscopic gatemon characterization. (a) False-colored SEM micrograph of the nanowire Josephson junction (light red) with a side gate (yellow) enabling V_G tuning. (b) Deviation of f_R, Δf_R, from the bare resonator frequency $f_{bare} = 6.732$ GHz for a triangle sweep in V_G. Note the change in direction of the V_G sweep, indicated by the dashed line. On return to the same V_G, f_R is roughly reproduced. (c) f_{01} versus V_G. Random, but sometimes reproducible jumps of f_{01} occur (at light gray lines). (d) Plot of f_{01} against f_R (orange dots) and dressed state fit (black) with coupling strength $g/2\pi = 60.8$ MHz, allowing the prediction and quick finding of f_{01}.

Studying the anharmonicity $\alpha = f_{02} - 2f_{01}$ of the gatemon in Figure 4.1 allows us to estimate the number of channels contributing to E_J (Section 2.3.4). In Figure 4.2(a), the extracted values of α from the scan in Figure 4.1(c) are plotted, and jumps in f_{01} are again indicated by gray vertical lines. Note again the change in direction of the voltages sweep, indicated by the dashed vertical line. Performing a full Hamiltonian diagonalization using the values of E_C and Δ obtained for the split-junction device (see Section 4.3) shows that $|\alpha|$ is reduced for E_J given by a short junction model in comparison to the SIS case [Figure 4.2(b) and Figure 2.12] [101]. Thus, at fixed f_{01}, α depends on the number of channels. As it is not possible to reliably extract the T_i at each value of V_G (the gatemon does not allow to tune the superconducting phase difference), we only present the α for a single channel [blue curve in Figure 4.2(b)] and a toy model with two and three channels of equal T_i (orange and green curves, respectively). The model with equal T_i sets an upper limit to $|\alpha|$ given a fixed number of channels. We can therefore conclude that the main contribution to the transmission comes from only a few channels. It cannot be excluded that additional, weakly transmitting channels also participate.

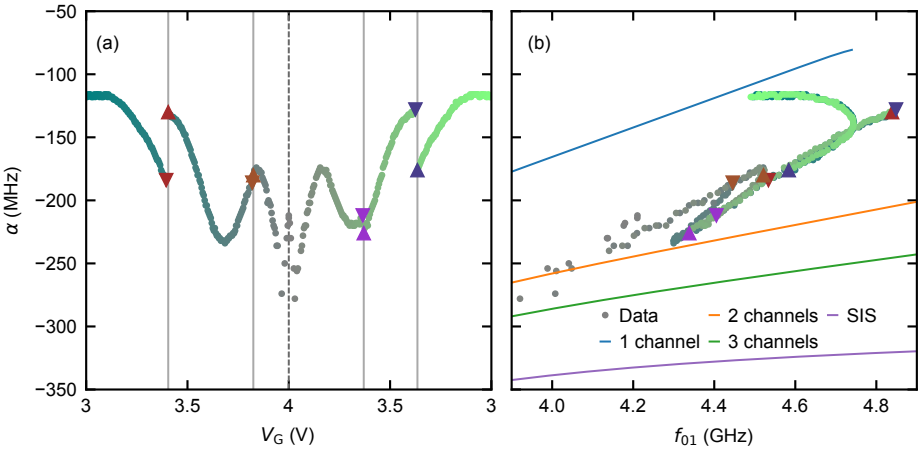

Figure 4.2: Channel number estimation for the gatemon in Figure 4.1. (a) Extracted anharmonicity α versus V_G. The dashed line indicates the change in direction of the V_G sweep. Markers and gray lines indicate jumps in f_{01}. (b) Anharmonicity versus f_{01}. Jumps in f_{01} are indicated by the markers [same as in (a)]. Curves indicate the anharmonicity as calculated from a full Hamiltonian diagonalization for a single channel (blue), two (orange) or three (green) equally transmitting channels (orange), and the SIS case (purple), also see Figure 2.12.

4.2.2 Extracting noise figures from time-domain characteristics

Although it is possible to extract a large amount of information already from spectroscopic measurements of the qubits, their time-domain characteristics reveal even more information with greater precision. For example, the strong V_G dependence of gatemon dephasing times allows a quantitative study of the effect of charge noise. In this subsection, let us discuss a framework that allows extraction of the relevant noise quantities a qubit is subject to based on the time-domain footprint of the qubit. Later on, we will also do the reverse process: by noise injection, the coherence time of a qubit can be controllably reduced. The combination and comparison of these two methods allows a reliable determination whether the instrumentation or on-chip noise is the dominant contribution.

In general, the coherence of a qubit is reduced in the presence of noise in one of the parameters λ that controls its frequency. A common way to characterize this noise is by measuring the Ramsey or echo times as a function of λ [3, 34, 177, 178]. The qubit is brought into the superposition state $(|0\rangle + |1\rangle)/\sqrt{2}$ where it is left for a time t during which it is potentially subjected to echoing pulses and then rotated into the σ_z basis where it is read out. The mean-squared phase-noise $\langle \phi^2(t) \rangle$ of the qubit accumulated at a time t under the presence of a noise with single-sided power spectral density (PSD, always single-sided

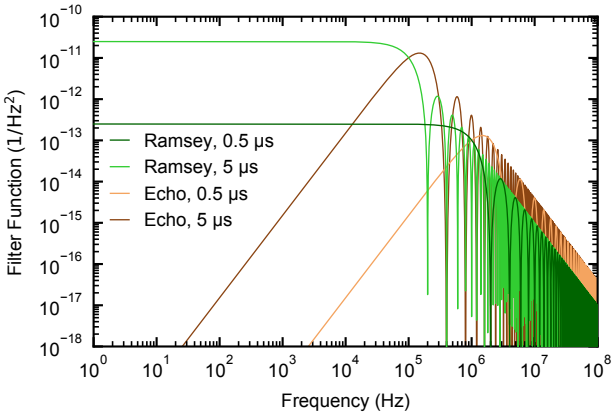

Figure 4.3: Filter functions for Ramsey and echo experiments for different time scales. Where echo experiments are largely insensitive to low-frequency noise, Ramsey experiments are more resilient to high-frequency noise.

unless explicitly mentioned) $\mathcal{S}_\lambda(f)$ when a echoing sequence with filter function $\mathcal{W}(f,t)$ is applied to the qubit is given as [117, 178]

$$\langle \phi^2(t) \rangle = (2\pi)^2 D_\lambda^2 \int_0^{f_{01}} \mathcal{S}_\lambda(f) \mathcal{W}(f,t) \mathrm{d}f, \tag{4.2}$$

where $D_\lambda = |\partial f_{01}/\partial\lambda|$ is the sensitivity of the qubit to λ. This let us express the expected measurement outcome of the qubit after the above described sequence as

$$\begin{aligned} \langle \sigma_z(t) \rangle &= \langle \cos(\phi(t)) \rangle \\ &= 1 - \frac{1}{2}\langle \phi^2(t) \rangle + \frac{3!\,!}{4!}\langle \phi^2(t) \rangle^2 \pm \dots \\ &= \sum_{n=0}^{\infty} \frac{(-1)^n}{n!} \left(\frac{\langle \phi^2(t) \rangle}{2} \right)^n \\ &= \exp\left[-\frac{\langle \phi^2(t) \rangle}{2} \right], \end{aligned} \tag{4.3}$$

where we assumed the noise to be Gaussian. Using Equation (4.2) and Equation (4.3) we can therefore link the noise PSD, the sensitivity to λ and the filter function to the measurement expectation value of the qubit,

$$\langle \sigma_z(t) \rangle = \exp\left[-\frac{1}{2}(2\pi)^2 \left(\frac{\partial f_{01}}{\partial \lambda} \right)^2 \int_0^{f_{01}} \mathcal{S}_\lambda(f) \mathcal{W}(f,t) \mathrm{d}f \right]. \tag{4.4}$$

Note that this does not necessarily lead to a purely exponential decay.

Let us now put Equation (4.4) in a more useful relation that allows us to extract the $1/f$ and white (frequency independent) noise contributions based on the time-domain characteristics of the qubit. To do this, we will calculate the integral in Equation (4.2) for $1/f$ and white noise in the case of an echo and a Ramsey sequence. The filter function for a Ramsey experiment is given as [117]

$$\mathcal{W}_{\mathrm{Ramsey}}(f,t) = \frac{\sin^2(\pi f t)}{(\pi f)^2}, \tag{4.5}$$

and the filter function for an echo sequence with one echo pulse is given by

$$\mathcal{W}_{\mathrm{SE1}}(f,t) = \tan^2(\pi f t/2)\frac{\sin^2(\pi f t)}{(\pi f)^2}, \tag{4.6}$$

as shown in Figure 4.3. We express the PSD of $1/f$ noise as $\mathcal{S}_{\lambda,1/\mathrm{f}} = A_\lambda/|f|$. In the case of a Ramsey sequence with $1/f$ noise, the integral in Equation (4.2) needs to be calculated from the lower cut-off frequency f_m, the inverse of the total measurement duration, and yields

$$\int_{f_\mathrm{m}}^{f_{01}} \mathcal{S}_{\lambda,1/\mathrm{f}}(f)\mathcal{W}_{\mathrm{Ramsey}}(f)\mathrm{d}f = A_\lambda \int_{f_\mathrm{m}}^{f_{01}} \frac{\sin^2(\pi f t)}{f(\pi f)^2}\mathrm{d}f \approx A_\lambda \cdot t^2 \cdot \ln\left(\frac{0.401}{f_\mathrm{m} t}\right) \tag{4.7}$$

where 0.401 appears as a numerical constant. In the case of a Ramsey sequence with white noise the integral yields

$$\begin{aligned}\int_0^{f_{01}} \mathcal{S}_{\lambda,\mathrm{W}}(f)\mathcal{W}_{\mathrm{Ramsey}}(f)\mathrm{d}f &= \mathcal{S}_{\lambda,\mathrm{W}} \int_0^{f_{01}} \frac{\sin^2(\pi f t)}{(\pi f)^2}\mathrm{d}f \\ &\approx \mathcal{S}_{\lambda,\mathrm{W}} \cdot \frac{t}{2}.\end{aligned} \tag{4.8}$$

For an echo sequence with $1/f$ noise, the integral yields

$$\int_0^{f_{01}} \mathcal{S}_{\lambda,1/\mathrm{f}}(f)\mathcal{W}_{\mathrm{Echo}}(f)\mathrm{d}f = A_\lambda \int_0^{f_{01}} \tan^2(\pi f t/2)\frac{\sin^2(\pi f t)}{f(\pi f)^2}\mathrm{d}f \approx A_\lambda \cdot t^2 \cdot \ln(2), \tag{4.9}$$

and for white noise the result is

$$\begin{aligned}\int_0^{f_{01}} \mathcal{S}_{\lambda,\mathrm{W}}(f)\mathcal{W}_{\mathrm{Echo}}(f)\mathrm{d}f &= \mathcal{S}_{\lambda,\mathrm{W}} \int_0^{f_{01}} \tan^2(\pi f t/2)\frac{\sin^2(\pi f t)}{(\pi f)^2}\mathrm{d}f \\ &\approx \mathcal{S}_{\lambda,\mathrm{W}} \cdot \frac{t}{2}.\end{aligned} \tag{4.10}$$

Note that these integrals can be computed explicitly for $f_{01}t \gg 1$ and the solutions are exact for $f_{01}t \to \infty$, which is a good approximation since typical coherence times are $\sim 10\ \mu$s in this work. Inserting Equation (4.8) and Equation (4.10) in Equation (4.4) reveals that the accumulated phase noise coming from a white noise spectrum is not reduced by echoing. On the other hand, in the case of $1/f$ noise, the mean-squared phase noise ratio is

$$\frac{\langle\phi^2(t)\rangle_{1/\mathrm{f,Ramsey}}}{\langle\phi^2(t)\rangle_{1/\mathrm{f,Echo}}} = \frac{\ln\left(\frac{0.401}{f_\mathrm{m} t}\right)}{\ln(2)} \sim 20 \tag{4.11}$$

for typical values, indicating that an echo sequence will increase the coherence time.

Let us now come back to Equation (4.4) and insert the results found in the exponent. The measurement expectation value does not need to follow an exponential decay, therefore we consider its $1/e$ time. The inverse of the $1/e$ time can be expressed as the dephasing rate $\Gamma_\varphi^{*,\mathrm{Echo}} = 1/T_\varphi^{*,\mathrm{Echo}} = 1/T_2^{*,\mathrm{Echo}} - 1/(2T_1)$. In the presence of white and $1/f$ noise, $\Gamma_\varphi^{\mathrm{Echo}}$ can be expressed as a quadratic function in terms of the sensitivity,

$$\Gamma_\varphi^{\mathrm{Echo}} = aD_\lambda^2 + bD_\lambda + c, \tag{4.12}$$

which allows us to extract the relevant noise parameters. These are a λ independent offset c, a $1/f$ noise contribution linear in D_λ and a white noise contribution quadratic in D_λ. The $1/f$ PSD can be quantified as

$$\sqrt{A_\lambda} = \frac{b}{\pi\sqrt{2\ln(2)}} \tag{4.13}$$

and the white noise is quantified as

$$\mathcal{S}_\mathrm{W} = \frac{a}{\pi^2}. \tag{4.14}$$

The same procedure can be applied for a Ramsey sequence,

$$\Gamma_\varphi^* = a^* D_\lambda^2 + b^* D_\lambda + c^*, \tag{4.15}$$

with

$$\sqrt{A_\lambda} = \frac{b^*}{\pi\sqrt{2\ln\left(\frac{0.401}{f_\mathrm{m} t}\right)}} \tag{4.16}$$

and

$$\mathcal{S}_\mathrm{W} = \frac{a^*}{\pi^2}. \tag{4.17}$$

Based on the ratio of $T_\varphi^\mathrm{Echo}/T_\varphi^*$ it is already possible to estimate whether white or $1/f$ noise is dominant. If the ratio is ~ 1, the dominant contribution is white noise because the echo pulses do not help. In the case of $1/f$ noise,

$$\frac{T_\varphi^\mathrm{Echo}}{T_\varphi^*} = \left[\frac{A_\lambda 2\ln\left(\frac{0.401}{f_\mathrm{m} t}\right)(\pi D_\lambda)^2}{A_\lambda 2\ln(2)(\pi D_\lambda)^2}\right]^{\frac{1}{2}} \approx \sqrt{\frac{\ln\left(\frac{0.401}{f_\mathrm{m} t}\right)}{\ln(2)}} \approx \sqrt{20} \approx 4.5 \tag{4.18}$$

for typical values. Determining the value of $T_\varphi^\mathrm{Echo}/T_\varphi^*$ therefore yields insight whether the noise process in λ is white or whether contributions at low frequencies are dominant. This framework will be used to extract white and $1/f$ noise contributions for both flux and voltage noise. Note that this procedure does not yield the true noise PSD the qubit experiences, only an effective white noise and an effective $1/f$ noise component. To obtain a frequency-resolved PSD other methods can be used, for example based on CPMG pulses [178–181] for frequencies of $\sim$ MHz or Fourier-transform of auto-correlation functions [182, 183] for frequencies $\sim$ Hz.

Let us now apply this framework and investigate the voltage noise a gatemon is subject to. Accompanying the measurements presented in Figure 4.1, also time-domain measurements were performed to extract dephsing information, Figure 4.4(a). We extract the voltage sensitivity $D_{V_\mathrm{G}} = |\partial f_{01}/\partial V_\mathrm{G}|$ of the gatemon using a polynomial interpolation in jump-free segments of f_{01} and analytically deriving it. The data clearly shows the presence of charge sweetspots, where D_{V_G} vanishes and the dephasing times correspondingly peak. The ratio $T_\varphi^\mathrm{Echo}/T_\varphi^* \sim 8$ observed on and off the sweetspots (data not shown) indicates that the dominant dephasing noise is $1/f$ like [117]. Therefore, we plot $\Gamma_\varphi^\mathrm{Echo}$ against $|\partial f_{01}/\partial V_\mathrm{G}|$ and fit the dependence with Equation (4.12) where we only use the linear contribution. We

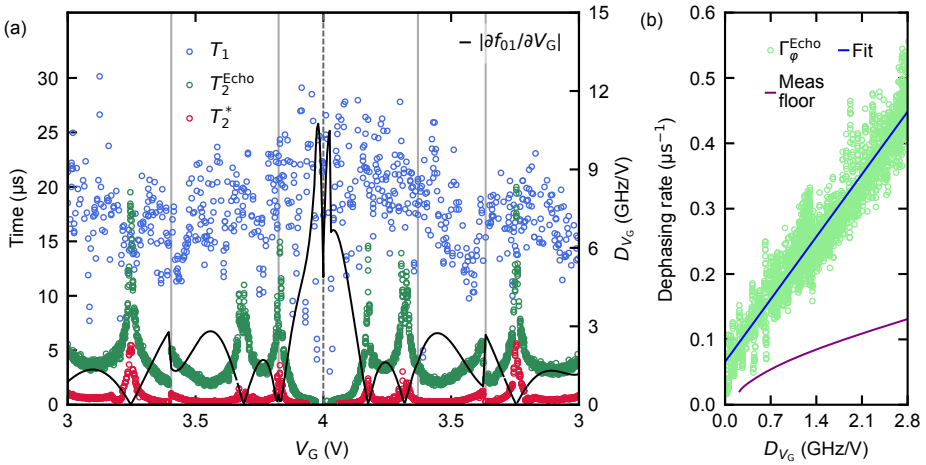

Figure 4.4: Time-domain characterization of the gatemon in Figure 4.1. (a) Gatemon T_1 (blue), T_2^{Echo} (green) and T_2^* (red) versus V_G. Both T_2^{Echo} and T_2^* are strongly correlated with the V_G sensitivity (black). The corresponding f_{01} is shown in Figure 4.1(c). (b) $\Gamma_\varphi^{\text{Echo}}$ against V_G sensitivity, extracted from (a). The fitted $1/f$ noise (blue) is above the setup-imposed dephasing limit (purple), indicating additional on-chip noise.

extract a voltage-noise-independent offset of 66 ms^{-1} and a $1/f$ voltage noise amplitude $\sqrt{A_V} = 26\ \mu$V, where $S_{V,1/f} = A_V/|f|$. The extracted voltage noise value now needs to be compared to the noise of our biasing electronics — like this it is possible to prove that our filtering is good enough.

4.2.3 Coherence limitation given a noise PSD

Whereas the previous sections focused on using the qubit as a detector to extract the noise it is subject to, we now control the noise environment of the qubit and make predictions about its coherence time. If the noise PSD the qubit sees is known, we can, using Equation (4.4), compute the expected lower limit to the dephasing rate of the qubit by numerically evaluating the integral. Note that this needs to be done self-consistently, as the filter function depends on the dephasing time. By measuring the noise output of the biasing electronics used and accounting for the transfer function of cables and filtering, it is therefore possible to calculate the limitation of the setup on the coherence time of the qubit. To verify this method, additional noise with a known PSD is injected and the computed limits are compared to the measured $\Gamma_\varphi^{\text{Echo}}$. The additional noise is produced by amplifying the zero output of an arbitrary waveform generator (AWG) and subsequent attenuation to control the amplitude using a variable attenuator (VATT), see Section A.1.4. When the VATT is set to 60 dB, the measured noise can not be discerned from the detector background. If it is set to 20 dB, the injected noise is dominant over the background noise in the frequency range from $\sim$ 10 kHz until 1 GHz. The measured noise PSD is shown in Figure 4.5, together with echo filter functions [Equa-

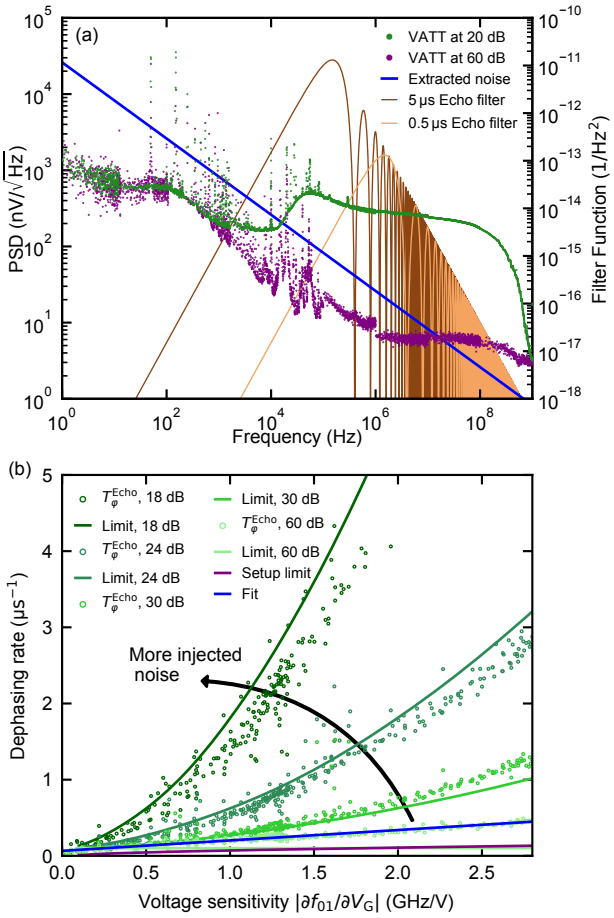

Figure 4.5: Voltage noise injection and coherence time limit. (a) Measured upper limit to the PSD of the V_G bias circuit noise (purple) and PSD with additionally injected amplified AWG noise (green), see Section A.1.4. The extracted noise experienced by the gatemon [blue, from Figure 4.4(b)] exceeds the setup noise floor. Echo filter functions (brown) indicate the frequencies at which the qubit is most sensitive to noise. (b) Computed dephasing rate limits (curves) agree well with measured dephasing rates (points) when the injected noise is dominant. If no noise is injected (purple), another noise source becomes dominant [blue, same fit curve as in Figure 4.4(b)].

tion (4.6)] with typical times. The background of the detectors used to measure the PSD is higher than the noise of the biasing electronics, hence this is only an upper limit to the actual noise. The noise the qubit sees, extracted from Figure 4.4(b), is also plotted, and higher than the measured background noise. This is already an indication that the measurement setup at room temperature does not limit the coherence of the qubit.

In Figure 4.5(b), dephasing rates for different noise levels are plotted and compared to the expected rates given the rescaled injected noise using Equation (4.4). In the cases where the injected noise is dominant, the agreement between prediction and measurement data is good. A strong deviation becomes apparent when no noise is injected, indicating the presence of another noise source. The extracted noise from that source (blue line in Figure 4.4 and Figure 4.5) exceeds the upper limit on the setup noise floor. As there are no other active devices in the V_G bias line, this indicates that on-chip charge noise dominates over electrical noise on the gate.

4.3 Flux-tunable split-junction device

Having discussed how we can describe the spectrum of flux-tunable split-junction devices in Section 2.3.3, let us now turn to the measurements performed on them. In this section we will first analyze the measured spectrum of one of these devices. Then, we will discuss its time-domain characteristics and determine the noise it is subject to using the same framework as in the previous section.

4.3.1 Spectroscopy

Following previous work [37], we first extract information about the SNS junctions by studying the spectrum of the flux-tunable, split-junction device. A current I in the flux-bias line changes the magnetic flux φ through the SQUID loop [Figure 4.6(a)], controlling the superconducting phase difference $\hat{\delta}$ between the transmon islands (Section 2.2.4). Both junctions of the SQUID loop have a Josephson energy that is given in the short-junction, single-channel limit by Andreev bound states with transmission probability T_i and energy $E_i(\delta_i)$, see Equation (2.1). Employing the Andreev bound-state model in the split-junction Cooper-pair-box Hamiltonian, Equation (2.17), yields good agreement with the observed spectrum [Figure 4.6(b)] [37]. The best-fit values of the induced gaps $\Delta_A/h = 46 \pm 4$ GHz and $\Delta_B/h = 38.5 \pm 0.9$ GHz are close to the 43 GHz of bulk Al [58, 157, 184], suggesting that the shell fully proximitizes the nanowire [83]. The fit yields $E_C/h = 278$ MHz which is in good agreement with electrostatic simulations and values extracted from SIS devices that have the same capacitor plate layout [2]. The extracted transmission probabilities are $T_A = 0.66 \pm 0.04$ and $T_B = 0.45 \pm 0.02$.

The extracted gap energies and transmission probabilities allow us to calculate the current-phase relation of the qubit, see Figure 4.7 [37]. Using Equation (2.7), we find that the maximal currents through the junctions are 193 and 99 nA, in agreement with more direct measurements [98].

4.3.2 Time-domain characteristics

We investigate the flux noise of the split-junction qubit by measuring coherence times as a function of flux offset. T_2^{Echo} is strongly dependent on flux and T_1 limited in a range around $\sim$ 20 MHz around the flux sweetspot, Figure 4.8. The noise is quantified using a second-order polynomial fit of $\Gamma_\varphi^{\text{Echo}}$ versus the flux sensitivity $D_\Phi = |\partial f_{01}/\partial\Phi|$ following the procedure in Section 4.2.2. We extract a white-noise contribution to the double-sided spectral density $S_{\Phi,\text{white}} = (60\ \text{n}\Phi_0/\sqrt{\text{Hz}})^2$ (from the quadratic term), a $1/f$ noise amplitude $\sqrt{A_\Phi} = 13.0\,\mu\Phi_0$ where $S_{\Phi,1/f} = A_\Phi/|f|$ (from the linear term), and a 2 ms^{-1} offset. This value of $\sqrt{A_\Phi}$ is on the high side of the range observed for flux-tunable SIS transmons [3, 28, 34, 35]. White flux noise has not been reported in these more standard systems. Due to fluctuations in f_{01}, which will be discussed in the next section, no T_φ^* data is presented here.

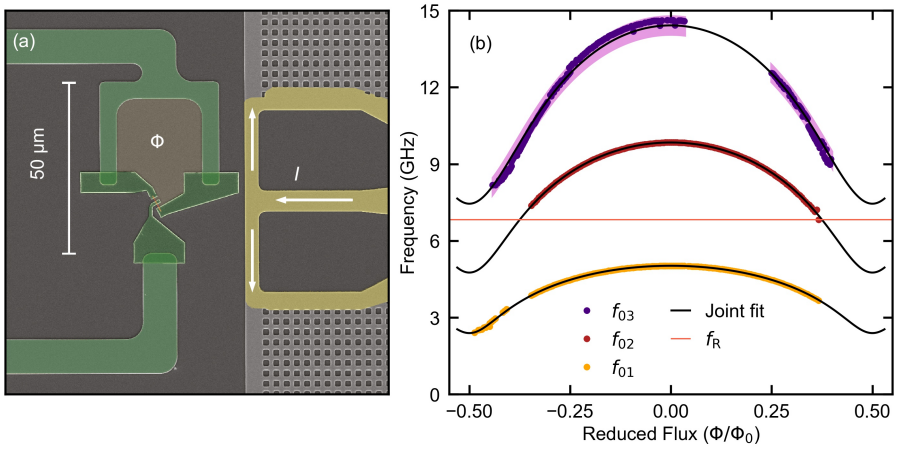

Figure 4.6: Spectroscopic characterization of a flux-tunable split-junction device. (a) False-colored SEM micrograph of the SQUID loop area. The current I in the flux-bias line (yellow) threads a magnetic flux Φ through the SQUID loop (green), tuning $E_J(\Phi)$. (b) The joint fit (black) of the first three transitions (orange, dark red and purple symbols) versus flux yields the transmission probability and the induced gap of each junction. The extracted values for the induced gap indicate that the nanowire is fully proximitized by the shell.

Figure 4.7: Current-phase relation of the flux-tunable split-junction device. Based on the extracted transmission probabilities, the current-phase relation of each of the junctions is calculated (red and orange). Comparing them to sinusoids (black), they are clearly skewed.

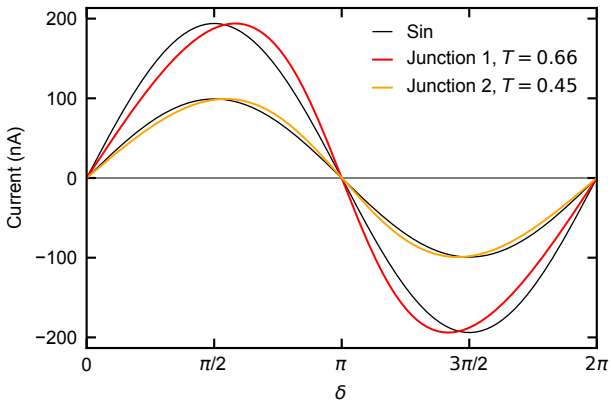

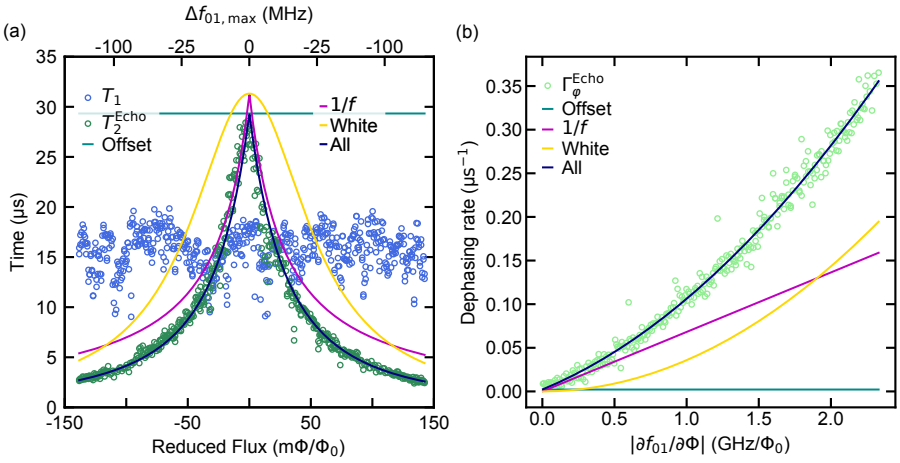

Figure 4.8: Time-domain characterizations of the flux-tunable split-junction device. (a) T_1 (blue) and T_2^{Echo} versus applied flux around the flux sweetspot. T_1 limits T_2^{Echo} at the qubit flux sweetspot $\Phi = 0$. A fit to T_2^{Echo} that includes the measured T_1 limit allows extraction of flux-independent (cyan), $1/f$ (pink) and white-noise (gold) contributions to the dephasing. $T_2^\star$ is typically below 4 μs. Top axis indicates the frequency detuning from the flux sweetspot. (b) Γ_2^{Echo} vs flux sensitivity, extracted from (a), with the different contributions to the fit.

4.4 Strongly coupled TLSs

Next to the weakly coupled voltage and flux noise discussed in Sections 4.2 and 4.3 there is another noise process in this type of qubit. A strong coupling of charge noise directly to the Josephson energy of the circuit makes the qubit switch between several f_{01} values. Here, we characterize this process by probing its PSD and spectroscopic signatures.

4.4.1 Ramsey-based detection

Ramsey measurements of the split-junction device in Figure 4.8(a) reveal a beating pattern of two exponentially decaying sinusoids, indicating a switching of f_{01} between two values f_{01}^{A} and f_{01}^{B}, see Figure 4.9. The observed frequency difference $\Delta f = f_{01}^{\text{A}} - f_{01}^{\text{B}} = 1.6$ MHz is nearly constant overnight, Figure 4.9(b). Because Δf is constant and much larger than the calculated charge dispersion [62] of 200 kHz, we conclude that the switching is due to a TLS coupling directly to the nanowire E_J. Furthermore, we attribute the correlated jumps in the two frequencies to other TLSs switching on slower timescales.

The slow change of f_{01}^{A} and f_{01}^{B} allows us to employ a Ramsey-based single-shot pulse sequence to monitor the state of the fast TLS in real time [Figure 4.9(c)] [59, 60]. By moni-

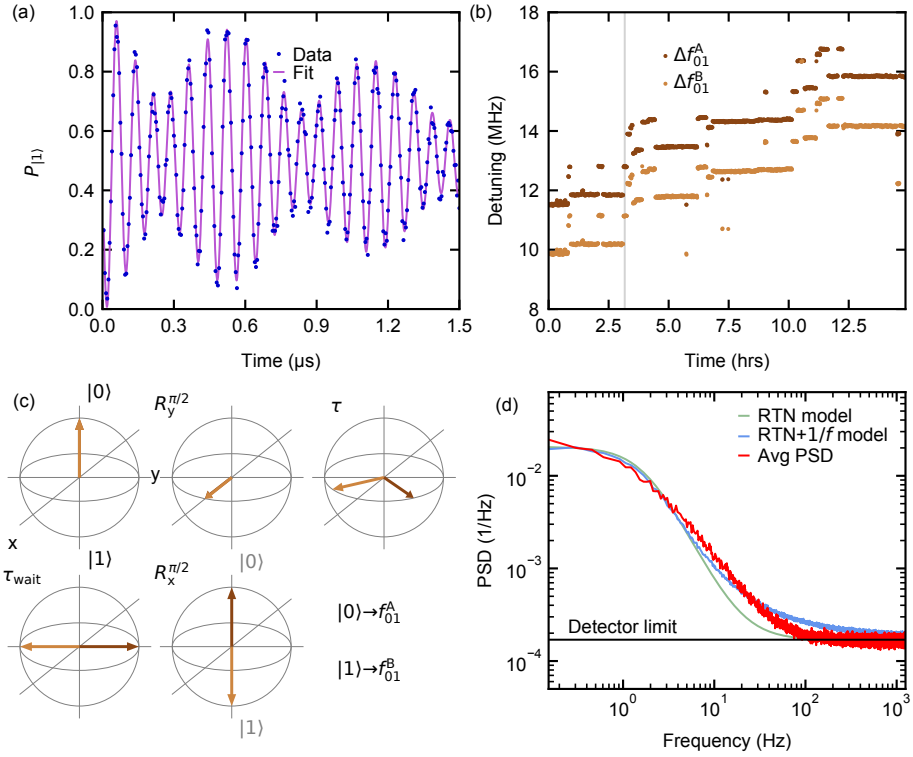

Figure 4.9: Frequency stability analysis of the flux-tunable qubit at the flux sweetspot. (a) Ramsey experiment (dots) with artificial detuning (12 MHz). The strongly coupled TLS yields a beating between two decaying sinusoids (purple, $\tau^{A} = 2.2\ \mu$s and $\tau^{B} = 2.0\ \mu$s). (b) The extracted detunings of repeated Ramsey experiments show a constant frequency spacing and drift of the center frequency. The gray vertical line indicates the trace in (a). (c) Pulse sequence of the Ramsey-type TLS-state detection scheme. The free evolution time τ is chosen as $\tau_{wait} = 1/2\Delta f$ for maximal contrast. (d) The PSD (red) of the TLS is computed from qubit state traces obtained by monitoring the qubit frequency real-time using the pulse sequence in (c). The PSD is fitted using RTN models with (blue) and without (green) $1/f$ noise.

toring the frequency state of the qubit every $\Delta t = 400\ \mu$s for $T = 6.6$ s, we track the TLS state $x_{\mathrm{TLS}}(t)$ over time. The PSDs $\mathcal{S}(f)$ of such traces, given as

$$\mathcal{S}(f) = \frac{(\Delta t)^2}{T}\left|\sum_{n=1}^{N} x_{\mathrm{TLS}}(n\cdot\Delta t)e^{-i2\pi f n}\right|^2, \tag{4.19}$$

are averaged to get an estimation of the TLS PSD, Figure 4.9(d). The TLS PSD can be approximated by an asymmetric random telegraph noise (RTN) model

$$\mathcal{S}(f) = \frac{8F^2\Gamma_\uparrow\Gamma_\downarrow}{(\Gamma_\uparrow+\Gamma_\downarrow)((\Gamma_\uparrow+\Gamma_\downarrow)^2+(2\pi f)^2)} + (1-F^2)\Delta t, \tag{4.20}$$

where $\Gamma_\uparrow = 10.5\ \mathrm{s}^{-1}$ and $\Gamma_\downarrow = 0.57\ \mathrm{s}^{-1}$ are the two switching rates and $F = 0.76$ is the detector fidelity.

Better agreement with the observed data can be achieved by taking the influence of $1/f$ noise into account, Figure 4.9(d). Given the switching rates $\Gamma_{\uparrow,\downarrow}$, the noise-free TLS traces are simulated using a Markov chain approach. Subsequently, $1/f$ frequency noise that is generated by spectrally filtering white noise is superimposed on the TLS traces. The action of the Ramsey experiment with evolution time τ_{wait} is thresholded to obtain the detector signal $d_{\mathrm{TLS}}(n\cdot\Delta t) = \mathrm{sign}(\sin(2\pi\cdot f_{\mathrm{n}}\tau_{\mathrm{wait}}))$ at the n-th time step, at which the frequency of the TLS is f_{n}. The detector fidelity (defined as $F = 1-\varepsilon_0-\varepsilon_1$, where $\varepsilon_{0,1}$ are the detection error probabilities for the $|0\rangle$ and $|1\rangle$ states) is taken into account by probabilistically flipping the thresholded values. PSDs of many such traces are calculated using Equation (4.19) and their average is compared to the experimental PSD. The experimental parameters of f_{01} difference $\Delta f = 1.683$ MHz, $\tau_{\mathrm{wait}} = 297$ ns and $\Delta t = 400\ \mu$s are used for the simulations. Switching rates $\Gamma_\uparrow = 9.25\ \mathrm{s}^{-1}$ and $\Gamma_\downarrow = 0.5\ \mathrm{s}^{-1}$ and fidelity $F = 0.76$ agree well with the values found with the asymmetric RTN model [Equation (4.20)]. The additional $1/f$ noise has an amplitude $\sqrt{A_{1/f}} = 102$ kHz. The resulting PSD matches the experimentally obtained PSD better than just an asymmetric RTN curve. This suggests that $1/f$ noise plays an important role.

4.4.2 Spectroscopic signatures

The switching of f_{01} between multiple values can be observed in several qubits, also in gatemons. Figure 4.10(a) shows repeated pulsed spectroscopy scans taken at fixed $V_{\mathrm{G}} = -3.45$ V. Four distinct, drifting values of f_{01} with semi-constant spacings are clearly visible. A possible explanation of the four frequencies is the strong coupling of two TLSs to E_{J}. A background of many weakly coupled TLSs causes the drift in the center frequency.

The difference between the values of f_{01} depends on the applied V_{G} [Figure 4.10(b,c)]. Pulsed spectroscopy scans are performed while V_{G} is swept up and down. For each scan, the multiple values of f_{01} are extracted and their average is set to $\Delta f = 0$ MHz. The frequency spacing between the peaks changes with V_{G}. We therefore interpret the V_{G}-sensitive TLSs that are influencing E_{J} to be charge traps in the vicinity of the NW junction. The frequencies do not return to the same value upon return to the same V_{G}. The drift of the center frequency

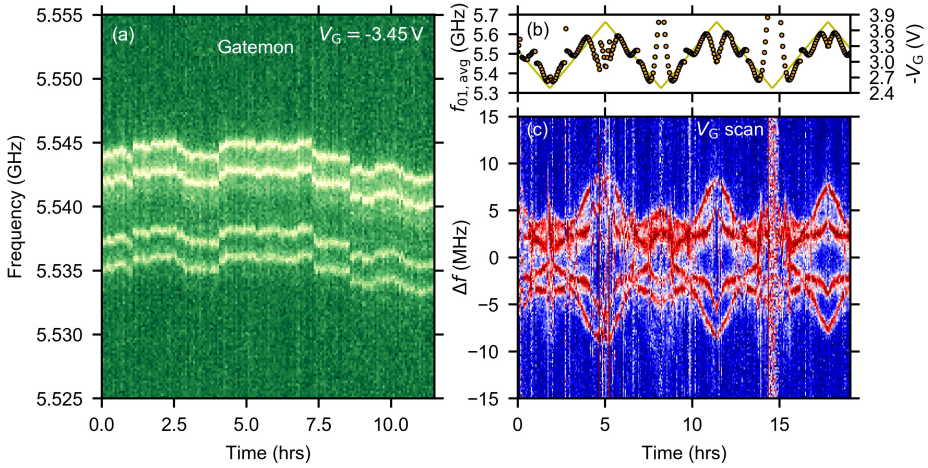

Figure 4.10: Frequency stability of a gatemon. (a) Repetitions of pulsed qubit spectroscopy scans show four distinct, drifting frequencies between which the qubit switches. (b) Average f_{01} (orange dots) and the triangle profile of V_G (yellow line) of the scan in (c). (c) Pulsed qubit spectroscopy while sweeping V_G in a triangle profile [shown in (b)]. Scans are centered around the extracted average f_{01}. The difference between the distinct f_{01} values changes with V_G, indicating a sensitivity of the TLSs to the electrostatic environment of the junction.

made it challenging to setup a reliable frequency state measurement (Figure 4.9). Hence, we were not able to estimate the PSD of these TLSs.

4.5 Conclusions

In this chapter, we have shown and characterized state-of-the-art gate- and flux-tunable nanowire transmons. Coherence times at voltage and flux sweetspots are limited by T_1. We used a general framework to extract white and $1/f$ components of voltage and flux noise. Comparing the noise of the gate biasing electronics to the noise the qubit experiences lets us conclude that the dominant voltage noise is on-chip and the filtering of the biasing lines used is good enough. The measured flux noise is on the high side of the typically observed range and has a white noise component of unclear origin to it. In addition to these weakly coupled noise processes, a third noise process, not commonly seen in transmon qubits is evidenced: the strong coupling of charge two-level systems to the Josephson energy. This results in the qubit frequency switching between different states. Using a Ramsey-based frequency detection scheme, the timescale of such a switching process is observed to be on the order of 100 ms.

As of now this is the most thorough study of nanowire transmons. Therefore, I take this opportunity to zoom out and give my personal opinion about their possible uses. When talking about qubits, the first application that jumps to my mind is a medium- to large-scale quantum computer. Naturally, nanowire transmons therefore might be possible candidates for the basic

building block of such a computer. And indeed, they have potential advantages over standard superconducting transmons. Where flux crosstalk can be a challenge for larger flux-tunable circuits [185], we could not find signs of gate voltage crosstalk. Flux-biasing leads to dissipation close to the qubit chip (unless superconducting connections are provided), a problem that could be circumvented by voltage control. Next to voltage tuning, the side gate can also be used for microwave control of the qubit, therefore reducing the number of access lines required substantially [47]. However, before these advantages can really be leveraged, several challenges need to be overcome. So far it was not possible for us to reliably determine based on -room temperature characteristics of nanowire transmons whether they will work or not — let alone what their typical frequency range will be. As of now, each of the qubits has its own 'personality', making the tuning of these qubits to a certain frequency value — especially because it is non-deterministic — challenging. Further on, their sensitivity to charge two-level systems makes it hard to achieve already single-qubit gates with fidelities exceeding the threshold for error correction [44]. The strong reduction of coherence away from voltage sweetspots due to on-chip charge noise, and our inability to engineer voltage sweetspots, furthers this problem. It is unclear to me whether these challenges can be overcome in the future by means of better fabrication. In the meantime, these qubits offer other exciting possibilities. Due to the inherent magnetic field resilience of their building blocks, they can withstand magnetic fields exceeding the critical field of bulk aluminum, see Chapter 5. This, and their high coherences, make them a suitable platform to study various effects in an applied parallel magnetic field. Further on, due to the high-precision measurements the cQED setup enables, it is possible to learn more about the wires and the fabrication techniques than just from dc transport measurements.

5 OPENING PANDORA'S BOX: APPLYING AN IN-PLANE MAGNETIC FIELD

F. Luthi, T. Stavenga, O. W. Enzing, A. Bruno, C. Dickel, N. K. Langford, M. A. Rol, T. S. Jespersen, J. Nygård, P. Krogstrup, L. DiCarlo

This chapter presents the first experiments subjecting the nanowire transmons of Chapter 4 to an in-plane magnetic field. The effect the in-plane field has on resonators, gatemons and flux-tunable split-junction devices is investigated. The focus is on identifying factors limiting the field compatibility of the transmons and finding solutions for improved performance in future generations of the experiment.

Parts of this chapter have been published in *PRL* **120**, 100502 (2018).

5.1 Introduction

In Chapter 4 we investigated the behavior and limitations of nanowire transmons in a well-shielded environment, without any magnetic fields applied. With an understanding of their limitations and the noise processes they are subject to, we now turn to applying an in-plane magnetic field ($B_{||}$). The same chip as in Chapter 4 is used for these experiments. The setup is modified to allow application of a single-axis magnetic field up to 2 T (Appendix A). The field is generated with a superconducting solenoid mounted to the still plate of the dilution refrigerator. All the magnetic shielding of the qubits and the radiation shield around the copper octobox that hosts the chip had to be removed for this. Without any radiation shielding besides the octobox that is exposed to the $\sim$ 800 mK radiation background of the still plate, T_1 times observed were only on the order of $\sim$ 1 μs. Only the use of an additional radiation shield compatible with the solenoid and thermalized to 20 mK could restore the previously observed high T_1 and coherence times.

It should be noted that the results presented here are a first try of this experiment, and none of the components have been optimized for field compatibility. The goal of this series of experiments was to identify parts of the setup that need to be improved such that a reliable control of flux-tunable split-junction devices in $B_{||} \sim 100$ mT can be achieved. To do so, first the bulk CQED elements, the resonators, are investigated. Although limitations in their performance can be identified, these limitations are not detrimental to CQED measurements in fields up to 100 mT. A strong decrease in the resonator Q_i due to on-chip wirebonds turning normal calls for the use of NbTiN airbridges. Next, a gatemon qubit is studied in $B_{||}$. Spectroscopy measurements suggest the use of nanowires with higher field-compatibility and magnetic vector field capabilities for future experiments. Initial measurements of flux-tunable split-junction devices highlight the requirements for magnetic-field stability and low noise. To summarize, a discussion of the identified limitations and ways to overcome them is given.

5.2 Response of the resonators

Before investigating the qubits presented in Chapter 4 in a magnetic field, it is important to have an understanding how the macroscopic CQED elements behave in a magnetic field. The resonators used here are made of NbTiN, which has an intrinsically high magnetic field compatibility [69, 145, 146, 172, 186]. Nonetheless, the right choice of geometry can influence their in-field performance substantially [187]. For our first magnetic field study, we directly use the samples presented in Chapter 4 with resonators that are not optimized for field compatibility. Therefore, we first focus on studying the behavior of resonators when a magnetic field is applied.

The instrument of choice to characterize resonators is a vector network analyzer (VNA). It returns the complex feedline transmission S_{21} as a function of frequency. Figure 5.1 shows $S_{21}(f)$ around the resonance frequency f_R of a resonator. The characteristic feature of a $\lambda/4$ resonator coupled to the feedline is a dip in transmission (Figure 5.1), as discussed in Section 2.4.1. In order to obtain a more accurate result than just considering $|S_{21}|$, the complex

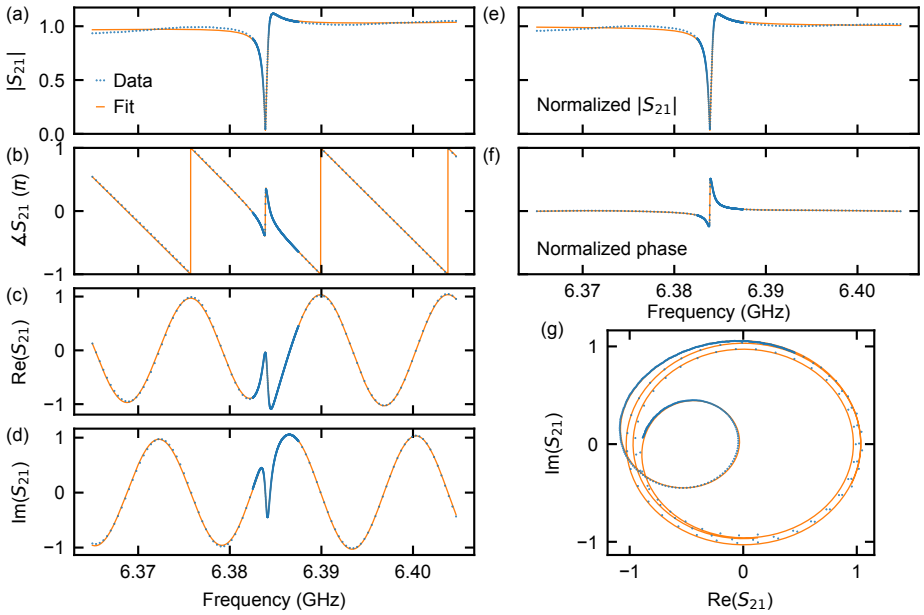

Figure 5.1: Measurement of a $\lambda/4$ resonator coupled to the feedline. The complex feedline transmission S_{21} is measured around the resonator frequency and fitted with Equation (2.26). (a)-(d) show amplitude, phase, real and imaginary part of data and fit. (e) $|S_{21}|$ is corrected for a frequency dependent slope of the background and normalized. (f) S_{21} is corrected for the propagation delay. (g) Resonator response in the complex plane.

expression of Equation (2.26) is fitted to the data. It accounts for a frequency-dependent linear slope in the feedline transmission, an amplitude scaling factor and the frequency-dependent linear propagation delay affecting the phase. Correcting for these uninteresting terms yields cleaner data [Figure 5.1(e) and (f)]. The presented fit yields $f_R = 6.384$ GHz, $Q_c = 9920$ and $Q_i = 260,000$. Resonator quality factors presented are obtained using this procedure. In order to optimize measurement speed, an average intra-resonator photon number of ~ 3000 was used.

With a method to extract the important quantities from a resonator, we now investigate their response to $B_{||}$ (Figure 5.2). Upon increase of $B_{||}$, f_R decreases. This is due to the reduction of the Cooper-pair density in the superconductor, leading to an increased kinetic inductance [Equation (2.31)], leading in turn to a reduced f_R [Equations (2.27) and (2.33)]. The usually observed reduction of $\Delta f_R(B_{||}) = f_R(B_{||}) - f_R(0)$ with $B_{||}$ due to kinetic inductance, $\Delta f_R(B_{||})/f_R(0) = -k \cdot B_{||}^2$ is also reproduced here [104, 146, 172, 188]. To extract more information about the effective film thickness and the electronic diffusion constant of the NbTiN film, the frequency response of the resonator to a perpendicular field $B_\perp$ would also need to be known (not possible with the setup used in these experiments). Further on,

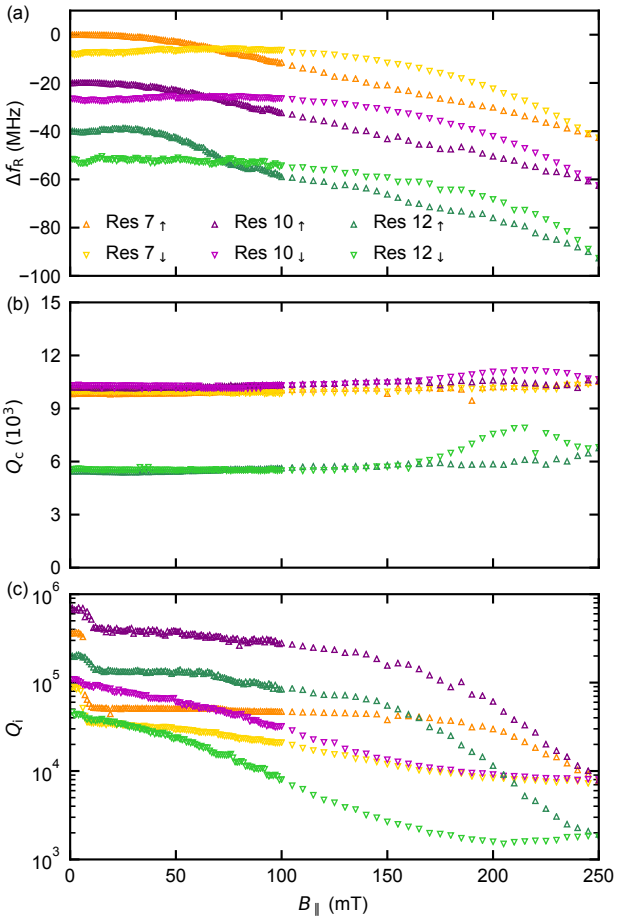

Figure 5.2: Behavior of the resonators when increasing $B_{||}$ from 0 to 250 mT and back to 0 mT. (a) Deviation Δf_R from the fundamental frequency at $B_{||} = 0$ mT. Different resonator traces are offset by 20 MHz each for clarity. (b) Coupling quality factor versus $B_{||}$. (c) Internal quality factor versus $B_{||}$. Note the sharp decrease in Q_i when sweeping from 6 to 10 mT and the more gradual decrease from 100 mT onwards. The initial Q_i values are not recovered after returning to zero field.

the induction of vortices will lead to a decrease in f_R as they also reduce the Cooper-pair density [66, 69, 189].

The hysteresis observed in the traces of $f_R(B_{||})$ [Figure 5.2(a)] cannot be explained by a change in kinetic inductance. However, a net magnetization of the superconducting film qualitatively explains this behavior [170]. The hysteretic magnetization changes the current distribution in the resonator, leading to changed f_R.

Whereas the small changes in f_R have no consequence in terms of performance of the circuit – the resonator can just be re-measured to re-calibrate the readout point – changes in Q_i are more worrisome. In Figure 5.2(b), a strong decrease of Q_i between 6 and 10 mT can be observed for all resonators. We attribute this to the Al on-chip wirebonds turning normal (Al has a bulk critical field of 10 mT [58, 190]) and hence becoming dissipative. The use of field-compatible NbTiN airbridges can solve this problem (Section 3.5.2).

Further on, a more gradual reduction in Q_i starting from $\sim$ 100 mT can be observed. We attribute this to the formation of vortices due to the misalignment of the field with respect to the plane of the chip. The vortices in the resonators experience a Lorentz force, causing them

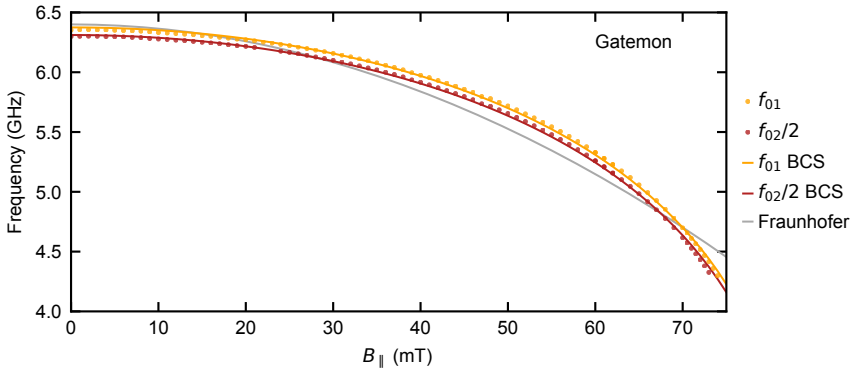

Figure 5.3: The gatemon f_{01} and $f_{02}/2$ monotonically decrease with $B_{||}$. Their field dependence is well described by a closing BCS gap with $B_c = 83.9\,\mathrm{mT}$. The model based on the flux penetration of an extended junction (Fraunhofer) provides neither qualitative nor quantitative agreement.

to dissipatively move around, lowering Q_i. This can be avoided by puncturing the resonators with holes such that no vortices are formed (Section 3.5.1). Further on, compensation of the residual perpendicular magnetic field, $B_\perp$, with a magnetic field pointing out of the chip plane will reduce this effect.

Although the field dependent reduction of Q_i is certainly not desirable, it does not restrain us from performing CQED experiments in a magnetic field. We will see, however, that in certain cases this field-dependent reduction of the quality factor poses a limitation on qubit T_1.

5.3 Spectroscopic features of the qubits

Let us now apply a $B_{||}$ to the gatemon qubit presented in Figure 4.1. For now we focus on the gatemon, as flux-tunable split-junction devices experience fluctuating f_{01} due to imperfect alignment and limited stability of $B_{||}$. First, we study the spectroscopic features of the gatemon. In order to disentangle effects from $B_{||}$ and V_G, we place the gatemon on the same V_G sweetspot at each value of $B_{||}$. We attribute the observed monotonic decrease in f_{01} with $B_{||}$ (Figure 5.3) to a reduced superconducting gap induced in the nanowire junction [104, 191],

$$\Delta(B_{||}) = \Delta(0)\sqrt{1 - \left(\frac{B_{||}}{B_c}\right)^2}, \tag{5.1}$$

where B_c is the critical field of the aluminum shell of the wire. This is the field dependence of the gap of a superconductor described in the BCS theory. We do not expect the bulk CQED elements on the chip to contribute significantly to this frequency change as they only exhibit

small frequency variations due to the high critical field of the NbTiN film (Figure 5.2) [146, 170, 192]. We approximate the Andreev bound state energy [Equation (2.1)] with

$$E_{\mathrm{ABS}}(T, \delta, B_{\parallel}) = \pm\Delta(B_{\parallel})\sqrt{1 - T\sin^2(\delta/2)}, \tag{5.2}$$

with the field dependence given in Equation (5.1). In the transmon limit, $f_{01} \approx \sqrt{8E_{\mathrm{J}}E_{\mathrm{C}}} - E_{\mathrm{C}}$ [62], therefore as a first approximation,

$$f_{01}(B_{\parallel}) \approx f_{01}(0) \cdot \left(1 - \left(\frac{B_{\parallel}}{B_{\mathrm{c}}}\right)^2\right)^{\frac{1}{4}}. \tag{5.3}$$

However, better results are obtained by Hamiltonian diagonalization. As f_{01} is higher than what is obtainable from a single channel (Figure 2.11) we assume a model with two contributing Andreev bound states. The Hamiltonian from Equation (2.16) therefore becomes

$$\hat{H}(B_{\parallel}) = 4E_{\mathrm{C}}\hat{n}^2 - E_{\mathrm{ABS}}(T_{\mathrm{A}}, \delta, B_{\parallel}) - E_{\mathrm{ABS}}(T_{\mathrm{B}}, \delta, B_{\parallel}). \tag{5.4}$$

This expression is diagonalized and fitted to f_{01} and $f_{02}/2$ while fixing $\Delta(0)$ as the bulk Al gap and E_{C} the value extracted for the split-junction device (Section 4.3.1). The best-fit parameters $T_{\mathrm{A,B}} = 0.95,\ 0.62$ and $B_{\mathrm{c}} = 83.9\ \mathrm{mT}$ match f_{01} and $f_{02}/2$ with an average of the absolute residuals of 12.6 MHz. The extracted B_{c} of the Al shell is similar to other measurements of wires from this growth batch [83]. Because $B_{\parallel}$ is not collinear with the nanowires, the B_{c} of different qubits varies between 50 and 90 mT, roughly correlating with the nanowire-to-$B_{\parallel}$ alignment. The B_{c} values stay constant during one cooldown and vary by $\sim 5\%$ between different cooldowns, provided the sample orientation is kept fixed. Explaining the data by flux penetration of an extended junction (Fraunhofer model) [104], where the qubit frequency is approximated by

$$f_{01}(B_{\parallel}) = f_{01}(0) \cdot \left|\frac{\sin\left(\pi B_{\parallel}/B_{\mathrm{v}}\right)}{\pi B_{\parallel}/B_{\mathrm{v}}}\right|^{1/2} \tag{5.5}$$

and $B_{\mathrm{v}}/2$ is the field at which the first full current cancellation occurs provides neither qualitative nor quantitative agreement.

The critical field of the qubits can be enhanced in various ways. First, $B_{\parallel}$ should be applied collinear with the nanowire. This is not possible with the setup used for these experiments, the sample can only be mounted in eight rotationally symmetric ways with a minimal rotation of 45° between them and $B_{\parallel}$ is sourced by a single-axis magnet, not allowing for rotations. Therefore, a vector magnet that allows for in-plane rotations is used in following experiments. Further on, if the Al shell does not cover all facets there is no Little-Parks effect that leads to the suppression of the induced superconductivity when odd multiples of the flux quantum are sourced through the wire [104, 153, 193]. Lastly, the thickness of the Al shell defines its field compatibility [104]. Indeed, wires with partially covering, thinner (7 nm instead of the 30 nm used here) Al shell can exhibit hard induced gaps up to 1 T [194–196].

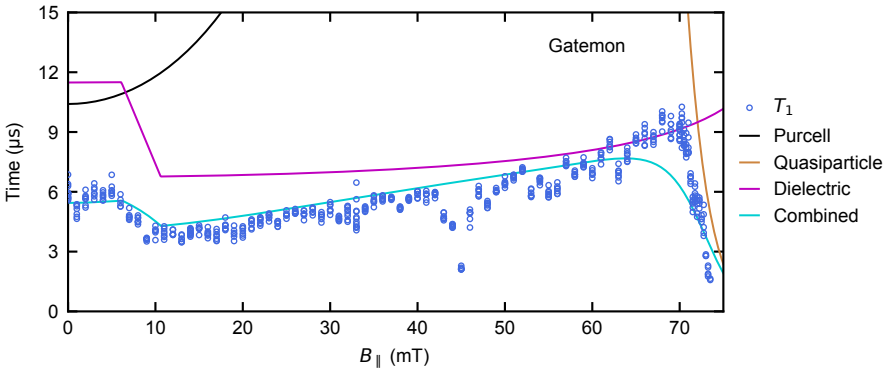

Figure 5.4: The gatemon T_1 versus $B_{||}$. At low $B_{||}$ (f_{01} near the resonator), T_1 is mainly Purcell limited (black). At $B_{||}$ close to B_c, the induced superconducting gap becomes so weak that quasiparticle tunneling dominates T_1 (brown, assuming the effective quasiparticle temperature to be 100 mK). In between, the step in T_1 can be attributed to Q_b (purple, Figures 5.5 and 5.6).The data is explained well by the combination of these three effects (cyan curve) that is not a fit. The dip in T_1 around 45 mT is reproducible and hysteretic, see Figure 5.7.

5.4 Time-domain characterization

5.4.1 Energy relaxation

Having gained an understanding of how f_{01} changes with $B_{||}$, let us now discuss the effect of $B_{||}$ on T_1. Accompanying the frequency measurements presented in Figure 5.3, also T_1 of the gatemon was measured at this V_G sweetspot (Figure 5.4). After an initial reduction between 6 and 10 mT, T_1 recovers when $B_{||}$ is increased until it sharply decreases around 70 mT. This is due to the contribution of three effects that limit T_1.

At small $B_{||}$, due to the small detuning between qubit and resonator, the Purcell effect limits T_1 to [127]

$$\Gamma_{\text{Purcell}} = \left(\frac{g}{2\pi(f_{01}-f_R)}\right)^2 2\pi\Delta f = \left(\frac{g}{2\pi(f_{01}-f_R)}\right)^2 \frac{2\pi f_R}{Q_l}. \tag{5.6}$$

Although this expression does not explicitly depend on $B_{||}$, f_{01} decreases with $B_{||}$, therefore increases the detuning and reduces the effect on T_1. The parameters of the resonator are $f_R = 6.747$ GHz, $g/2\pi = 60.8$ MHz and $Q_l = 11,380$.

Close to the maximal $B_{||}$ value at which the qubit can be observed, quasiparticle (QP) tunneling is the factor limiting T_1. Typically, this effect is only observed when increasing the temperature at which the experiments are performed [59, 60]. The transmon energy relaxation rate Γ_{qp} due to the presence of quasiparticles is given as [156, 197, 198]

$$\Gamma_{qp} \approx \frac{2\chi_{qp}}{\sqrt{\pi}}\sqrt{\frac{\Delta f_{01}}{h}}, \quad \text{where} \quad \chi_{qp} = \sqrt{\frac{2\pi T_R k_B}{\Delta}} e^{\frac{k_b T_R}{\Delta}} \tag{5.7}$$

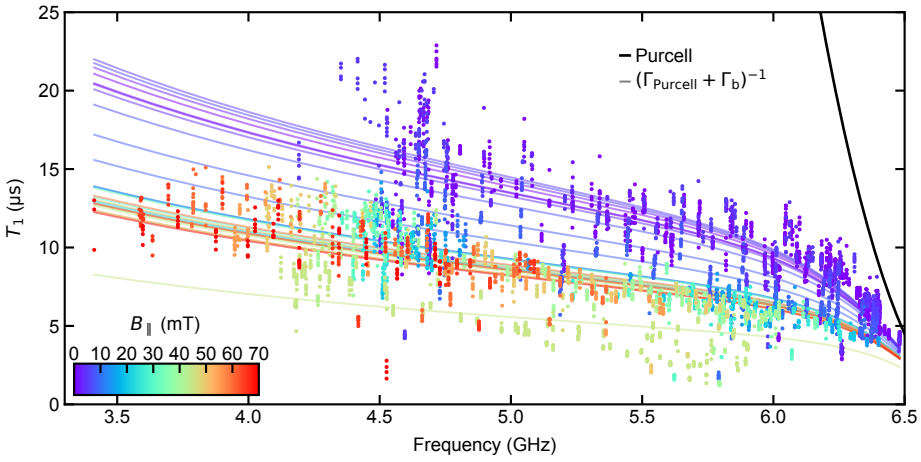

Figure 5.5: By changing V_G, T_1 versus f_{01} of the gatemon is measured for various $B_\parallel$ ($B_\parallel$ increasing with the rainbow spectrum). Accounting for the Purcell effect (black curve), we fit at each value of $B_\parallel$ a background quality factor Q_b [Equation (5.10), fine curves], see Figure 5.6.

is the QP density normalized to the Cooper-pair density assuming a thermal equilibrium at T_R. Inserting Equation (5.1) as the expression for the superconducting gap in Equation (5.7) makes

$$\Gamma_{qp}(B_\parallel) = 2\sqrt{\frac{2f_{01}(B_\parallel)k_B T_R}{h}} e^{\frac{k_B T_R}{\Delta(B_\parallel)}}, \tag{5.8}$$

where $\Delta(B_\parallel)$ is given in Equation (5.1) and $f_{01}(B_\parallel)$ can be approximated with Equation (5.3) or explicitly calculated with a Hamiltonian diagonalization. Although the BCS theory predicts an exponential suppression of the QP density below the gap, various experiments over different systems find that there is an excess QP density [131, 157, 199–201]. Assuming a typical T_R of ~ 100 mK yields reasonable agreement with the exponentially sharp reduction of T_1 observed in Figure 5.4.

The third contribution to the energy relaxation times presented in Figure 5.4 can be modeled as a background quality factor Q_b. This model [12] assumes a constant quality factor, similar to the internal qualüthi factor of a resonator, for example imposed by dielectric losses, resulting in a frequency-dependent energy relaxation rate

$$\Gamma_b = \frac{2\pi f_{01}}{Q_b}. \tag{5.9}$$

We quantify this contribution by fixing $B_\parallel$ and measuring T_1 as a function of f_{01} by sweeping V_G (Figure 5.5). At each value of $B_\parallel$, this procedure is repeated and the data is fitted with the model

$$\frac{1}{T_1(f_{01}, B_\parallel)} = \Gamma_{\text{Purcell}}(f_{01}, B_\parallel) + \Gamma_b(f_{01}), \tag{5.10}$$

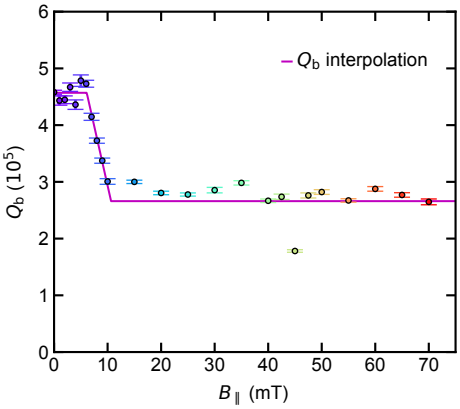

Figure 5.6: Background quality factor versus $B_{||}$. Each point is extracted from fitting the f_{01} dependence of T_1 at a certain $B_{||}$ with the model of Equation (5.10) (Figure 5.5). The step-like decrease in Q_b is in qualitative agreement with measurements of resonator Q_i versus $B_{||}$, see Figure 5.2.

where $Q_b(B_{||})$ is a $B_{||}$-dependent background quality factor. The extracted $Q_b(B_{||})$ shows a step-like behavior (Figure 5.6), in qualitative agreement with what was observed for the resonator Q_i (Figure 5.2). Again, we surmise that the proximity of Al on-chip wirebonds turning normal is the reason for the step-like reduction in Q_b.

Combining these three rates makes the total expression for the T_1 limit,

$$\frac{1}{T_1(B_{||})} = \Gamma_{\text{Purcell}}(B_{||}) + \Gamma_b(B_{||}) + \Gamma_{qp}(B_{||}). \tag{5.11}$$

Where the Purcell effect is dominating when the qubit is still close to the resonator, the reduced background quality factor imposes the limitation above $B_{||} = 10$ mT. Close to the maximum field at which the qubit is still observable, the gap becomes so weak that QPs make the dominant contribution. The data in Figure 5.4 is well reproduced without fitting it directly.

A further feature in the T_1 data of Figure 5.4 is a dip around 45 mT. It is reproducible, but its position depends on the sweep direction (Figure 5.7). If $B_{||}$ is increased, the dip occurs around 45 mT, if the field is lowered, it occurs around 35 mT. Note that also in Figure 5.5 the T_1 values measured at 45 mT are consistently lower than at other $B_{||}$ values, which is reflected in a reduced Q_b at 45 mT (Figure 5.6). This excludes an explanation where the

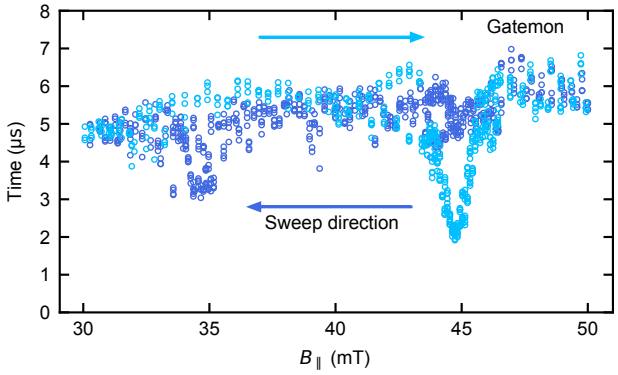

Figure 5.7: Hysteresis in T_1 versus $B_{||}$. Upon increasing $B_{||}$ from 0 mT on, there is a reproducible reduction in T_1 around 45 mT. When sweeping $B_{||}$ in the other direction, the T_1 reduction is less pronounced and only appears around 35 mT.

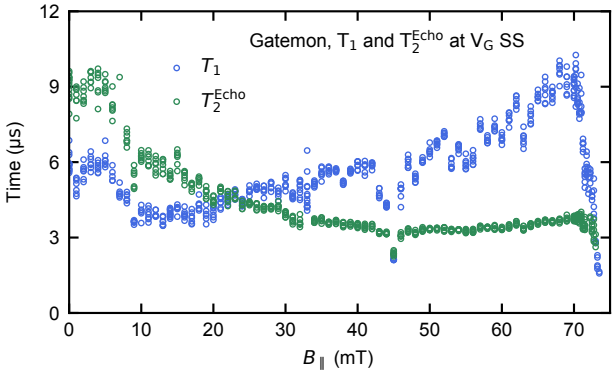

Figure 5.8: At each value of $B_\parallel$, the gatemon is tuned to a V_G sweetspot (SS) to measure T_1 (same data set as in Figure 5.4) and T_2^{Echo} (blue and green symbols). At low values of $B_\parallel$, T_2^{Echo} is T_1 limited and stays roughly around 3 μs from 40 mT on.

coupling of the qubit to a Zeeman-split lossy ensemble with an according g factor of $g \approx 9.2$ would be responsible for this effect. So far, we could not find an explanation for this effect.

5

5.4.2 Dephasing

Let us now investigate how the dephasing times of the gatemon change with $B_\parallel$. Accompanying the T_1 scan in Figure 5.4, also T_2^{Echo} was measured (Figure 5.8). The data is taken in such a way that at each value of $B_\parallel$ the qubit is tuned onto the same V_G sweetspot again. At low values of $B_\parallel$, T_2^{Echo} is T_1 limited. However, from $B_\parallel \sim 20$ mT on, T_2^{Echo} is lower than the observed T_1. Following the procedure discussed in Section 4.2.2 and plotting the dephasing rates as a function of sensitivity does, however, not yield any insight - the dephasing rate saturates at some value, irrespective of the sensitivity. This is not in agreement with an expected limit to Γ_2^{Echo} given noise in $B_\parallel$.

In order to investigate this behavior further, V_G scans at fixed values of $B_\parallel$ are performed, and f_{01}, T_1 and T_2^{Echo} are measured (example for 50 mT in Figure 5.9). To extract the sensitivity of the qubit to V_G, f_{01} is interpolated with a polynomial. Strikingly, we find the value of maximal T_2^{Echo} to be away from the V_G sweetspot.

This procedure is repeated at different fields, and the extracted dephasing rates are plotted versus sensitivity (Figure 5.10). At low $B_\parallel$, Γ_2^{Echo} is linear in D_{V_G}, indicating that the voltage $1/f$ noise is the limiting factor. As $B_\parallel$ is increased, Γ_2^{Echo} has different slopes for positive and negative sensitivities, and is in general increased. Interestingly, also the points of minimal dephasing are deviating from the zero-sensitivity point. The data are interpolated with separate linear slopes on either side of the sensitivity point with minimal Γ_2^{Echo} that are averaged to obtain an effective $1/f$ voltage noise amplitude at each value of $B_\parallel$ (Figure 5.11). A slight decrease in the extracted noise amplitude with $B_\parallel$ can be observed, the origin of which we do not understand.

We compare the Γ_2^{Echo} extracted at the V_G sweetspot (Figure 5.8) with the extracted minimal Γ_2^{Echo} when performing a V_G sweep at fixed $B_\parallel$ (Figure 5.12). At low values of $B_\parallel$ we find a good agreement. However, as $B_\parallel$ increases the deviation becomes more prominent.

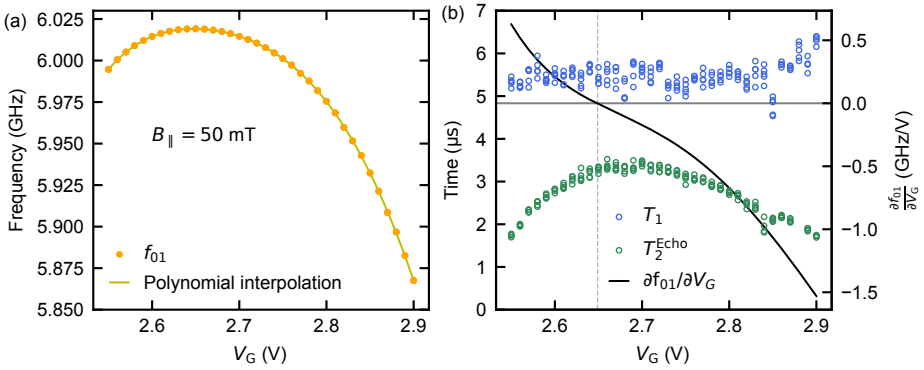

Figure 5.9: At each value of $B_{||}$ (this example is at $B_{||} = 50$ mT) f_{01}, T_1 and T_2^{Echo} are measured as a function of V_G. (a) The measured values of f_{01} are interpolated with a polynomial to extract the sensitivity. (b) As the excursion in f_{01} is small, T_1 is roughly constant. T_2^{Echo} depends on V_G, but its maximum value is shifted with respect to the point of vanishing V_G-sensitivity (dashed gray line).

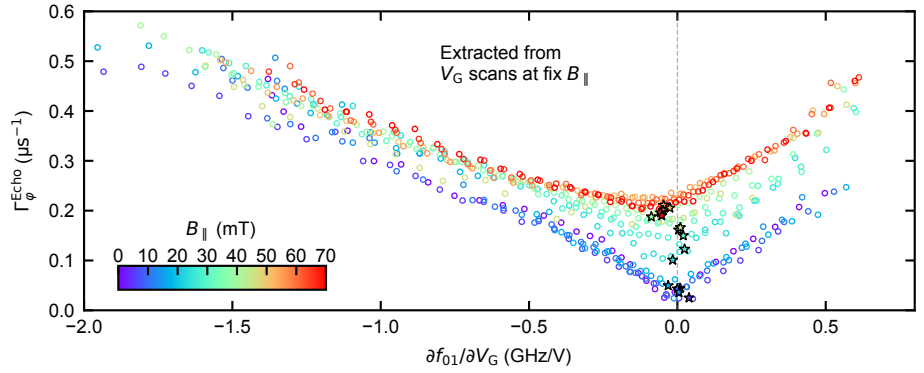

Figure 5.10: Γ_2^{Echo} versus V_G sensitivity at different values of $B_{||}$ ($B_{||}$ increasing with the rainbow spectrum). $B_{||}$ is kept fixed while a V_G scan is performed (Figure 5.9). Stars indicate interpolated minimal dephasing rates. Note the deviation of the dephasing minima from the zero-sensitivity point (dashed gray line).

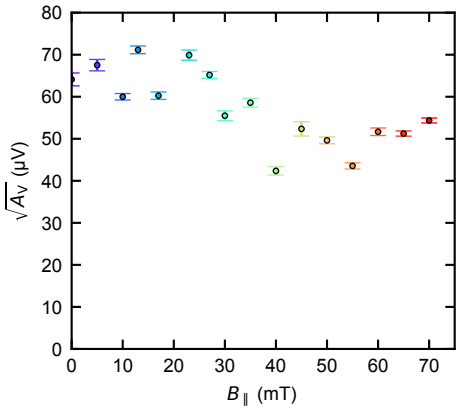

Figure 5.11: Averaged extracted $1/f$ V_G noise amplitude versus $B_{||}$. Data extracted from scans shown in Figure 5.10. A weak decrease in the noise amplitude with field can be observed.

The saturation of the dephasing rate, the reduction of the observed effective voltage noise and the deviation of the point of minimal dephasing from the zero-sensitivity point with $B_{||}$ are not yet well understood. A possible explanation is that the sensitivity to the dominant on-chip charge noise differs from $\partial f_{01}/\partial V_G$ away from $B_{||} = 0$ around the V_G sweetspot tracked. During that cooldown it was not possible to study the dephasing around multiple V_G sweetspots to confirm this hypothesis. However, subsequent cooldowns with the same sample revealed varying $\Gamma_2^{\text{Echo}}(B_{||})$ dependences, depending on the V_G sweetspot chosen.

5.5 Flux-tunable split-junction devices in $B_{||}$

Let us now turn our focus to the first attempt at controlling a flux-tunable split-junction device in a magnetic field. This is a considerably more difficult task than controlling a gatemon in field, as already smallest deviations in flux though the SQUID loop affect the qubit frequency. The perpendicular field corresponding to threading a flux quantum through the SQUID loop of the device is

$$B_\perp = \frac{\Phi_0}{A} \approx 5\ \mu\text{T}, \tag{5.12}$$

where the area A of the SQUID loop is $(20\ \mu\text{m})^2$. We are, however, sensitive to changes much smaller than Φ_0. This means that if there is a residual $B_\perp$ in the field applied (imperfect alignment between the chip plane and $B_{||}$), f_{01} will change. By counting the number of flux cycles the qubit undergoes when changing the applied field, we estimate the misalignment between chip and field to be $\sim 1^\circ$. This means however, that any noise in the sourced field will have a strong impact on f_{01}. The sensitivity to the noise in $B_{||}$ can be reduced by canceling the $B_{||}$ misalignment using a vector magnet. This, however, comes at the cost of additional noise in the cancellation field. Although the large inductance of the solenoid (0.7 H) will provide good low-pass filtering, it is therefore important to have low-noise current sources. To improve the general noise performance, persistent-current solenoids can be used [202]. If a persistent current running though the solenoid provides the magnetic fields, the noise of the current sources will not be translated to noise in the magnetic fields.

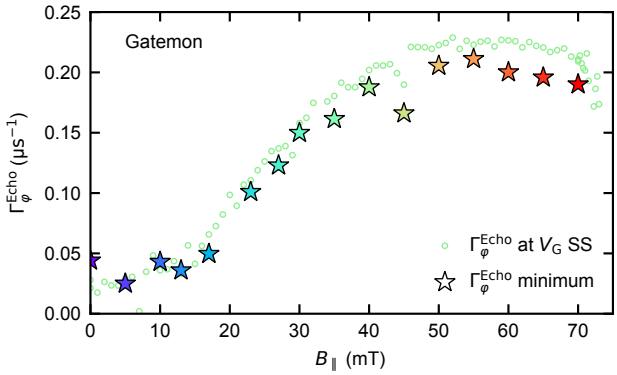

Figure 5.12: Γ_2^{Echo} versus $B_{||}$. Circles are Γ_2^{Echo} values at the V_G sweetspot, extracted from data in Figure 5.8. Star symbols denote the minimal Γ_2^{Echo}, data from Figures 5.9 and 5.10. The data sets show good agreement at low $B_{||}$ and deviate above 40 mT as Γ_2^{Echo} is no longer minimal at the zero-sensitivity point.

Figure 5.13 shows a two-tone spectroscopy measurement of f_{01} of a split-junction device as a function of applied flux in a magnetic field of 50 mT. On the flux sweetspot, the qubit line is quite well defined [blue line in Figure 5.13(b)] as the qubit is first-order insensitive to changes in flux. However, already slightly off the sweetspot the measured trace is considerably more noisy, indicating that f_{01} changes fast on the timescale of the measurement ($\sim$ 1.5 min per line cut). It is worth noting that the noise background has a periodicity which we attribute to the low-frequency vibrations of the pulsed tube of the dry cryostat. The solenoid sourcing the magnetic field and the sample holder are not rigidly connected to each other. Therefore, a relative motion of the sample holder and the solenoid is possible. It will lead to a change in the flux through the SQUID loop as the sourced field is not perfectly homogeneous. This means that f_{01} changes with the periodicity of the pulsed tube cycle. This can be confirmed by switching the pulsed tube compressor off for a brief amount of time — the two-tone spectroscopy traces off the flux sweetspot become sharp like the ones on the sweetspot. This vibration-induced noise is a problem when flux-sensitive measurements are to be made. It is therefore important to reduce its effect on the qubits. We designed a new, more rigid sample holder to reduce the amount of noise, and designed smaller SQUID loops to become less sensitive to noise (Chapter 6).

Further challenges are the long-term stability of the magnetic field and varying magnetic fields that are generated by external sources. Whilst adequate current sources and persistent current solenoids help to increase the stability of the sourced field, the field experienced by the qubits can be perturbed by other sources. In the vicinity of the setup ($\sim$ 10 m), there are several other cryostats that can source vector magnetic fields. For typical qubit measurements, changes in the sourced magnetic fields of these cryostats are not a problem because of passive magnetic shielding around the qubits (in the cryostat at base temperature, consisting of two layers of Cryoperm, a high-μ_r metal, and a superconducting Al shield). Using the passive magnetic shielding commonly used in the group is not possible in our setup as it would not allow for applying $B_{||}$. Therefore, a passive external magnetic shield providing a shielding factor of $\sim$ 80 still allowing us to apply $B_{||}$ is designed (Appendix A).

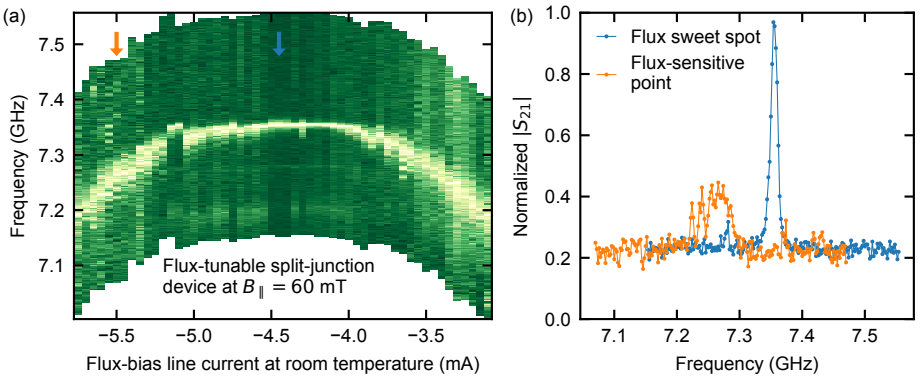

Figure 5.13: Flux-tuning of a split-junction device at $B_{||} = 60$ mT. (a) Two-tone spectroscopy scans versus the applied flux-bias line current at room temperature that tunes the flux Φ through the SQUID loop. On the flux sweetspot, a good signal can be obtained. As the sensitivity to Φ is increased, the f_{01} line broadens and noise due to pulse tube induced vibrations becomes apparent. (b) Line cuts along the arrows in (a) showing that the f_{01} peak at the flux sweetspot (blue) is much sharper than away from the sweetspot (orange).

5.6 Conclusions

This is the first demonstration of coherence in superconducting qubits in magnetic fields exceeding the critical field of Al. We have identified the closing of the induced superconducting gap to be the limiting factor for the maximally applicable $B_{||}$. The alignment of the applied field with the nanowire axis increases the maximal field at which the qubits can be operated. After an initial decrease due to the Al on-chip wirebonds turning normal, T_1 stays unaffected by the magnetic field until the induced superconducting gap is so weak that QP poisoning becomes a problem. The sensitivity of the qubit to the dominant on-chip charge noise starts to differ from $\partial f_{01}/\partial V_G$ when a field is applied. Further on, the stability and the noise of the applied $B_{||}$ does not yet allow for more elaborate measurements of flux-tunable split-junction qubits in field.

Let us now summarize the identified limitations to field compatibility and field stability, and discuss solutions to overcome them. We start with what we can learn from the behavior of the resonators in $B_{||}$. When applying $B_{||} > 6$ mT, the Q_i drops substantially due to the on-chip wirebonds. In order to avoid normal-conducting elements in the vicinity of resonators and qubits, field-resilient NbTiN airbridges can be used (Section 3.5.2). To avoid the slow decrease of Q_i attributed to a remnant $B_\perp$ that sets in for $B_{||} \geq 100$ mT, several measures are taken. Firstly, a compensation solenoid that can source a field $B_\perp$ to cancel misalignment is installed. Secondly, the resonators are punctured with holes to increase their resilience towards a potentially remaining $B_\perp$ [171, 187, 203, 204]. And lastly, the thickness of the NbTiN film used is reduced to 70 nm to enhance its parallel critical field [104, 146, 205, 206]. Moving on to the spectroscopic signatures of the qubits in field, we observed the imperfect

alignment of $B_{||}$ with respect to the nanowire axis to be reducing the maximal field at which the qubits can be operated, an effect also seen in other works [207, 208]. As placement of nanowires in a certain direction more precisely than to a few tens of degrees is challenging, a vector magnetic field in the sample plane is desirable. With a vector magnetic field, in-situ alignment of the magnetic field is possible. Further on, the wires should have an epitaxially grown Al shell that is thinner ($\sim$ 10 nm) than the one used for these experiments (30 nm) to allow for higher critical fields [194–196, 209]. In order to avoid Little-Parks oscillations, the shell should not be fully covering all facets of the wire [104, 153, 193]. To increase the stability of the sourced magnetic field, and to allow for measurements of flux-tunable split-junction qubits in field, several changes need to be made. A passive magnetic shield that cancels external fields and still allows to source fields of $\sim$ 1 T needs to be installed. The noise in the field can be reduced using magnets operating in persistent current mode. The effect of vibrations of the setup due to the pulsed tube can be suppressed by the use of a more rigid sample holder. Further on, the sensitivity to noise in $B_{||}$ can be reduced by reducing the area of the SQUID loops. The reduced SQUID loop area comes at the cost that flux-bias lines are not sufficient any more to source a flux quantum through the SQUID loop. However, it is possible to use the out-of plane field sourced by the compensation coil to flux bias the SQUID loops. In case that these measures are not sufficient to reduce the effect of vibrations, stroboscopic measurements locked to the pulsed tube can be used [210].

We have discussed limiting effects of $B_{||}$ on nanowire transmons and identified ways to overcome them. The identified steps give a clear way forward, and their implementation will be discussed in Chapter 6. However, it is still valuable to also look around for other possible implementations of a flux tunable qubit in $B_{||}$. I now discuss my personal view on advantages and disadvantages of other candidate systems. Instead of using resonators in the CPW geometry, it would be possbile to use NbTiN nanowire resonators that exhibit good field compatibility [172]. Notably, this type of resonator is not plagued by vortex nucleation up to perpendicular fields of 350 mT, reducing problems in fine-tuning and stability. It has shown stable Q_i up to $B_{||} = 6$ T. Although Q_i of these resonators has so far not been shown to exceed 10^5, it might not be a critical limitation as high readout fidelities still can be achieved. Using this architecture with a Q_i of 10^5 for parts the qubit capacitor plates might however impose a limit of ~ 3 μs on T_1 for a qubit operating at 5 GHz [Equation (5.9)]. We decided not to implement this design, as resonators in the CPW geometry with holes are more straight forward to fabricate and have shown higher Q_i, also up to $B_{||} = 5.5$ T [146]. There are also different ways to define a Josephson junction that is resilient to magnetic fields. Recent material development has demonstrated that also InSb nanowires can be grown with an epitaxial aluminum shell that induces a hard superconducting gap [196, 211, 212]. Therefore, these wires would make a good alternative to the InAs wires used so far. However, there are no published results of superconducting qubits using InSb nanowires as the nonlinear element. Having shown InAs based qubits to be a working system, we therefore decided to continue using the InAs nanowires. Besides nanowires, and therefore not part of this study, other implementations of field-compatible Josephson junctions are possible. For example, graphene Josephson junctions have been shown to operate in magnetic fields of $B_{||} = 1$ T.

However, none of the implementations has shown coherence or energy relaxation times exceeding 100 ns [213, 214]. A further possibility is to use field-compatible SIS Josephson junctions, for example based on thin-film Al [100]. Their $B_{||}$ compatibility has been demonstrated up to 350 mT. Recently, transmons with Josephson junctions based on proximitized two-dimensional electron gases (2DEG) have been realized [175]. The critical fields of the superconducting gap induced in the 2DEG can reach up to 2.3 T [215]. However, substrate dielectric losses limit T_1 to $\sim 2\ \mu$s, making them so far not optimal candidates.

6 ADDING THE IN-PLANE FIELD AS A PARAMETER TO THE TOOLBOX OF CQED

F. Luthi, T. Stavenga, J. Assendelft, O. W. Enzing, A. Bruno, C. Dickel, N. K. Langford, M. A. Rol, T. S. Jespersen, J. Nygård, P. Krogstrup, L. DiCarlo

This chapter presents solutions to the previously identified challenges that come about when transmons are operated in an in-plane magnetic field. After implementation of these improvements, time-domain measurements of flux-tunable split-junction devices are demonstrated to be possible.

6.1 Introduction

In this chapter, the technical improvements of the setup addressing the problems identified in Chapter 5 are discussed. Specifically, the improvements are:

- Reduction of the thickness of the NbTiN film to make it more resilient towards applied magnetic fields;
- Addition of an array of 100 nm diameter holes in resonator and qubit capacitor plates to avoid vortex formation;
- NbTiN airbridges;
- A coil that sources an out-of-plane field that can compensate a potential misalignment between sample and sourced magnetic field;
- A two-axis solenoid capable of sourcing a rotatable in-plane magnetic field;
- Nanowires that have only a partially covering, thinner Al shell;
- A more rigid sample holder to avoid vibrations;
- Passive magnetic shielding that still allows us to source a magnetic field;
- Persistent current switches for the in-plane field solenoids;
- SQUID loop area reduction to reduce the sensitivity to noise.

Where possible, the effect of these improvements are discussed individually. Together, they allow taking of time-domain data of flux-tunable split-junction qubits at field of $B_{||} = 50$ mT. The last part of the chapter summarizes the current status of the experiment. Although all the necessary individual ingredients have been shown to work, combining them remains an open challenge due to fabrication difficulties.

6.2 Bulk CQED elements

Let us first discuss the solutions to the factors limiting the in-field performance of the bulk CQED elements. The field compatibility of the NbTiN film is increased by reducing its thickness from our group's standard 200 nm to 70 nm. If the film thickness of a Type II superconductor is substantially below the London penetration depth (for NbTiN, $\lambda \approx 270$ nm, see Section 2.4.1), the parallel field at which vortices are formed is substantially heightened [104, 146, 205, 206]. Further on, the center conductor of the resonators are punctured with an array of holes (Section 3.5.1, Figure 3.8) [131, 146, 174, 203]. This avoids the formation of vortices in the superconducting film, because the field lines can go through the holes. Further on, a superconducting coil that can source an out-of-plane field $B_{\perp}$ was installed (Appendix A). This field helps to mitigate alignment discrepancies between the sample plane and the sourced $B_{||}$. Note that this perpendicular coil can also be used to flux-tune split-junction qubits.

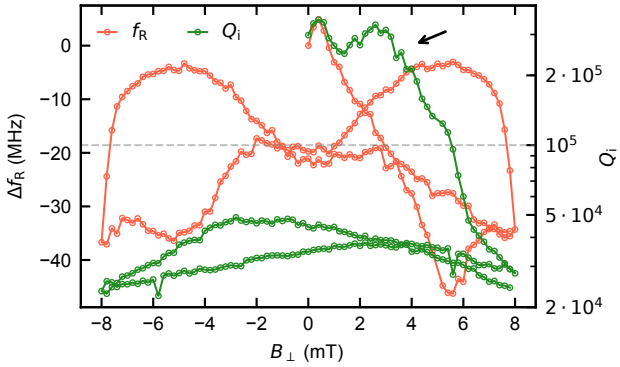

Figure 6.1: Response of a resonator with holes to an applied $B_\perp$ ($B_{||} = 0$ mT). $B_\perp$ is swept from 0 to +8, to -8 and back to $+8$ mT. f_R gives a strong response to $B_{||}$, peaking at optimal alignment and then quickly reducing. The curve is hysteretic, and the maximal value is not restored upon return to $B_\perp = 0$ mT. Due to the holes in the resonator, Q_i is insensitive to $B_\perp$ for small excursions, but decreases rapidly and does not restore once a certain field (black arrow, ~ 4 mT) is surpassed.

Figure 6.1 shows the effect of $B_\perp$ on a resonator. The $B_\perp$ sweep starts from a virgin, zero-field cooled film ($B_\perp = 0$ mT), is taken to a maximal value of $+8$ mT, brought to -8 mT and back to $+8$ mT. Upon small excursions already, f_R gives a clear signal. For the optimal alignment, f_R is maximal and starts decreasing for non-optimal $B_\perp$. Hence, making small changes to $B_\perp$ to optimize f_R is a convenient way to determine the optimal $B_\perp$ value. After an excursion in $B_\perp$, its maximal value is not restored. The hysteretic behavior of f_R can be explained by the flux density in the resonator that depends on its field history [170]. While f_R shows an immediate response to $B_\perp$, Q_i is resilient towards small excursions, which we attribute to the introduced holes. Indeed, resonators on the same chip that had no holes showed a much faster decrease of Q_i with $B_{||}$ (data not shown). We interpret that at $B_{||} \sim 4$ mT, where Q_i starts to decrease (indicated by a black arrow in Figure 6.1), all holes are threaded by a flux quantum. Further increase of $B_{||}$ will lead to the formation of vortices, reducing Q_i. This 'critical' field B_c^h corresponds roughly with the expectation given the hole density $n_h = 4.6$ holes/μm^2,

$$B_c^h = \Phi_0 \cdot n_h \approx 9 \text{ mT}. \tag{6.1}$$

The discrepancy can be explained by flux focusing due to the Meissner effect where field-enhancement factors of ~ 2 are not unusual [216, 217], or the lack of an independent calibration of $B_\perp$. At the moment, $B_\perp$ is only calculated via the current-to-field factor of the coil determined by the coil geometry, distance to the sample and winding number.

In Chapter 5 it was identified that the single-axis magnetic field used poses substantial restrictions on the usability of the setup. Due to the inability to align the sourced field $B_{||}$ with the nanowire axis, the maximal field at which the nanowires can be operated at was reduced.

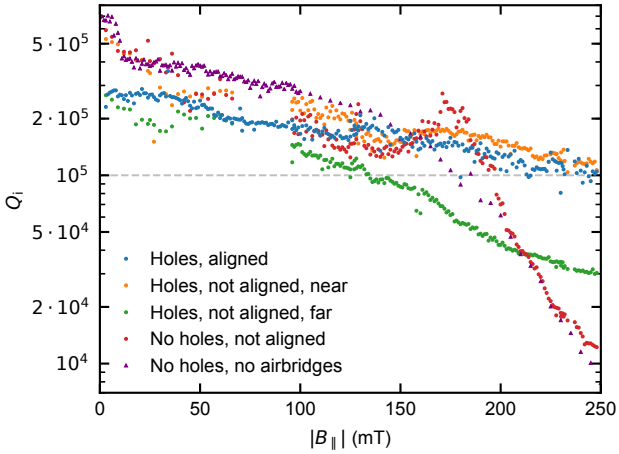

Figure 6.2: Comparison of the Q_i of resonators as a function of $|B_\parallel|$. Resonators with NbTiN airbridges (round symbols) do not exhibit the reduction in Q_i at 10 mT, opposed to the resonator with on-chip wirebonds [purple, same data as in Figure 5.2(c)]. The presence of holes and proximity to the resonator to which $B_\perp$ is aligned determines Q_i for $|B_\parallel| > 150$ mT.

Also, to improve the stability of the sourced field, persistent current capabilities are desired. Hence, we installed a two-axis solenoid (2 T and 0.5 T) that can source a rotatable in-plane field. Both of these axes have persistent current capabilities.

As mistakes in the control of the magnetic field can cause a large loss of time (e.g. warming up of the film to $\sim$ 20 K and subsequent cooling to base again, taking roughly a day), an intuitive control via the measurement software is important. To avoid field excursions out of the sample plane, the coordinate system in which the magnetic field is expressed is chosen to be cylindrical. An alignment procedure determines the (with respect to the magnetic field axes) tilted plane of the sample. This tilted plane will then be set as the standard plane of the cylindrical coordinate system. The alignment procedure works as follows: $B_\parallel$ is increased in a certain direction, and at each step $B_\perp$ is changed to maximize f_R. Once a desired field value is reached, this point in field is defined as being a point in the sample plane. A further point in the sample plane is obtained by changing the angle of $B_\parallel$ in small steps, whilst also performing the f_R maximization by changing $B_\perp$. Together with the origin (zero field), these three points define the sample plane. Now, when changing the magnetic field, only the magnitude $|B_\parallel|$ and the angle θ need to be specified. The sweep direction is then determined, and the step sizes in the three solenoid directions are subdivided such that only a minimal excursion out of the sample plane happens. This procedure enables an intuitive control of field angle and magnitude and avoids mistakes.

This field control, together with NbTiN airbridges and holes in the resonators are necessary to achieve values of $Q_i \sim 10^5$ at $|B_\parallel| > 150$ mT (Figure 6.2). Resonators that have on-chip wirebonds experience a reduction in Q_i around $|B_\parallel| = 10$ mT [purple symbols in Figure 6.2, same data as in Figure 5.2(c)]. The use of NbTiN airbridges (Section 3.5.2) mitigates this problem, confirming the hypothesis that the on-chip wire bonds turning normal

conducting are a source of loss. Resonators that do not have holes (red and purple symbols in Figure 6.2) exhibit a sharp decrease of Q_i in $|B_{||}| > 200$ mT. This can be attributed to the sourcing of vortices in the film, leading to loss. Because the coil sourcing $B_\perp$ is not large in comparison to the chip (coil radius is 6.5 mm, chip is 2×7 mm, distance coil to chip is ~ 6 mm), $B_\perp$ exhibits an inhomogeneity of $\sim 10\%$ (as determined by magnetostatic calculations). This means that although we align $B_\perp$ with respect to a resonator in the center of the chip (blue symbols in Figure 6.2), the alignment is not perfect over the whole chip. A result of this is that resonators located in proximity to the one with respect to which the field was aligned exhibit better field compatibility (orange symbols) than ones that are far away (green symbols). This could be avoided if a more homogeneous field was used. Nonetheless, the resonators are good enough such that we can perform CQED experiments at magnetic fields up to at least 250 mT.

6.3 Qubits

In this section we address the identified improvements needed for the qubits. First, we discuss the effect of an in-plane vector field. The effects of this technical upgrade on the qubits will be investigated using the chip of Chapter 4 and Chapter 5. We study the dependence of f_{01} and T_1 on $|B_{||}|$ and θ. Then, we will turn to the next technical improvement, the use of InAs nanowires that have a thinner Al shell that only covers two facets of the core. The thinner shell enables a higher field compatibility [194–196]. Further on, because the shell is not forming a superconducting loop, Little-Parks oscillations are avoided [153, 193]. However, before more extensive studies are made, a proof of concept is made by just measuring the zero-field characteristics of transmons that employ partly covered wires.

6.3.1 Vector field control

The qubit f_{01} not only shows a clear dependence on $|B_{||}|$ (Chapter 5), but also on θ (Figure 6.3). Keeping $|B_{||}|$ fixed, scans of f_{01} where θ is swept from -90° to $+90^\circ$ are performed. Where at low $|B_{||}|$ (≤ 10 mT) only weak changes in f_{01} can be observed, these become more drastic at larger fields. An angle $\theta_0 = -69^\circ$ of optimal alignment, where f_{01} is reduced the least with $|B_{||}|$, can be extracted [blue arrow in Figure 6.3(a)]. Note that this angle corresponds to within $\sim 5^\circ$ to the angle extracted from optical images. Further on, it does not change with $|B_{||}|$, Figure 6.3(b). At fields below 20 mT, however, an accurate extraction is challenging because of the only weakly changing f_{01}.

A more detailed measurement of the f_{01} dependence on $|B_{||}|$ along this direction is shown in Figure 6.4. Similar to Figure 5.4, the decrease in f_{01} is well described by the model of Equation (5.1) with $B_c = 85.6$ mT. Interestingly, if $|B_{||}|$ is increased in the direction perpendicular to the nanowire, Equation (5.1) still describes f_{01} well, although with a different $B_c = 50.4$ mT [orange in Figures 6.3 and 6.4]. In a toy model, the nanowire can therefore be thought of as having two critical fields, one in axial direction and one perpendicular to

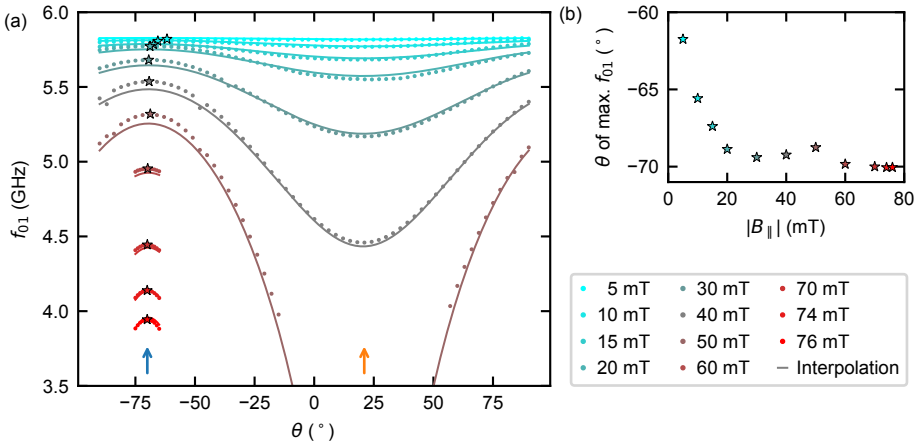

Figure 6.3: f_{01} versus $|B_\parallel|$ and θ for a transmon with a full-shell nanowire. (a) Data is obtained by fixing $|B_\parallel|$ and changing θ. For field values $|B_\parallel| \geq 50$ mT only partial angle scans are taken as the visibility of f_{01} is reduced at low frequencies. Data is interpolated with Equation (6.2), only the wire alignment angle θ_0 is fitted. The values of the critical fields are obtained independently by sweeping the field at best and worst alignment angles [indicated by blue and orange arrows (Figure 6.4)]. Star symbols indicate the angle of maximal f_{01}, extracted from a parabolic fit at each $|B_\parallel|$ value. (b) Angle of maximal f_{01} is roughly constant with $|B_\parallel|$.

it. The frequency of the qubit can thus be calculated by diagonalizing the Hamiltonian of Equation (2.16) where the superconducting gap is given by

$$\Delta(|B_\parallel|,\theta) = \sqrt{1 - \left(\frac{|B_\parallel|\cos(\theta-\theta_0)}{B_{c,g}}\right)^2 - \left(\frac{|B_\parallel|\sin(\theta-\theta_0)}{B_{c,b}}\right)^2}, \tag{6.2}$$

where $B_{c,g}$ ($B_{c,b}$) is the critical field along (perpendicular to) the wire. Without fitting the data directly, but just using the independently extracted θ_0, $B_{c,g}$ and $B_{c,b}$, the model of Equation (6.2) explains the data reasonably well (Figure 6.3). At a given θ, the effective critical field can therefore be expressed as

$$B_c(\theta) = \frac{1}{\sqrt{\left(\frac{\cos(\theta-\theta_0)}{B_{c,g}}\right) + \left(\frac{\sin(\theta-\theta_0)}{B_{c,b}}\right)}}. \tag{6.3}$$

This confirms that the alignment of the field with the wire direction is of great importance.

Next, we investigate T_1 as a function of field and angle. Although the same chip as in Chapters 4 and 5, where T_1 values exceeded 15 μs, was used, the typically measured T_1 values did not exceed 5 μs. We will later discuss that we think this is due to the decrease in shielding quality that came about when the two-axis solenoid was installed. Unfortunately, this was not yet known when performing these experiments. Figure 6.5 shows averaged T_1 values

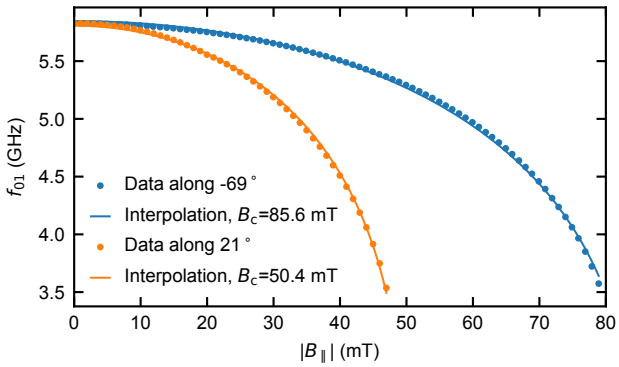

Figure 6.4: Scan of f_{01} versus $|B_{||}|$ along (blue) and perpendicular to (orange) the nanowire axis of the same full-shell qubit as in Figure 6.3. Interpolating the data with the model of Equation (5.1) yields good agreement.

of the same qubit as discussed in Figures 6.3 and 6.4 as a function of $|B_{||}|$ for different values of θ. When $|B_{||}|$ is considerably smaller than $B_c(\theta)$, T_1 is limited to 5 μs. Close to $B_c(\theta)$, the T_1 values reduce sharply, comparable to the situation in Figure 5.4. Using the previously determined angle dependence of B_c and the quasi-particle limit of Equation (5.7) explains the sharp decrease. If the same data is instead plotted as a function of f_{01} [Figure 6.5(b)] the data for different θ lie on top of each other. This confirms the hypothesis that the closing of the induced superconducting gap is the reason for the sharp decrease in T_1.

6.3.2 Partially covered wires

In Chapter 5 we have identified the thick and fully covering Al shell of the nanowires to be a limiting factor for the field compatibility of the nanowire transmons. A possible solution to this limitation is using nanowires that have an Al shell that is thinner and does not cover the full wire. The first step to confirming this hypothesis is to show that transmons made with these wires perform well in zero-field conditions. The measurement results presented from here on are obtained with nanowires that have a $\sim$ 130 nm thick InAs core of which two facets are covered with a 7 nm thick, epitaxially grown Al shell. Although the Al shell is not covering the wire fully it still induces a hard superconducting gap, as measured in transport.

In Figure 6.6, the workability of a gatemon with a nanowire that has a 7 nm Al shell covering only two facets at $B_{||} = 0$ mT is demonstrated. Its f_{01} changes by $\sim$ 1 GHz when V_G is changed by 0.3 V, demonstrating that side-gate tunability is still working fine. Note that there are comparatively more jumps in f_{01} than for the full-shell wire device. This might originate from the exposure of larger parts of the InAs core to air. Due to these jumps a reliable extraction of the voltage noise experienced by the qubit is not possible as a polynomial interpolation of the only small jump-free segments of f_{01} versus V_G leads is error-prone. Irrespective of that, T_1 reaches $\sim$ 10 μs, and at V_G sweet spots T_2^{Echo} reaches 5 μs. Further investigations of the factors limiting T_1 or T_2^{Echo} were not performed. The goal of this experiment was primarily to confirm that these partially covered yield transmons with high coherence times.

The induced superconducting gap persists up to higher $|B_{||}|$ values in transport measurements than what we observe to be the maximal field at which the qubits presented here are still operational. Out of curiosity, the field is aligned with the nanowire axis and increased.

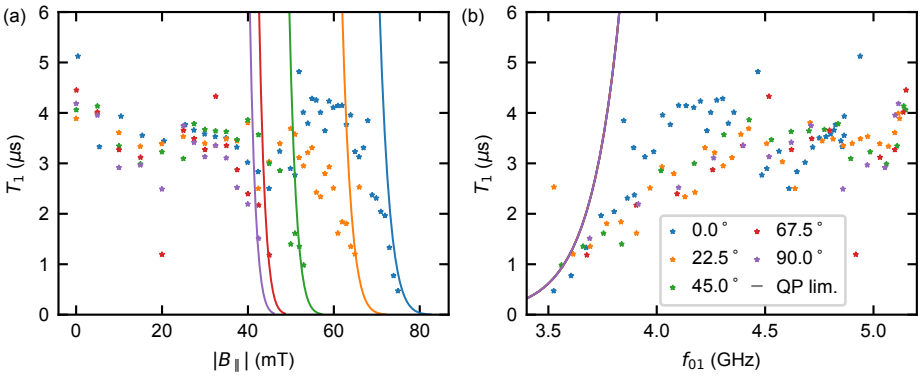

Figure 6.5: T_1 versus $|B_{||}|$ and field angle for the same full-shell qubit as Figures 6.3 and 6.4. The T_1 (symbols) are limited to $\sim$ 5 μs until the induced superconducting gap starts to close (curves). (a) For different alignment angles, this happens at different $B_{||}$. (b) Same data plotted as a function of frequency. Data and limits of different θ coincide.

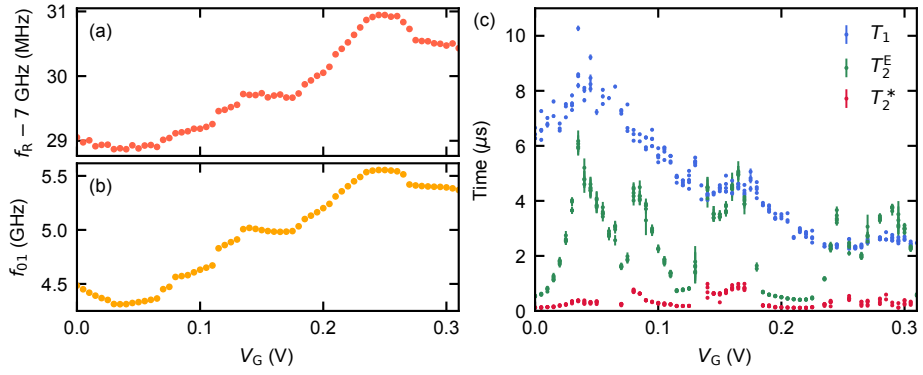

Figure 6.6: Characterization of a gatemon with an Al shell that covers only two facets, $B_{||} = 0$ mT. (a, b) Measured values of f_R and f_{01} respectively as a function of V_G. Several frequency jumps can be observed. (c) At each V_G point, T_1 (blue), T_2^{Echo} (green) and $T_2^\star$ (red) are measured. The observed values of T_1 close to 10 μs indicate that the induced gap is still hard, although the Al coverage is not full anymore.

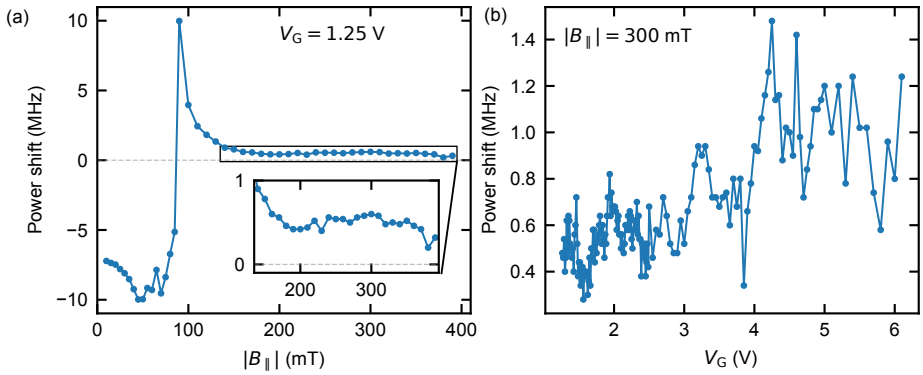

Figure 6.7: Indication of remnant Josephson energy in fields $|B_{||}| \geq 300$ mT for a gatemon. (a) Resonator power shift versus $|B_{||}|$ ($B_{||}$ in nanowire-direction). The powers shift changes sign as f_{01} crosses f_R. Inset is a zoom-in of the data for $|B_{||}| \geq 165$ mT, showing it is small, but non-vanishing. (b) The power shift changes as a function of V_G, indicating that the remnant Josephson energy is still gate tunable.

Because the qubit f_{01} is not visible any more for $|B_{||}| > 100$ mT, we measure the power shift χ of the resonator (Figure 6.7). A finite χ indicates the presence of a non-linear element. As f_{01} crosses the resonator, χ changes sign. Interestingly, although f_{01} is not resolvable any more, the power shift is still clearly resolvable. Note that for all other qubits-resonator pairs (where $B_{||}$ is now not aligned with the wire) $\chi = 0$ MHz, indicating that none of these qubits work any more. To confirm that the observed power shift is indeed due to a remnant E_J, χ is measured as a function of V_G [Figure 6.7(b)]. It reveals changes comparable to the ones observed in f_{01} when V_G is swept. However, attempts to find a well-defined f_{01} line remained unsuccessful.

6.4 Flux control in the in-plane magnetic field

In Chapter 5 a series of challenges for flux control in an applied $B_{||}$ have been identified. In this section we will discuss how the proposed improvements are implemented and what their effect is. Then, we will outline the procedure required for aligning the field with the nanowire of split-junction devices. The flux-control of a split junction device is demonstrated by measuring its spectrum at 70 mT. The time-domain characterization of the device under test shows that flux noise is not the dominant decoherence mechanism. The high level of background radiation limits both T_1 and coherence of the qubits. By addressing this problem with additional shielding, T_1 values of ~ 10 μs are restored.

6.4.1 Technical improvements

In order to suppress interfering magnetic fields from other sources, the use of passive magnetic shielding is desirable. The ramping of vector magnets in adjacent cryostats can lead to

small, but detectable variations of flux through the SQUID loops of the split-junction devices, changing their f_{01}. A passive magnetic shield surrounding the sample diverts the lines of interfering fields and mitigates this problem. However, a requirement of the setup is to be still able to apply a magnetic field to the sample. A passive magnetic shield in vicinity to the sample is therefore not possible, as it would prevent also the intended $B_{||}$ to be applied. Further on, if the saturation field of the shielding material is surpassed, the shield will become magnetized and unusable. These seemingly contradicting requirements can be fulfilled by the use of a double-layer shield that is mounted around the whole cryostat [Appendix A, Figure A.3(a)]. The outer layer of the shield is made of μ-metal, a nickel-iron alloy with high relative magnetic permeability of $\sim 4.7 \cdot 10^5$ [218]. This layer provides a strong magnetic shielding factor for the enclosed area, including the sample. The inner layer is made of pure iron, which has a high saturation field but only a modest shielding factor. Its role is to protect the μ-metal layer from getting magnetized by the solenoid that sources $B_{||}$. The total magnetic shielding factor at the sample position is ~ 80, according to magnetostatic simulations performed by the manufacturer. In order to assess the effect of the magnetic shield, measurements of the same device in the same cooldown were taken. Where f_{01} would significantly change over the course of minutes when no shield was used, it was stable once the shield was mounted (data not shown). In order to minimize the residual field at which the film turns superconducting [131, 171, 219, 220] it is mounted before cooling down the cryostat.

The next technical improvements implemented address the changes in f_{01} due to the vibrations generated by the pulsed tube of the cryostat (Chapter 5). As the sample holder and the solenoid sourcing $B_{||}$ are not rigidly mounted together, vibrations of the cryostat can lead to a changing positions of the SQUID loop. Field inhomogeneity leads to a change in flux through the SQUID loop, clearly observable in two-tone spectroscopy measurements (Figure 5.13). By using a more rigid sample holder (Appendix A), an attempt was made to reduce this noise. If the sample holder is more rigid, the relative movement between sample and solenoid is suppressed, leading to smaller change in flux through the SQUID loop. This measure alone did not eliminate the problem, as determined by the measurements performed. Therefore, it was necessary to also reduce the sensitivity to this noise. As the flux is given by $\Phi = B_{\perp} \cdot A$, reducing the area A of the SQUID loop reduces the sensitivity to changes in $B_{\perp}$. We chose to reduce A from 400 μm^2 to $\sim$ 10 μm^2, hence reducing the sensitivity to flux noise by a factor of 40. This comes at the price that it is now not possible anymore to flux-bias the split-junction devices with a flux-bias line. However, the coil sourcing the $B_{\perp}$ compensation field can be used for this. The problem of vibrations blurring f_{01} could not be observed anymore after implementing these two measures.

In order to prevent any higher-frequency noise affecting the performance of split-junction devices, persistent current solenoids are used (Appendix A). Such noise can originate from current noise in the solenoid current supplies. The use of persistent current solenoids is standard in many applications that require high fields, such as MRI or quantum dot systems [202]. Next to the connection to the power supply, the solenoid leads are connected to each other by superconducting leads through a switch [Figure 6.8(a)]. If the switch is closed it is superconducting, and a persistent current will flow through the solenoid via the switch. This generates

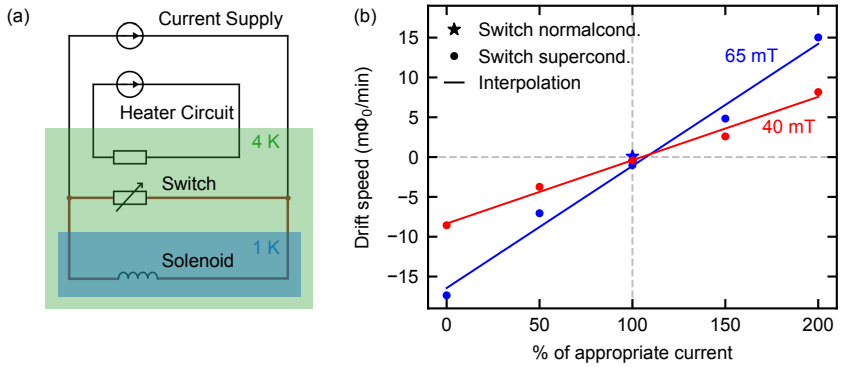

Figure 6.8: Persistent current solenoid characterization. (a) Schematic of the setup. Brown leads indicate superconducting wires. A heater determines the state of the switch. If the switch is superconducting, a persistent current can flow. The switch needs to be normal conducting to change the current in the solenoid. (b) Drift speed of flux-tunable split-junction devices due to the persistent current decay as a function of supplied current (see text for details). Applying a current $\sim 5\%$ above the nominal value when the switch is superconducting counters the drift.

6

a very stable magnetic field. However, the current through the solenoid cannot be changed, as the current supply is also shorted via the switch and the formed superconducting loop opposes any change in flux. This means that the noise of the current supply does not translate to a noise in the generated field. If the switch is open (which is done by turning the switch normal by heating it), the current in the solenoid can be changed. Ramping the field therefore needs to happen with an open (heated) persistent current switch.

In reality, the persistent current in the solenoid is not quite persistent, but decays slowly over time. We estimate the time constant by monitoring the voltage across the solenoid when interrupting the persistent current after it was in persistent current mode for roughly a day. With the solenoid inductance of $L = 0.7$ H it is possible to calculate the current difference and therefore the decay time constant of $\sim$ 4 years. This corresponds to an effective series resistance of 5.8 nΩ, in agreement with reports from other persistent current magnet setups [221]. The decay can be attributed to a small series resistance, for example, non-perfectly superconducting solder joints. An alternative explanation is that the vibrations cause the sourced field to induce Eddy currents in nearby metals, leading to dissipation.

The small decay in persistent current leads to a noticeable drift in f_{01} of split-junction qubits [Figure 6.8(b)]. It can be quantified by monitoring the $B_{||}$ value of a flux sweetspot over time (or more precisely, f_{01} at a flux-sensitive point). The decay speed of the persistent current depends on what current is still supplied by the current source [221]. We find that applying a current that is roughly 5% larger than the nominal value required for sourcing a field counters the persistent current decay. Hence, when measurements in a persistent field are performed, the solenoid is powered up to the required field value while the switch is open.

Then, the switch is closed and a persistent current flows. Finally, the current supply is tuned to supply a 5% higher current to counter any decay.

6.4.2 Measurements of the spectrum

Combining these improvements gives the setup a sufficient field stability and low enough noise to control flux-tunable split-junction devices in an applied $B_{||}$. The flux noise is suppressed using a more rigid sample holder and by operating the solenoids in a persistent current mode, and the sensitivity to it is reduced by the use of smaller SQUID loops. The field stability is ensured by the passive magnetic shield and compensating for the decay of the persistent current. Thus, we now turn to the characterization of flux-tunable split junction devices in $B_{||}$. First, we need to find θ such that the field is aligned with the nanowire axis [Figure 6.9(a, b)]. Its approximate value can be guessed by extracting the angle of the nanowire with respect to the field axes from optical pictures. The fine tuning of this angle is performed at $|B_{||}| = 60$ mT in order to get a clear frequency change. Due to imperfect alignment, all changes in $B_{||}$ lead to changes in $B_{\perp}$. This means that at each $B_{||}$, the qubit flux sweetspot needs to be determined again by changing $B_{\perp}$. Its frequency, $f_{01,\max}$, is determined by interpolating $f_{01}(B_{\perp})$ with a second-order polynomial. This procedure is repeated at a fixed $|B_{||}|$ for different θ and the resulting $f_{01,\max}(\theta)$ are interpolated with a second-order polynomial to extract the angle of optimal alignment.

Next, $B_{||}$ is increased along the angle of optimal alignment, and the dependence of $f_{01,\max}$ on $B_{||}$ is studied [Figure 6.9(c, d)]. The same procedure as before is used, where at each value of $|B_{||}|$, $f_{01,\max}$ is determined by interpolating $f_{01}(B_{\perp})$. The resulting spectrum of $f_{01,\max}(|B_{||}|)$ shows that the field compatibility of the device is substantially higher than what was found for the full-shell devices (Chapter 5). This proves that the hypothesis of the thick and fully covering Al shell indeed was a limitation to the field compatibility of the transmons. Interpreting this spectrum, however, proves to be more challenging. The previously used toy-model of the closing of the induced superconducting gap [Equation (5.1)] does not yield qualitative agreement. Also an explanation where the junction area is reduced due to flux penetration, yielding a Fraunhofer pattern, does not explain the observed $f_{01,\max}(|B_{||}|)$. The Little-Parks effect cannot explain this either because the nanowire is no longer covered by a full Al shell. Further effects that can play a role are the change in the momentum operator due to a non-zero vector potential and multi-mode interference [207]. This is, however, strongly dependent on geometry and disorder and requires simulations that are beyond the scope of this work.

In comparable works, a similar effect was observed [222]. There, a gatemon was subjected to fields of up to 1 T. The gatemon frequency shows a lobe structure, and has minima around $B_{\min,1} \sim 0.225$ T and $B_{\min,2} \sim 0.675$ T. The data is interpreted that at these points an odd number of half-integer multiples of Φ_0 thread the cross-section of the nanowire, leading to interference effects that suppress the induced gap. As the current density in the nanowire is concentrated at its surface, the geometry forms effectively a superconducting cylinder in a magnetic field. The field induces a supercurrent and enforces an integer number of flux quanta through the cylinder. Close to half-integer multiples of a flux quantum, the

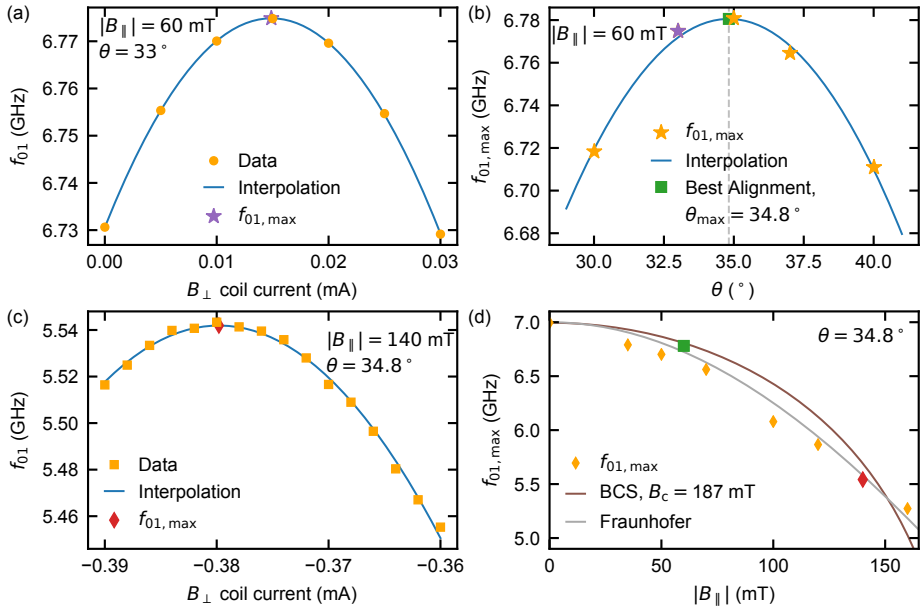

Figure 6.9: $B_{||}$-alignment procedure and field compatibility of a flux-tunable split-junction device. (a) At a fixed $B_{||}$, f_{01} is measured as a function of $B_\perp$, and the sweet spot frequency $f_{01,\max}$ is extracted using a quadratic fit. (b) This procedure is repeated for several angles of $B_{||}$ while keeping $|B_{||}|$ constant. A quadratic fit to the resulting $f_{01,\max}$ yields the optimal alignment angle. (c) To determine the field dependence of the qubit, $f_{01,\max}$ needs to be determined at each value of $|B_{||}|$ similar to (a). (d) $B_{||}$ dependence of $f_{01,\max}$. None of the models discussed in the text yield a good agreement. A possible explanation for this could be multi-mode scattering.

superconductivity in the cylinder is suppressed as it can not support a large enough supercurrent though its core. The calculated effective diameter of the interference loop, given as $d_{\text{eff}} = \sqrt{2\Phi_0/\pi B_{\min,1}} \approx 76$ nm, is smaller than the nanowire diameter of ~ 100 nm. This is expected as the current density must be within the nanowire. These findings agree with simulations [223] and recent observations in full-shell nanowires [224, 225] and could also explain the $B_{||}$ behavior of the devices presented here.

To demonstrate the control of the flux-tunable split-junction devices in $B_{||}$, we measure the spectrum of one such device at 70 mT (Figure 6.10). For this, the sample device as in Figure 6.9 is used. As observed in well-shielded environments at zero field, the device behaves transmon-like near the flux sweetspot. Around the full-frustration point, the spectrum rather resembles one of a flux qubit. The transitions f_{02} and f_{03} are visible in direct spectroscopy around the full-frustration point. Note that there is a splitting of the lines due to the reduced suppression of the charge dispersion for higher levels [62]. Switching of the background charges leads to shifts in the resonator frequency due to the finite coupling between

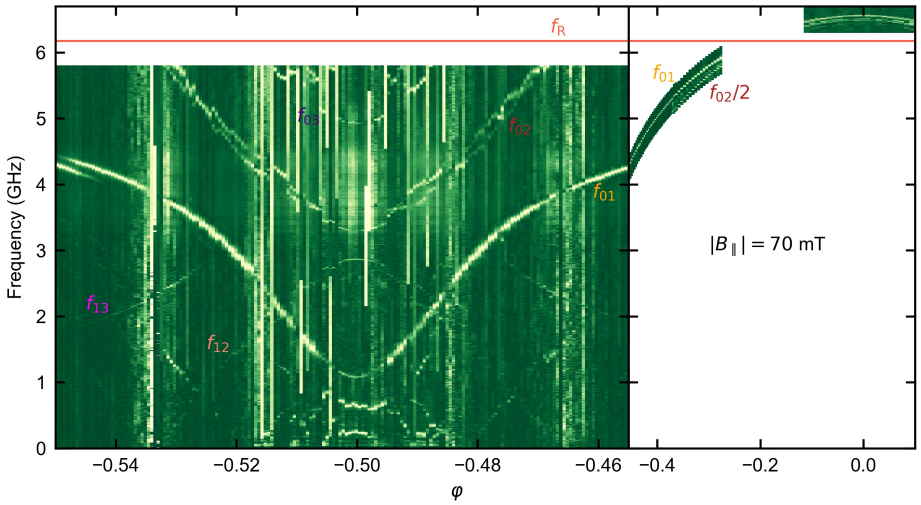

Figure 6.10: Demonstration of flux tuning in a split-junction device in $B_{||} = 70$ mT, aligned with the nanowire. Left part of the figure is a zoom-in around the full-frustration point. The f_{01} transition is well-defined, but the reduced supperssion of the charge dispersion for f_{02} and f_{03} make these lines less visible. The data quality is deteriorated where transitions cross the readout resonator.

higher levels and the resonator in these devices. This in turn leads to a deterioration of the data quality at these flux values. In order to fit this spectrum, the model of Equation (2.16) would need to be adjusted such that it is also valid in $B_{||}$ [226]. It is, however, questionable how much insight could be gained from this, therefore the presented data should rather be taken as a proof of the high level of stability in the flux-sensitive measurements in $B_{||}$. The origin of the avoided crossing in f_{01} at $\varphi = -0.545$ is not known. This dataset took ~ 16 hours to acquire, which demonstrates the high flux-stability of the setup even at 70 mT.

6.4.3 Time-domain characterizations

After demonstrating flux control in an applied $B_{||}$, we now turn to demonstrating that also time-domain measurements can be performed. A magnetic field of $|B_{||}| = 50$ mT is applied along the nanowire axis of a split-junction qubit similar to the one presented in Figures 6.9 and 6.10. Figure 6.11(a) shows its time-domain characteristics and f_{01} as a function of reduced flux. Similar to the data shown in Figure 6.5, the energy relaxation and dephasing times are comparatively short here. This could be observed for all the six working qubits showing measurable T_1 on the chip.

Not known at the time the data was taken, these times were limited by a photon background of elevated temperature. Against expectations, T_1 does not increase with f_{01} but rather seems to be increasing with applied flux. A possible explanation is that the change in $B_\perp$ that is used to tune the flux though the SQUID loop also has an effect on the vortex

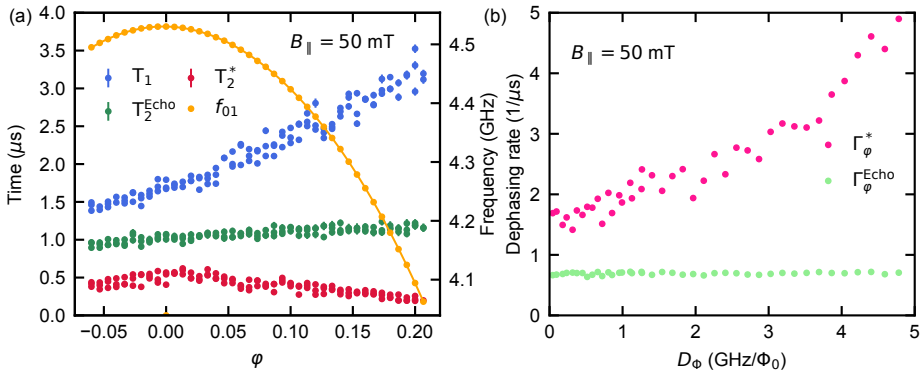

Figure 6.11: Time-domain characteristics of a flux-tunable split-junction qubit in $B_{||} = 50\,\mathrm{mT}$. (a) T_1, T_2^{Echo} and $T_2^\star$ as a function of reduced flux. f_{01} (right axis) is interpolated to extract the flux sensitivity. (b) Echo and Ramsey dephasing rates versus flux sensitivity.

distribution in the qubit. A reduction the number of vortices would lead to a mitigation of their contribution to the qubit energy relaxation rate [131, 157]. Interestingly, the T_2^{Echo} data does not seem to show a strong dependence on φ. Due to its small values and the photon background of elevated temperature that is dominating contribution, no conclusions on a potential reduction in flux noise (Chapter 1) are drawn. The large discrepancy between $\Gamma_\varphi^{\mathrm{Echo}}$ and Γ_φ^* [Figure 6.11(b)] indicates that low-frequency contributions are dominating the flux-noise spectrum. A potential source of low-frequency flux noise are the changes in $B_\perp$ induced by vibrations of the setup due to the pulsed tube.

The priority after acquiring this dataset was therefore finding and fixing the source of high loss and dephasing such that higher-quality data can be taken. For this reason, a more detailed study of flux noise versus applied field was not yet performed. As the short T_1 could be observed for all the qubits on the chip (and also previously cooled down devices in that setup configuration did not show better T_1), off-chip sources were suspected to be the reason for the high loss. The residual excited-state population, which can be extracted from single-shot readout measurements [227, 228], is consistently measured to be around $\sim$ 20% on this chip during this cooldown [Figure 6.12(a)]. We suspect that the reduced quality of radiation shielding is responsible for this. Due to the shape of the two-axis solenoid used in the experiments presented, the radiation shielding of the 50 mK stage of the cryostat is compromised. The solenoid, thermalized at the 1 K stage, protrudes into the shield can that should ensure a 50 mK photon environment. The radiation shielding of the sample is therefore exposed to a black-body photon background of temperature $\sim$ 1 K, corresponding to a peak in photon energy at $\sim$ 60 GHz, leading to the observed high residual population.

This problem is addressed by a improving the shielding of the setup further (Appendix A). A copper radiation shield encloses the two-axis solenoid, thermalized to the 50 mK stage, is installed (Figure A.7). To increase the photon absorption efficiency, its inside is spray-painted with Aeroglaze Z306 [229]. Cooling down a new device with the new shielding conditions

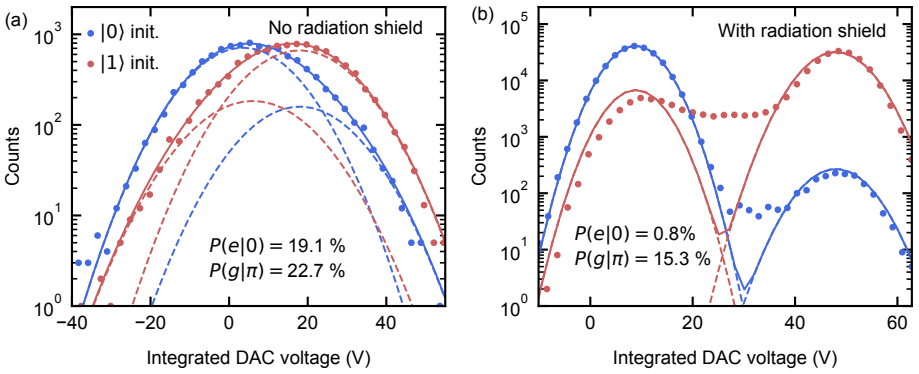

Figure 6.12: Measured residual populations for two different setup configurations. After preparation in $|1\rangle$ (red) [$|0\rangle$ (blue)], the qubit is measured and the integrated readout voltage is binned. The resulting histograms are fitted with a sum of two Gaussians. Their relative amplitude indicates the residual state population. (a) The 2-axis solenoid at 1 K protruded into the 50 mK radiation shield, leading to a high residual excited state populations of $\sim 20\%$ on all the qubits on the chip. (b) A further radiation shield solves this problem and brings the residual excitation to below 1%.

yields a residual excited state population of $< 1\%$ [Figure 6.12(b)], comparable to standard cQED setups [150, 230]. Note that for both measurements shown in Figure 6.12 the measurement time (1 μs) was a significant fraction of T_1, and therefore relaxation during the measurement leads to counts between the two main Gaussian distributions.

The high temperature of the radiation background was not only responsible for the high level of residual excited state populations, but also for the poor time-domain characteristics. With the radiation shield in place, the time-domain characteristics of the device from Figure 6.12(b) are measured. With T_1 and T_2^{Echo} being ~ 10 μs, we conclude that the additional radiation shield solved the before observed problem of short T_1 and T_2^{Echo}. Unfortunately, this qubit was the only qubit on the chip that showed good T_1 and T_2^{Echo}. It is not

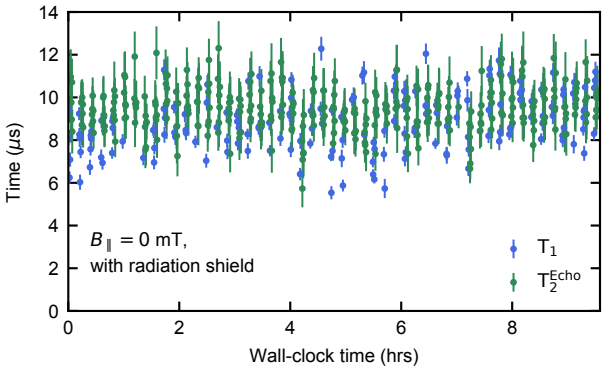

Figure 6.13: Repeated time-domain characterization experiments of an untunable nanowire transmon at $B_{||} = 0$ mT. The installation of the radiation shield restores the typical energy relaxation and coherence times.

flux-tunable, although it is a split-junction device. A possible reason for this might be that the carrier density in the junctions is depleted and therefore no transport through the wire is possible (the junction is pinched off). Although it is not possible to perform flux-sensitive measurements with this chip, it shows that all the individual components required to perform flux-sensitive measurements in an applied $B_{||}$ work.

6.5 Conclusion

This chapter described how the problems that arise when performing flux-sensitive measurements in a magnetic field can be overcome. The field compatibility of the superconducting NbTiN film is enhanced by reducing its thickness to 70 nm, clearly below its magnetic penetration depth [104, 146, 205, 206]. A potential improper alignment of the in-plane magnetic field $B_{||}$ is mitigated by fabricating holes into the resonators and transmon capacitor islands [131, 146, 174, 203]. In order to cancel the misalignment, a coil that sources a perpendicular magnetic field $B_{\perp}$ is installed. The residual $B_{\perp}$ is minimized by adjusting it such that f_R is maximized for increasing values of $B_{||}$. The use of NbTiN airbridges eliminates the need for on-chip Al wirebonds that lead to loss in fields above 10 mT. Implementing these measures allowed us to observe coplanar waveguide resonators that showed $Q_i > 10^5$ in $B_{||}$ up to 250 mT.

The use of InAs nanowires that have a thinner, only partially covering, epitaxially grown Al shell further increases the maximal field at which these qubits can be observed [194–196]. Their time-domain characteristics are comparable to the one of transmons that employ nanowires with a fully covering Al shell, as demonstrated by measurements performed at $B_{||} = 0$ mT. A two-axis solenoid is installed such that $B_{||}$ can be aligned collinear to the nanowire axis of a given qubit which maximizes its field compatibility. It is, however, unclear what the limiting factor for the field compatibility of these transmons is.

In order to be able to measure flux-tunable split-junction devices in an applied $B_{||}$, a series of technical improvements was made. First, the use of an external, passive magnetic shield provides a more stable field environment and protects the sample from interference while still allowing to apply strong magnetic fields. The noise in the magnetic field, as observed by the qubits, is reduced by a more sturdy sample holder, reducing the relative vibrations between sample and solenoid. Further on, the use of persistent current solenoids mitigates noise originating from the current sources. The small but finite decay of persistent current in the solenoids needs to be compensated in order to counter any drift in magnetic field. The sensitivity of the qubits towards flux noise is reduced by choosing a smaller SQUID loop, meaning that they need to be tuned with the coil supplying $B_{\perp}$. In this setting, it was possible to perform spectroscopy and time-domain measurements of flux-tunable qubits. However, due to the photonic radiation background at elevated temperature, the time-domain characteristics of the qubits were poor. After the installation of an additional radiation shield, T_1 and T_2^{Echo} are again around 10 μs.

Although final proof that high coherence in flux-tunable split-junction qubits in applied in-plane magnetic fields is possible remains to be delivered, all the components necessary to

do so are demonstrated to be working. Unfortunately, current issues in fabrication that lead to a poor yield in working transmons inhibited us from showing that. In the current state of the setup, resonators with high $Q_i > 10^5$ at $B_{||} = 250$ mT, and transmons with T_1 and T_2^{Echo} of ~ 10 μs are working. $B_{||}$ has been shown to have a low enough noise and a high enough stability to allow for time-domain experiments of split-junction qubits at fields of 70 mT. Therefore, I do not expect any further major complications once a next fabrication round produces a generation of working split-junction devices.

In my opinion, it is probably fair to say that combining superconductors with large magnetic fields and nanowires is not straightforward. It is an environment that is rich in physics. This is as much an advantage of the system under consideration as it is a disadvantage. With the clear goal of demonstrating flux-tunable split-junction devices in mind, we rather tried to get rid of such effects than study them in detail. This reflects in the fact that the focus of this chapter is rather on achieving high coherence times in nanowire transmons in a magnetic field than exactly understanding what, for example, the field dependence of their frequency is. Now that a substantial amount of engineering is done and the desired stability of the measurement setup is achieved, it will be possible to investigate how flux noise reacts to a magnetic field. The stable CQED setup can also be used for different purposes, for example to obtain insights into how SNS junctions behave in an applied magnetic field with a high precision.

7 CONCLUSION AND OUTLOOK

7.1 Conclusion

This section summarizes the experimental results and findings of this thesis. I started working on the project when the first papers on the subject were published. The work here in Delft [37] aimed at demonstrating voltage- and flux-tunable devices, and understanding their physics. A key promise of the architecture was the compatibility with magnetic fields, as the superconductors used as well as the nanowires were independently shown to be resilient towards magnetic fields [69, 231]. In this previous work, coherence of the presented devices could not yet be directly observed. In a paralleling approach in Copenhagen [38], comparable devices were demonstrated. The key difference was the use of nanowires with an epitaxially grown aluminum shell [83, 153]. This enabled demonstration of coherence in the devices, and voltage-controlled z-gates could be performed. The combination of these two approaches therefore promised transmon qubits that show coherence in an applied magnetic field.

Chapter 3 describes the fabrication of nanowire transmons. The device fabrication combines the standard circuit quantum electrodynamics processes with nanowire etching and contacting recipes. Crucially, the nanowires we use have an epitaxially grown aluminum shell that induces a hard superconducting gap. As the reliability of the device fabrication fluctuates, optimizations of the turn-around time of the design-fabrication-measurement cycle are made. For example, an image recognition software analyzes optical images to automatically generate etch- and contacting masks. Until now, device yield is not unity, and it is not understood why – it appears that there is a hidden parameter we do not control. A possible explanation are surface adsorbants on the nanowire that lead to a positive pinch-off voltage.

In Chapter 4, we benchmark nanowire transmons in a well-shielded environment free of magnetic fields, and investigate their limitations [158]. The combination of InAs nanowires that have an epitaxially grown Al shell with the cQED geometry and fabrication recipes of our group yields state-of-the-art devices. We extract the flux noise of flux-tunable split-junction devices. We find it to have a noise spectrum with a $1/f$ noise amplitude that is on the high side of the typically observed spectrum, as well as a white noise contribution [35]. As voltage tuning the Josephson energy was not yet a standard procedure in our group, special care was taken to quantify the observed voltage noise. By comparing decoherence rate predictions based on consciously injected voltage noise with measured decoherence rates, we could show that the weakly coupled $1/f$ voltage noise comes from on-chip sources. Additional to the weakly coupled voltage noise, also strongly coupled charge-sensitive two-level systems are observed. They cause the qubit frequency to switch between two values. Ramsey-based frequency state detection schemes reveal the switching rates to be on the order of $10\ \mathrm{s}^{-1}$. This type of noise, the direct coupling of charge two-level systems to the Josephson energy, was here evidenced for the first time.

In Chapter 5, we subjected these same devices to an in-plane magnetic field. The resonators, although not optimized for field compatibility, yielded sufficient performance in magnetic fields up to $\sim 150\ \mathrm{mT}$. The qubit frequencies monotonically decreased with magnetic field, following the trend of a closing superconducting gap. Energy relaxation and coherence times of gatemons could be measured up to $70\ \mathrm{mT}$. This constitutes the first demonstra-

tion of superconducting qubits operating in magnetic fields higher than the bulk gap of aluminum. Above the respective critical field of the qubits, the induced superconducting gap was too weak and quasiparticle poisoning strongly enhanced their energy relaxation rates. From these initial measurements in a magnetic field, several ways of improving the field compatibility of the sample and the stability of the setup were identified.

Chapter 6 addresses the issues with setup and samples identified in Chapter 5 that limited the field compatibility of the devices. We started using a thinner superconducting film and airbridges made of NbTiN. The installation of a coil to compensate for residual perpendicular magnetic fields and the addition of holes to avoid vortex formation in resonators and qubit capacitors allowed us to further increase the field compatibility of the bulk circuit quantum electrodynamics elements. Combined, these measures allowed us to operate resonators with intrinsic quality factors of $> 10^5$ in fields of 250 mT. By using nanowires that have a thinner Al shell, which does not cover all facets of the InAs core, the field up to which working qubits can be observed was enhanced to 140 mT. Important for this was the alignment of the magnetic field with the nanowire axis. To enable in-situ alignment, a vector magnet was installed. Flux control of split-junction devices was demonstrated in magnetic fields exceeding 100 mT. A more rigid cold finger, persistent current mode of the solenoids and an external magnetic shield reduced the noise in the magnetic field as seen by the qubits. Further on, the sensitivity of the split-junction devices to noise was decreased by reducing the area of their SQUID loop. Together, these measures enabled us to measure time-domain characteristics of flux-tunable split-junction devices in a magnetic field of 70 mT. Unfortunately, the performance of the qubits was limited by a high temperature radiation background. Improving the shielding of the sample eliminated this problem: energy relaxation and echo dephasing times of $\sim 10\ \mu$s were restored. So far, device fabrication issues kept us from definitely delivering the final proof that all components work smoothly together.

I expect that with a new round of devices it will be possible to control flux-tunable split-junction devices with high coherence in an in-plane magnetic field. The fabrication and setup optimizations for field-compatibility ensure that the bulk circuit quantum electrodynamics components are not a limiting factor. The setup has been shown to provide a stable enough magnetic field, and in-field flux-tuning of the split-junction devices has been demonstrated. With the new radiation shield in place, the previously evident high coherence times of the samples could be restored. Therefore, there is nothing in the way preventing detailed investigations of flux noise in a magnetic field as described in Chapter 1.

7.2 Looking into the future

7.2.1 Flux-noise in a magnetic field

Let us now discuss the intended experiments that should shed light on the microscopic origin of flux noise. A first step is determining the amplitude of the $1/f$ flux noise at 1 Hz as a function of magnetic field and temperature. This can be done by measuring the (echo) dephasing rates as a function of flux sensitivity of the qubit (Sections 4.2.2 and 4.3.2), and repeating this procedure for various fields and temperatures. At a field of 70 mT, even at a bath tem-

perature of 100 mK, the dephasing rate is reduced by a factor of ~ 1.5 in comparison to 0 mT (Figure 1.2). This signature is clearly discernible by time-domain measurements. Note that flux-insensitive gatemon qubits on the same chip can be used to verify that a change in decoherence of split-junction devices is indeed related to a change in flux noise. The saturation of the temperature dependence yields information about the effective temperature of the bath of two-level systems causing the flux noise. Further on, the magnetic field dependence will give information about the effective g factor.

In addition to a reduction in the noise background, also a direct observation of the electron spin resonance or hyperfine transition should be possible. If the qubits can be tuned on resonance with any of these transitions, their dephasing rates will enhance substantially. This has been observed for resonators in electron spin resonance experiments as a function of field [27, 232]. Also flux qubits that have frequencies that can be tuned down to 1 GHz observed an increased energy loss at the frequency of the hydrogen hyperfine splitting [18], although this experiment was performed only in a zero-field environment. Note that for transmons, as opposed to flux qubits, no increase in the energy relaxation rate is expected as there is no transversal coupling to flux. By measuring the frequency dependence of the transmon dephasing rate at various magnetic fields, we could therefore explore the spectrum of ensembles creating flux noise. Adapting the geometry used in Ref. [18], it would also be possible to explore that spectrum by monitoring the energy relaxation rate.

An indirect way of observing the hyperfine and electron spin resonance transitions can be chosen if the tunability of the qubits is not sufficient to bring it on resonance with these transitions. By shining a strong microwave tone of variable frequency on the sample, the ensembles held responsible for flux noise can be driven. Therefore, if a split-junction qubit is parked on a flux-sensitive spot, its dephasing rate should increase when a transition is driven. Away from the transition, the drive will not have an effect on the qubit dephasing rate. Monitoring the qubit coherence as a function of the frequency of a drive tone of the bath will therefore also reveal the spectrum of the ensemble.

A combination of these methods should allow us to further our understanding of the microscopic origin of flux noise. Ideally, the experiment is repeated for different surface treatments of the sample. One example of such a treatment is outlined in Ref. [28] where it is ensured that Lewis base-site defects are occupied with non-magnetic species promises to reduce flux noise coming from adsorbed oxygen. This process should also reduce the visibility of the electron spin resonance line of the adsorbed oxygen. An annealing step before the cooldown has shown to free the sample surface of physisorbed atomic hydrogen [27, 232]. Directly showing that such a procedure reduces the observed flux noise and rids the sample of an observable absorption peak at the hyperfine frequency would be a clear indication that indeed physisorbed hydrogen is partly responsible for flux noise. Further surface treatments could include illumination of the sample with UV light to promote photodesorbtion of magnetic species [28]. With an understanding of the origin of flux noise, more targeted fabrication precautions can be taken to eliminate it. This will have a large impact in the circuit quantum electrodynamics community as currently flux noise is one of the limiting factors for

two-qubit gates [148, 233]. The performance of two-qubit gates will in turn greatly impact the performance of surface codes [47] and quantum simulations [234–236].

7.2.2 The future of SNS transmons

The Josephson element of transmon qubits can be impelmented in various ways. Clearly, the most prominent one to date is the SIS tunnel junction [77]. Further demonstrations so far have been delivered with atomic break junctions [237], semiconducting nanowires [37–39, 101, 158], graphene [213, 214] and two-dimensional electron gases [175]. It is conceivable that selective-area-growth methods [238] and other two-dimensional structures [239] can be used to implement comparable junctions.

Because SIS tunnel junctions are promising candidates for small- or medium-scale quantum computing, the question arises whether implementations with different junctions also might be of use for comparable applications. Before potential contestants become viable alternatives, reliability and fabrication control of their junctions needs to be increased. Without fast (room-temperature) indicators and deterministic tuning of these qubits, larger circuits will require an impractical amount of manual tuning. Even if a targeted engineering of voltage sweetspots would be possible, fluctuating two-level systems that are strongly coupled to the Josephson energy of the devices lead to a reduction of their coherence time. The efficient fabrication of high-quality structures is a further challenge. Transferring materials onto the quantum chip to form the junction (nanowires, graphene) is error prone and intense in manual labor. It is also unclear whether the lossy substrates that can be used to directly define the junctions (2DEG, selective-area-growth methods) will yield high-coherence CQED elements if they are directly fabricated on top of it. If these challenges proof to be too hard to be overcome, I do not think that this technology will have applications in quantum computing. Nonetheless, it still can be used to perform various experiments and to investigate junctions fabricated from novel materials [239].

However, if these fabrication challenges can be overcome, interesting possibilities open up. So far, there has not been any indication of voltage crosstalk between different gatemons. This will ease the tune-up of a chip, as no crosstalk matrix needs to be inverted in order to apply a bias targeted to a single qubit whilst leaving the others untouched. Also the simultaneously applying two-qubit gates would require less finetuning [240]. Because the gate voltage can be provided using the same control line as the microwave pulses, a reduction in the number of control lines by a factor of almost two compared to schemes relying on flux-tunable qubits can be achieved [47]. Reducing the number of control lines required per qubit will be a major task in realizing medium- and large-scale quantum computers [241].

Further on, a reliable fabrication of SNS junctions that exhibit quantized conductance [41–43] would greatly ease the qubit control. In Figure 7.1(a), we simulate the dependence of the transmission values on the applied gate voltage. Upon increase of V_G, more and more transmission channels become fully transmitting. Once fully transmitting, their transmission value stays constant at 1. The resulting gatemon spectrum [Figure 7.1(b)] exhibits plateaus in f_{01}, making the gatemon insensitive to noise in V_G. This is will increase their coherence, as noise in V_G is a limiting factor (Chapter 4). Further on, this enables semi-digital voltage

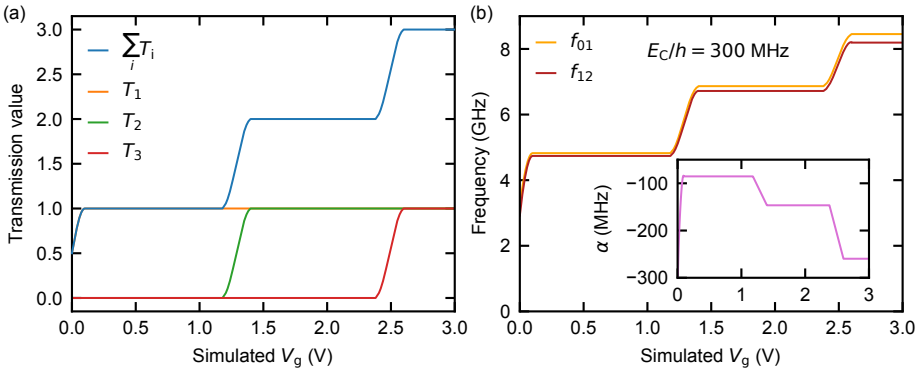

Figure 7.1: Simulated gatemon with with quantized transmission channels. (a) As the applied gate voltage increases, subsequently more transmission channels contribute to the transport through the junction. Once activated, the transmission channels stay at unity transmission. (b) Qubit frequencies corresponding to the transmission values in (a). Semi-digital voltage z-gates or even two-qubit gates can be implemented because of the insensitivity of the qubit frequency to the applied gate voltage. Inset: computed anharmonicity α as a function of V_G.

gates that are insensitive to small errors in $V_G(t)$ (though errors in timing will still influence the gate performance). These gates can take the form of single-qubit z-gates or two-qubit gates [38, 39]. Note that whereas two-qubit gates based on flux-coupling typically have one of the qubits reside in a spot where it is sensitive to flux noise (and hence has a higher decoherence rate) [242, 243], this would not be the case for such voltage gates. This might enable higher two-qubit gate fidelities.

Further on, tunable resonators can be engineered with voltage controlled nanowires [40]. Tunable resonators can be of great help to implement on-demand coupling between qubits, potentially reducing frequency-crowding problems [244–246]. Especially if the nanowire can be fully depleted of charge carriers, completely suppressing transport through it, high on-off ratios of the coupling can be achieved. This would reduce the problem of spurious couplings between qubits [240].

7.2.3 SNS qubits as charge-parity detectors in a magnetic field

For experiments and applications that require an in-plane magnetic field, qubits based on SNS junctions are promising candidates. As demonstrated in this thesis, they remain coherent when a magnetic field is applied. Further experiments in Copenhagen and Delft have shown that such qubits can withstand magnetic fields of 1 T [222]. Several schemes for topological quantum computation rely on the conversion of the quantum state to a charge for readout [55–57]. Because transmons can act as good charge-parity detectors, SNS transmons are natural choice for this task.

One way of performing charge-parity checks is to use a Ramsey-based detection scheme (Section 4.4) [59, 113]. The charge state shifts the frequency of the qubit, and the two frequen-

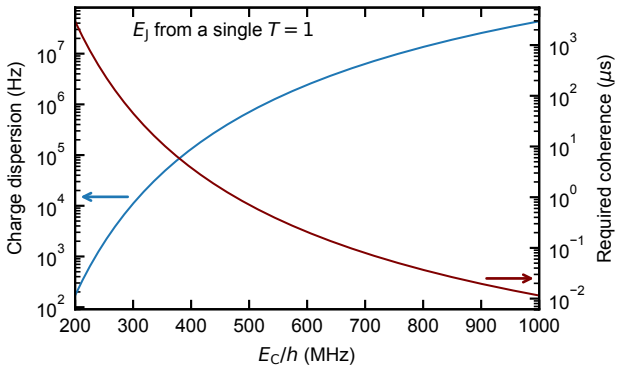

Figure 7.2: Because the charge dispersion of a SNS transmon with a single, fully transmitting channel increases when E_C is increased (blue), the coherence required to perform a Ramsey-based charge-parity detection decreases (brown, right axis).

cies differ by Δf (charge dispersion). This difference is determined by the choice of E_C (Figure 2.7) [62]. To obtain maximum contrast in a Ramsey-based sate detection scheme, the waiting time τ_w has to be chosen $\tau_w = 1/2\Delta f$. The coherence of the qubit therefore needs to be $T_2^\star > 1/2\Delta f$ in order for this scheme to work. In Figure 7.2 we assume an SNS transmon with a single, fully transmitting channel and variable E_C. The E_C of the transmon therefore needs to be chosen such that the obtainable coherence (limited by other sources) on the operating point is larger than the required coherence. Figure 7.2 shows that a Ramsey-based charge-parity readout is feasible with current coherence times if E_C is chosen appropriately.

7.2.4 Alternative junctions for field-compatible transmons

The bulk circuit quantum electrodynamics structures described in this work have been shown to be able withstand an applied in-plane magnetic field. The InAs nanowires used are one way of ensuring the field compatibility of the junction. Next to this property, they also exhibit rich and interesting physics. For experiments where the qubits are only supposed to be field compatible, and the nanowire properties of the junction are not essential, different junctions could be used. One option are graphene-based van der Waals heterostructures that are voltage tunable and withstand magnetic fields [247–249]. Several circuit quantum electrodynamics experiments with graphene junctions have been performed, showing field compatibility and temporal coherence [213, 214, 250].

A further option for field-compatible junctions are thin-film aluminum-based SIS Josephson junctions. These junctions have successfully been used as spectrometers and on-chip microwave sources in magnetic fields of several 100 mT [100, 191, 251, 252]. If the out-of-plane magnetic field component is canceled, their superconducting gap follows the trend of Equation (5.1) with a B_c up to 1180 mT [191]. Therefore, the use of thin-film aluminum SIS junctions might enable the fabrication of field-compatible SIS transmons.

7.2.5 Signatures of Majorana zero modes

Further on, signatures of Majorana zero modes are predicted to appear directly in the spectrum of adequately engineered transmons [253]. The nanowire that constitutes the Joseph-

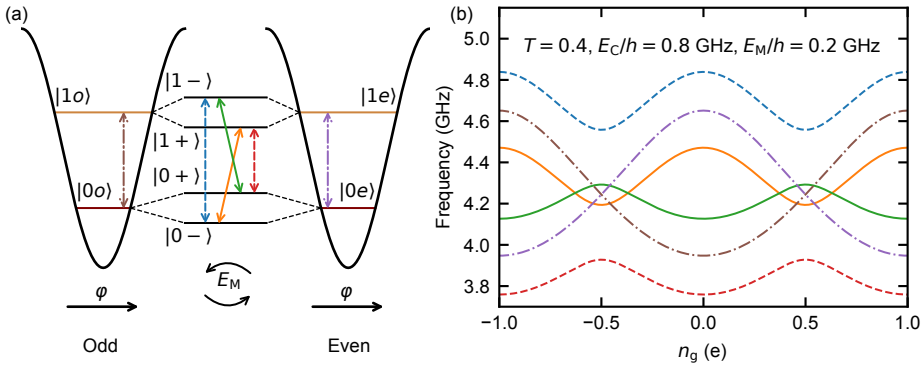

Figure 7.3: Working principle of a 'Majorana transmon' [253]. (a) Energy potential of the two charge parities of a transmon (black). In the absence of a Majorana coupling ($E_M/h = 0$), the charge parity conserving microwave transitions between $|0, o/e\rangle$ and $|1, o/e\rangle$ (dash-dotted) are allowed. For $E_M/h > 0$, the two charge parity manifolds are coupled, leading to hybridized states $|0/1, o/e\rangle$. Charge parity conserving (dashed) and non-conserving coherent transitions (solid) are allowed between these states. (b) Spectrum of a nanowire transmon. For $E_M/h = 0$, the spectrum is $2e$ periodic (Figure 2.7). For $E_M/h > 0$, the spectrum is $1e$ periodic.

7

son junction of the so-called 'Majorana transmon' (MT) operates in the topological regime. The presence of the Majorana modes essentially couples the different charge parity manifolds (denoted with $|o, e\rangle$) with coupling energy E_M [Figure 7.3(a)]. This leads to a hybridization of the $|0, o\rangle$ and $|0, e\rangle$ ($|1, o\rangle$ and $|1, e\rangle$) states, lifting their degeneracy. Where the charge parity is conserved in the more standard version of the transmon (it can change because of quasiparticle tunneling, but not coherently), coherent transitions between the two charge parity manifolds are allowed in the MT. The Hamiltonian of the MT is given as

$$\hat{H} = E_C(\hat{n} - n_g)^2 - E_J(\hat{\delta}) - E_M i\gamma_2\gamma_3 \cos(\hat{\delta}/2), \tag{7.1}$$

with the parity $i\gamma_2\gamma_3$ of the local fermion at the junction. Note that Equation (7.1) is written in the $1e$ basis. For further information on this Hamiltonian, the reader is kindly referred to the relevant literature [51, 52, 253, 254]. Written in the $1e$ basis, the Hamiltonian of Equation (7.1) can be diagonalized to obtain the energy levels, similar to Section 2.3.1.

The transitions between the hybridized levels leave a signature in the spectrum of the MT [Figure 7.3(b)]. For the presented simulations, the Josephson energy is assumed to be provided by a single transmission channel with transmission $T = 0.4$ and $E_C/h = 0.8$ GHz. In the case of $E_M/h = 0$ (dash-dotted transitions), the spectrum is $2e$ periodic, and the two charge parity manifolds do not mix. For $E_M/h = 0.2$ GHz, the charge manifolds hybridize and form non-degenerate states with transitions between them. Some of these transitions are still charge parity conserving (dashed), while others change the parity (solid). In this case, a $1e$ periodicity emerges. These transitions can be driven using microwaves, and can

be observed in the spectrum of the MT. If the coupling is large enough, they will leave a clear signature [Figure 7.3(b)].

A MT could in principle be fabricated with the methods described in Chapter 3. In order to observe the signatures of Majorana zero modes that appear in the spectrum of the device, an island of the transmon needs to be gate tunable. The addition of a voltage gate to one of the transmon islands is straightforward [113]. Groups both in Copenhagen and in Delft are investigating this system [222]. The use of InSb instead of InAs wires might be beneficial, as this relaxes the requirements on the applied magnetic field [42, 43, 196, 211]. The assessment whether a regime with $E_M/h = 0.2$ GHz can experimentally be achieved is beyond the scope of this work. Recent works, however, indicate that a $E_M/h \sim$ GHz is feasible [255].

7.2.6 Coupling to spin qubits

The coupling of different quantum systems promises to combine their advantages. A combined system would, for example, allow to have a part for fast computations and a 'quantum hard drive' to store quantum information for a longer time until it is needed again for further computations [65]. Transmons are good candidates to perform fast computations. Due to their large dipole moment, they can easily be coupled to microwave cavities. The challenge is therefore largely in coupling the second quantum system of interest strongly (with a coupling strength exceeding the decay rates of the coupling cavity and the quantum system) to the same microwave cavity. This can be achieved considerably easier for ensembles than for individual emitters, as the ensemble coupling strength increases with $\sqrt{N}$, where N is the number of emitters. Accordingly, the coupling of a transmon to an spin-ensemble of NV centers in diamond [68, 256, 257] as well as to magnons (collective spins) in ferromagnets [258, 259] has been demonstrated.

The coupling between different engineerable solid state systems is of great interest, as it is more straight-forward to implement these on one chip. Appealing platforms for this are charge quantum dots and spin qubits [75, 76, 260]. Using high-impedance resonators, the strong coupling of a microwave cavity to charge double quantum dots was demonstrated [261, 262]. The high impedance of the resonator results in larger voltage amplitudes, thereby increasing the coupling to the quantum dots. Subsequently, also the coupling of a transmon to a double quantum dot via a high-impedance resonator was realized [73].

More desirable than coupling to GaAs-based charge qubits is the coupling to spin qubits in silicon where long coherence times have been demonstrated [263–266]. In recent experiments [72, 267], also the strong coupling of such qubits to high-impedance resonators was demonstrated. However, as the frequency of the spin qubit is given by the Zeeman splitting, a magnetic field of $\sim$ 100 mT is necessary to operate these qubits in the GHz frequency regime. In order to realize an experiment comparable to the one described in Ref. [73], transmons that can withstand such a field are required. Gatemons are a natural choice, as they are also mostly insensitive to noise in the external field. Further on, they are compatible with the fabrication steps of the spin qubits in Ref. [72], and readily couple to the high-impedance resonators in that work.

An experiment comparable to the one of Ref. [73] can therefore readily be implemented. The dephasing rate of spin qubits in [72] is $\gamma_s/2\pi = 2.5$ MHz and the resonator linewidth is $\kappa/2\pi = 5.4$ MHz. Because the spin-photon coupling is $g_s/2\pi = 13$ MHz, the strong coupling condition $g_s > \kappa,\ \gamma_s$ is achieved. A resonator Q_i on that substrate of $\sim 10^5$ is feasible (personal communication with N. Samkharadze). This would limit the transmon T_1 to ~ 4 μs at 4 GHz (Equation (5.9)), putting a lower limit on $\gamma_{tr}/2\pi > 0.125$ MHz. As the coupling between the microwave resonator and a transmon can easily reach $g_{tr}/2\pi = 50$ MHz [Figure 4.1(d)], also the transmon-cavity system will be in the strong coupling limit. A direct coupling mediated via virtual photons can then be achieved by tuning the transmon and the spin qubit on resonance, away from the cavity. The effective coherent interaction strength between the two systems is then given as $2J \sim g_{tr}g_s/(1/|\Delta_{tr}|+1/|\Delta_s|)$, where Δ_{tr}, Δ_s are the respective detunings from the resonator, and can exceed the linewidth of the coupled system [268, 269]. This experiment would therefore demonstrate the coupling of a fast quantum processor to a potentially long-lived quantum memory.

APPENDIX A: EXPERIMENTAL SETUP

This appendix presents the experimental setup. This includes the microwave setup for qubit control and readout as well as the dc biasing of the qubits. It is also describes the shielding of the sample, and the installation of the solenoids sourcing the magnetic fields.

A.1 CQED measurement setup

In this section various aspects of the measurement setup are discussed. We start with the control electronics necessary to perform cQED measurements. The generation of appropriate microwave signals, the read-out, and dc biasing of qubits is discussed.

A.1.1 Microwave setup

Microwave tones for qubit control and readout are generated, modulated and combined at room temperature (Figure A.1). For transmission measurements of the sample, the frequency of a single microwave source is swept. Like this, the resonance frequency and quality factors of resonators can be determined. For qubit spectroscopy measurements [114], the frequency of the readout tone is kept fixed at the frequency of a resonator. The frequency of an additional microwave source is swept. When it hits the qubit frequency, the qubit is brought into a mixed state. This leads to a shift in the resonator frequency, and therefore a different transmission value. If pulses are to be applied, the arbitrary waveform generator (AWG) generates a DRAG pulse [112], consisting of the sum of a Gaussian and its derivative. The pulse is up-converted to the qubit frequency using an IQ mixer. If necessary, it can be further amplified with a power amplifier. Typically, the generated pulse is frequency modulated to avoid mixer leakage at the qubit frequency. All these signals are combined using microwave splitters. In order to filter out unwanted higher-frequency noise, an 8 GHz reflective low-pass filter is used. A notch-filter at the resonator frequency can reduce the number of spurious photons in the readout resonator. For easy diagnostics, a part of the signal is routed to a spectrum analyzer using a directional coupler.

The combined signals are routed into the fridge where they undergo attenuation at the 4 K and mixing chamber (MC) stages. This attenuation reduces the (thermal) noise floor that is generated by the electronics. A homemade weakly absorptive eccosorb filter further reduces the unwanted IR background. It is sandwiched in-between two attenuators to suppress standing waves.

A.1.2 Read-out line

In the experiments presented in this work, single-shot readout assignment fidelities exceeding 75% are not required. Therefore, the choice was made to abstain from quantum-limited amplification [270–272] of the readout signals to reduce setup complexity. The first readout stage is therefore a low-noise high-electron-mobility-transistor (HEMT) amplifier that provides 40 dB gain at 4 K. In order not to suffer from the 4 K noise the amplifier sends towards the sample, the signal is passed through two cryogenic circulators with an isolation of $\sim$ 20 dB each. To avoid unnecessary losses in the readout line, superconducting coaxial cables are used to route the signal from the MC plate to the HEMT. From the HEMT to room temperature, silver-plated copper-nickel (inner), stainless steel (outer) coaxial cables are used as they too have lower losses than all-stainless-steel coaxial cables.

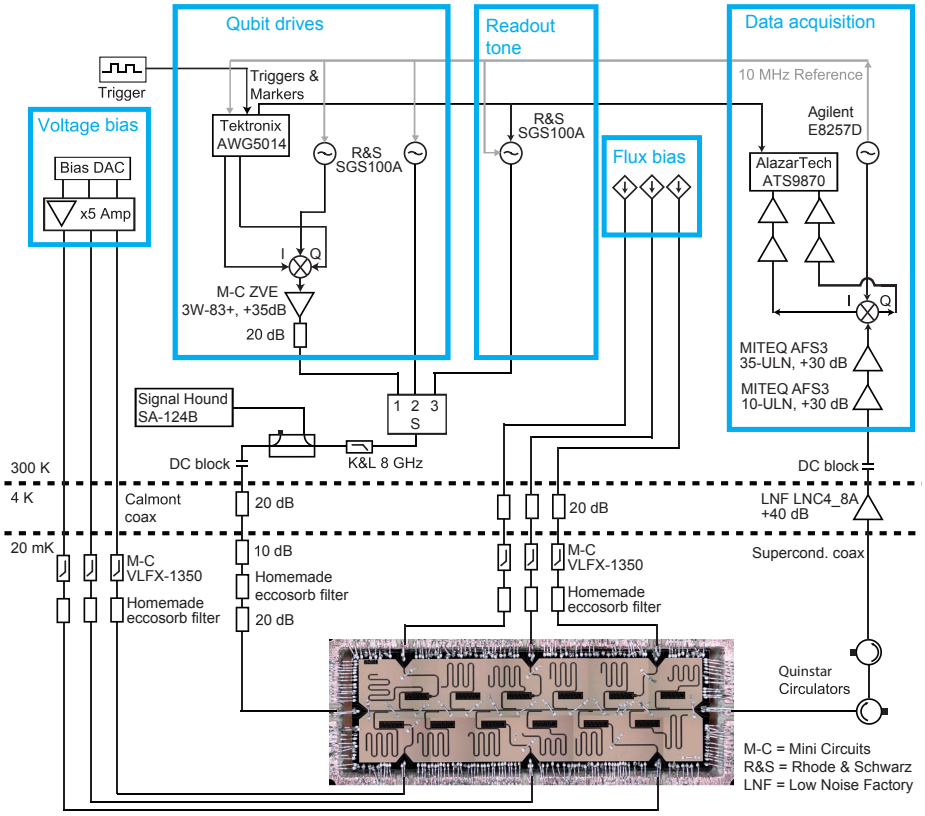

Figure A.1: Optical micrograph of the cQED chip and schematic of the experiment showing microwave and dc connectivity in- and outside the dilution refrigerator. Silver features crossing the feedline and bias lines are on-chip wire bonds. In later versions of the experiment they are replaced with airbridges.

At room temperature, the signal is further amplified by $\sim$ 60 dB using Miteq amplifiers. An IQ mixer multiplies the signal with a local oscillator detuned typically 25 MHz with respect to the readout signal. The resulting I and Q quadratures of the signal, now modulated with the detuning frequency, are then further amplified and digitized. The digitized signal can be processed digitally.

A.1.3 dc-Biasing

The dc current for flux biasing the split-junction devices using flux-bias lines (Section 4.3) is provided by home-built low-noise current sources mounted in a TU Delft IVVI-DAC2 rack. The currents are brought to the mixing chamber (MC) plate of the fridge using semi-rigid stainless steel coaxial cables. A first stage of filtering happens at the 4 K plate where the currents are attenuated by 20 dB. The voltage to bias the gatemons is provided by DACs of the IVVI rack, which are amplified with a 5 V/V battery-driven amplifier. The lines leading the voltage to

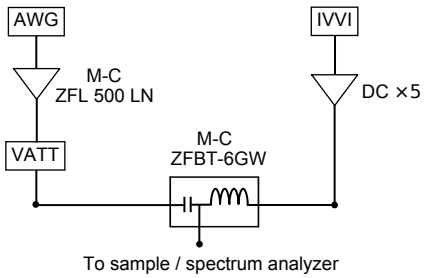

Figure A.2: Schematic of the circuit used in Section 4.2.3 to inject a controlled amount of voltage noise at various dc voltage bias points. The zero-output of an AWG is amplified and subsequently attenuated using a variable attenuator (VATT). The generated noise is then combined using a bias tee with the dc signal and sent to the sample or a spectrum analyzer.

the MC plate are Calmont coaxial cables with a cut-off frequency of 100 MHz. Both the flux- and voltage lines are further low-pass filtered at the MC plate. A LC reflective filter and an absorptive homemade eccosorb filter on each line ensure low noise characteristics.

A.1.4 Controlled noise injection

The procedure described to calculate the dephasing limit in Section 4.2.3 is verified on a gatemon, where additional V_G noise is injected to be the dominating dephasing contribution [Figure 4.5(a)]. Noise is generated by amplifying the 0-output of a Tektronix AWG 5014 with a Mini-Circuits ZFL 500 LN amplifier. Its amplitude is controlled by a Weinschel Aeroflex 8320 variable attenuator (VATT). The noise is injected to the DC biasing circuit using a Mini-Circuits ZFBT-6GW bias tee (Figure A.2). The noise PSDs for the VATT at 60 dB attenuation (no added noise) and at 20 dB (added noise dominates) are measured with a SRS SR770 FFT network analyzer in the range $1 - 10^5$ Hz. The range between 10^5 and 10^9 Hz is measured with a Rigol DSA 815 spectrum analyzer [Figure 4.5(a)]. The PSDs are measured after the bias tee, and the transfer function correction of the Calmont coaxial line (Figure A.1) is applied to the measured spectra. Note that the noise level measured for the VATT at 60 dB is not discernible from the spectrum analyzer background. Hence, the data shown in Figure 4.5(a) only gives an upper limit to the noise floor.

A.1.5 Control software

In oder to automate experiments and facilitate efficient data processing, a potent software platform is imperative [273]. In our lab, a home-made python-based software packet called PycQED is used for this purpose [274]. It enables control of the measurement hardware and automatically logs all the instrument settings. It manages the data acquisition and automatically generates basic plots of the measurement results. Additionally, also more involved data processing and fitting can be performed in this framework.

A.2 The low-temperature environment

The experiments discussed in this thesis are performed in a Leiden Cryogenics CF-450 dilution refrigerator that provides a base temperature of $\sim$ 20 mK [Figure A.3(a)]. This is

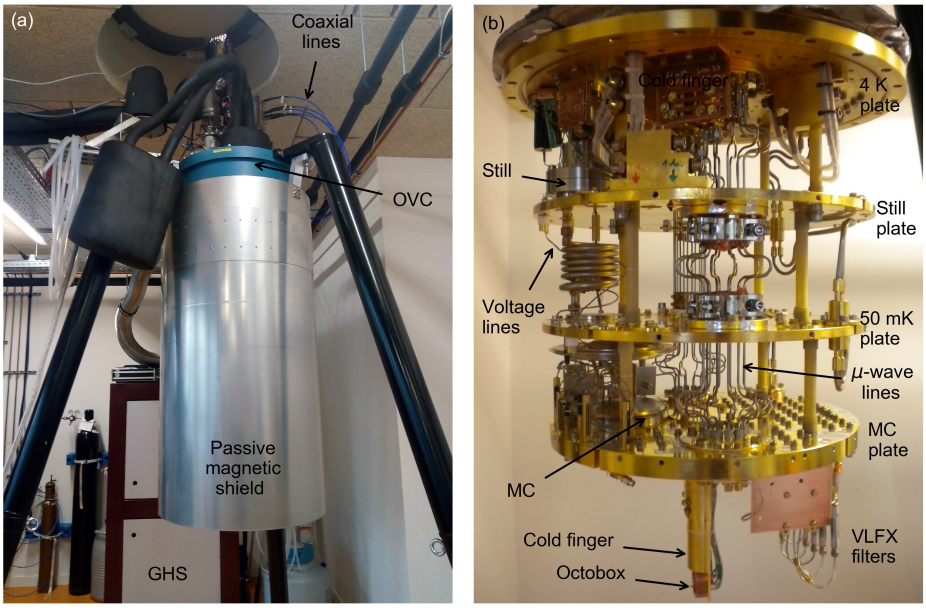

Figure A.3: Photographs of the dilution refrigerator. (a) During operation, the passive magnetic shield is mounted around the outer vacuum chamber (OVC). Microwave, flux and voltage signals are brought into the cryostat via break-outs on the top. The gas handling system (GHS) can be seen in the background. (b) The low-temperature stages with the cryostat shields removed. Lower plates are subsequently colder. Microwave and flux signals are brought to the octobox that is mounted on the cold finger via semi-rigid coaxial cables. Voltage signals are applied via flexible coaxial lines. Also visible are the mixing chamber (MC) and the still, crucial parts of the ^{3}He/^{4}He cooling circuit.

A

achieved by providing a 4 K environment using a pulsed tube, and a further cooling circuit based on the ^{3}He/^{4}He phase separation [275]. To ensure a low noise background, radiation and magnetic shielding is required. As low-temperature magnetic shielding is not a viable option in the present experiments (Section 6.4), an external magnetic shield is used [Figure A.3(a)]. Low radiation backgrounds are achieved by enclosing colder temperature stages in light-tight shields. A radiation shield is mounted at every temperature stage (except for the MC stage).

Figure A.3(b) shows a photograph of the inside of the dilution refrigerator. The 4 K temperature stage is directly cooled with a pulsed tube, the lower temperature stages are additionally cooled with the ^{3}He/^{4}He cooling circuit. Microwave and flux signals are brought to the sample via semi-rigid stainless steel coaxial lines. For voltage signals, flexible Calmont coaxial cables are used.

Let us now discuss the shielding of the sample in more detail. The sample is glued into a recess of a printed circuit board (PCB, Figure A.4). The electrical connections between sample and the microwave strip lines on the PCB are made by aluminum wire bonds. Likewise,

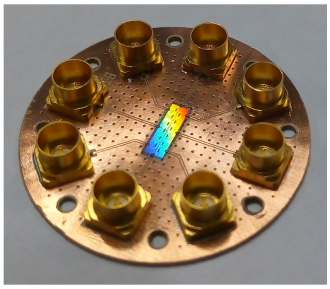

Figure A.4: Photograph of a sample mounted in a printed circuit board (PCB), originally designed in the Schoelkopf group at Yale. Control signals are brought to the PCB via eight SMP connectors. Microwave strip lines route the signals on the PCB to the sample. The hole pattern in the ground plane lets the sample appear in rainbow colors. Sample dimensions are 2×7 mm.

good electrical grounding is ensured by wire bonds that connect the ground of the PCB with the sample ground. The SMP solder connectors allow to connect the strip lines on the PCB with the microwave lines that lead to room temperature. The PCB is covered with a copper shim to minimize packaging slot modes. This packet is then mounted inside another copper box, the so-called octobox [Figure A.3(b)]. The octobox is bolted against the cold finger and itself again packaged inside a light-tight copper radiation shield (sample radiation shield, not shown). The inside of the sample radiation shield is coated with a mixture of Stycast and silicon carbide for increased infrared shielding [134].

A.3 The solenoid setup

During the course of this work, magnetic fields were applied in various ways to the sample. Here we discuss the setups used to apply single-axis and vector fields.

A.3.1 Single-axis solenoid

Initial experiments in a magnetic field were performed using only a single-axis solenoid (Chapter 5). The solenoid is made of NbTi wires that turn superconducting at ~ 10 K. It can provide a magnetic filed up to 2 T. The design of the fridge is such that mounting the solenoid on the 4 K plate is not favorable. This would be desirable for safety reasons – a quench of the magnet would not directly evaporate the helium mixture. Instead, the solenoid is mounted in the radiation shield of the still stage (~ 800 mK, Figure A.5). To make room for the solenoid,

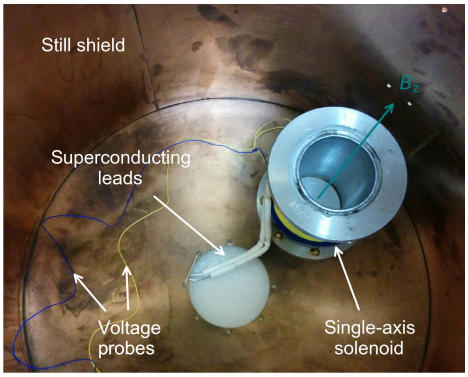

Figure A.5: Photograph of a single axis solenoid mounted on the radiation shield of the still stage. The cold finger that hosts the sample protrudes into the solenoid bore when the solenoid is mounted. Superconducting leads connect to persistent current switches (not visible) that allow operation of the solenoid in persistent current mode. Wires allow direct probing of the charging voltage of the magnet.

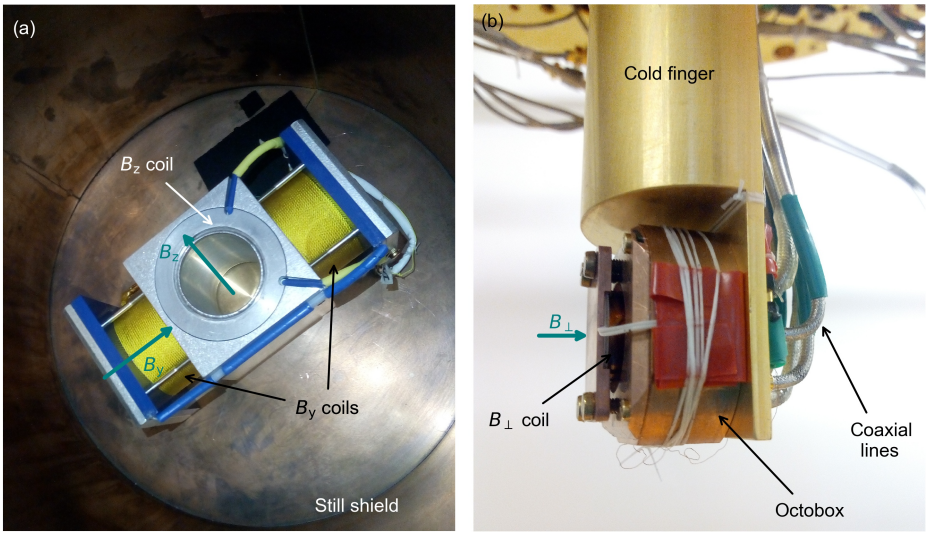

Figure A.6: Photographs of the magnet setup. (a) The two-axis solenoid that is used to source $B_{||}$ is directly mounted on the still shield. Superconducting leads connect to the persistent current switches mounted on the 4 K plate (not shown). (b) The cold finger ensures a good thermal connection and low vibrations between the MC plate and the octobox. Coaxial lines bring control signals into the octobox where the sample resides. A small coil that is mounted on the octobox sources $B_\perp$. An additional light-tight radiation shield is mounted directly to the cold finger (not shown). When mounted, this assembly protrudes into the bore of the B_z coil.

the 50 mK shield needs to have a cut-out. This compromises its shielding properties. The elevated temperature of the radiation background makes the above mentioned sample radiation shield around the cold finger necessary. When the solenoid is mounted, the cold finger assembly with the sample radiation shield protrudes into the bore of the solenoid.

A.3.2 Vector-field solenoid

Now we discuss how the vector magnetic field described in Chapter 6 is sourced. The in-plane vector magnetic filed $B_{||}$ is provided by a two-axis solenoid [Figure A.6(a)]. The solenoid is again directly bolted onto the radiation shield that is connected to the still plate of the cryostat. The strong (z) solenoid axis has a bore into which the cold finger assembly protrudes. The weaker (y) axis consists of two solenoids around the z-axis solenoid. Both axis can be operated in persistent current mode (Section 6.4). The required persistent current switches (not shown) are mounted on the 4 K plate, as the cooling power available on the still plate is insufficient. However, the solenoids need to have a superconducting connection to the persistent current switches [Figure 6.8(a)]. This poses an inconvenience when opening the cryostat, as it requires dismounting the persistent current switches.

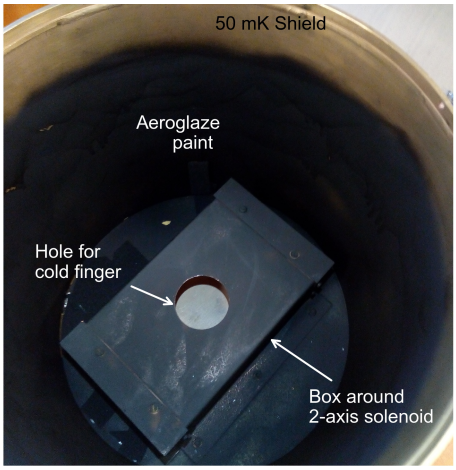

Figure A.7: Photograph of the radiation shield that is thermalized at the 50 mK plate. The bottom of the shield is cut open to allow space for the 2-axis solenoid [Figure A.6(a)]. To ensure good radiation shielding, an additional copper box is bolted against the shield to cover the 2-axis solenoid. The inside of the shield is painted black using Aeroglaze to minimize the radiation background.

The out-of-plane field $B_\perp$ is provided by a small superconducting coil that is mounted directly on the backside of the octobox [Figure A.6(b)]. It allows compensation of misalignment errors of the setup and can be used to flux-tune split-junction devices with a small SQUID loop (Section 6.4). It is not possible to operate this coil in persistent current mode, which poses a limitation to the setup. Also, due to non-uniformity, the magnitude of the sourced field varies by $\sim 10\%$ over the sample area (data not shown). It might therefore be desirable to use a three-axis persistent current solenoid in the future.

A.4 50 mK radiation shield

Like the single-axis solenoid, the two-axis solenoid protrudes into the volume of the 50 mK shield, requiring it to have a cut-out that compromises its shielding performance. However, the two-axis solenoid is considerably bigger, deteriorating the situation even further. This led to the situation that the sample radiation shield was no longer sufficient to ensure a low temperature of the background radiation (Section 6.4.3). This problem could be fixed by bolting a copper box onto the 50 mK shield that extends over the two-axis solenoid. To further lower the temperature of the radiation background, the inside of the shield is spray-painted with Aeroglaze (Figure A.7). These combined measures resulted in a low radiation background as measured by residual qubit excitation (Section 6.4.3).

ACKNOWLEDGEMENTS

It goes without saying that all what you have just read in this thesis would not have been possible without the help of many. So I would like to take this opportunity to express my deepest gratitude to all who have contributed in one way or another: friends, colleagues and family – what would I be without your care, support and encouragement?

My interest in quantum computing was sparked in a lecture of Andreas Wallraff when I was still in Zürich. When it became time to look around for a possible PhD position, I quickly realized that the Quantum Transport group here in Delft offered everything I was looking for. The group spirit and openness I've experienced even on my intake interview, combined with the passionately performed high-quality research, made my decision to come here straightforward. The following years only strengthened this impression. I would like to thank the **leadership of QuTech**. Tripling the size of the institute while keeping the team spirit intact is not an easy task, but you managed to do that to large parts. None of us take the luxurious situation in which we are – inspiring people, access to world-class facilities and instrumentation, fantastic support – for granted. As the icing on the cake, there are regular fun activities such as sports days, uitjes and BBQs. Many thanks to everyone who has contributed to realize such a unique environment.

I would like to thank the **members of the committee** for careful evaluation of my thesis. I hope it can spark your interest. I would be thrilled if that also held true for the readership expanding further than the committee. **Attila**, thank you also for being on the committees of all my master students.

Leo, first of all thank you for taking me as your PhD student. These four years in Delft were a invaluable experience, and I learned a great deal in many ways. During this time, you were clearly one of the persons with the most influence on me, and I hope I didn't stretch your patience too much. Next to all the physics, you have taught me many lessons about persistence, thoroughness and life in general (and probably infected me with your labeling fetish). You know that I did not enjoy every moment of working with you – but I certainly do not regret my decision to do a PhD in your group. It was very comforting to know that you always had my back. I highly appreciated the fact that from a certain point on I was to large parts free to make the decisions in my project, and that you gave me the opportunity to go to so many schools and conferences. Thank you for making me grow as a person and as a scientist.

I would like to thank the master students that have been part of the nanowire team. It was fun and inspiring to work together, and I have learned a lot from all of you. **Thijs**, I am glad you decided to do your master end project with me, and then later also returned to pursue a PhD on this project. We make a great team, and working together with you was always a pleasure. I am honored that you are my paranymph. I am glad to know that the future of this project

is in good hands with you – I'm sure you're going to find joy and success. All the best to you and **Lucia**! **Oscar**, I have always admired your efficiency and organizational skills. It was great fun working together with you, and we achieved a lot. It is a pity that the Digimon chip ended up on your shelf instead of in a fridge – none the less we advanced our understanding of the system significantly. I wish you and **Michelle** all the best for the future, and hope that you can enjoy many more trips all around the world together. **Joep**, you are the person of choice when it comes to making holes into everything and anything. Your friendly, curious and precise way was a great addition to the team. I'm sure you will be equally enthusiastic about shooting interesting experiments to space as you are about football! **Elmore**, you are the latest addition to the nanowire team. Having witnessed your smarts, I'm sure you're going to find interesting results together with Thijs. I'm looking forward to learning about the findings of the two of you.

When I was just starting here, our group was considerably smaller than what it is now. As a beginning PhD student, the active and fun environment was just what I was looking for. **Chris**, as the senior PhD student you had the role of my bigger brother. You showed me the ways and arts of our trade, and you became a good friend; but please, don't step on my kapsalon any more. I still admire your cleverness that you know to apply in so many situations. Thank you for all the music evenings at your place, and thank you for making me your paranymp. I'm glad that you found an interesting position in Germany, welcome to the 'weird qubit team'! I'm sure you and **Jasmin** will be happy together in Köln. **Nathan**, both your creativity and your love to detail have inspired me. You were always there to help me out, even when closing the fridge took until dawn. I have learned a great deal from you in all aspects of scientific work, but also real-life topics. I will never forget our discussions (and your strategy of winning arguments by attrition), and wish you and your family all the best. **Alessandro**, you make me question the boarder between creativity and craziness. Thank you for educating me in the arts of the cleanroom, and showing me so many useful tricks. Everyone can learn from your intuition. Good luck with your family! Also you, **Stefano**, contributed to the dynamic environment of our group with your sharp comments and nice sense of humor. Thank you very much for guiding me around at Rigetti, and that I could stay at your place. I hope you and your family enjoy sunny California.

Of course I would also like to thank all the current members of the group, and hope that we can keep in touch even when I'm on the other side of the big puddle. Although we usually worked on different projects, the unique spirit of the group is something I will never forget. **Niels**, it was great fun to do measurements together in the aquarium, the quality of your day usually seems strongly correlated with whether or not you can come up with a good pun. The code you write is not always easy to read out, but you are happy to help with any sort of problem. Thank you for guiding us through so many group meetings, your structured ways clearly reduced their entropy. I'm glad you asked me to correct the homework of **Anne-Marije** – all the best to the two of you! Sorry **Adriaan** for complaining so much about PycQED and your GIT policies (and for getting you a speeding ticket). I think that many labs can be jealous of our software platform, and you played a key role in its development. Thank you for improving it in so many ways, it eased our lives greatly. Best of luck and success with the

rest of your PhD! Thank you **Ramiro** for always pulling me out of the dirt when I screwed up the dependencies on my computer again. Your creativity and awake spirit are such an enrichment to the group. Whether you're winning dance battles on Bourbon street, explain Argentinian politics, fish for alligators or convince the crowd that it's beer o'clock, you always do it wholeheartedly. **Brian**, I'm still in awe by how fast you've picked up all the skills of an experimentalist. Thank you for always taking the time to answer my questions related to theory in a way that resonates with me. I enjoyed our many evenings studying Kultur Im Zeitgeist. **Jules**, thank you for all your help concerning hardware – I have to admit that your Eccosorb filters are better than mine! I wish you and Niels a lot of success with Qblox, and hope that I will be a regular customer. **Tom** & **Xavi**, although we didn't work very closely together, I still find it great that you guys spend a lot of time here. Thank you very much for some truly eye-opening discussions. **Xiang**, I am still dreaming of the spicy nightmare! You have as much a talent for sales as for creating interesting moments. Good luck with starting your own group in China. I'm sure that **Miguel** will now fill your shoes. **Marios**, you have interesting and deep insights in physics, thank you for sharing them with me. I wish you and your family all the best. Thank you very much **Nandini** for all the help in the cleanroom and interesting discussions about India. I wish you all the best lasering our devices to the correct frequencies. **Christos**, you are the newest member of the fab team. May the cleanroom gods be in your favor. Thank you **Filip** for the explanations about hyperfine splittings. Probably we will work on comparable things on different sides of the ocean. **Luc**, make sure to keep your energy and your enthusiasm! **Boris**, I hope you manage to simulate the surface code with leakage. **Slava**, I tried sending this to you via WhatsApp, but for some reason that didn't work. You're a great addition to the team, and I wish you all the best for your postdoc in our group. At this point it is also important to mention everyone who did a bachelors or masters project in our group during the time I was here: **Bart**, **Sjoerd**, **Rick**, **Xinghan**, **Serwan**, **Livio**, **Sarwan**, **Jaap**, **Malay**, **Florian**, **Marc** and **René**. Thank you for enthusiastically contributing to something that is bigger than the sum of its parts.

Further on, I am very grateful towards the electronics team of our group. Although I am probably the PhD student in our group that was interacting the least with you, I still profited hugely from your presence. **Jacob**, it is great to have you around, not just because of your vast technical knowledge. Your calm and thought-through nature as well as your organizational talent helped to make the group a nicer place in many ways. **Wouter** and **Duije**, your immense knowledge about hardware and microwave electronics is invaluable for the group, thank you for educating me in this subject. Your talks shed some light into the inner workings of what were black boxes for me. Thanks to you, **Nadia**, I appreciate the pitfalls of electrostatic simulations much more. Also thank you, **Stan** and **Gerco**, for many nice moments.

Dave, it was great having you here for two years. Your thoroughness and fabrication knowledge is as inspiring to me as your musical talent – even when you need to resort to alternative forms of drumsticks. Thank you for supporting me to get the position at Intel, and for your hospitality when I was visiting Portland. I'm looking forward to many more interesting discussions about American politics and fabrication. Thank you **Jim** for giving me this fan-

tastic opportunity. I'm very much looking forward to working together with you, **Tom**, **Roman**, **Jeanette**, **Lester** and the rest of the team!

A big thank you goes to our collaborators in Copenhagen. You have provided us with state-of-the-art nanowires, without which all these experiments wouldn't have been possible. **Peter**, I thank you and your team for this fantastic material and your helpful explanations. In this context I would also like to thank **David** and **Akira** for providing us with world-class NbTiN. Without this material, which is literally the basis of our devices, it would hardly have been possible to achieve our results. Also you, **Anton**, have helped us a lot with your deep understanding of our system. Thank you **Willemijn**, **Arno**, **Gijs** and **Angela** for sharing insights to your experiments.

Special thanks go to all the people who keep our lab running smoothly: you are the silent heroes. **Jelle**, **Siebe**, **Roy**, **Mark** and **Remco**, it is clear that without you we could not do what we are doing. Thank you very much for keeping this place in a good condition at all times. **Olaf**, you always have good advice when it comes to taming our fridges. Your vast knowledge of cryogenic systems is an invaluable resource for QuTech. **Nico**, you have changed the workshop dramatically. Your precision, design suggestions and fast delivery have hugely benefited not only our, but also many other projects. Every university can be envious of such a machine shop. **Jason**, you're the go-to guy for so many things. Thank you for placing gold plating orders, and sorry for always forgetting to send you the project code. **Raymond Jr.**, **Raymond Sr.** and **Martijn**, your expertise in electronics is certainly one of the strong points of QuTech. Thank you very much for the useful course and so many explanations. Also the team at **DEMO** was always of great help. Further on, I would like to thank the management support team. **Marja**, **Chantal**, **Joanna**, and everyone else - you work magic behind the scenes. We sometimes do not notice that you are there, because you are doing such a great job – but rest assured, we highly appreciate your work.

A fair share of my time here I've spent in the cleanroom. Many thanks to the **Kavli Nanolab staff** for keeping the facilities and the machines up and running. Having access to such good cleanroom facilities is imperative for our research. Thank you **Ewan** for always generating some variety in the rather monotonous cleanroom days, and **Iman** for sharing your vast cleanroom knowledge.

Importantly, I would like to thank my friends in QuTech outside the DiCarlo group. I am grateful for countless thought-provoking impulses, fun encounters and the occasional beer in TPKV. I strongly hope that we manage to keep in touch. **Michiel**, your vast knowledge is only outmatched by your quick wits. Thank you for enduring so many of my rants, and always being there to talk to. Although I have the utmost trust in your explanations of nanowire physics, I can not say the same about your rakija recommendations. I'm honored that you are my paranymph, and I'm sorry for flying off too early to be at your defense (I don't intend to miss my plane though). **James**, 'we should work together' are probably the words we exchanged the most. While that never really happened, I'm happy that we spent a lot of time together outside the lab. You throw fantastic house parties, and have a great sense of humor. **Norbert**, I have always admired your sharp argumentation and your efficiency. We did several obstacle runs together, and I'm glad that these didn't cost you any teeth. Thank you for organizing the

trip to Nürnberg and München, and I hope you enjoy your time in Zürich. **Alex**, sorry for misunderstanding you every now and then – but sometimes you do look a bit upset. We had countless fun evenings together, talking about everything and nothing. Thank you for your thought-provoking way. **Fokko**, thank you for participating in many sportive activities and organizing the QuTech teams for the sports day. Together with **Anne-Marije**, **Filip** and **Norbert**, we organized the best QuTech uitje that ever took place and ever will take place. We know that deep down everyone liked cycling in the rain, it's part of living in the Netherlands. Together with you, **Jonas**, all these evenings of correcting countless homeworks were a lot more bearable. We had a great time on the road trip in California. Thank you very much **Gláucia** for so many discussions about how to manage our supervisors. **Davide**, thank you for being a great hosemate. **Jouri**, it's a pity we got to play squash only once. Thank you **Damaz** for sharing some exquisite Whiskeys with me at late nights in the lab. **Chris M.**, sorry for making bad jokes when Borussia was loosing. **Ben**, I hope that you manage to get to Mars (not just because I'm sick of hearing your joke with the flag). Thank you to my office mates **Amrita**, **Matt**, **Vukan**, **Nicolò**, **Nick**, **Hao** and **Jiyin**. Further on I would also like to thank everyone in QuTech I had nice and inspiring interactions with: **Srijit**, **Jasper**, **Nodar**, **Guoji**, **Suzanne**, **Peter**, **Jelmer**, **Vigdis**, **JP**, **Udi**, **Daniël**, **Jie**, **Luca**, **Francesco**, **Max**, **Will**, **Maarten**, and many more. Each one of you contributes to making QuTech this vibrant and stimulating environment we all value so much.

One of the highlights during the first year of my PhD were the IDEA league summer schools on quantum information. Many thanks to the speakers and the organizers. The strength of the bonds between the participants increased at a higher rate from school to school than price of beverages increased from city to city. This lead to us having several reunions over the past three years. Although the amount of scientific content decreased with every subsequent meeting, the fun certainly didn't. I would like to thank **Stephanie**, **Stevan**, **Önder** and **Hans** for giving us nice lectures on our first reunion. Our further activities included a seminar in ballistic transport, exercise hours in applied optics, several field studies of remnant medieval traditions, real-life simulation of low-pressure gases and experiments on the effect of annealing of biological masses. **Arne**, thank you very much for the hospitality at your place and organizing the reunions in Aachen/Köln. **Patrick**, our ideas about the rules of Flunkyball might differ, but it was always fun to play. **Philip**, thank you for preparing the Feuerzangenbowle, it was fantastic. Also many thanks to all other usual participants that were not mentioned before, **Felix**, **Nora**, **Tim**, **Bernardus**, **Johannes**, **Michele** and **Andreas**. I have greatly enjoyed these weekends, and will keep them in best memory.

Another constant during my time here was the gymnastics association **Pegasus**. I was welcomed warmly the day after my arrival in the Netherlands, and the trainings were always a great addition to my days. Many thanks to the trainers **Lisanne**, **Rick**, **Bas O.**, **Olaf**, **Geertje**, **Lieke**, and **Bas A.** for showing me new elements and saving me from breaking my neck – especially the latter I always highly appreciated. Clearly, Pegasus wouldn't be the fun association it is known as if there wasn't also a strong social component. **Roel**, **Yuan**, **Corne**, **Rogier**, **Mitchel**, **Jordi**, **Lennert**, **Marije**, **Flora**, **Marcel**, **Niels**, **Karin**, and many more: thank you for making so many competitions, feestjes and uitjes unforgettable.

Lastly, I would like to thank my family and friends in Switzerland. **Michael**, fasch jedes mal wänn ich id Schwiiz zrugg cho bin häsch du dir chöne d Ziit nää zum mit mir uf en Berg ue, go Gokart fahre oder Metzgete ässe. Ich ha die Uusflüüg immer sehr gnosse, und hoff, dass sich das au i de Zuäkunft mal wieder git. **Jan** und **Patrick**, au ihr sind immer mal für en Spass z ha gsi, viele Dank! **Stefan**, mir hend eus divärsi mal da in Delft troffe. Härzliche Dank für feini Fondues, Wanderige i de Düüne und intressanti Diskussione, sowie hilfriichi Tips zum akademische Läbe. **Caroline**, heel erg bedankt voor je gastvrijheid, en dat je zoveel tijd hebt genomen om me Nederlands te leren. Ik waardeer het enorm. **Nienke**, bedankt voor al je steun en alle leuke en onvergetelijke momenten. Je verrijkt mijn leven op zoveel verschillende manieren. Ik kijk uit naar onze toekomstige avonturen. **Samuel**, Brüederhärz, obs in Schnee gaht, sänkrächt d Berge duruuf oder per Sprung us em Flugzüüg use – du bisch immer debii und für alles z ha. Härzliche Danke für so vil Gspröch, Erlüüterige zu dim Fachgebiet wo mini Wältaaschauig gänderet händ, dini Bsüech da in Delft und au dass du dir immer Ziit gno häsch wänn ich mal i de Schwiiz gsi bi. **Daniel** und **Ida**, Papa und Mama, als mini Eltere hend ihr natüürlich de wichtigsti Teil a minere Erziehig gleistet und s Fundamänt für mini Uusbildig gleit. Ich danke eu ganz härzlich für e wunderbari Chindheit, dass ihr mich bi all mine Entschäidige understützt händ, und dass ihr mir s Gschänk vo de Neugier id Wiege gleit händ. Eusi all-Sunntigaabiglichä Konferänze sind immer en wichtige Teil i minere Wuchä, und ich hoffe, dass mer die au chönd biiphalte i dä Zuäkunft.

CURRICULUM VITÆ

Florian LÜTHI

14.11.1990	Born in Schwyz, Switzerland.

Education

2003–2009	Secondary School Kantonsschule Rychenberg, Winterthur, Switzerland (2003–2005) Kantonsschule im Lee, Winterthur, Switzerland (2005–2009)
2009-2014	Undergraduate studies in Physics Eidgenössische Technische Hochschule, Zürich (2009-2012) Uppsala Universitet, Uppsala (Fall 2012) Eidgenössische Technische Hochschule, Zürich (2012-2014) Master end project: *Thesis:* Characterization of Coplanar Waveguide Resonators in Parallel Magnetic Fields *Advisor:* Prof. dr. A. Wallraff
2014-2019	Ph.D. in experimental Physics Technische Universiteit Delft *Thesis:* Circuit Quantum Electrodynamics in a Magnetic Field *Advisor:* Prof. dr. L. Di Carlo

LIST OF PUBLICATIONS

3. **F. Luthi**, T. Stavenga, O. W. Enzing, A. Bruno, C. Dickel, N. K. Langford, M. A. Rol, T. S. Jespersen, J. Nygård, P. Krogstrup, L. DiCarlo, *Evolution of nanowire transmon qubits and their coherence in a magnetic field*, Physical Review Letters **120**, 100502 (2018).

2. N. K. Langford, R. Sagastizabal, M. Kounalakis, C. Dickel, A. Bruno, **F. Luthi**, D. J. Thoen, A. Endo, L. DiCarlo, *Experimentally simulating the dynamics of quantum light and matter at deep-strong coupling*, Nature Communications **8**, 1715 (2017).

1. M. A. Rol, C. C. Bultink, T. E. O'Brien, S. R. de Jong, L. S. Theis, X. Fu, **F. Luthi**, R. F. L. Vermeulen, J. C. de Sterke, A. Bruno, D. Deurloo, R. N. Schouten, F. K. Wilhelm, L. DiCarlo, *Restless tuneup of high-fidelity qubit gates*, Physical Review Applied **7**, 041001 (2017).

REFERENCES

[1] M. A. NIELSEN and I. L. CHUANG. *Quantum computation and quantum information*. 2000. (see page: 2)

[2] N. K. LANGFORD, R. SAGASTIZABAL, M. KOUNALAKIS, C. DICKEL, A. BRUNO, F. LUTHI, D. THOEN, A. ENDO, and L. DICARLO. *Experimentally simulating the dynamics of quantum light and matter at deep-strong coupling*. Nat. Comm., **8**, 1715, 2017. (see pages: 2, 24, 28, 29, 40, 49, 52, and 60)

[3] M. HUTCHINGS, J. B. HERTZBERG, Y. LIU, N. T. BRONN, G. A. KEEFE, M. BRINK, J. M. CHOW, and B. PLOURDE. *Tunable superconducting qubits with flux-independent coherence*. Phys. Rev. Appl., **8** (4), 044 003, 2017. (see pages: 2, 7, 29, 54, and 60)

[4] F. WELLSTOOD, C. URBINA, and J. CLARKE. *Excess noise in dc SQUIDs from 4.2 K to 0.022 K*. IEEE T. Magnetics, **23** (2), 1662–1665, 1987. (see page: 3)

[5] E. PALADINO, Y. M. GALPERIN, G. FALCI, and B. L. ALTSHULER. $1/f$ *noise: Implications for solid-state quantum information*. Rev. Mod. Phys., **86**, 361–418, 2014. (see page: 3)

[6] F. WELLSTOOD. *The unusual behavior of* $1/f$ *flux noise at temperatures below 1 K*, 2010. (see page: 3)

[7] R. H. KOCH, D. P. DIVINCENZO, and J. CLARKE. *Model for* $1/f$ *flux noise in SQUIDs and qubits*. Phys. Rev. Lett., **98**, 267 003, 2007. (see page: 3)

[8] S. MACHLUP. *Noise in semiconductors: Spectrum of a two-parameter random signal*. J. Appl. Phys., **25** (3), 341–343, 1954. (see pages: 3, 6)

[9] P. DUTTA and P. M. HORN. *Low-frequency fluctuations in solids:* $1/f$ *noise*. Rev. Mod. Phys., **53**, 497–516, 1981. (see pages: 3, 6)

[10] R. C. BIALCZAK, R. MCDERMOTT, M. ANSMANN, M. HOFHEINZ, N. KATZ, E. LUCERO, M. NEELEY, A. D. O'CONNELL, H. WANG, A. N. CLELAND, and J. M. MARTINIS. $1/f$ *flux noise in Josephson phase qubits*. Phys. Rev. Lett., **99**, 187 006, 2007. (see page: 3)

[11] S. M. ANTON, J. S. BIRENBAUM, S. R. O'KELLEY, V. BOLKHOVSKY, D. A. BRAJE, G. FITCH, M. NEELEY, G. C. HILTON, H.-M. CHO, K. D. IRWIN, F. C. WELLSTOOD, W. D. OLIVER, A. SHNIRMAN, *et al.* *Magnetic flux noise in dc SQUIDs: Temperature and geometry dependence*. Phys. Rev. Lett., **110**, 147 002, 2013. (see page: 3)

[12] C. WANG, C. AXLINE, Y. Y. GAO, T. BRECHT, Y. CHU, L. FRUNZIO, M. H. DEVORET, and R. J. SCHOELKOPF. *Surface participation and dielectric loss in superconducting qubits*. Appl. Phys. Lett., **107** (16), 162601, 2015. (see pages: 3, 34, and 74)

[13] J. GAO, M. DAAL, A. VAYONAKIS, S. KUMAR, J. ZMUIDZINAS, B. SADOULET, B. A. MAZIN, P. K. DAY, and H. G. LEDUC. *Experimental evidence for a surface distribution of two-level systems in superconducting lithographed microwave resonators*. Appl. Phys. Lett., **92** (15), 152505, 2008.

[14] P. MACHA, S. VAN DER PLOEG, G. OELSNER, E. ILICHEV, H.-G. MEYER, S. WÜNSCH, and M. SIEGEL. *Losses in coplanar waveguide resonators at Millikelvin temperatures*. Appl. Phys. Lett., **96** (6), 062 503, 2010. (see page: 3)

[15] L. FAORO and L. B. IOFFE. *Microscopic origin of low-frequency flux noise in Josephson circuits*. Phys. Rev. Lett., **100**, 227 005, 2008. (see pages: 3, 4, and 6)

[16] H. BLUHM, J. A. BERT, N. C. KOSHNICK, M. E. HUBER, and K. A. MOLER. *Spinlike susceptibility of metallic and insulating thin films at low temperature*. Phys. Rev. Lett., **103**, 026 805, 2009. (see pages: 3, 4)

[17] S. SENDELBACH, D. HOVER, A. KITTEL, M. MÜCK, J. M. MARTINIS, and R. MCDERMOTT. *Magnetism in SQUIDs at Millikelvin temperatures*. Phys. Rev. Lett., **100**, 227 006, 2008. (see page: 3)

[18] C. M. QUINTANA, Y. CHEN, D. SANK, A. G. PETUKHOV, T. C. WHITE, D. KAFRI, B. CHIARO, A. MEGRANT, R. BARENDS, B. CAMPBELL, Z. CHEN, A. DUNSWORTH, A. G. FOWLER, *et al. Observation of classical-quantum crossover of* $1/f$ *flux noise and its paramagnetic temperature dependence*. Phys. Rev. Lett., **118**, 057 702, 2017. (see pages: 3, 4, 5, 8, and 104)

[19] J. BURNETT, L. FAORO, I. WISBY, V. GURTOVOI, A. CHERNYKH, G. MIKHAILOV, V. TULIN, R. SHAIKHAIDAROV, V. ANTONOV, P. MEESON, A. TZALENCHUK, and T. LINDSTRÖM. *Evidence for interacting two-level systems from the 1/f noise of a superconducting resonator*. Nat. Comm., **5**, 4119, 2014. (see page: 3)

[20] T. LANTING, M. H. AMIN, A. J. BERKLEY, C. RICH, S.-F. CHEN, S. LAFOREST, and R. DE SOUSA. *Evidence for temperature-dependent spin diffusion as a mechanism of intrinsic flux noise in SQUIDs*. Phys. Rev. B, **89**, 014 503, 2014. (see page: 3)

[21] R. DE SOUSA. *Dangling-bond spin relaxation and magnetic* $1/f$ *noise from the amorphous-semiconductor/oxide interface: Theory*. Phys. Rev. B, **76**, 245 306, 2007. (see page: 4)

[22] S. CHOI, D.-H. LEE, S. G. LOUIE, and J. CLARKE. *Localization of metal-induced gap states at the metal-insulator interface: Origin of flux noise in SQUIDs and superconducting qubits*. Phys. Rev. Lett., **103**, 197 001, 2009. (see page: 4)

[23] D. LEE, J. L. DUBOIS, and V. LORDI. *Identification of the local sources of paramagnetic noise in superconducting qubit devices fabricated on* α*-*Al_2O_3 *substrates using density-functional calculations*. Phys. Rev. Lett., **112**, 017 001, 2014. (see page: 4)

[24] H. WANG, C. SHI, J. HU, S. HAN, C. C. YU, and R. Q. WU. *Candidate source of flux noise in SQUIDs: Adsorbed oxygen molecules*. Phys. Rev. Lett., **115**, 077 002, 2015. (see page: 4)

[25] A. F. BEDILO, E. I. SHUVARAKOVA, A. A. RYBINSKAYA, and D. A. MEDVEDEV. *Characterization of electron-donor and electron-acceptor sites on the surface of sulfated alumina using spin probes*. J. Phys. Chem., **118** (29), 15 779–15 794, 2014. (see page: 4)

[26] D. A. MEDVEDEV, A. A. RYBINSKAYA, R. M. KENZHIN, A. M. VOLODIN, and A. F. BEDILO. *Characterization of electron donor sites on* Al_2O_3 *surface*. Phys. Chem. Chem. Phys., **14**, 2587–2598, 2012. (see page: 4)

[27] S. E. DE GRAAF, A. A. ADAMYAN, T. LINDSTRÖM, D. ERTS, S. E. KUBATKIN, A. Y. TZALENCHUK, and A. V. DANILOV. *Direct identification of dilute surface spins on* Al_2O_3*: Origin of flux noise in quantum circuits*. Phys. Rev. Lett., **118**, 057 703, 2017. (see pages: 4, 5, 8, and 104)

[28] P. KUMAR, S. SENDELBACH, M. A. BECK, J. W. FREELAND, Z. WANG, H. WANG, C. C. YU, R. Q. WU, D. P. PAPPAS, and R. MCDERMOTT. *Origin and reduction of* $1/f$ *magnetic flux noise in superconducting devices*. Phys. Rev. Appl., **6**, 041 001, 2016. (see pages: 4, 5, 29, 60, and 104)

[29] M. A. RUDERMAN and C. KITTEL. *Indirect exchange coupling of nuclear magnetic moments by conduction electrons*. Phys. Rev., **96**, 99–102, 1954. (see page: 4)

[30] T. KASUYA. *A theory of metallic ferro- and antiferromagnetism on Zener's model*. Progress of Theoretical Physics, **16** (1), 45–57, 1956.

[31] K. YOSIDA. *Magnetic properties of Cu-Mn alloys*. Phys. Rev., **106**, 893–898, 1957. (see page: 4)

[32] Z. CHEN and C. C. YU. *Comparison of Ising spin glass noise to flux and inductance noise in SQUIDs*. Phys. Rev. Lett., **104**, 247 204, 2010. (see page: 4)

[33] J. WU and C. C. YU. *Modeling flux noise in SQUIDs due to hyperfine interactions*. Phys. Rev. Lett., **108**, 247 001, 2012. (see pages: 4, 6)

[34] F. YOSHIHARA, K. HARRABI, A. O. NISKANEN, Y. NAKAMURA, and J. S. TSAI. *Decoherence of flux qubits due to* $1/f$ *flux noise*. Phys. Rev. Lett., **97**, 167 001, 2006. (see pages: 7, 29, 54, and 60)

[35] W. D. OLIVER and P. B. WELANDER. *Materials in superconducting quantum bits*. MRS bulletin, **38** (10), 816–825, 2013. (see pages: 7, 29, 34, 60, and 102)

[36] J. JOHANSSON, P. NATION, and F. NORI. *Qutip: An open-source Python framework for the dynamics of open quantum systems*. Comp. Phys. Comm., **183** (8), 1760–1772, 2012. (see page: 11)

[37] G. DELANGE, B. VAN HECK, A. BRUNO, D. J. VAN WOERKOM, A. GERESDI, S. R. PLISSARD, E. P. A. M. BAKKERS, A. R. AKHMEROV, and L. DICARLO. *Realization of microwave quantum circuits using hybrid superconducting-semiconducting nanowire Josephson elements*. Phys. Rev. Lett., **115**, 127 002, 2015. (see pages: 13, 15, 21, 23, 30, 31, 32, 41, 52, 60, 102, and 105)

[38] T. W. LARSEN, K. D. PETERSSON, F. KUEMMETH, T. S. JESPERSEN, P. KROGSTRUP, J. NYGÅRD, and C. M. MARCUS. *Semiconductor-nanowire-based superconducting qubit*. Phys. Rev. Lett., **115**, 127 001, 2015. (see pages: 13, 15, 41, 52, 102, and 106)

[39] L. CASPARIS, T. W. LARSEN, M. S. OLSEN, F. KUEMMETH, P. KROGSTRUP, NYGÅRD, K. D. J. PETERSSON, and C. M. MARCUS. *Gatemon benchmarking and two-qubit operations*. Phys. Rev. Lett., **116**, 150 505, 2016. (see pages: 13, 31, 52, 105, and 106)

[40] L. CASPARIS, N. PEARSON, A. KRINGHØJ, T. LARSEN, F. KUEMMETH, J. NYGÅRD, P. KROGSTRUP, K. PETERSSON, and C. MARCUS. *Voltage-controlled superconducting quantum bus*. arXiv preprint arXiv:1802.01327, 2018. (see pages: 13, 52, and 106)

[41] I. VAN WEPEREN, S. R. PLISSARD, E. P. A. M. BAKKERS, S. M. FROLOV, and L. P. KOUWENHOVEN. *Quantized conductance in an InSb nanowire*. Nano Lett., **13** (2), 387–391, 2013. (see pages: 13, 105)

[42] J. KAMMHUBER, M. C. CASSIDY, H. ZHANG, N. GÜL, F. PEI, M. W. A. DE MOOR, B. NIJHOLT, K. WATANABE, T. TANIGUCHI, D. CAR, S. R. PLISSARD, E. P. A. M. BAKKERS, and L. P. KOUWENHOVEN. *Conductance quantization at zero magnetic field in InSb nanowires*. Nano Lett., **16** (6), 3482–3486, 2016. (see page: 109)

[43] E. M. T. FADALY, H. ZHANG, S. CONESA-BOJ, D. CAR, N. GÜL, S. R. PLISSARD, R. L. M. OP HET VELD, S. KÖLLING, L. P. KOUWENHOVEN, and E. P. A. M. BAKKERS. *Observation of conductance quantization in InSb nanowire networks*. Nano Lett., **17** (11), 6511–6515, 2017. (see pages: 13, 105, and 109)

[44] M. A. ROL, C. C. BULTINK, T. E. O'BRIEN, S. R. DE JONG, L. S. THEIS, X. FU, F. LUTHI, R. F. L. VERMEULEN, J. C. DE STERKE, A. BRUNO, D. DEURLOO, R. N. SCHOUTEN, F. K. WILHELM, *et al.* *Restless tuneup of high-fidelity qubit gates*. Phys. Rev. Appl., **7**, 041 001, 2017. (see pages: 13, 40, and 66)

[45] A. G. FOWLER, A. M. STEPHENS, and P. GROSZKOWSKI. *High-threshold universal quantum computation on the surface code*. Phys. Rev. A, **80**, 052 312, 2009. (see page: 14)

[46] C. HORSMAN, A. G. FOWLER, S. DEVITT, and R. V. METER. *Surface code quantum computing by lattice surgery*. New J. Phys., **14** (12), 123 011, 2012.

[47] R. VERSLUIS, S. POLETTO, N. KHAMMASSI, B. TARASINSKI, N. HAIDER, D. J. MICHALAK, A. BRUNO, K. BERTELS, and L. DICARLO. *Scalable quantum circuit and control for a superconducting surface code*. Phys. Rev. Appl., **8**, 034 021, 2017. (see pages: 14, 28, 66, and 105)

[48] M. FREEDMAN, A. KITAEV, M. LARSEN, and Z. WANG. *Topological quantum computation*. Bulletin of the American Mathematical Society, **40** (1), 31–38, 2003. (see page: 14)

[49] C. NAYAK, S. H. SIMON, A. STERN, M. FREEDMAN, and S. DAS SARMA. *Non-abelian anyons and topological quantum computation*. Rev. Mod. Phys., **80**, 1083–1159, 2008.

[50] J. D. SAU, R. M. LUTCHYN, S. TEWARI, and S. DAS SARMA. *Generic new platform for topological quantum computation using semiconductor heterostructures*. Phys. Rev. Lett., **104**, 040 502, 2010. (see page: 14)

[51] R. M. LUTCHYN, J. D. SAU, and S. DAS SARMA. *Majorana fermions and a topological phase transition in semiconductor-superconductor heterostructures*. Phys. Rev. Lett., **105**, 077 001, 2010. (see pages: 14, 108)

[52] Y. OREG, G. REFAEL, and F. VON OPPEN. *Helical liquids and Majorana bound states in quantum wires*. Phys. Rev. Lett., **105**, 177 002, 2010. (see page: 108)

[53] V. MOURIK, K. ZUO, S. M. FROLOV, S. R. PLISSARD, E. P. A. M. BAKKERS, and L. P. KOUWENHOVEN. *Signatures of Majorana fermions in hybrid superconductor-semiconductor nanowire devices*. Science, **336** (6084), 1003–1007, 2012. (see page: 14)

[54] J. ALICEA, Y. OREG, G. REFAEL, F. VON OPPEN, and M. P. FISHER. *Non-abelian statistics and topological quantum information processing in 1D wire networks*. Nat. Phys., **7** (5), 412–417, 2011. (see page: 14)

[55] T. HYART, B. VAN HECK, I. C. FULGA, M. BURRELLO, A. R. AKHMEROV, and C. W. J. BEENAKKER. *Flux-controlled quantum computation with Majorana fermions*. Phys. Rev. B, **88**, 035 121, 2013. (see pages: 14, 106)

[56] S. PLUGGE, A. RASMUSSEN, R. EGGER, and K. FLENSBERG. *Majorana box qubits*. New J. Phys., **19** (1), 012 001, 2017. (see page: 14)

[57] T. KARZIG, C. KNAPP, R. M. LUTCHYN, P. BONDERSON, M. B. HASTINGS, C. NAYAK, J. ALICEA, K. FLENSBERG, S. PLUGGE, Y. OREG, C. M. MARCUS, and M. H. FREEDMAN. *Scalable designs for quasiparticle-poisoning-protected topological quantum computation with Majorana zero modes*. Phys. Rev. B, **95**, 235 305, 2017. (see pages: 14, 106)

[58] E. P. HARRIS and D. E. MAPOTHER. *Critical field of superconducting aluminum as a function of pressure and temperature above 0.3 K*. Phys. Rev., **165**, 522–532, 1968. (see pages: 14, 22, 60, and 70)

[59] D. RISTÈ, C. C. BULTINK, M. J. TIGGELMAN, R. N. SCHOUTEN, K. W. LEHNERT, and L. DICARLO. *Millisecond charge-parity fluctuations and induced decoherence in a superconducting transmon qubit*. Nat. Comm., **4**, 1913, 2013. (see pages: 14, 41, 62, 73, and 106)

[60] K. SERNIAK, M. HAYS, G. DE LANGE, S. DIAMOND, S. SHANKAR, L. D. BURKHART, L. FRUNZIO, M. HOUZET, and M. H. DEVORET. *Hot nonequilibrium quasiparticles in transmon qubits*. Phys. Rev. Lett., **121**, 157 701, 2018. (see pages: 14, 62, and 73)

[61] A. WALLRAFF, D. I. SCHUSTER, A. BLAIS, L. FRUNZIO, R.-S. HUANG, J. MAJER, S. KUMAR, S. M. GIRVIN, and R. J. SCHOELKOPF. *Strong coupling of a single photon to a superconducting qubit using circuit quantum electrodynamics*. Nature, **431**, 162–167, 2004. (see pages: 14, 32)

[62] J. KOCH, T. M. YU, J. GAMBETTA, A. A. HOUCK, D. I. SCHUSTER, J. MAJER, A. BLAIS, M. H. DEVORET, S. M. GIRVIN, and R. J. SCHOELKOPF. *Charge-insensitive qubit design derived from the Cooper pair box*. Phys. Rev. A, **76**, 042 319, 2007. (see pages: 14, 18, 26, 29, 62, 72, 95, and 107)

[63] Z. WANG, S. SHANKAR, Z. MINEV, P. CAMPAGNE-IBARCQ, A. NARLA, and M. DEVORET. *Cavity attenuators for superconducting qubits*. arXiv:1807.04849, 2018. (see pages: 14, 18, and 28)

[64] F. JELEZKO, T. GAEBEL, I. POPA, A. GRUBER, and J. WRACHTRUP. *Observation of coherent oscillations in a single electron spin*. Phys. Rev. Lett., **92**, 076 401, 2004. (see page: 14)

[65] A. IMAMOGLU. *Cavity QED based on collective magnetic dipole coupling: Spin ensembles as hybrid two-level systems*. Phys. Rev. Lett., **102**, 083 602, 2009. (see pages: 14, 109)

[66] D. I. SCHUSTER, A. P. SEARS, E. GINOSSAR, L. DICARLO, L. FRUNZIO, J. J. L. MORTON, H. WU, G. A. D. BRIGGS, B. B. BUCKLEY, D. D. AWSCHALOM, and R. J. SCHOELKOPF. *High-cooperativity coupling of electron-spin ensembles to superconducting cavities*. Phys. Rev. Lett., **105**, 140 501, 2010. (see pages: 14, 70)

[67] Y. KUBO, F. R. ONG, P. BERTET, D. VION, V. JACQUES, D. ZHENG, A. DRÉAU, J.-F. ROCH, A. AUFFEVES, F. JELEZKO, J. WRACHTRUP, M. F. BARTHE, P. BERGONZO, *et al. Strong coupling of a spin ensemble to a superconducting resonator*. Phys. Rev. Lett., **105**, 140 502, 2010. (see page: 14)

[68] Y. KUBO, C. GREZES, A. DEWES, T. UMEDA, J. ISOYA, H. SUMIYA, N. MORISHITA, H. ABE, S. ONODA, T. OHSHIMA, V. JACQUES, A. DRÉAU, J.-F. ROCH, *et al. Hybrid quantum circuit with a superconducting qubit coupled to a spin ensemble*. Phys. Rev. Lett., **107**, 220 501, 2011. (see pages: 14, 109)

[69] V. RANJAN, G. DE LANGE, R. SCHUTJENS, T. DEBELHOIR, J. P. GROEN, D. SZOMBATI, D. J. THOEN, T. M. KLAPWIJK, R. HANSON, and L. DICARLO. *Probing dynamics of an electron-spin ensemble via a superconducting resonator*. Phys. Rev. Lett., **110**, 067 004, 2013. (see pages: 14, 68, 70, and 102)

[70] S. FELTON, A. M. EDMONDS, M. E. NEWTON, P. M. MARTINEAU, D. FISHER, D. J. TWITCHEN, and J. M. BAKER. *Hyperfine interaction in the ground state of the negatively charged nitrogen vacancy center in diamond*. Phys. Rev. B, **79**, 075 203, 2009. (see page: 14)

[71] G. FUCHS, V. DOBROVITSKI, D. TOYLI, F. HEREMANS, C. WEIS, T. SCHENKEL, and D. AWSCHALOM. *Excited-state spin coherence of a single nitrogen–vacancy centre in diamond*. Nat. Phys., **6** (9), 668, 2010. (see page: 14)

[72] N. SAMKHARADZE, G. ZHENG, N. KALHOR, D. BROUSSE, A. SAMMAK, U. MENDES, A. BLAIS, G. SCAPPUCCI, and L. VANDERSYPEN. *Strong spin-photon coupling in silicon*. Science, **359** (6380), 1123–1127, 2018. (see pages: 14, 109, and 110)

[73] P. SCARLINO, D. VAN WOERKOM, U. MENDES, J. KOSKI, A. LANDIG, C. ANDERSEN, S. GASPARINETTI, C. REICHL, W. WEGSCHEIDER, K. ENSSLIN, *et al. Coherent microwave photon mediated coupling between a semiconductor and a superconductor qubit*. arXiv preprint arXiv:1806.10039, 2018. (see pages: 14, 109, and 110)

[74] C. MONROE, D. MEEKHOF, B. KING, S. JEFFERTS, W. ITANO, D. WINELAND, and P. GOULD. *Resolved-sideband Raman cooling of a bound atom to the 3D zero-point energy*. Phys. Rev. Lett., **75** (22), 4011–4014, 1995. (see page: 18)

[75] J. T. MUHONEN, J. P. DEHOLLAIN, A. LAUCHT, F. E. HUDSON, R. KALRA, T. SEKIGUCHI, K. M. ITOH, D. N. JAMIESON, J. C. MCCALLUM, A. S. DZURAK, *et al. Storing quantum information for 30 seconds in a nanoelectronic device*. Nat. Nanotech., **9** (12), 986, 2014. (see pages: 18, 109)

[76] D. LOSS and D. P. DIVINCENZO. *Quantum computation with quantum dots*. Phys. Rev. A, **57**, 120–126, 1998. (see pages: 18, 109)

[77] Y. NAKAMURA, Y. PASHKIN, and J. TSAI. *Coherent control of macroscopic quantum states in a single-Cooper-pair box*. Nature, **398**, 786, 1999. (see pages: 18, 27, and 105)

[78] J. M. MARTINIS, S. NAM, J. AUMENTADO, and C. URBINA. *Rabi oscillations in a large Josephson-junction qubit*. Phys. Rev. Lett., **89**, 117 901, 2002.

[79] I. CHIORESCU, Y. NAKAMURA, C. J. P. M. HARMANS, and J. E. MOOIJ. *Coherent quantum dynamics of a superconducting flux qubit*. Science, **299** (5614), 1869–1871, 2003. (see page: 18)

[80] M. H. ABOBEIH, J. CRAMER, M. A. BAKKER, N. KALB, D. J. TWITCHEN, M. MARKHAM, and T. H. TAMINIAU. *One-second coherence for a single electron spin coupled to a multi-qubit nuclear-spin environment*. Nat. Comm., **9**, 2552, 2018. (see page: 18)

[81] V. BOUCHIAT, D. VION, P. JOYEZ, D. ESTEVE, and M. H. DEVORET. *Quantum coherence with a single Cooper pair*. Phys. Scr., **T76**, 165, 1998. (see page: 18)

[82] Y.-J. DOH, J. A. VAN DAM, A. L. ROEST, E. P. BAKKERS, L. P. KOUWENHOVEN, and S. DE FRANCESCHI. *Tunable supercurrent through semiconductor nanowires*. Science, **309** (5732), 272–275, 2005. (see pages: 18, 31)

[83] W. CHANG, S. M. ALBRECHT, T. S. JESPERSEN, F. KUEMMETH, P. KROGSTRUP, J. NYGÅRD, and C. M. MARCUS. *Hard gap in epitaxial semiconductor–superconductor nanowires*. Nat. Nanotech., **10**, 2015. (see pages: 22, 41, 42, 60, 72, and 102)

[84] C. W. J. BEENAKKER. *Universal limit of critical-current fluctuations in mesoscopic Josephson junctions*. Phys. Rev. Lett., **67** (27), 3836–3839, 1991. (see pages: 20, 22)

[85] A. FURUSAKI, H. TAKAYANAGI, and M. TSUKADA. *Josephson effect of the superconducting quantum point contact*. Phys. Rev. B, **45**, 10 563–10 575, 1992. (see page: 18)

[86] B. D. JOSEPHSON. *Possible new effects in superconductive tunnelling*. Phys. Lett., **1** (7), 251–253, 1962. (see page: 18)

[87] A. ANDREEV. *The thermal conductivity of the intermediate state in superconductors*. Sov. Phys. JETP, **46**, 1823–1828, 1964. (see page: 19)

[88] L. BRETHEAU. *Localized excitations in superconducting atomic contacts: Probing the Andreev doublet*. PhD Dissertation, Ecole Polytechnique X, 2013. (see page: 20)

[89] J.-D. PILLET. *Tunneling spectroscopy of the Andreev bound states in a carbon nanotube*. PhD Dissertation, L'UNIVERSITE PARIS VI, 2011.

[90] M. CHAUVIN. *The Josephson effect in atomic contacts*. PhD Dissertation, L'UNIVERSITE PARIS VI, 2005.

[91] D. J. VAN WOERKOM. *Semiconductor nanowire Josephson junctions*. PhD Dissertation, TU Delft, 2017. (see page: 21)

[92] Y. NAZAROV and Y. BLANTER. *Quantum transport*. Cambridge University Press, 1st edition, 2009. (see pages: 23, 24)

[93] N. B. KOPNIN. *Theory of superconductivity*, 2006. (see page: 20)

[94] G. E. BLONDER, M. TINKHAM, and T. M. KLAPWIJK. *Transition from metallic to tunneling regimes in superconducting microconstrictions: Excess current, charge imbalance, and supercurrent conversion*. Phys. Rev. B, **25**, 4515–4532, 1982. (see page: 20)

[95] C. KITTEL. *Introduction to solid state physics*. Wiley, 1996. (see page: 20)

[96] P. F. BAGWELL. *Suppression of the Josephson current through a narrow, mesoscopic, semiconductor channel by a single impurity*. Phys. Rev. B, **46**, 12 573–12 586, 1992. (see pages: 20, 21)

[97] R. LANDAUER. *Electrical resistance of disordered one-dimensional lattices*. The Philosophical Magazine: A Journal of Theoretical Experimental and Applied Physics, **21** (172), 863–867, 1970. (see page: 20)

[98] E. M. SPANTON, M. DENG, S. VAITIEKĖNAS, P. KROGSTRUP, J. NYGÅRD, C. M. MARCUS, and K. A. MOLER. *Current–phase relations of few-mode InAs nanowire Josephson junctions*. Nat. Phys., **13** (12), 1177, 2017. (see pages: 21, 23, and 60)

[99] M. HAYS, G. DE LANGE, K. SERNIAK, D. J. VAN WOERKOM, D. BOUMAN, P. KROGSTRUP, J. NYGÅRD, A. GERESDI, and M. H. DEVORET. *Direct microwave measurement of Andreev-bound-state dynamics in a semiconductor-nanowire Josephson junction*. Phys. Rev. Lett., **121**, 047 001, 2018. (see page: 21)

[100] D. J. VAN WOERKOM, A. PROUTSKI, B. VAN HECK, D. BOUMAN, J. I. VÄYRYNEN, L. I. GLAZMAN, P. KROGSTRUP, J. NYGÅRD, L. P. KOUWENHOVEN, and A. GERESDI. *Microwave spectroscopy of spinful Andreev bound states in ballistic semiconductor Josephson junctions*. Nat. Phys., **13** (9), 876–881, 2017. (see pages: 21, 23, 82, and 107)

[101] A. KRINGHØJ, L. CASPARIS, M. HELL, T. W. LARSEN, F. KUEMMETH, M. LEIJNSE, K. FLENSBERG, P. KROGSTRUP, J. NYGÅRD, K. D. PETERSSON, and C. M. MARCUS. *Anharmonicity of a superconducting qubit with a few-mode Josephson junction*. Phys. Rev. B, **97**, 060 508, 2018. (see pages: 22, 31, 52, 53, and 105)

[102] S. CHUANG, Q. GAO, R. KAPADIA, A. C. FORD, J. GUO, and A. JAVEY. *Ballistic InAs nanowire transistors*. Nano Lett., **13** (2), 555–558, 2013. (see page: 22)

[103] T. S. JESPERSEN, M. L. POLIANSKI, C. B. SØRENSEN, K. FLENSBERG, and J. NYGÅRD. *Mesoscopic conductance fluctuations in InAs nanowire-based SNS junctions*. New J. Phys., **11** (11), 113 025, 2009. (see page: 22)

[104] M. TINKHAM. *Introduction to Superconductivity*. McGraw-Hill, New York, 2nd edition, 1996. (see pages: 22, 35, 69, 71, 72, 80, 81, 84, and 99)

[105] M. F. GOFFMAN, C. URBINA, H. POTHIER, J. NYGÅRD, C. M. MARCUS, and P. KROGSTRUP. *Conduction channels of an InAs-Al nanowire Josephson weak link*. New J. Phys., **19** (9), 092 002, 2017. (see page: 23)

[106] K. LANG, S. NAM, J. AUMENTADO, C. URBINA, and J. M. MARTINIS. *Banishing quasiparticles from Josephson-junction qubits: Why and how to do it*. IEEE Transactions on Applied Superconductivity, **13** (2), 989–993, 2003. (see page: 23)

[107] K. OSBORNE and J. M. MARTINIS. In *Les Houches 2003 conference proceedings*.

[108] R. W. SIMMONDS, K. M. LANG, D. A. HITE, S. NAM, D. P. PAPPAS, and J. M. MARTINIS. *Decoherence in Josephson phase qubits from junction resonators*. Phys. Rev. Lett., **93**, 077 003, 2004. (see page: 23)

[109] V. AMBEGAOKAR and A. BARATOFF. *Tunneling between superconductors*. Phys. Rev. Lett., **10**, 486–489, 1963. (see page: 24)

[110] A. BLAIS, R.-S. HUANG, A. WALLRAFF, S. M. GIRVIN, and R. J. SCHOELKOPF. *Cavity quantum electrodynamics for superconducting electrical circuits: An architecture for quantum computation*. Phys. Rev. A, **69**, 062 320, 2004. (see pages: 25, 32, 37, and 52)

[111] Y. NAKAMURA, Y. A. PASHKIN, T. YAMAMOTO, and J. S. TSAI. *Charge echo in a Cooper-pair box*. Phys. Rev. Lett., **88**, 047 901, 2002. (see page: 27)

[112] F. MOTZOI, J. M. GAMBETTA, P. REBENTROST, and F. K. WILHELM. *Simple pulses for elimination of leakage in weakly nonlinear qubits*. Phys. Rev. Lett., **103**, 110 501, 2009. (see pages: 27, 112)

[113] J. A. SCHREIER, A. A. HOUCK, J. KOCH, D. I. SCHUSTER, B. R. JOHNSON, J. M. CHOW, J. M. GAMBETTA, J. MAJER, L. FRUNZIO, M. H. DEVORET, S. M. GIRVIN, and R. J. SCHOELKOPF. *Suppressing charge noise decoherence in superconducting charge qubits*. Phys. Rev. B, **77**, 180 502, 2008. (see pages: 28, 106, and 109)

[114] D. I. SCHUSTER, A. A. HOUCK, J. A. SCHREIER, A. WALLRAFF, J. M. GAMBETTA, A. BLAIS, L. FRUNZIO, J. MAJER, M. H. DEVORET, S. M. GIVIN, and R. J. SCHOELKOPF. *Resolving photon number states in a superconducting circuit*. Nature, **445**, 515, 2007. (see pages: 28, 112)

[115] L. STEFFEN, Y. SALATHE, M. OPPLIGER, P. KURPIERS, M. BAUR, C. LANG, C. EICHLER, G. PUEBLA-HELLMANN, A. FEDOROV, and A. WALLRAFF. *Deterministic quantum teleportation with feed-forward in a solid state system*. Nature, **500** (7462), 319–22, 2013. (see page: 28)

[116] P. V. KLIMOV, J. KELLY, Z. CHEN, M. NEELEY, A. MEGRANT, B. BURKETT, R. BARENDS, K. ARYA, B. CHIARO, Y. CHEN, A. DUNSWORTH, A. FOWLER, B. FOXEN, *et al. Fluctuations of energy-relaxation times in superconducting qubits*. Phys. Rev. Lett., **121**, 090 502, 2018. (see page: 28)

[117] J. M. MARTINIS, S. NAM, J. AUMENTADO, K. M. LANG, and C. URBINA. *Decoherence of a superconducting qubit due to bias noise*. Phys. Rev. B, **67**, 094 510, 2003. (see pages: 29, 55, and 57)

[118] J. E. MOOIJ, T. P. ORLANDO, L. LEVITOV, L. TIAN, C. H. VAN DER WAL, and S. LLOYD. *Josephson persistent-current qubit*. Science, **285** (5430), 1036–1039, 1999. (see page: 30)

[119] S. DE FRANCESCHI, J. A. VAN DAM, E. P. A. M. BAKKERS, L. F. FEINER, L. GUREVICH, and L. P. KOUWENHOVEN. *Single-electron tunneling in InP nanowires*. Appl. Phys. Lett., **83** (2), 344–346, 2003. (see page: 31)

[120] D. M. POZAR. *Microwave engineering*. John Wiley & Sons, Hoboken, 4 edition, 2005. (see pages: 33, 36)

[121] M. JERGER, S. POLETTO, P. MACHA, U. HÜBNER, E. IL'ICHEV, and A. V. USTINOV. *Frequency division multiplexing readout and simultaneous manipulation of an array of flux qubits*. Appl. Phys. Lett., **101** (4), 042 604, 2012. (see page: 33)

[122] A. BRUNO, G. DE LANGE, S. ASAAD, K. L. VAN DER ENDEN, N. K. LANGFORD, and L. DICARLO. *Reducing intrinsic loss in superconducting resonators by surface treatment and deep etching of silicon substrates*. Appl. Phys. Lett., **106**, 182 601, 2015. (see pages: 33, 34, and 40)

[123] M. S. KHALIL, M. J. A. STOUTIMORE, F. C. WELLSTOOD, and K. D. OSBORN. *An analysis method for asymmetric resonator transmission applied to superconducting devices*. J. Appl. Phys., **111** (5), 054510, 2012. (see page: 33)

[124] R. BARENDS. *Photon-detecting superconducting resonators*. PhD Dissertation, TU Delft, 2009. (see page: 34)

[125] M. REED. *Entanglement and quantum error correction with superconducting qubits*. PhD Dissertation, Yale University, 2013. (see page: 34)

[126] E. M. PURCELL, H. C. TORREY, and R. V. POUND. *Resonance absorption by nuclear magnetic moments in a solid*. Phys. Rev., **69**, 37–38, 1946. (see page: 34)

[127] A. A. HOUCK, J. A. SCHREIER, B. R. JOHNSON, J. M. CHOW, J. KOCH, J. M. GAMBETTA, D. I. SCHUSTER, L. FRUNZIO, M. H. DEVORET, S. M. GIRVIN, and R. J. SCHOELKOPF. *Controlling the spontaneous emission of a superconducting transmon qubit*. Phys. Rev. Lett., **101**, 080502 (pages 4), 2008. (see pages: 34, 73)

[128] J. M. MARTINIS, K. B. COOPER, R. MCDERMOTT, M. STEFFEN, M. ANSMANN, K. D. OSBORN, K. CICAK, S. OH, D. P. PAPPAS, R. W. SIMMONDS, and C. C. YU. *Decoherence in Josephson qubits from dielectric loss*. Phys. Rev. Lett., **95**, 210 503, 2005. (see page: 34)

[129] M. SANDBERG, M. R. VISSERS, J. S. KLINE, M. WEIDES, J. GAO, D. S. WISBEY, and D. P. PAPPAS. *Etch induced microwave losses in titanium nitride superconducting resonators*. Appl. Phys. Lett., **100** (26), 262605, 2012.

[130] A. MEGRANT, C. NEILL, R. BARENDS, B. CHIARO, Y. CHEN, L. FEIGL, J. KELLY, E. LUCERO, M. MARIANTONI, P. J. J. O'MALLEY, D. SANK, A. VAINSENCHER, J. WENNER, *et al. Planar superconducting resonators with internal quality factors above one million*. Appl. Phys. Lett., **100** (11), 113510, 2012.

[131] I. NSANZINEZA and B. L. T. PLOURDE. *Trapping a single vortex and reducing quasiparticles in a superconducting resonator*. Phys. Rev. Lett., **113**, 117 002, 2014. (see pages: 34, 47, 74, 84, 92, 97, and 99)

[132] J. WENNER, R. BARENDS, R. C. BIALCZAK, Y. CHEN, J. KELLY, E. LUCERO, M. MARIANTONI, A. MEGRANT, P. J. J. O'MALLEY, D. SANK, A. VAINSENCHER, H. WANG, T. C. WHITE, *et al. Surface loss simulations of superconducting coplanar waveguide resonators*. Appl. Phys. Lett., **99** (11), 113 513, 2011. (see page: 34)

[133] G. CALUSINE, A. MELVILLE, W. WOODS, R. DAS, C. STULL, V. BOLKHOVSKY, D. BRAJE, D. HOVER, D. K. KIM, X. MILOSHI, *et al. Analysis and mitigation of interface losses in trenched superconducting coplanar waveguide resonators*. Appl. Phys. Lett., **112** (6), 062 601, 2018. (see page: 34)

[134] R. BARENDS, J. WENNER, M. LENANDER, Y. CHEN, R. C. BIALCZAK, J. KELLY, E. LUCERO, P. O'MALLEY, M. MARIANTONI, D. SANK, H. WANG, T. C. WHITE, Y. YIN, *et al. Minimizing quasiparticle generation from stray infrared light in superconducting quantum circuits*. Appl. Phys. Lett., **99**, 113 507, 2011. (see pages: 34, 116)

[135] A. DUNSWORTH, B. CAMPBELL, Z. CHEN, B. CHIARO, C. NEILL, J. WENNER, and J. MARTINIS. *Low loss multi-layer wiring for superconducting qubits*. Bulletin of the American Physical Society, 2018. (see page: 34)

[136] S. GEVORGIAN, L. J. P. LINNER, and E. L. KOLLBERG. *CAD models for shielded multilayered CPW*. IEEE T. Microwave Theory Tech., **43** (4), 772–779, 1995. (see page: 35)

[137] M. GÖPPL, A. FRAGNER, M. BAUR, R. BIANCHETTI, S. FILIPP, J. M. FINK, P. J. LEEK, G. PUEBLA, L. STEFFEN, and A. WALLRAFF. *Coplanar waveguide resonators for circuit quantum electrodynamics*. J. Appl. Phys., **104** (11), 113 904, 2008. (see page: 35)

[138] J. KRUPKA, J. BREEZE, A. CENTENO, N. ALFORD, T. CLAUSSEN, and L. JENSEN. *Measurements of permittivity, dielectric loss tangent, and resistivity of float-zone silicon at microwave frequencies*. IEEE T. Microwave Theory Tech., **54** (11), 3995–4001, 2006. (see page: 35)

[139] E. CHEN and S. Y. CHOU. *Characteristics of coplanar transmission lines on multilayer substrates: modeling and experiments*. IEEE T. Microwave Theory Tech., **45** (6), 939–945, 1997. (see page: 35)

[140] R. VOLLMER. *Fast and scalable readout for fault-tolerant quantum computing with superconducting qubits*. Master's thesis, TU Delft, 2018. (see page: 35)

[141] K. WATANABE, K. YOSHIDA, T. AOKI, and S. KOHJIRO. *Kinetic inductance of superconducting coplanar waveguides*. Jap. J. Appl. Phys., **33** (10R), 5708, 1994. (see page: 35)

[142] D. J. THOEN, B. G. C. BOS, E. HAALEBOS, T. KLAPWIJK, J. BASELMANS, and A. ENDO. *Superconducting NbTiN thin films with highly uniform properties over a ∅ 100 mm wafer*. IEEE T. Appl. Supercon., **27** (4), 1–5, 2017. (see pages: 35, 40)

[143] L. YU, N. NEWMAN, and J. M. ROWELL. *Measurement of the coherence length of sputtered $Nb_{0.62}Ti_{0.38}N$ thin films*. IEEE T. Appl. Supercon., **12** (2), 1795–1798, 2002.

[144] L. YU, R. K. SINGH, H. LIU, S. Y. WU, R. HU, D. DURAND, J. BULMAN, J. M. ROWELL, and N. NEWMAN. *Fabrication of niobium titanium nitride thin films with high superconducting transition temperatures and short penetration lengths*. IEEE T. Appl. Supercon., **15** (1), 44–48, 2005.

[145] D. J. VAN WOERKOM, A. GERESDI, and L. P. KOUWENHOVEN. *One minute parity lifetime of a NbTiN Cooper-pair transistor*. Nat. Phys., **11** (7), 547, 2015. (see pages: 35, 68)

[146] J. KROLL, F. BORSOI, K. VAN DER ENDEN, W. UILHOORN, D. DE JONG, M. QUINTERO-PÉREZ, D. VAN WOERKOM, A. BRUNO, S. PLISSARD, D. CAR, *et al.* *Magnetic field resilient superconducting coplanar waveguide resonators for hybrid cQED experiments*. arXiv preprint arXiv:1809.03932, 2018. (see pages: 35, 47, 68, 69, 72, 80, 81, 84, and 99)

[147] E. T. JAYNES and F. W. CUMMINGS. *Comparison of quantum and semiclassical radiation theories with application to the beam maser*. Proceedings of the IEEE, **51** (1), 89–109, 1963. (see page: 36)

[148] D. RISTÈ, S. POLETTO, M. Z. HUANG, A. BRUNO, V. VESTERINEN, O. P. SAIRA, and L. DICARLO. *Detecting bit-flip errors in a logical qubit using stabilizer measurements*. Nat. Comm., **6**, 6983, 2015. (see pages: 40, 49, and 105)

[149] C. C. BULTINK, M. A. ROL, T. E. O'BRIEN, X. FU, B. C. S. DIKKEN, C. DICKEL, R. F. L. VERMEULEN, J. C. DE STERKE, A. BRUNO, R. N. SCHOUTEN, and L. DICARLO. *Active resonator reset in the nonlinear dispersive regime of circuit QED*. Phys. Rev. Appl., **6**, 034 008, 2016. (see page: 40)

[150] C. DICKEL, J. J. WESDORP, N. K. LANGFORD, S. PEITER, R. SAGASTIZABAL, A. BRUNO, B. CRIGER, F. MOTZOI, and L. DICARLO. *Chip-to-chip entanglement of transmon qubits using engineered measurement fields*. Phys. Rev. B, **97**, 064 508, 2018. (see page: 98)

[151] S. ASAAD, C. DICKEL, S. POLETTO, A. BRUNO, N. K. LANGFORD, M. A. ROL, D. DEURLOO, and L. DICARLO. *Independent, extensible control of same-frequency superconducting qubits by selective broadcasting*. npj Quantum Inf., **2**, 16 029, 2016. (see pages: 40, 49)

[152] B. G. C. BOS, D. J. THOEN, E. HAALEBOS, P. GIMBEL, T. KLAPWIJK, J. BASELMANS, and A. ENDO. *Reactive magnetron sputter deposition of superconducting niobium titanium nitride thin films with different target sizes*. IEEE T. Appl. Supercon., **27** (4), 1–5, 2017. (see page: 40)

[153] P. KROGSTRUP, N. L. B. ZIINO, W. CHANG, S. M. ALBRECHT, M. H. MADSEN, E. JOHNSON, J. NYGÅRD, C. M. MARCUS, and T. S. JESPERSEN. *Epitaxy of semiconductor–superconductor nanowires*. Nat. Mater., **14**, 2015. (see pages: 41, 72, 81, 87, and 102)

[154] T. D. STANESCU and S. DAS SARMA. *Superconducting proximity effect in semiconductor nanowires*. Phys. Rev. B, **87**, 180 504, 2013. (see page: 41)

[155] S. TAKEI, B. M. FREGOSO, H.-Y. HUI, A. M. LOBOS, and S. DAS SARMA. *Soft superconducting gap in semiconductor Majorana nanowires*. Phys. Rev. Lett., **110**, 186 803, 2013. (see page: 41)

[156] J. M. MARTINIS, M. ANSMANN, and J. AUMENTADO. *Energy decay in superconducting Josephson-junction qubits from nonequilibrium quasiparticle excitations*. Phys. Rev. Lett., **103**, 097 002, 2009. (see pages: 41, 73)

[157] C. WANG, Y. Y. GAO, I. M. POP, U. VOOL, C. AXLINE, T. BRECHT, R. W. HEERES, L. FRUNZIO, M. H. DEVORET, G. CATELANI, L. I. GLAZMAN, and R. J. SCHOELKOPF. *Measurement and control of quasiparticle dynamics in a superconducting qubit*. Nat. Comm., **5**, 5836, 2014. (see pages: 41, 60, 74, and 97)

[158] F. LUTHI, T. STAVENGA, O. W. ENZING, A. BRUNO, C. DICKEL, N. K. LANGFORD, M. A. ROL, T. S. JESPERSEN, J. NYGÅRD, P. KROGSTRUP, and L. DICARLO. *Evolution of nanowire transmon qubits and their coherence in a magnetic field*. Phys. Rev. Lett., **120**, 100 502, 2018. (see pages: 41, 102, and 105)

[159] K. FLÖHR, M. LIEBMANN, K. SLADEK, H. Y. GÜNEL, R. FRIELINGHAUS, F. HAAS, C. MEYER, H. HARDTDEGEN, T. SCHÄPERS, D. GRÜTZMACHER, and M. MORGENSTERN. *Manipulating InAs nanowires with submicrometer precision*. Rev. Sci. Instrum., **82** (11), 113 705, 2011. (see page: 42)

[160] M. SCHEFFLER, S. NADJ-PERGE, L. P. KOUWENHOVEN, M. T. BORGSTRÖM, and E. P. A. M. BAKKERS. *Tunable double quantum dots in InAs nanowires*. Phys. E, **40** (5), 1202 – 1204, 2008. (see page: 42)

[161] ITSEEZ. *Open source computer vision library*, 2015. (see page: 44)

[162] T. STAVENGA. *Transmon qubits with a nanowire Josephson junction*. Master's thesis, TU Delft, 2016. (see page: 44)

[163] N. OTSU. *A threshold selection method from gray-level histograms*. IEEE T. Sys. Man and Cyb., **9**, 62 – 66, 1979. (see page: 44)

[164] J. SERRA. *Image analysis & mathematical morphology*. Academic Press, 1997. (see page: 44)

[165] J. CANNY. *A computational approach to edge detection*. IEEE T. PAMI, **8**, 679 – 698, 1986. (see page: 44)

[166] D. H. BALLARD. *Generalizing the Hough transform to detect arbitrary shapes*. Pattern recognition, **13** (2), 111–122, 1981. (see page: 44)

[167] TRANSENE COMPANY, INC. *Aluminum etchant type D*, 2018. (see page: 46)

[168] G. FÜLÖP, S. D'HOLLOSY, L. HOFSTETTER, A. BAUMGARTNER, J. NYGÅRD, C. SCHÖNENBERGER, and S. CSONKA. *Wet etch methods for InAs nanowire patterning and self-aligned electrical contacts*. Nanotechnology, **27** (19), 195 303, 2016. (see page: 47)

[169] D. B. SUYATIN, C. THELANDER, M. T. BJÖRK, I. MAXIMOV, and L. SAMUELSON. *Sulfur passivation for ohmic contact formation to InAs nanowires*. Nanotechnology, **18** (10), 105 307, 2007. (see page: 47)

[170] D. BOTHNER, T. GABER, M. KEMMLER, D. KOELLE, R. KLEINER, S. WÜNSCH, and M. SIEGEL. *Magnetic hysteresis effects in superconducting coplanar microwave resonators*. Phys. Rev. B, **86**, 014 517, 2012. (see pages: 47, 70, 72, and 85)

[171] C. SONG, T. HEITMANN, M. DEFEO, K. YU, R. MCDERMOTT, M. NEELEY, J. M. MARTINIS, and B. PLOURDE. *Microwave response of vortices in superconducting thin films of Re and Al*. Phys. Rev. B, **79** (17), 174 512, 2009. (see pages: 80, 92)

[172] N. SAMKHARADZE, A. BRUNO, P. SCARLINO, G. ZHENG, D. P. DIVINCENZO, L. DICARLO, and L. M. K. VANDERSYPEN. *High-kinetic-inductance superconducting nanowire resonators for circuit QED in a magnetic field*. Phys. Rev. Appl., **5**, 044 004, 2016. (see pages: 47, 68, 69, and 81)

[173] K. H. KUIT, J. R. KIRTLEY, W. VAN DER VEUR, C. G. MOLENAAR, F. J. G. ROESTHUIS, A. G. P. TROEMAN, J. R. CLEM, H. HILGENKAMP, H. ROGALLA, and J. FLOKSTRA. *Vortex trapping and expulsion in thin-film $YBa_2Cu_3O_{7-\delta}$ strips*. Phys. Rev. B, **77**, 134 504, 2008. (see page: 47)

[174] J. ASSENDELFT. *Increasing the magnetic field compatibility and field stability of nanowire transmons*. Master's thesis, TU Delft, 2018. (see pages: 48, 49, 84, and 99)

[175] L. CASPARIS, M. R. CONNOLLY, M. KJAERGAARD, N. J. PEARSON, A. KRINGHØJ, T. W. LARSEN, F. KUEMMETH, T. WANG, C. THOMAS, S. GRONIN, G. C. GARDNER, M. J. MANFRA, C. M. MARCUS, *et al.* *Superconducting gatemon qubit based on a proximitized two-dimensional electron gas*. Nat. Nanotech., **13**, 2018. (see pages: 52, 82, and 105)

[176] D. I. SCHUSTER, A. WALLRAFF, A. BLAIS, L. FRUNZIO, R.-S. HUANG, J. MAJER, S. M. GIRVIN, and R. J. SCHOELKOPF. *ac stark shift and dephasing of a superconducting qubit strongly coupled to a cavity field*. Phys. Rev. Lett., **94**, 123 602, 2005. (see page: 52)

[177] G. ITHIER, E. COLLIN, P. JOYEZ, P. J. MEESON, D. VION, D. ESTEVE, F. CHIARELLO, A. SHNIRMAN, Y. MAKHLIN, J. SCHRIEFL, and G. SCHÖN. *Decoherence in a superconducting quantum bit circuit*. Phys. Rev. B, **72**, 134 519, 2005. (see page: 54)

[178] J. BYLANDER, S. GUSTAVSSON, F. YAN, F. YOSHIHARA, K. HARRABI, G. FITCH, D. G. CORY, Y. NAKAMURA, J.-S. TSAI, and W. D. OLIVER. *Noise spectroscopy through dynamical decoupling with a superconducting flux qubit*. Nat. Phys., **7** (7), 565–570, 2011. (see pages: 54, 55, and 57)

[179] H. Y. CARR and E. M. PURCELL. *Effects of diffusion on free precession in nuclear magnetic resonance experiments*. Phys. Rev., **94**, 630–638, 1954.

[180] S. MEIBOOM and D. GILL. *Modified spin-echo method for measuring nuclear relaxation times*. Rev. Sci. Instrum., **29** (8), 688–691, 1958.

[181] E. KAWAKAMI. *Characterization of an electron spin qubit in a Si/SiGe quantum dot*. PhD Dissertation, TU Delft, 2016. (see page: 57)

[182] F. YAN, J. BYLANDER, S. GUSTAVSSON, F. YOSHIHARA, K. HARRABI, D. G. CORY, T. P. ORLANDO, Y. NAKAMURA, J.-S. TSAI, and W. D. OLIVER. *Spectroscopy of low-frequency noise and its temperature dependence in a superconducting qubit*. Phys. Rev. B, **85**, 174 521, 2012. (see page: 57)

[183] D. SANK, R. BARENDS, R. C. BIALCZAK, Y. CHEN, J. KELLY, M. LENANDER, E. LUCERO, M. MARIANTONI, A. MEGRANT, M. NEELEY, P. J. J. O'MALLEY, A. VAINSENCHER, H. WANG, *et al.* *Flux noise probed with real time qubit tomography in a Josephson phase qubit*. Phys. Rev. Lett., **109**, 067 001, 2012. (see page: 57)

[184] H. PAIK, D. I. SCHUSTER, L. S. BISHOP, G. KIRCHMAIR, G. CATELANI, A. P. SEARS, B. R. JOHNSON, M. J. REAGOR, L. FRUNZIO, L. I. GLAZMAN, S. M. GIRVIN, M. H. DEVORET, and R. J. SCHOELKOPF. *Observation of high coherence in Josephson junction qubits measured in a three-dimensional circuit QED architecture*. Phys. Rev. Lett., **107**, 240 501, 2011. (see page: 60)

[185] L. DICARLO, M. D. REED, L. SUN, B. R. JOHNSON, J. M. CHOW, J. M. GAMBETTA, L. FRUNZIO, S. M. GIRVIN, M. H. DEVORET, and R. J. SCHOELKOPF. *Preparation and measurement of three-qubit entanglement in a superconducting circuit*. Nature, **467**, 574, 2010. (see page: 66)

[186] R. LUTCHYN, E. BAKKERS, L. KOUWENHOVEN, P. KROGSTRUP, C. MARCUS, and Y. OREG. *Majorana zero modes in superconductor–semiconductor heterostructures*. Nat. Rev. Mat., page 1, 2018. (see page: 68)

[187] D. BOTHNER, T. GABER, M. KEMMLER, D. KOELLE, and R. KLEINER. *Improving the performance of superconducting microwave resonators in magnetic fields*. Appl. Phys. Lett., **98** (10), 102 504, 2011. (see pages: 68, 80)

[188] J. E. HEALEY, T. LINDSTRÖM, M. S. COLCLOUGH, C. M. MUIRHEAD, and A. Y. TZALENCHUK. *Magnetic field tuning of coplanar waveguide resonators*. Appl. Phys. Lett., **93** (4), 043 513, 2008. (see page: 69)

[189] S. E. D. GRAAF, A. V. DANILOV, A. ADAMYAN, T. BAUCH, and S. E. KUBATKIN. *Magnetic field resilient superconducting fractal resonators for coupling to free spins*. J. Appl. Phys., **112** (12), 123 905, 2012. (see page: 70)

[190] J. F. COCHRAN and D. E. MAPOTHER. *Superconducting transition in aluminum*. Phys. Rev., **111**, 132–142, 1958. (see page: 70)

[191] D. LAROCHE, D. BOUMAN, D. J. VAN WOERKOM, A. PROUTSKI, C. MURTHY, D. I. PIKULIN, C. NAYAK, R. J. VAN GULIK, J. NYGÅRD, P. KROGSTRUP, L. P. KOUWENHOVEN, and A. GERESDI. *Observation of the 4π-periodic Josephson effect in indium arsenide nanowires*. Nat. Comm., **10** (1), 245, 2019. (see pages: 71, 107)

[192] M. POPINCIUC, V. E. CALADO, X. L. LIU, A. R. AKHMEROV, T. M. KLAPWIJK, and L. M. K. VANDERSYPEN. *Zero-bias conductance peak and Josephson effect in graphene-NbTiN junctions*. Phys. Rev. B, **85**, 205 404, 2012. (see page: 72)

[193] W. A. LITTLE and R. D. PARKS. *Observation of quantum periodicity in the transition temperature of a superconducting cylinder*. Phys. Rev. Lett., **9**, 9–12, 1962. (see pages: 72, 81, and 87)

[194] S. M. ALBRECHT, A. HIGGINBOTHAM, M. MADSEN, F. KUEMMETH, T. S. JESPERSEN, J. NYGÅRD, P. KROGSTRUP, and C. MARCUS. *Exponential protection of zero modes in Majorana islands*. Nature, **531** (7593), 206, 2016. (see pages: 72, 81, 87, and 99)

[195] M. T. DENG, S. VAITIEKENAS, E. B. HANSEN, J. DANON, M. LEIJNSE, K. FLENSBERG, J. NYGÅRD, P. KROGSTRUP, and C. M. MARCUS. *Majorana bound state in a coupled quantum-dot hybrid-nanowire system*. Science, **354** (6319), 1557–1562, 2016.

[196] S. GAZIBEGOVIC, D. CAR, H. ZHANG, S. C. BALK, J. A. LOGAN, M. W. DE MOOR, M. C. CASSIDY, R. SCHMITS, D. XU, G. WANG, *et al. Epitaxy of advanced nanowire quantum devices*. Nature, **548** (7668), 434, 2017. (see pages: 72, 81, 87, 99, and 109)

[197] R. M. LUTCHYN, L. I. GLAZMAN, and A. I. LARKIN. *Kinetics of the superconducting charge qubit in the presence of a quasiparticle*. Phys. Rev. B, **74**, 064 515, 2006. (see page: 73)

[198] G. CATELANI, R. J. SCHOELKOPF, M. H. DEVORET, and L. I. GLAZMAN. *Relaxation and frequency shifts induced by quasiparticles in superconducting qubits*. Phys. Rev. B, **84**, 064 517, 2011. (see page: 73)

[199] J. AUMENTADO, M. W. KELLER, J. M. MARTINIS, and M. H. DEVORET. *Nonequilibrium quasiparticles and $2e$ periodicity in single-Cooper-pair transistors*. Phys. Rev. Lett., **92**, 066 802, 2004. (see page: 74)

[200] I. M. POP, K. GEERLINGS, G. CATELANI, R. J. SCHOELKOPF, L. I. GLAZMAN, and M. H. DEVORET. *Coherent suppression of electromagnetic dissipation due to superconducting quasiparticles*. Nature, **508** (7496), 369–72, 2014.

[201] U. VOOL, I. M. POP, K. SLIWA, B. ABDO, C. WANG, T. BRECHT, Y. Y. GAO, S. SHANKAR, M. HATRIDGE, G. CATELANI, M. MIRRAHIMI, L. FRUNZIO, R. J. SCHOELKOPF, *et al. Non-poissonian quantum jumps of a fluxonium qubit due to quasiparticle excitations*. Phys. Rev. Lett., **113**, 247 001, 2014. (see page: 74)

[202] K. W. CHAN, W. HUANG, C. H. YANG, J. C. C. HWANG, B. HENSEN, T. TANTTU, F. E. HUDSON, K. M. ITOH, A. LAUCHT, A. MORELLO, and A. S. DZURAK. *Assessment of a silicon quantum dot spin qubit environment via noise spectroscopy*. Phys. Rev. Appl., **10**, 044 017, 2018. (see pages: 78, 92)

[203] D. BOTHNER, C. CLAUSS, E. KOROKNAY, M. KEMMLER, T. GABER, M. JETTER, M. SCHEFFLER, P. MICHLER, M. DRESSEL, D. KOELLE, and R. KLEINER. *Reducing vortex losses in superconducting microwave resonators with microsphere patterned antidot arrays*. Appl. Phys. Lett., **100** (1), 012 601, 2012. (see pages: 80, 84, and 99)

[204] B. CHIARO, A. MEGRANT, A. DUNSWORTH, Z. CHEN, R. BARENDS, B. CAMPBELL, Y. CHEN, A. FOWLER, I. C. HOI, E. JEFFREY, J. KELLY, J. MUTUS, C. NEILL, *et al. Dielectric surface loss in superconducting resonators with flux-trapping holes*. Supercond. Sci. Technol., **29** (10), 104 006, 2016. (see page: 80)

[205] S. POSEN, M. K. TRANSTRUM, G. CATELANI, M. U. LIEPE, and J. P. SETHNA. *Shielding superconductors with thin films as applied to rf cavities for particle accelerators*. Phys. Rev. Appl., **4**, 044 019, 2015. (see pages: 80, 84, and 99)

[206] T. TAN, M. A. WOLAK, N. ACHARYA, A. KRICK, A. C. LANG, J. SLOPPY, M. L. TAHERI, L. CIVALE, K. CHEN, and X. X. XI. *Enhancement of lower critical field by reducing the thickness of epitaxial and polycrystalline MgB_2 thin films*. APL Materials, **3** (4), 041 101, 2015. (see pages: 80, 84, and 99)

[207] K. ZUO, V. MOURIK, D. B. SZOMBATI, B. NIJHOLT, D. J. VAN WOERKOM, A. GERESDI, J. CHEN, V. P. OSTROUKH, A. R. AKHMEROV, S. R. PLISSARD, D. CAR, E. P. A. M. BAKKERS, D. I. PIKULIN, *et al. Supercurrent interference in few-mode nanowire Josephson junctions*. Phys. Rev. Lett., **119**, 187 704, 2017. (see pages: 81, 94)

[208] J. D. S. BOMMER, H. ZHANG, Ö. GÜL, B. NIJHOLT, M. WIMMER, F. N. RYBAKOV, J. GARAUD, D. RODIC, E. BABAEV, M. TROYER, D. CAR, S. R. PLISSARD, E. P. A. M. BAKKERS, *et al. Spin-orbit protection of induced superconductivity in Majorana nanowires*. arXiv preprint arXiv:1807.01940, 2018. (see page: 81)

[209] M.-T. DENG, S. VAITIEKĖNAS, E. PRADA, P. SAN-JOSE, J. NYGÅRD, P. KROGSTRUP, R. AGUADO, and C. M. MARCUS. *Nonlocality of Majorana modes in hybrid nanowires*. Phys. Rev. B, **98**, 085 125, 2018. (see page: 81)

[210] S. BOGDANOVIĆ, S. B. VAN DAM, C. BONATO, L. C. COENEN, A.-M. J. ZWERVER, B. HENSEN, M. S. Z. LIDDY, T. FINK, A. REISERER, M. LONČAR, and R. HANSON. *Design and low-temperature characterization of a tunable microcavity for diamond-based quantum networks*. Appl. Phys. Lett., **110** (17), 171 103, 2017. (see page: 81)

[211] Ö. GÜL, H. ZHANG, J. D. BOMMER, M. W. DE MOOR, D. CAR, S. R. PLISSARD, E. P. BAKKERS, A. GERESDI, K. WATANABE, T. TANIGUCHI, *et al. Ballistic Majorana nanowire devices*. Nat. Nanotech., **13** (3), 192, 2018. (see pages: 81, 109)

[212] H. ZHANG, C.-X. LIU, S. GAZIBEGOVIC, D. XU, J. A. LOGAN, G. WANG, N. VAN LOO, J. D. BOMMER, M. W. DE MOOR, D. CAR, *et al. Quantized Majorana conductance*. Nature, **556** (7699), 74, 2018. (see page: 81)

[213] J. I.-J. WANG, D. RODAN-LEGRAIN, L. BRETHEAU, D. L. CAMPBELL, B. KANNAN, D. KIM, M. KJAERGAARD, P. KRANTZ, G. O. SAMACH, F. YAN, J. L. YODER, K. WATANABE, T. TANIGUCHI, *et al. Coherent control of a hybrid superconducting circuit made with graphene-based van der Waals heterostructures*. Nat. Nanotech., page 1, 2018. (see pages: 82, 105, and 107)

[214] J. KROLL, W. UILHOORN, K. VAN DER ENDEN, D. DE JONG, K. WATANABE, T. TANIGUCHI, S. GOSWAMI, M. CASSIDY, and L. KOUWENHOVEN. *Magnetic field compatible circuit quantum electrodynamics with graphene Josephson junctions*. Nat. Comm., **9** (1), 4615, 2018. (see pages: 82, 105, and 107)

[215] J. SHABANI, M. KJAERGAARD, H. J. SUOMINEN, Y. KIM, F. NICHELE, K. PAKROUSKI, T. STANKEVIC, R. M. LUTCHYN, P. KROGSTRUP, R. FEIDENHANS'L, S. KRAEMER, C. NAYAK, M. TROYER, *et al. Two-dimensional epitaxial superconductor-semiconductor heterostructures: A platform for topological superconducting networks*. Phys. Rev. B, **93**, 155 402, 2016. (see page: 82)

[216] H. J. SUOMINEN, J. DANON, M. KJAERGAARD, K. FLENSBERG, J. SHABANI, C. J. PALMSTRØM, F. NICHELE, and C. M. MARCUS. *Anomalous Fraunhofer interference in epitaxial superconductor-semiconductor Josephson junctions*. Phys. Rev. B, **95**, 035 307, 2017. (see page: 85)

[217] J. E. HEALEY, T. LINDSTRÖM, M. S. COLCLOUGH, C. M. MUIRHEAD, and A. Y. TZALENCHUK. *Magnetic field tuning of coplanar waveguide resonators*. Appl. Phys. Lett., **93** (4), 043 513, 2008. (see page: 85)

[218] MAGNETIC SHIELDS LTD. *MuMetal technical data*, 2018. (see page: 92)

[219] C. SONG, M. P. DEFEO, K. YU, and B. L. T. PLOURDE. *Reducing microwave loss in superconducting resonators due to trapped vortices*. Appl. Phys. Lett., **95** (23), 232 501, 2009. (see page: 92)

[220] K. YU, T. W. HEITMANN, C. SONG, M. P. DEFEO, B. L. T. PLOURDE, M. B. S. HESSELBERTH, and P. H. KES. *Asymmetric weak-pinning superconducting channels: Vortex ratchets*. Phys. Rev. B, **76**, 220 507, 2007. (see page: 92)

[221] S. YAMAMOTO and T. YAMADA. *Initial magnetic field decay of the superconducting magnet in persistent current mode*. IEEE T. Magnetics, **24** (2), 1292–1294, 1988. (see page: 93)

[222] T. W. LARSEN. *Mesoscopic superconductivity towards protected qubits*. PhD Dissertation, University of Copenhagen, 2018. (see pages: 94, 106, and 109)

[223] G. W. WINKLER, A. E. ANTIPOV, B. VAN HECK, A. A. SOLUYANOV, L. I. GLAZMAN, M. WIMMER, and R. M. LUTCHYN. *A unified numerical approach to semiconductor-superconductor heterostructures*. arXiv preprint arXiv:1810.04180, 2018. (see page: 95)

[224] S. VAITIEKĖNAS, M.-T. DENG, P. KROGSTRUP, and C. MARCUS. *Flux-induced Majorana modes in full-shell nanowires*. arXiv preprint arXiv:1809.05513, 2018. (see page: 95)

[225] R. M. LUTCHYN, G. W. WINKLER, B. VAN HECK, T. KARZIG, K. FLENSBERG, L. I. GLAZMAN, and C. NAYAK. *Topological superconductivity in full shell proximitized nanowires*. arXiv preprint arXiv:1809.05512, 2018. (see page: 95)

[226] L. TOSI, C. METZGER, M. GOFFMAN, C. URBINA, H. POTHIER, S. PARK, A. L. YEYATI, J. NYGÅRD, and P. KROGSTRUP. *Spin-orbit splitting of Andreev states revealed by microwave spectroscopy*. arXiv preprint arXiv:1810.02591, 2018. (see page: 96)

[227] F. MALLET, F. R. ONG, A. PALACIOS-LALOY, F. NGUYEN, P. BERTET, D. VION, and D. ESTEVE. *Single-shot qubit readout in circuit quantum electrodynamics*. Nat. Phys., **5**, 791–795, 2009. (see page: 97)

[228] M. D. REED, L. DICARLO, B. R. JOHNSON, L. SUN, D. I. SCHUSTER, L. FRUNZIO, and R. J. SCHOELKOPF. *High-fidelity readout in circuit quantum electrodynamics using the Jaynes-Cummings nonlinearity*. Phys. Rev. Lett., **105**, 173 601, 2010. (see page: 97)

[229] E. J. WOLLACK, R. E. KINZER, and S. A. RINEHART. *A cryogenic infrared calibration target*. Rev. Sci. Instrum., **85** (4), 044 707, 2014. (see page: 97)

[230] X. Y. JIN, A. KAMAL, A. P. SEARS, T. GUDMUNDSEN, D. HOVER, J. MILOSHI, R. SLATTERY, F. YAN, J. YODER, T. P. ORLANDO, S. GUSTAVSSON, and W. D. OLIVER. *Thermal and residual excited-state population in a 3D transmon qubit*. Phys. Rev. Lett., **114**, 240 501, 2015. (see page: 98)

[231] L. P. ROKHINSON, X. LIU, and J. K. FURDYNA. *The fractional ac Josephson effect in a semiconductor–superconductor nanowire as a signature of Majorana particles*. Nat. Phys., **8** (11), 795, 2012. (see page: 102)

[232] S. DE GRAAF, L. FAORO, J. BURNETT, A. ADAMYAN, A. Y. TZALENCHUK, S. KUBATKIN, T. LINDSTRÖM, and A. DANILOV. *Suppression of low-frequency charge noise in superconducting resonators by surface spin desorption*. Nat. Comm., **9** (1), 1143, 2018. (see page: 104)

[233] R. BARENDS, J. KELLY, A. MEGRANT, A. VEITIA, D. SANK, E. JEFFREY, T. C. WHITE, J. MUTUS, A. G. FOWLER, B. CAMPBELL, Y. CHEN, Z. CHEN, B. CHIARO, *et al. Superconducting quantum circuits at the surface code threshold for fault tolerance*. Nature, **508** (7497), 500, 2014. (see page: 105)

[234] R. BARENDS, L. LAMATA, J. KELLY, L. GARCÍA-ÁLVAREZ, A. FOWLER, A. MEGRANT, E. JEFFREY, T. WHITE, D. SANK, J. MUTUS, B. CAMPBELL, Y. CHEN, Z. CHEN, *et al. Digital quantum simulation of fermionic models with a superconducting circuit*. Nat. Comm., **6**, 7654, 2015. (see page: 105)

[235] A. KANDALA, A. MEZZACAPO, K. TEMME, M. TAKITA, M. BRINK, J. M. CHOW, and J. M. GAMBETTA. *Hardware-efficient variational quantum eigensolver for small molecules and quantum magnets*. Nature, **549** (7671), 242, 2017.

[236] A. KANDALA, K. TEMME, A. D. CORCOLES, A. MEZZACAPO, J. M. CHOW, and J. M. GAMBETTA. *Extending the computational reach of a noisy superconducting quantum processor*. arXiv preprint arXiv:1805.04492, 2018. (see page: 105)

[237] C. JANVIER, L. TOSI, L. BRETHEAU, Ç. GIRIT, M. STERN, P. BERTET, P. JOYEZ, D. VION, D. ESTEVE, M. GOFFMAN, H. POTHIER, and C. URBINA. *Coherent manipulation of Andreev states in superconducting atomic contacts*. Science, **349** (6253), 1199–1202, 2015. (see page: 105)

[238] F. KRIZEK, J. E. SESTOFT, P. ASEEV, S. MARTI-SANCHEZ, S. VAITIEKĖNAS, L. CASPARIS, S. A. KHAN, Y. LIU, T. C. V. STANKEVIČ, A. M. WHITICAR, A. FURSINA, F. BOEKHOUT, R. KOOPS, *et al. Field effect enhancement in buffered quantum nanowire networks*. Phys. Rev. Materials, **2**, 093 401, 2018. (see page: 105)

[239] A. K. GEIM and I. V. GRIGORIEVA. *Van der Waals heterostructures*. Nature, **499** (7459), 419, 2013. (see page: 105)

[240] M. GONG, M.-C. CHEN, Y. ZHENG, S. WANG, C. ZHA, H. DENG, Z. YAN, H. RONG, Y. WU, S. LI, F. CHEN, Y. ZHAO, F. LIANG, *et al. Genuine 12-qubit entanglement on a superconducting quantum processor*. arXiv preprint arXiv:1811.02292, 2018. (see pages: 105, 106)

[241] D. P. FRANKE, J. S. CLARKE, L. M. VANDERSYPEN, and M. VELDHORST. *Rent's rule and extensibility in quantum computing*. arXiv preprint arXiv:1806.02145, 2018. (see page: 105)

[242] L. DICARLO, J. M. CHOW, J. M. GAMBETTA, L. S. BISHOP, B. R. JOHNSON, D. I. SCHUSTER, J. MAJER, A. BLAIS, L. FRUNZIO, S. M. GIRVIN, and R. J. SCHOELKOPF. *Demonstration of two-qubit algorithms with a superconducting quantum processor*. Nature, **460**, 240, 2009. (see page: 106)

[243] J. M. MARTINIS and M. R. GELLER. *Fast adiabatic qubit gates using only σ_z control*. Phys. Rev. A, **90**, 022 307, 2014. (see page: 106)

[244] R. C. BIALCZAK, M. ANSMANN, M. HOFHEINZ, M. LENANDER, E. LUCERO, M. NEELEY, A. D. O'CONNELL, D. SANK, H. WANG, M. WEIDES, J. WENNER, T. YAMAMOTO, A. N. CLELAND, *et al. Fast tunable coupler for superconducting qubits*. Phys. Rev. Lett., **106**, 060 501, 2011. (see page: 106)

[245] Y. CHEN, C. NEILL, P. ROUSHAN, N. LEUNG, M. FANG, R. BARENDS, J. KELLY, B. CAMPBELL, Z. CHEN, B. CHIARO, A. DUNSWORTH, E. JEFFREY, A. MEGRANT, *et al. Qubit architecture with high coherence and fast tunable coupling*. Phys. Rev. Lett., **113**, 220 502, 2014.

[246] D. C. MCKAY, S. FILIPP, A. MEZZACAPO, E. MAGESAN, J. M. CHOW, and J. M. GAMBETTA. *Universal gate for fixed-frequency qubits via a tunable bus*. Phys. Rev. Appl., **6**, 064 007, 2016. (see page: 106)

[247] K. S. NOVOSELOV, A. K. GEIM, S. V. MOROZOV, D. JIANG, M. I. KATSNELSON, I. V. GRIGORIEVA, S. V. DUBONOS, and A. A. FIRSOV. *Two-dimensional gas of massless Dirac fermions in graphene*. Nature, **438** (7065), 197, 2005. (see page: 107)

[248] V. E. CALADO, S. GOSWAMI, G. NANDA, M. DIEZ, A. R. AKHMEROV, K. WATANABE, T. TANIGUCHI, T. M. KLAPWIJK, and L. M. VANDERSYPEN. *Ballistic Josephson junctions in edge-contacted graphene*. Nat. Nanotech., **10** (9), 761–764, 2015.

[249] M. B. SHALOM, M. ZHU, V. FAL'KO, A. MISHCHENKO, A. KRETININ, K. NOVOSELOV, C. WOODS, K. WATANABE, T. TANIGUCHI, A. GEIM, *et al. Quantum oscillations of the critical current and high-field superconducting proximity in ballistic graphene*. Nat. Phys., **12** (4), 318–322, 2016. (see page: 107)

[250] F. E. SCHMIDT, M. D. JENKINS, K. WATANABE, T. TANIGUCHI, and G. A. STEELE. *A ballistic graphene superconducting microwave circuit*. Nat. Comm., **9** (1), 4069, 2018. (see page: 107)

[251] D. J. VAN WOERKOM, A. PROUTSKI, R. J. J. VAN GULIK, T. KRIVÁCHY, D. CAR, S. R. PLISSARD, E. P. A. M. BAKKERS, L. P. KOUWENHOVEN, and A. GERESDI. *Josephson radiation and shot noise of a semiconductor nanowire junction*. Phys. Rev. B, **96**, 094 508, 2017. (see page: 107)

[252] A. PROUTSKI, D. LAROCHE, B. V. HOOFT, P. KROGSTRUP, J. NYGÅRD, L. P. KOUWENHOVEN, and A. GERESDI. *Broadband microwave spectroscopy of semiconductor nanowire-based Cooper-pair transistors*. arXiv preprint arXiv:1901.10992, 2019. (see page: 107)

[253] E. GINOSSAR and E. GROSFELD. *Microwave transitions as a signature of coherent parity mixing effects in the Majorana-transmon qubit*. Nat. Comm., **5**, 4772, 2014. (see pages: 107, 108)

[254] A. Y. KITAEV. *Unpaired Majorana fermions in quantum wires*. Physics-Uspekhi, **44** (10S), 131, 2001. (see page: 108)

[255] D. M. VAN ZANTEN, D. SABONIS, J. SUTER, J. I. VÄYRYNEN, T. KARZIG, D. I. PIKULIN, E. C. O'FARRELL, D. RAZMADZE, K. D. PETERSSON, P. KROGSTRUP, and C. M. MARCUS. *Photon assisted tunneling of zero modes in a Majorana wire*. arXiv preprint arXiv:1902.00797, 2019. (see page: 109)

[256] Y. KUBO, I. DINIZ, C. GREZES, T. UMEDA, J. ISOYA, H. SUMIYA, T. YAMAMOTO, H. ABE, S. ONODA, T. OHSHIMA, V. JACQUES, A. DRÉAU, J.-F. ROCH, *et al.* *Electron spin resonance detected by a superconducting qubit*. Phys. Rev. B, **86**, 064 514, 2012. (see page: 109)

[257] C. GREZES, B. JULSGAARD, Y. KUBO, M. STERN, T. UMEDA, J. ISOYA, H. SUMIYA, H. ABE, S. ONODA, T. OHSHIMA, V. JACQUES, J. ESTEVE, D. VION, *et al.* *Multimode storage and retrieval of microwave fields in a spin ensemble*. Phys. Rev. X, **4**, 021 049, 2014. (see page: 109)

[258] Y. TABUCHI, S. ISHINO, A. NOGUCHI, T. ISHIKAWA, R. YAMAZAKI, K. USAMI, and Y. NAKAMURA. *Coherent coupling between a ferromagnetic magnon and a superconducting qubit*. Science, **349** (6246), 405–408, 2015. (see page: 109)

[259] D. LACHANCE-QUIRION, Y. TABUCHI, S. ISHINO, A. NOGUCHI, T. ISHIKAWA, R. YAMAZAKI, and Y. NAKAMURA. *Resolving quanta of collective spin excitations in a millimeter-sized ferromagnet*. Science Advances, **3** (7), 2017. (see page: 109)

[260] E. KAWAKAMI, P. SCARLINO, D. R. WARD, F. BRAAKMAN, D. SAVAGE, M. LAGALLY, M. FRIESEN, S. N. COPPERSMITH, M. A. ERIKSSON, and L. VANDERSYPEN. *Electrical control of a long-lived spin qubit in a Si/SiGe quantum dot*. Nat. Nanotech., **9** (9), 666, 2014. (see page: 109)

[261] X. MI, J. V. CADY, D. M. ZAJAC, P. W. DEELMAN, and J. R. PETTA. *Strong coupling of a single electron in silicon to a microwave photon*. Science, **355** (6321), 156–158, 2017. (see page: 109)

[262] A. STOCKKLAUSER, P. SCARLINO, J. V. KOSKI, S. GASPARINETTI, C. K. ANDERSEN, C. REICHL, W. WEGSCHEIDER, T. IHN, K. ENSSLIN, and A. WALLRAFF. *Strong coupling cavity QED with gate-defined double quantum dots enabled by a high impedance resonator*. Phys. Rev. X, **7**, 011 030, 2017. (see page: 109)

[263] A. M. TYRYSHKIN, S. TOJO, J. J. L. MORTON, H. RIEMANN, N. V. ABROSIMOV, P. BECKER, H.-J. POHL, T. SCHENKEL, M. L. W. THEWALT, K. M. ITOH, and S. A. LYON. *Electron spin coherence exceeding seconds in high-purity silicon*. Nat. Mater., **11**, 143, 2012. (see page: 109)

[264] M. VELDHORST, J. HWANG, C. YANG, A. LEENSTRA, B. DE RONDE, J. DEHOLLAIN, J. MUHONEN, F. HUDSON, K. M. ITOH, A. MORELLO, and A. DZURAK. *An addressable quantum dot qubit with fault-tolerant control-fidelity*. Nat. Nanotech., **9** (12), 981, 2014.

[265] S. ROCHETTE, M. RUDOLPH, A.-M. ROY, M. CURRY, G. T. EYCK, R. MANGINELL, J. WENDT, T. PLUYM, S. CARR, D. WARD, M. LILLY, M. CARROLL, and M. PIORO-LADIÈRE. *Single-electron-occupation metal-oxide-semiconductor quantum dots formed from efficient poly-silicon gate layout*. arXiv preprint arXiv:1707.03895, 2017.

[266] G. ZHENG, N. SAMKHARADZE, M. NOORDAM, N. KALHOR, D. BROUSSE, A. SAMMAK, G. SCAPPUCCI, and L. VANDERSYPEN. *Rapid high-fidelity gate-based spin read-out in silicon*. arXiv preprint arXiv:1901.00687, 2019. (see page: 109)

[267] X. MI, M. BENITO, S. PUTZ, D. M. ZAJAC, J. M. TAYLOR, G. BURKARD, and J. R. PETTA. *A coherent spin–photon interface in silicon*. Nature, **555** (7698), 599, 2018. (see page: 109)

[268] J. MAJER, J. M. CHOW, J. M. GAMBETTA, B. R. JOHNSON, J. A. SCHREIER, L. FRUNZIO, D. I. SCHUSTER, A. A. HOUCK, A. WALLRAFF, A. BLAIS, M. H. DEVORET, S. M. GIRVIN, and R. J. SCHOELKOPF. *Coupling superconducting qubits via a cavity bus*. Nature, **449**, 443, 2007. (see page: 110)

[269] M. A. SILLANPÄÄ, J. I. PARK, and R. W. SIMMONDS. *Coherent quantum state storage and transfer between two phase qubits via a resonant cavity*. Nature, **449**, 438, 2007. (see page: 110)

[270] B. ABDO, F. SCHACKERT, M. HATRIDGE, C. RIGETTI, and M. DEVORET. *Josephson amplifier for qubit readout*. Appl. Phys. Lett., **99** (16), 162 506, 2011. (see page: 112)

[271] R. VIJAY, D. H. SLICHTER, and I. SIDDIQI. *Observation of quantum jumps in a superconducting artificial atom*. Phys. Rev. Lett., **106**, 110 502, 2011.

[272] C. MACKLIN, K. O'BRIEN, D. HOVER, M. E. SCHWARTZ, V. BOLKHOVSKY, X. ZHANG, W. D. OLIVER, and I. SIDDIQI. *A near–quantum-limited Josephson traveling-wave parametric amplifier*. Science, **350** (6258), 307–310, 2015. (see page: 112)

[273] C. DICKEL. *Scalability and modularity for transmon-based quantum processors*. PhD Dissertation, TU Delft, 2018. (see page: 114)

[274] M. ROL, C. DICKEL, S.ASAAD, N. LANGFORD, C. BULTINK, R. SAGASTIZABAL, N. LANGFORD, G. DE LANGE, X. FU, S. DE JONG, F. LUTHI, and W. VLOTHUIZEN. *PycQED*, 2016. (see page: 114)

[275] F. POBELL. *Matter and methods at low temperatures*. Springer, 3 edition, 2007. (see page: 115)